Lanthanide Energy Transfer Donors on Nanoparticles Surfaces : From Fundamental Mechanisms to Multiplexed Biosensing

Chi Chen

université PARIS-SACLAY

NNT : 2019SACLS196

UNIVERSITÉ PARIS SUD
Comprendre le monde, construire l'avenir

Lanthanide Energy Transfer Donors on Nanoparticles Surfaces: From Fundamental Mechanisms to Multiplexed Biosensing

Thèse de doctorat de l'Université Paris-Saclay
Préparée à l'Université Paris-Sud

École doctorale n°575 :
electrical, optical, bio : physics and engineering (EOBE)

Spécialité de doctorat: Physique
(Electronique et Optoélectronique, Nano et Microtechnologies)

Thèse présentée et soutenue à Orsay, le 5 Juillet 2019, par

M. Chi Chen

Composition du Jury :

Mme Fabienne Mérola Directrice de Recherche, Université Paris-Sud	Présidente
Mme Adriana Zaleska-Medynska Professeur, University of Gdansk	Rapporteur
M. Thomas Just Sørensen Professeur, University of Copenhagen	Rapporteur
M. Christophe Dubessy Maître de Conférences, Université de Rouen	Examinateur
M. Niko Hildebrandt Professeur, Université Paris-Sud	Directeur de thèse

Thèse de doctorat

université PARIS-SACLAY

ÉCOLE DOCTORALE
Physique et ingénierie : électrons, photons, sciences du vivant (EOBE)

Titre : Transfert d'énergie entre lanthanides et nanoparticules: des mécanismes fondamentaux aux biosenseurs multiplexés

Mots clés : points quantiques, terbium, multiplexage, fluorescence, code à barres, FRET

Résumé : Le multiplexage optique basé sur des nanoparticules offre de nombreux avantages pour la biodétection et l'imagerie à multiparamètres. Toutefois, les modifications apportées à un paramètre entraînent également la modification d'autres paramètres. Par conséquent, la couleur, la durée de vie ou l'intensité ne peuvent pas être utilisées, respectivement, comme paramètre indépendant. Cette thèse peut être divisée en deux aspects. Le premier concerne le développement d'un multiplexage à une seule nanoparticule avec un temps résolu, basé sur le transfert d'énergie par résonance de type Förster (FRET) des complexes de lanthanides aux points quantiques (QD) et ensuite aux colorants fluorescents. Une investigation systématique de toutes les différentes combinaisons avec une large gamme de donneurs et d'accepteurs sur le QD est présentée, et les résultats expérimentaux sont comparés à la modélisation théorique. Le résultat ne contribue pas seulement à une compréhension complète de ces voies de transfert d'énergie compliquée entre multi donneurs / accepteurs sur des nanoparticules, mais offre également la possibilité d'utiliser les modèles pour développer de nouvelles stratégies permettant de preparer le QD avec une couleur, une durée de vie et une intensité réglables de manière indépendante. Le deuxième aspect porte sur le mécanisme de transfert d'énergie du Tb à la nanoparticule d'or (AuNP). Le transfert d'énergie par nanosurface (NSET) s'est révélé être un mécanisme opérationnel pour l'extinction des PL par les AuNP, une information importante pour le développement, la caractérisation et l'application de nanobiocapteurs basés sur l'extinction des PL par les AuNP.

Title : Lanthanide energy transfer donors on nanoparticles surfaces: from fundamental mechanisms to multiplexed biosensing

Keywords : quantum dots, terbium, multiplexing, fluorescence, barcoding, FRET

Abstract : Optical multiplexing based on nanoparticles provides many advantages for multiparameter biosensing and imaging. However, the changes in one parameter also lead to changing of other parameters, and thus, color, lifetime, or intensity could not be used as an independent parameter, respectively. This thesis can be divided into two aspects. The first one focuses on developing time-resolved single-nanoparticle multiplexing based on Förster resonance energy transfer (FRET) from lanthanide complexes to quantum dot (QD) to fluorescent dyes. Systematical investigation of all different combinations with a broad range of numbers of donors and acceptors on QD are presented, and the experimental results are compared with theoretical modelling. The result do not only contribute to a full understanding of such complicated multi donor-acceptor energy transfer pathways on nanoparticles but also open the opportunity to use the models for developing new strategies to achieve the QD with independent tunable color, lifetime and intensity. The second aspect focuses on the energy transfer mechanism from Tb to gold nanoparticle (AuNP). Nanosurface energy transfer (NSET) proved to be an operational mechanism in PL quenching by AuNPs, which is important information for the development, characterization, and application of nanobiosensors based on PL quenching by AuNPs.

Université Paris-Saclay
Espace Technologique / Immeuble Discovery
Route de l'Orme aux Merisiers RD 128 / 91190 Saint-Aubin, France

To my beautiful, talented, and curious wife Xin Geng.

Acknowledgment

First and foremost I would like to express my special appreciation my supervisor Prof. Niko Hildebrandt, who provided many precious opportunities and constant support during my PhD and acted as a role model to me not only academically but also in life. There are many things Niko has taught me, but nothings was more precious than his enthusiasm to pursue pure science and push the boundaries of human knowledge (*e.g.*, FRET). I still remember one day we discussed a huge and complicated work, and he said: "I know all of this takes a long time but this is what science is actually about. We need to remember that we are primarily making science for science and not for our career. "

I thank Prof. Adriana Zaleska-Medynska and Prof. Thomas Just Sørensen for being the reviewers of my PhD thesis.

I also want to thank our collaborators Dr. Liang Huang, Dr. Martinus H. V. Werts, Dr. Jurriaan M. Zwier, and Prof. Ben Corry for their kindness, availability and scientific support, and all the co-authors of my publications.

Many thanks to all former and current members of the NanoBioPhotonics group. My special thanks to Dr. Shashi Bhuckory, Dr. Yu-Tang Wu, and Dr. Xue Qiu for their continuous guidance, patience and valuable time devoted in sharing their technical and scientific knowledge with me. I also thank Dr. Marcelina Cardoso Dos Santos, Vjona Cifliku, and Meryem Sennad for cell culture.

I also want to thank Carlos Mingoes and Tudor Haruta for translating in hospital when I was injured, Dr. Xavier Zambrana Puyalto for suggesting the funny book

"Surely You're Joking, Mr. Feynman!", Dr. Akram Yahia-Ammar for translating in CPMA, Dr. Mariia Dekaliuk for helping to find a nice apartment near our lab, Jiajia Guo and Jingyue Xu for providing real hot food when I first came to France, and Bilguissou Diallo for her help with translation of my abstract,

I thank the IDEX Paris-Saclay (Investissements d'avenir) for my PhD fellowship.

Of course, thanks must go to my parents. They do not speak English and have no idea what nanophotonics is, but they always try their best to support and encourage me in every possible way.

Last but not least, my deepest gratitude goes to my wonderful wife Xin Geng. Although she is not a scientist, she always listens curiously to me for sharing my research ideas. The idea of single-nanoparticle barcoding is inspired from a talk in which I want to explain her the spectroscopic ruler. Without her companionship and encouragement, it would have been impossible for me to go through the last three years with full of enthusiasm.

These days in Paris were the happiest three years I have had. Not only FRET theory from "*Captain FRET*", I also learned a lot of art and culture knowledge from the museums. Thanks to everyone I have met along the way.

List of publications

Original publications

1. Chi Chen, Ben Corry, Liang Huang, Niko Hildebrandt. FRET-Modulated Multihybrid Nanoparticles for Brightness-Equalized Single-Wavelength Barcoding. *Journal of the American Chemical Society* **2019**, *141*, 11123-11141.

2. Chi Chen, Lijiao Ao, Yu-Tang Wu, Vjona Cifliku, Marcelina Cardoso Dos Santos, Emmanuel Bourrier, Martina Delbianco, David Parker, Jurriaan M. Zwier, Liang Huang, Niko Hildebrandt. Single-Nanoparticle Cell Barcoding by Tunable FRET from Lanthanides to Quantum Dots. *Angewandte Chemie International Edition* **2018**, *41*, 13686-13690.

3. Chi Chen, Clyde Midelet, Shashi Bhuckory, Niko Hildebrandt, and Martinus H. V. Werts. Nanosurface Energy Transfer from Long-Lifetime Terbium Donors to Gold Nanoparticles. *The Journal of Physical Chemistry C* **2018**, *122*, 17566-17574.

4. Chi Chen, Pengfei Zhang, Li Zhang, Duyang Gao, Guanhui Gao, Yong Yang, Wenjun Li, Ping Gong, Lintao Cai. Long-Decay Near-Infrared-Emitting Doped-Quantum Dots for Lifetime-Based in Vivo pH Imaging. *Chemical Communications* **2015**, *51*, 11162-11165.

5. Chi Chen, Pengfei Zhang, Guanhui Gao, Duyang Gao, Yong Yang, Hong Liu, Yuhui Wang, Ping Gong, Lintao Cai. Near-Infrared-Emitting Two-Dimensional Codes Based on Lattice-Strained Core/(Doped) Shell Quantum Dots with Long Fluorescence Lifetime. *Advanced Material* **2014**, *26*, 6313-6317.

6. Chi Chen, Xuewen He, Li Gao, Nan Ma. Cation Exchange-Based Facile Aqueous Synthesis of Small, Stable, and Nontoxic Near-Infrared Ag_2Te/ZnS Core/Shell Quantum Dots Emitting in the Second Biological Window. *ACS Applied Materials & Interfaces* **2013**, *5*, 1149-1155.

7. Guanhui Gao, Chi Chen, Xiaobin Xie, Yantao Su, Shendong Kang, Guichi Zhu, Duyang Gao, Achim Trampert, Lintao Cai. Toward Edges-Rich MoS_2 Layers via

Chemical Liquid Exfoliation Triggering Distinctive Magnetism. *Materials Research Letters* **2017**, *5*, 267-275.

8. Li Zhang, Chi Chen, Wenjun Li, Guanhui Gao, Ping Gong, Lintao Cai. Living Cell Multilifetime Encoding Based on Lifetime-Tunable Latticed-Strained Quantum Dots. *ACS Applied Materials & Interfaces* **2016**, *8*, 13187-13191.

Oral presentations

1. Chi Chen, Niko Hildebrandt. Live-Cell Encoding by Single-Nanoparticle FRET Multiplexing. *ACS National Meeting & Exposition*, Orlando, USA, **2019**, 31/03-04/04.

2. Chi Chen, Niko Hildebrandt. Particle Encoding using Terbium-to-Quantum Dot FRET. *8th International Colloids conference*, Shanghai, China, **2018**, 10/06-13/06.

Poster presentations

1. Chi Chen, Clyde Midelet, Shashi Bhuckory, Martinus H. V. Werts, Niko Hildebrandt. Resonance Energy Transfer to Gold Nanoparticles Explained by Long-Lifetime Terbium Donors. *10th International Conference on f-Elements (ICFE-10),* Lausanne, Switzerland, **2018**, 03/09-06/09.

Contents

1. Introduction

"Every science begins as philosophy and ends as art; it arises in hypothesis and flows into achievement."

— Will Durant

This sentence is from a book called "The Story of Philosophy". Or we also can call it "The beauty of Philosophy". We know the natural philosophy is considered to be the precursor of natural science. But why every science ends as art? What is art? In my opinion, art is the expression of imaginative, conceptual, original ideas with technical skill and emotional power, or we can say beauty is art. Euler's Identity shows a profound connection between the most fundamental numbers in mathematics and exhibits the mathematical beauty. Maxwell's Equations establish unified electromagnetic theory. They bring together electricity, magnetism, and light as different manifestations of the same phenomenon, and show the physical beauty. I also want to discovery the beauty in my research field, and I believe it has been there.

The aim of this thesis is to study the Förster resonance energy transfer (FRET) mechanism in lanthanides-quantum dot (QD)-fluorescent dyes systems and utilize the FRET modulated multi-hybrid nanoparticle for time-resolved multiplexing, and the study of energy transfer mechanism from long lifetime Tb donors to gold nanoparticles (AuNPs). Time-resolved multiplexing has many advantages, and we also find the beauty of time based multiplexing. The three temporal optical detection windows can be regarded as metaphor of the three clocks in Dali's "The Persistence of Memory" (**Figure 1.1 right**). Inspired by this painting, we designed this picture (**Figure 1.1 left**), in which the three clocks with red, green, and blue color perfectly represent the idea of that were used for RGB (red, green, blue) barcoding. Other elements in this painting have also been replaced by the materials using in our study, including a single-nanoparticle assembly (orange

clock covered by ants in the original) on the bottom left, a microscope objective (the "monster" in the original) in the center (below the blue clock), and a microscope slide with encoding cells (the platform or pool in the original) on the top left.

Figure 1.1. The imitative work of "The Persistence of Memory" **(left)** and the original painting by Salvador Dali **(right)**.

The first study (**Chapter 3**) demonstrates the possibility of single-nanoparticle cell barcoding based on lanthanides complex to QD FRET. In order to obtain the optical encoding with higher capacity, the majority of principle was mixing of different luminescent molecules or nanoparticles in microbeads or cells. Designing different concentration-independent codes without mixing various nanoparticles and by using single-wavelength excitation and emission for multiplexed imaging is extremely challenging. As illustrated in **Figure 1.2**, we report the synthesis of QDs coated with SiO_2 of different shell thicknesses (6 and 12 nm). Attachment of lanthanide (Ln) complexes (Tb and Eu) with long photoluminescence(PL)-lifetimes on the SiO_2 shells resulted in different Ln-to-QD distances, which, in turn, led to different PL decay times due to distance-dependent FRET. Thus, four specific QD PL decays (all at 640 nm upon excitation of the Ln complexes at 349 nm) were designed with Tb-QD (SiO_2-6nm), Tb-QD (SiO_2-12nm), Eu-QD (SiO_2-6nm), and Eu-QD (SiO_2-12nm) and used as well-defined single-particle codes to label live cells. To recognize the live-cell codes, time-gated fluorescence microscopy was employed and four different cell types could be distinguished by a single measurement. The information density of the single particle encoding can be further enlarged by using

donors with various Ln complexes and QD acceptors with different colors. Thus, our time-gated Ln-to-QD FRET concept has the potential to significantly advance fluorescence cell-encoding. However, one important drawback of this strategy is the significant variation in brightness of the different codes. We will address this issue in the second study.

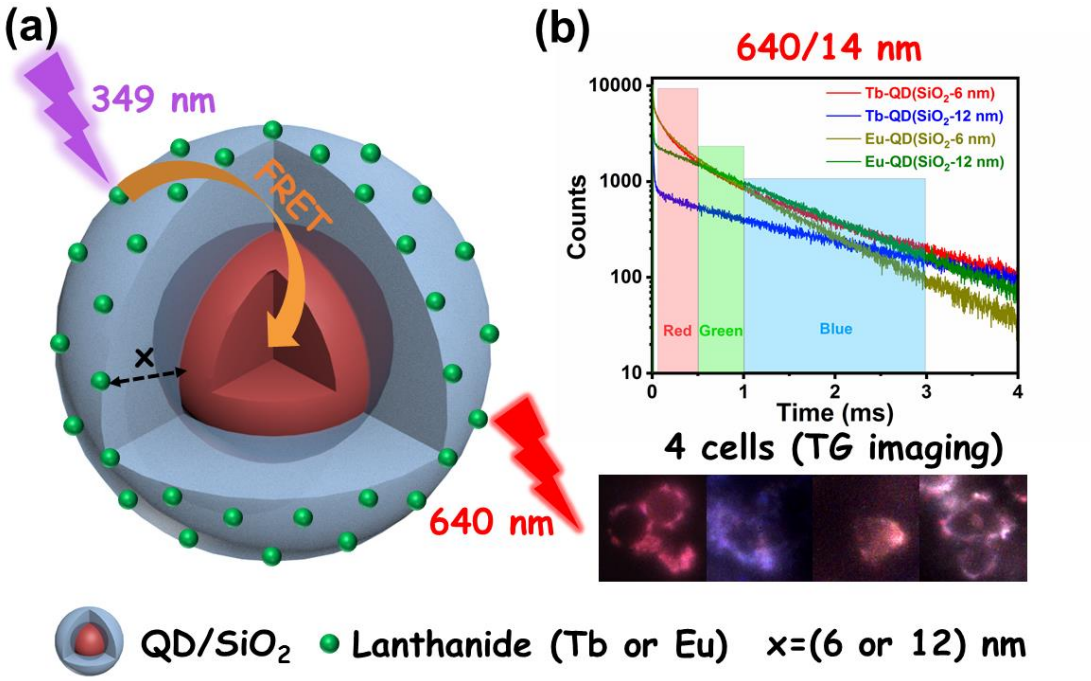

Figure 1.2. **(a)** QDs with SiO_2 coatings of different thicknesses (x=6 or 12 nm) functionalized with Eu-1 or Lumi4-Tb for single-wavelength temporal PL barcoding. **(b)** The RGB encoding principle based on three distinct TG PL intensity fractions for each of the four FRET-specific PL decays and four encoded cells.

The second study (**Chapter 4**) focuses on multiple donor-acceptor FRET systems with QDs. QDs are the most versatile fluorophores for FRET because they can function as both donor and acceptor for a multitude of fluorophores attached to their surface. However, a complete understanding of multi-donor-acceptor FRET networks on QDs and their full employment into advanced fluorescence sensing and imaging have not been accomplished. In this chapter, we provide a holistic photophysical analysis of such multi-donor-QD-multi-acceptor FRET systems using time-resolved and steady-state PL spectroscopy and Monte Carlo simulations. Multiple terbium-complex (Tb) donors (1 to 191 units) and Cy5.5 dye acceptors (1 to 60 units) were attached to a central QD and the entire range of combinations of single and multiple FRET pathways was investigated by Tb, QD,

and Cy5.5 PL. Experimental and simulation results were in excellent agreement and could disentangle the distinct contributions of hetero-FRET, homo-FRET, and dye-dimerization. The FRET efficiency was independent of the number of Tb donors and dependent of the number of Cy5.5 acceptors, which could be used to independently adapt the PL intensity by the number of Tb donors and PL lifetime by the number of Cy5.5 acceptors. As shown in **Figure 1.3**, we used this unique tuning capability to prepare Tb-QD-Cy5.5 conjugates with distinct QD PL lifetimes but similar QD PL intensities. These brightness-equalized multi-hybrid FRET nanoparticles were applied to optical barcoding via three time-gated PL intensity detection windows, which resulted in an encoding of the distinct PL decay curves into simple RGB ratios. Direct applicability was demonstrated by an efficient RGB distinction of different nanoparticle-encoded microbeads within the same field of view with both single-wavelength excitation and detection on a standard fluorescence microscope. In addition to imaging and biosensing, controlled photophysical tuning of FRET-modulated multi-hybrid QDs for single-wavelength PL encoding has the potential to advance other photonic applications, such as data storage, security labeling, optogenetics, or molecular computing.

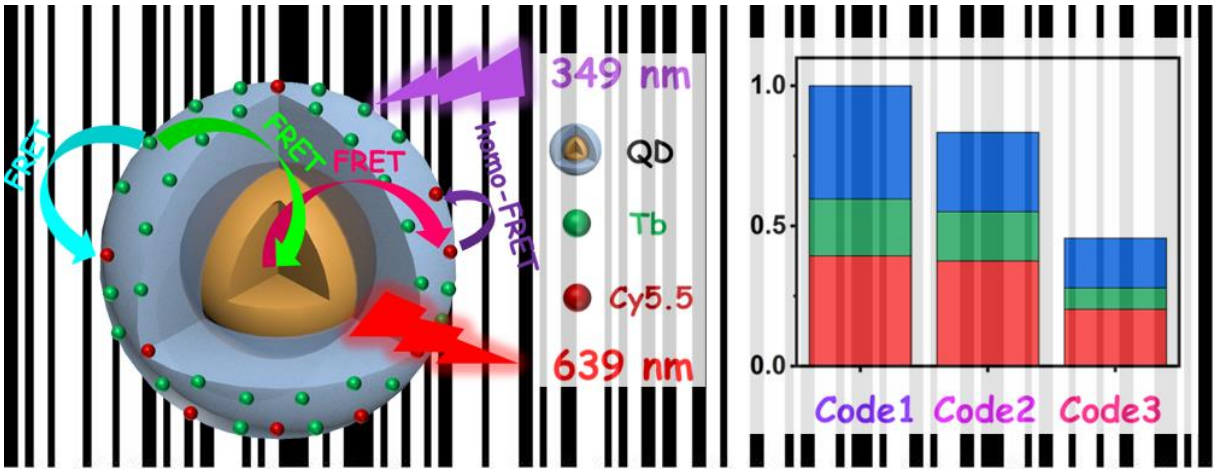

Figure 1.3. FRET-modulated multi-hybrid nanoparticles for brightness-equalized single-wavelength barcoding.

In the third study (**Chapter 5**) we attempt to understand the energy transfer mechanism from long lifetime Tb donors to AuNPs. The application of PL quenching by AuNPs has expanded the applicability of optical probe methodologies in biochemistry, biodiagnostics, and biomolecular imaging. Understanding the

energy transfer mechanism plays a fundamental role in developing optical ruler methodologies. Both Förster resonance energy transfer (FRET, $\sim R^{-6}$ distance dependence) and nanosurface energy transfer (NSET, $\sim R^{-4}$ distance dependence) have been considered as the correct theory for the quenching mechanism. However, the significant differences of the distance dependence of both resonance energy transfer mechanisms can lead to strong variations in the energy transfer process. In this chapter, we investigate PL lifetime quenching of terbium complexes (Tb) conjugated to streptavidin when bound to biotinylated Au-NPs of different diameters (5, 30, 50, and 80 nm)(**Figure 1.4**). The binding of Tb-labeled streptavidin (Tb-sAv) to biotinylated AuNPs (biot-AuNPs) was studied using light-scattering spectroscopy. Quenching of the PL of Tb-sAv upon binding to biot-AuNPs of different diameters (5, 30, 50, 80 nm) was studied by time-resolved PL spectroscopy. Energy-transfer efficiencies were found to be practically independent of the AuNP size. Analysis according to FRET theory yielded donor–acceptor distances that were inconsistent and far beyond the expected Tb–AuNP distance. In contrast, the NSET model yielded a good agreement between the Tb-to-AuNP surface distance estimated from the geometry of the Tb-sAv/biotin-AuNP assembly (4.5 nm) and those calculated from PL lifetime analysis, which range from 4.0 to 6.3 nm. Our findings strongly suggest that NSET (and not FRET) is the operational mechanism in PL quenching by AuNPs, which is important information for the development, characterization and application of nanobiosensors based on PL quenching by AuNPs.

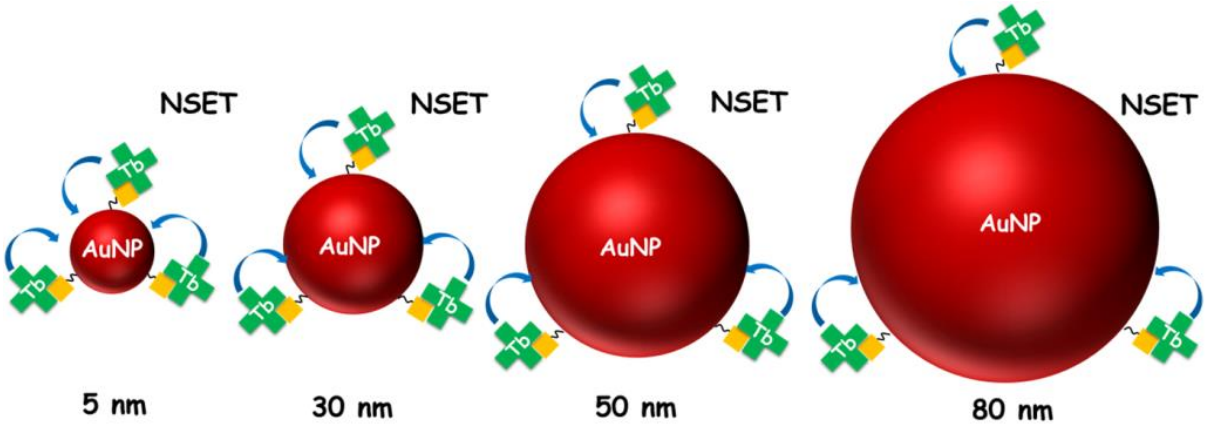

Figure 1.4. NSET Model using Tb labeled streptavidin (sAv) and biotinylated Au-NPs.

After this introduction, a theoretical background on resonance energy transfer, QDs, luminescent lanthanides, fluorescent dyes, AuNPs, and time-resolved measurement will be presented (**Chapter 2**). Three experimental studies will follow in a paper-style with an introduction, materials and method, results and discussion, and a conclusion. A summary addressing the results obtained from the experimental studies will be discussed and an outlook on future research. Appendix and bibliography follow at the end of the thesis.

2. Background

This chapter will introduce basic knowledge of Förster resonance energy transfer (FRET) mechanisms, quantum dots (QDs), luminescent lanthanides, fluorescent dyes, gold nanoparticles (AuNPs), and time-resolved (TR) measurement in an attempt to understand how to design and perform lanthanides-to-QDs D-A pairs based FRET and lanthanides-to-AuNPs pairs based NSET experiment. In particular, we are interested in studying the multiple donors and acceptors based FRET model for calculating desired photophysical properties adapted to advanced fluorescence biosensing and imaging applications. The understanding of such a model will be facilitated by a deep understanding of such complicated multi donor-acceptor energy transfer pathways on nanoparticles.

This chapter will be organized by first examining in **Section (2.1)** FRET mechanism in terms of FRET theory, multiple donors and/or acceptors FRET. **Section (2.2)** will examine optical properties and surface functionalization of QDs, and how QDs can server as donor, acceptor, or relay. The next **Section (2.3)** will examine photophysics of luminescent lanthanide complexes and nanoparticle, and the advantage of lanthanide complexes in donor based FRET. **Section (2.4)** will focus on dye aggregates and homo FRET of fluorescent dyes. **Section (2.5)** will focus on the surface plasmon resonance (SPR) and nanosurface energy transfer (NSET) of AuNPs. Finally, **Section (2.6)** will examine the TR measurement and TR based optical multiplexing.

2.1 Förster resonance energy transfer

Resonance energy transfer (RET) is based on the concept of a fluorophore as an oscillating dipole, which can exchange energy with another dipole with a similar resonance frequency.[1] The best known RET mechanism is Förster resonance energy transfer (FRET), which is considered to occur when the donor and acceptor can be reasonably approximated as point dipoles. For the observation of FRET, the following conditions should be met:[2]

(i) The donor must be a fluorophore and has a reasonably large quantum yield.

(ii) Spectral overlap must exist between the emission of donor and the absorption of acceptor.

(iii) Donor and acceptor must be close, but not too close.

(iv) The orientation factor should not be zero.

In addition, when the excited state donor is created through a chemical reaction or enzyme-catalyzed biochemical reaction, the RET phenomena are referred to as bioluminescence or chemiluminescence resonance energy transfer (BRET or CRET), respectively. In general, Förster theory applies equal well to both of them. The FRET mechanism does not generally apply in cases where the donor or acceptor cannot be approximated as a point dipole, which frequently occurs with energy transfer to metal surfaces. The latter are more appropriately described as nanosurface energy transfer (NSET). The discussion below will present some very basic knowledge and mathematics needed of FRET theory **(2.1.1)**, multiple donors and/or acceptors based FRET **(2.1.2)** to design and perform FRET based experiments, and is mainly extracted from reference [2].

2.1.1 Förster resonance energy transfer theory

Förster resonance energy transfer (FRET) is an electrodynamic phenomenon, and the theory behind resonance energy transfer was mainly contributed by Theodor Förster in 1940s.[2] FRET is a nonradiative energy transfer process between a donor (D) molecule in the excited state and an acceptor (A) molecule in the ground state with an efficiency that is dependent on the distance R^{-6} between D and A.

FRET occurs without the appearance of a photon and is the result of long range dipole–dipole interactions between the donor and acceptor. It can be represented by Coulombic coupling (coupling of two charges) V_{Coul}. V_{Coul} should be dominant at the distance range of 1-20 nm, which is usually considered FRET distance. In this case, orbital overlap-related mechanisms and radiative mechanisms play minor roles. The FRET rate can be represented by Fermi's golden rule (**Equation 2.1**):

$$k_{\mathrm{FRET}} = \frac{2\pi}{\hbar}|V|^2\rho \tag{2.1}$$

Where $\hbar$ is the reduced Planck constant, V is the electronic coupling between D and A, and ρ is the density of the interacting initial and final energetic states,

which is related to the spectral overlap integral J (the overlap of D emission and A absorption, defined in the wavelength or wavenumber scale). In Equation 2.1, V can be replaced by the R^{-3} distance dependent V_{Coul} (**Equation 2.2**):

$$V_{\mathrm{Coul}} = \frac{\kappa|\vec{\mu}_{\mathrm{D}}||\vec{\mu}_{\mathrm{A}}|}{4\pi\varepsilon_0 n^2 R^3} \tag{2.2}$$

Where $\vec{\mu}_{\mathrm{D}}$ and $\vec{\mu}_{\mathrm{A}}$ are the transition dipole moments of D and A, κ is the orientation factor between them, ε_0 is the vacuum permittivity, n is the refractive index, and R is the distance between D and A.

After substituting **Equation 2.2** into **Equation 2.1**, the FRET rate can be descripted as following **Equation 2.3**:

$$k_{\mathrm{FRET}} = \frac{9\,(\ln 10)\kappa^2\Phi_{\mathrm{D}}}{128\pi^5 N_{\mathrm{A}} n^4 \tau_{\mathrm{D}} R^6} J \tag{2.3}$$

Where Φ_{D} is the luminescence quantum yield of D in absence of energy transfer, N_{A} is Avogadro's number (6.023×10^{23} mol^{-1}), and τ_{D} is the luminescence lifetime of D.

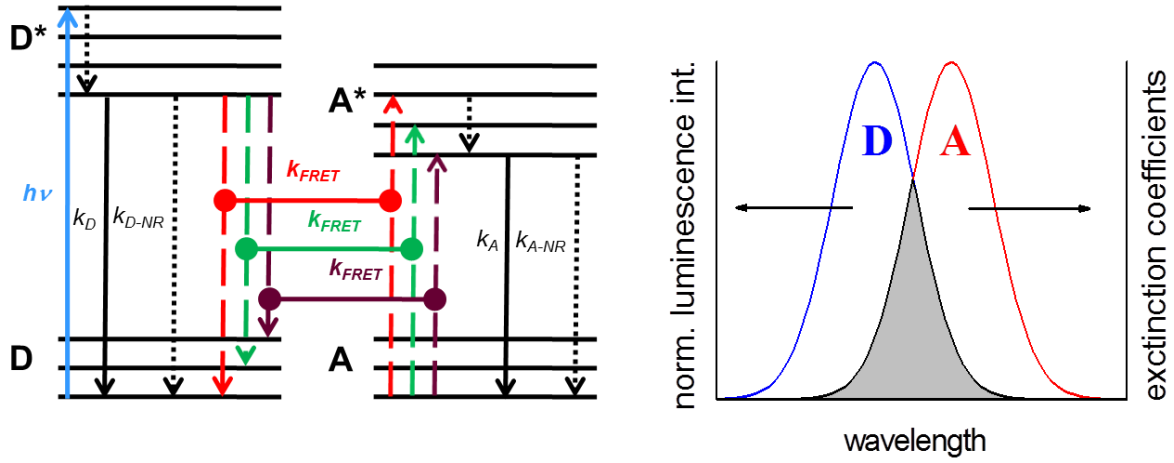

Figure 2.1. (Left) Basic FRET principle. In the Jablonski diagram (simplified energy level scheme), the donor is excited by $h\nu$ from an electronic ground state (D) to an excited state (D*), and then goes to an excited electronic ground state by inner relaxation (vibrational and rotational-dotted arrow), and finally goes back to ground state by radiative decay (k^{R}), nonradiative decay (k^{NR}), or FRET (k_{FRET}). The FRET process happens when the difference between the respective energy levels are equal, in other words the donor and acceptor share the same electronic transitions (horizontal lines with dots on each end). After FRET, the acceptor is in an excited state (A*), then goes to its ground state (A) by radiative or nonradiative decay. **(Right)** The overlap (gray area) of the area normalized emission spectrum of D (*cf.* **Equation 2.6**) and the molar absorptivity spectrum of A (ε_{A}) defines the overlap integral J (*cf.* **Equation 2.5**). (Adapted from reference [2]. Copyright 2013 Wiley-VCH Verlag GmbH & Co. KGaA)

Basic principle of FRET is presented in a simplified Jablonski diagram in **Figure**

2.1 (left), electronic transitions from a higher to a lower energy level in D lead to electronic transitions from a lower to higher energy level in A, if these transitions are in energetic resonance.

Förster distance (R_0), at which energy transfer and spontaneous decay of the excited donor are equally probable ($k_{\mathrm{FRET}} = k_{\mathrm{D}}^{\mathrm{R}} + k_{\mathrm{D}}^{\mathrm{NR}} = \tau_{\mathrm{D}}^{-1}$), the FRET efficiency E_{FRET} is 50%, can be calculated by **Equation 2.4** (replace k_{FRET} with τ_{D}^{-1} and R with R_0):

$$R_0^6 = \frac{9\,(\ln 10)\kappa^2 \Phi_{\mathrm{D}}}{128\pi^5 N_{\mathrm{A}} n^4} J \tag{2.4}$$

The spectral overlap integral J (defined in wavelength scale) is shown in **Figure 2.1(right)** and given by **Equation 2.5**:

$$J = \int \bar{I}_{\mathrm{D}}(\lambda)\varepsilon_{\mathrm{A}}(\lambda)\lambda^4 \mathrm{d}\lambda \tag{2.5}$$

Where $\varepsilon_{\mathrm{A}}(\lambda)$ is the acceptor molar absorptivity (or extinction coefficient) spectrum, $\bar{I}_{\mathrm{D}}(\lambda)$ is the donor emission spectrum normalized to unity and is given by **Equation 2.6**:

$$\int \bar{I}_D(\lambda)\, d\lambda = 1 \tag{2.6}$$

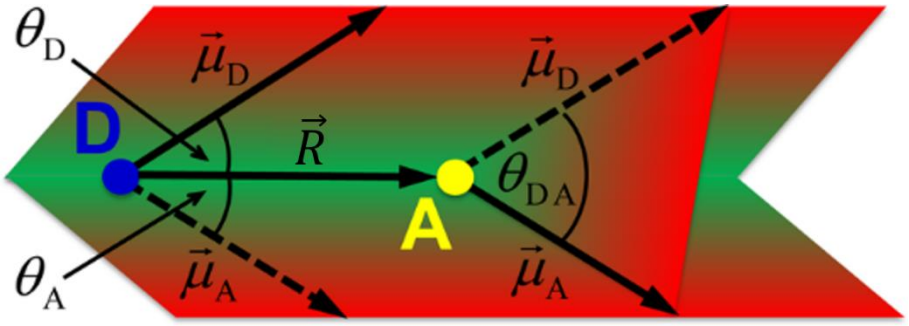

Figure 2.2. FRET dipole orientation factor κ^2 can be calculated by orientation of the D emission transition dipole moment $\vec{\mu}_{\mathrm{D}}$, the A absorption transition dipole moment $\vec{\mu}_{\mathrm{A}}$ and the D–A connection vector $\vec{R}$. (Reproduced from reference [3]. Copyright 2017 American Chemical Society)

The orientation factor κ^2 can be calculated using the different angles and the unit vectors of $\vec{\mu}_D$, $\vec{\mu}_A$, and $\vec{R}$ (**Equation 2.7**):

$$\kappa^2 = \left[\hat{\mu}_{\mathrm{D}} \cdot \hat{\mu}_{\mathrm{A}} - 3\left(\hat{\mu}_{\mathrm{D}} \cdot \hat{R}\right)\left(\hat{\mu}_{\mathrm{A}} \cdot \hat{R}\right)\right]^2 = \left[\cos\theta_{\mathrm{DA}} - 3\cos\theta_{\mathrm{D}}\cos\theta_{\mathrm{A}}\right]^2 \tag{2.7}$$

where $\hat{\mu}_{\mathrm{D}}$, $\hat{\mu}_{\mathrm{A}}$, and $\hat{R}$ represent the unit vectors of $\vec{\mu}_{\mathrm{D}}$, $\vec{\mu}_{\mathrm{A}}$, and $\vec{R}$, respectively. As show in **Figure 2.2**, θ_{DA} is the angle between the donor and acceptor transition moments, θ_{D} and θ_{A} are the angles between the donor and acceptor transition

dipole moments and the donor-acceptor connecting vector $\vec{R}$. According to the **Equation 2.7**, κ^2can range from 0 to 4 depending on the relative orientation of donor and acceptor transition dipole moments. For instance, 0 can occur for the perpendicular transition dipole moments, 4 for head-to-tail parallel transition dipoles moments, and 1 for the parallel transition dipole moments. Generally, κ^2 is assumed equal to 2/3, which is the value for D and A that are free to rotate any possible orientation during the FRET time ($1/k_{\mathrm{FRET}}$), which means that the average rotation rate is much higher than the average FRET rate.

Combination of **Equations 2.3** and **2.4** leads to the relation between the FRET rate, the luminescence decay time of the donor, and the distances (R^{-6} distance dependence of the FRET rate, **Equation 2.8**):

$$k_{\mathrm{FRET}} = \tau_{\mathrm{D}}^{-1}\left[\frac{R_0}{R}\right]^6 \tag{2.8}$$

Then the FRET efficiency is given by **Equation 2.9**:

$$E_{\mathrm{FRET}} = \frac{k_{\mathrm{FRET}}}{k_{\mathrm{FRET}}+k_{\mathrm{D}}^{\mathrm{R}}+k_{\mathrm{D}}^{\mathrm{NR}}} = \frac{k_{\mathrm{FRET}}}{k_{\mathrm{FRET}}+\tau_{\mathrm{D}}^{-1}} = \frac{1}{1+(R/R_0)^6} = \frac{R_0^6}{R_0^6+R^6} \tag{2.9}$$

As shown in **Figure 2.3**, FRET efficiency is most sensitive in a region between ca.0.5-2.0 R_0 (yellow) and exhibits very steep curve in a region between ca. 0.7-1.3 R_0 (green). FRET changes become extremely difficult to measure beyond this region (red).

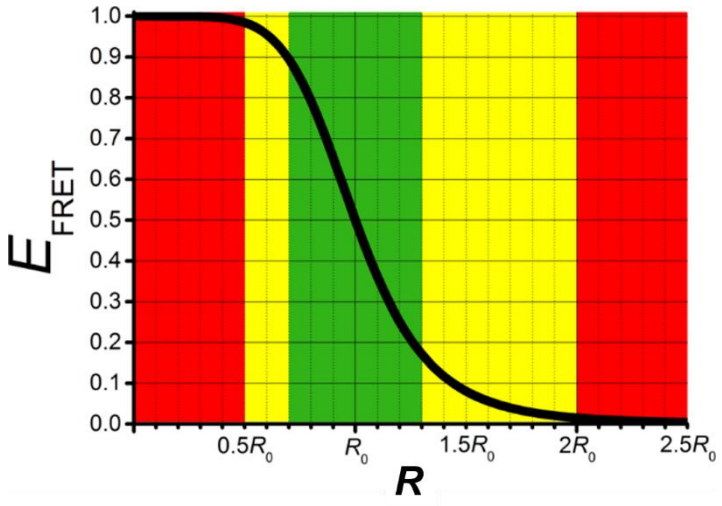

Figure 2.3. FRET efficiency as a function of the donor-acceptor distance (R) shows R^{-6} distance dependence and leads to a steep curve around R_0. (Reproduced from reference [3]. Copyright 2017 American Chemical Society)

FRET efficiency can also be calculated by the measurable PL properties including intensity (I), lifetime (τ), and quantum yield (Φ) using **Equation 2.10**:

$$E_{\mathrm{FRET}} = 1 - \frac{I_{\mathrm{DA}}}{I_{\mathrm{D}}} = 1 - \frac{\tau_{\mathrm{DA}}}{\tau_{\mathrm{D}}} = 1 - \frac{\Phi_{\mathrm{DA}}}{\Phi_{\mathrm{D}}} \tag{2.10}$$

where D is the donor in absence of the acceptor, and DA is the donor in presence of the acceptor.

2.1.2 FRET with multiple donors and/or acceptors

Nanoparticles (*e.g.,* QDs) possess nontrivial surface areas, and usually can assemble multiple donors and acceptors on their surface. The D/A and A/D ratio can influence the FRET properties (sensitization and FRET efficiency). However, theoretical model for FRET system with multiple (m) donors and multiple (n) acceptors was only considered by a few studies.[4]–[7] According to Raicu's theoretical model for FRET with m donors and/or n acceptors, FRET efficiency is solely dependent on the number of acceptors and the efficiency of a single D–A pair.[7] The relation between FRET efficiency and the number of acceptors also has been shown in an experimental study by Mattoussi's group using n Cy3 acceptors around a QD donor,[8] which was the same as the theoretical model and can be descripted by the following **Equation 2.11**:

$$E_{\mathrm{FRET}}^{\mathrm{multi}} = 1 - \frac{I_{\mathrm{DA}}(n)}{I_{\mathrm{D}}} = 1 - \frac{\tau_{\mathrm{DA}}(n)}{\tau_{\mathrm{D}}} = 1 - \frac{\Phi_{\mathrm{DA}}(n)}{\Phi_{\mathrm{D}}} = \frac{nR_0^6}{nR_0^6+R^6} = \frac{nE_{\mathrm{FRET}}}{1+(n-1)E_{\mathrm{FRET}}} \tag{2.11}$$

An increasing FRET efficiency with an increasing number of n (acceptors per donor) is logical, because acceptors provide n possible FRET pathways to the excited donor, and therefore, the probability of de-exciting via FRET increases.

For m donors around a QD acceptor, as mentioned above, the FRET efficiency does not change with an increasing number of m.[7] However, the probability of acceptor FRET-sensitization will increase with an increasing number of m and can be given by the following **Equation 2.12**.

$$P_{\mathrm{A}} = 1 - (1 - E_{\mathrm{FRET}})^m = 1 - \left(\frac{R^6}{R_0^6+R^6}\right)^m \tag{2.12}$$

Based on a Monte Carlo simulation model,[4] Corry and co-workers considered the influence from different excitation intensities and designed a model to calculate

FRET efficiencies between *m* donors and *n* acceptors in complex geometries.[5],[6] It is significant because high excitation intensities may lead to many excited donors and/or acceptors, and as a result the already excited acceptors will be unavailable for FRET and decrease the FRET efficiency. This means that **Equation 2.11** is valid only for the FRET system with low excitation intensities, in which all donors and acceptors have already gone back to ground states before the excitation. It is the same in the case of the probability of acceptor FRET-sensitization. So the **Equation 2.12** is invalid for the FRET system with high excitation intensities or excited state of A is much longer than the one of D. However, **Equation 2.11** and **2.12** is valid for cases in which the excited state lifetime of D is much longer than the one of A (*e.g.*, lanthanide D and QD). When there are enough photons to excite several Tb (on the QD) and the QD, sequential FRET (all with the same FRET efficiency) from each Tb to the QD can occur due to the extremely long exited state lifetime of the Tb. For example: 10 Tb and the QD are excited, in the very beginning after the pulsed excitation (several 100 ns) the QD is excited and FRET cannot occur. After ca. 100 ns, the QD decays back to its ground state and can then become an acceptor (within these 100 ns, the probability of Tb de-excitation is small due to the ms lifetime). The QD will get FRET-sensitized by one Tb and then directly give away that energy (fluorescence within ns) and can be excited again. As the probability that the other 9 Tb are still excited is high due to the ms lifetime, the QD can be FRET sensitized again, and thus the FRET efficiency of this system will be constant but the probability of acceptor excitation increases with high intensities pulsed excitation. These FRET processes were studied in this thesis.

2.2 Quantum dots

Quantum dots (QDs) are luminescent inorganic semiconductor nanoparticles mainly composed of II-VI (CdS, CdSe, CdTe, ZnS, ZnSe, ZnTe), III-V (GaAs, GaN, GaP, InAs, InP), IV-VI (PbS, PbSe), I-VI(Ag_2S, Ag_2Se, Ag_2Te), and I-III-VI (AgInS, AgInSe, CuInS, CuInSe) groups of the periodic table, and also composed by alloyed structure, core/shell structure, and doped structure of these materials. **Figure 2.4** represents the spectral range of emission for the most widely studied types of

semiconductor nanocrystals. The size of these nanoparticles that is usually between 1-10 nm in diameter (zero-dimensional nanomaterials) is smaller or close to their Exciton Bohr Radius. In 1982, Efros *et al.*[9] and Ekimov *et al.*[10] demonstrated that the ultra-small size of particle has a decisive effect on its optical and electrical properties. In 1983, Brus and colleagues at Bell Laboratories first reported colloidal QDs.[11] From then on, QD began to attract scientists' attention. In 1993, Bawendi *et al.* synthesized nearly monodisperse QDs in the high temperature organic solution.[12] Since the synthesized product was soluble in the organic phase, main application fields of QDs were focused on high density memory and photovoltaic equipment.[13],[14] Until 1998, Chan *et al.*[15] and Bruchez *et al.*[16] pointed out that the water solubility and biocompatibility of QDs can be solved by attaching thioglycolic acid to the surface of QDs or by coating with hydroxyl group functionalized SiO_2 shell, which successfully established a scientific foundation for the application in life science. The discussion below will focus on the optical properties **(2.2.1)** and surface functionalization **(2.2.2)** of QDs and examine how QD serves as FRET donor/acceptor/relay **(2.2.3)**.

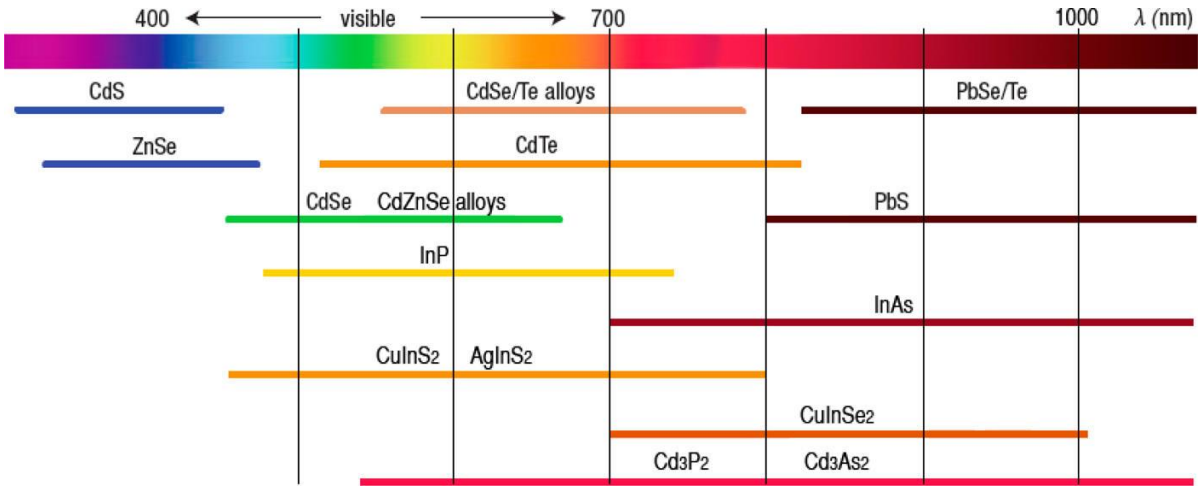

Figure 2.4. Spectral range of the photoluminescent emission for the most widely studied types of semiconductor nanocrystals. (Reproduced from reference [17]. Copyright 2016 American Chemical Society)

2.2.1 Optical properties

QDs possess electronic properties that are intermediate between those of bulk semiconductors and discrete molecules. When a bulk semiconductor is excited by photons, an electron is promoted into the quasi-continuum conduction band (CB)

leaving a positively charged hole in the valence band (VB). The electron and the hole can bind to each other to form an exciton, and the distance in electron-hole pair is referred to as the exciton Bohr radius. Since the size of QDs is on the same order as the size of the exciton Bohr radius, when an exciton is created, the density of electronic states is not enough to form complete band structures and quantization of the energy levels can be observed at the band edges. The spatial confinement of excitons in QDs leads to a phenomenon known as quantum confinement, which has a direct effect on the boundaries of the bandgap. As illustrated in **Figure 2.5**, the inter-bandgap energy of QD can be tuned by the size of the nanoparticle. Due to the quantum confinement effect, the band gap of QD will increase as the particle radius decreases, and therefore a series of different emission wavelengths from the ultraviolet (UV) to the near-infrared (NIR) region can be obtained.[18]

From the perspective of fluorescent labeling, QDs possess many desirable photophysical properties.[19] (i) Broad and continuous absorption spectrum allows free selection of excitation wavelength. (ii) Both high molar absorption coefficient (10^5–10^6 M^{-1} cm^{-1} at first excitonic absorption peak, increasing toward UV wavelengths) and quantum yields (up to 100%) lead to high brightness, which is essential for single particle tracking. (iii) Narrow, size-dependent, and symmetric emission spectra spanning from UV to NIR region are ideal for multi-color experiment. Generally, high quality and monodisperse QDs yield emission profiles with (full-width at half-maximum) FWHM which are typically in the range of 25-35 nm. It has been reported high-quality core-shell CdSe/CdS QDs with narrow emission line widths (FWHM ~20 nm) can be achieved through a slow growth rate of the shell.[20] (iv) Large effective Stokes shifts are efficient separations of the excitation and emission lights. (v) Remarkable photostability (strong resistance to photobleaching and chemical degradation) provides powerful support for long-term real-time bioimaging. (vi) High multiphoton action cross sections allow excitation with NIR light to have deeper tissue penetration and decrease autofluorescence from the biological matrix. It has been reported high-resolution in vitro and in vivo imaging can be achieved by combining three-photon excitation of ZnS nanocrystals and visible emission from Mn^{2+} dopants.[21]

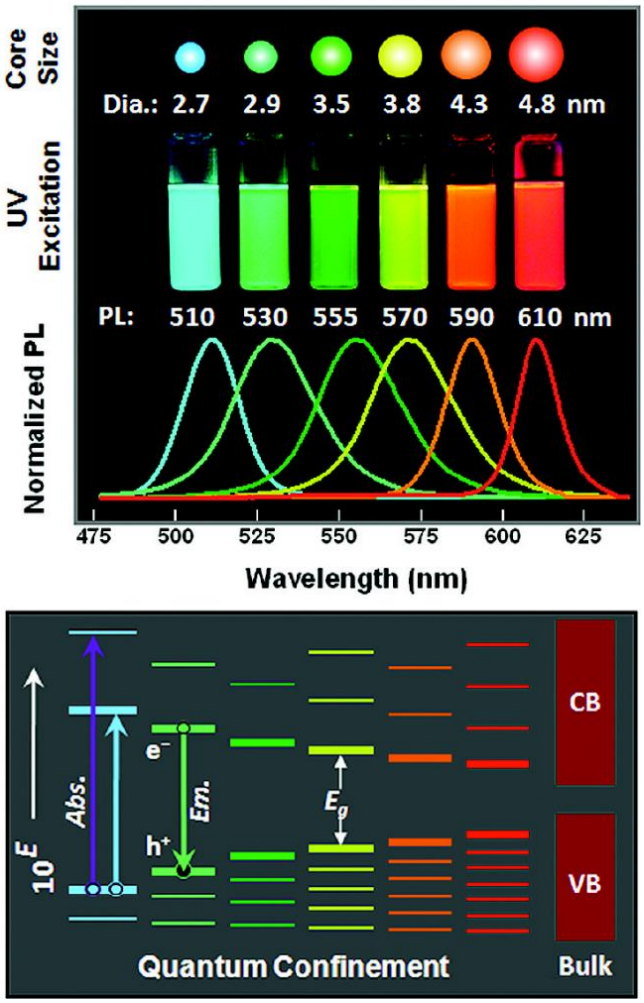

Figure 2.5. Top: Cartoon, photograph, and PL spectra illustrating progressive color changes of CdSe/ZnS QDs with increasing nanocrystal size. **Bottom:** Qualitative changes in QD energy levels with increasing nanocrystal size. E_g represent the bandgaps energies. Continuous conduction band (CB) and valence band (VB) of bulk semiconductor shown as comparison. (Reproduced from reference [18]. Copyright 2011 American Chemical Society)

2.2.2 Surface functionalization

The surface functionalization of QD is a major issue for biomedical applications because most of high quality QDs are synthesized using hydrophobic surface ligands at high temperatures, therefore, as-prepared QDs are not directly soluble in aqueous media. For the purposes of making them stable in aqueous solution, as illustrated in **Figure 2.6**, there are mainly three different strategies: (i) ligand exchange, (ii) encapsulation, and (iii) silica coating.

Ligand exchange is the strategy by which the original hydrophobic surface ligands on the QD surface are replaced with hydrophilic ligands. Essentially these hydrophilic ligands consist of two functional components: the anchoring group(s)

and hydrophilic group(s). Thiol based molecules (mercaptoacetic acid (MAA),[22]–[24] mercaptopropionic acid (MPA),[25]–[27] mercaptoundecanoic acid (MUA),[28],[29] and dihydrolipoic acid (DHLA)[30]) are the most frequently used ligands due to their reasonably strong affinity for Cd and Zn, which are the most common metals on the surface of QD. However, the colloidal stability of QD coated with these ligands relies on deprotonation in of the carboxyl groups, limiting the usable pH range of QD. In order to solve the poor colloidal stability of thiol ligands, the thiol ligands were modified with poly (ethylene glycol) (PEG) to expand the usable pH range of QD.[31],[32] It has been reported that PEG-appended DHLA derivatives have been developed to enhance colloidal stability across a pH range from weakly acidic to strongly basic aqueous media.[33]–[35] The advantage of ligand exchange is that QD with small hydrodynamic diameter can be prepared, which is essential for FRET based biosensing applications.

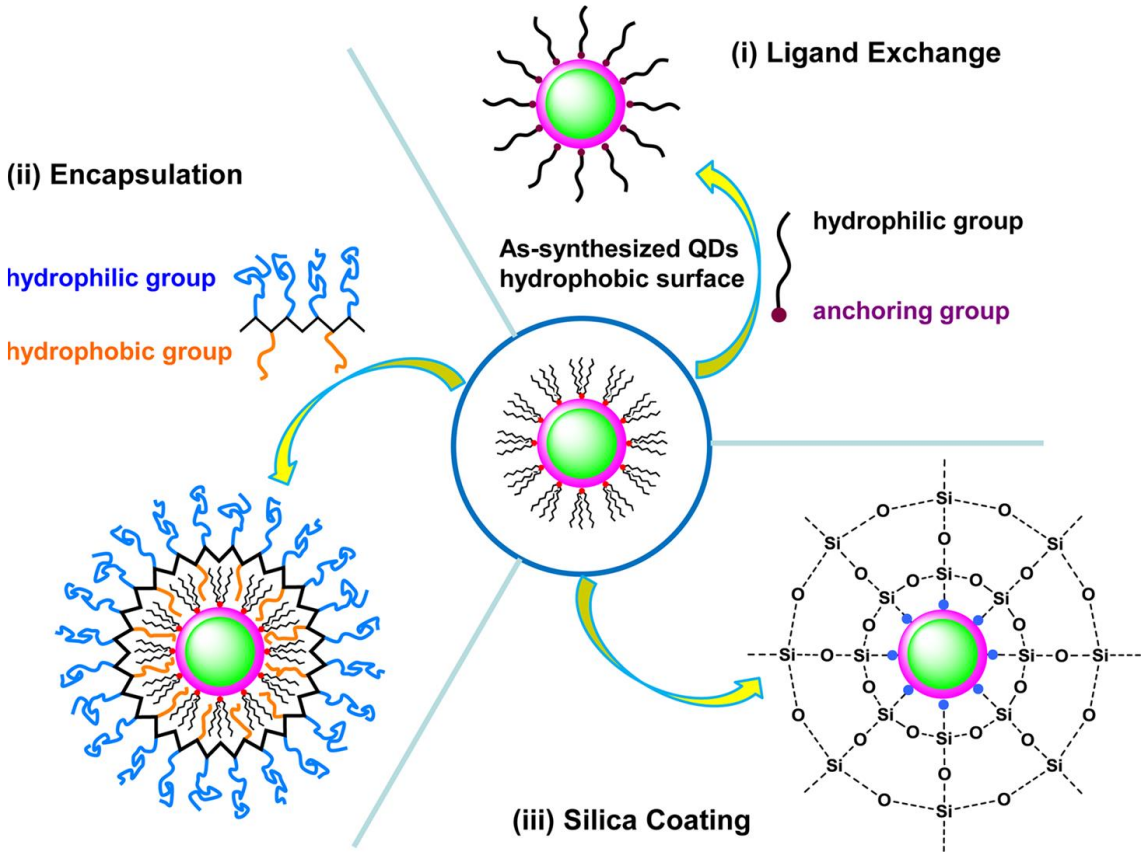

Figure 2.6. Schematic overview of different strategies for surface functionalization of QD: **(i)** ligand exchange, **(ii)** encapsulation, or **(iii)** silica coating chemistries. The center represents an as-synthesized QD in organic solvent with its hydrophobic surface of organic ligands. (Reproduced from reference [3]. Copyright 2017 American Chemical Society)

Encapsulation is a strategy by which to incorporate the QD with extraneous amphiphilic molecules via hydrophobic interactions. Surfactants such as phospholipids and amphiphilic polymers are commonly used amphiphilic ligands. In 2002, Dubertret *et al*. encapsulated individual QD in micelles and demonstrated them for both in vitro and in vivo imaging.[36] Since these encapsulation techniques do not modify the original ligand on the QD surface and prevent water interacting with this surface, QD almost preserve their original QY after encapsulation. However, this strategy often results in large hydrodynamic diameter, which is not optimal for FRET applications.

Silica coating is a method by which to form nucleation sites on the surface through ligand exchange using (3-mercaptopropyl) trimethoxysilane, followed by further shell growth with silane molecules such as tetraethoxysilane via hydrolysis and condensation,[37],[38] or a water-in-oil reverse microemulsion method.[39]–[41] The silica shell is quite robust and makes QD highly stable. Moreover, the silica shell is nontoxic and can be easier to functionalize with bioconjugation reagents. Despite significant advances in uniformity and size control of silica coating, the silica shell is still relatively thick compared to materials prepared with ligand exchange methods. Even so, there are fewer energy transfer and bioimaging studies by using silica shell coated QD.[42],[43] Recently, we developed lanthanide complex doped QD/SiO_2 system and demonstrated them for FRET based living cell barcoding.[44] We assembled the Tb-Lumi4 or Eu-1 on the QD surface with different thickness of silica shell (6 nm and 12 nm), and observed strong FRET signals due to large Förster distance (up to 12.2 nm) of Ln-QD FRET pairs.

2.2.3 QD as FRET donor/acceptor/relay

QD as FRET donor

QDs can act as FRET donor, acceptor or relay. Most often, QDs are used as FRET donor due to their unique photophysical properties. As illustrated in **Figure 2.7**, compared with organic dye donors, the broad absorption spectra of QD donors can be excited in the blue/UV range, hundreds of nanometers from their emission maximum. This property leads to significant minimization of direct acceptor excitation and can enhance the FRET sensitivity. QD donors can be regarded as

nanoantenna due to their high extinction coefficients (>10^7 M^{-1} cm^{-1}), which increase sensitivity of FRET assay. The emission spectra of QDs are quite narrow and symmetrical, which means the donor emission does not leak into the acceptor detection channel. The surface area of QDs can assemble several acceptors around a single donor, which can allow "tuning" of FRET efficiency.

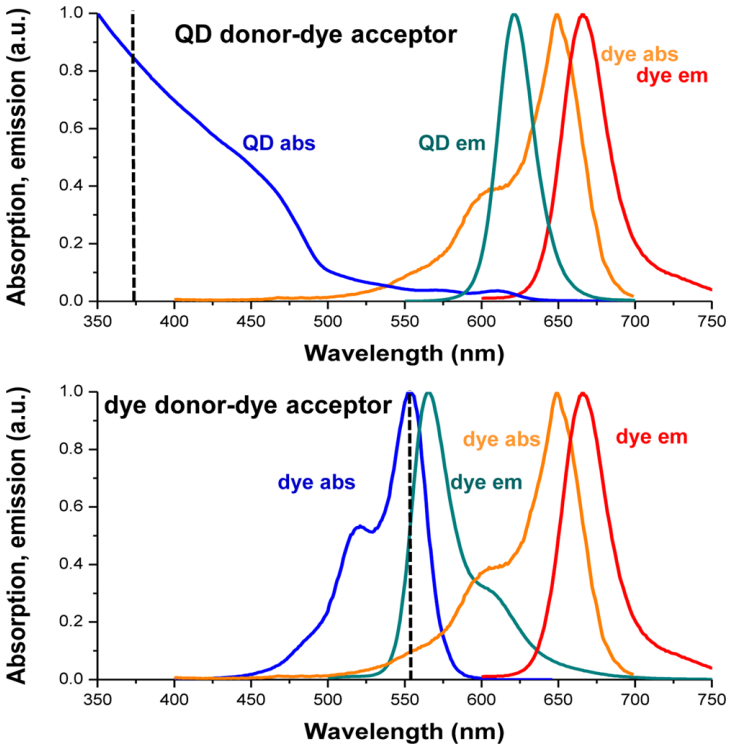

Figure 2.7. Comparative absorption and emission spectra of a hypothetical QD donor-dye acceptor **(top)** and dye donor-dye acceptor **(bottom)** FRET pair illustrating the photophysical differences between a QD donor and a dye donor (black dotted line: putative excitation lines). (Reproduced from reference [3]. Copyright 2017 American Chemical Society)

In 2001, Willard *et al.* demonstrated QD donor based FRET to a dye-labeled biomolecule.[36] They conjugated a biotinylated bovine serum albumin (BSA) onto the QD surface, then mixed with dye-labeled streptavidin (dye-sAv) and observed a QD emission quenching with a dye emission increasing. In 2003, Patolsky *et al.* used DNA-based QD FRET to follow the dynamics of DNA replication on the QD.[45] They incorporated dye-labeled nucleotides into a nascent strand hybridized to the thiolated-DNA on the QD surface using a polymerase, and observed the spectroscopic signature of FRET after replication. The same year, Medintz *et al.* demonstrated protein-based QD FRET sensor using dye-labeled cyclodextrin binding to surface immobilized labeled or unlabeled maltose-binding

proteins (MBPs).[46] They used the MBP terminal His6-tag to conjugate proteins on the QD surface directly, which allow to precisely control the number and orientation of MBP. The number of QDs as FRET donor-based sensors has increased considerably since these early contributions. In particular, we are interested in QD donor-to-multiple dyes acceptors based FRET mechanism and their application. The studies about this system are listed in **Table 2.1**, which open the opportunity to use this system for fabricating desired photophysical properties for biosensing applications.

Table 2.1. QD as donor based multiple (*n*) acceptors FRET system.

Acceptors	*n*	Donors	Application	Mechanism investigated	Ref.
QSY9, (Cy3, Cy3.5)	0~10	QD 530	/	yes	[46]
Cy3	0~10	QD510, 530, 555	/	yes	[8]
biot-Au NPs (2~3 nm)	~9	sAv-QDs (rod shape)	detection for avidin	no	[47]
Rhodamine Red-X,	0~48	QD545	extracellular matrix metalloproteinases (MMPs) activity in normal and cancerous breast cells	no	[48]
mOrange, mOrange M163K	15.7 and 16.5	QD 520	sensing intracellular pH	no	[49]
EYFP, Atto647	0~18	QD	/	yes	[50]
(A555, A647)	(0,0)~(7,7)	QD	multiplexed protease sensing	yes	[51]
Cy3-Cy3.5-Cy5- Cy5.5	1~8	QD525	/	yes	[52]
A555/A647	0~16	QD, A488	detection of the activity of nanomolar concentrations of trypsin	yes	[53]
(A555, A647)	(0,0)~(7,7)	Green-emitting QD	tracking the activity of trypsin and chymotrypsin	no	[54]
(A555, A647)	(0,0)~(12,18)	QD520b, QD525a	/	yes	[55]
A610 or A633. A555 or A647	0~30	QD 525, 530a, 540a, 550, 575, 600, 650	/	yes	[56]
(A555, Cy3.5 or At594, A647.)(L,M,N)	L = 0, 2, 5, 8 (or L = 0, 3, 6, 9); M = 0, 2, 5, 8; N = 0, 2, 5, 8.	QD	quantitative tracking the proteolytic activities of trypsin, chymotrypsin, and enterokinase	yes	[57]

QD as FRET acceptor

In 2005, Clapp et al. studied dye-to-QD configuration and found no evidence for FRET with both steady state and time-resolved spectroscopy, even when the dye/QD ratio was increased up to 10.[58] They assumed that the direct QD excitation and excited-state lifetime difference should be responsible for this result. When organic dyes are excited, QDs are always directly excited at the same time due to their broad absorption spectra. Moreover, the relatively long excited-state lifetime of a QD (usually tens to hundreds of ns) compared to that of a typical organic dye (usually a few ns) leads to a very high probability that the dye will decay back to its ground state before the QD and therefore they cannot effectively serve as acceptors for a proximal excited dye.[59] They tested a Ru-based dye as donor (with several hundreds of ns lifetime) and observed significant lifetime quenching in the presence of a QD acceptor. This was the first indicator that long excited-state lifetime donors may unlock QD acceptor based FRET.

Although dye-to-QD based FRET configurations are generally unfavorable, QDs acceptor-based FRET has gradually been established using some non-traditional donors such as lanthanide complexes, chemiluminesent and bioluminescent molecules, and upconverting NPs (UCNPs).[59] The main issue of QDs as FRET acceptors is their broad and intense absorption, which means there are efficient excitation at all wavelengths shorter than their emission wavelength. In order to inhibit or decrease direct excitation of the QDs, there are three different strategies: (i) Lanthanide complexes usually possess a much longer excited-state lifetime compared to that of QDs, which can be measured by time-gated detection void of contribution of directly excited QDs. Hildebrandt and Charbonniere *et al.* demonstrated clear evidence for QDs to be used as FRET acceptors by combining them with Tb and Eu-complex donors.[60],[61] Although such lanthanides complex need to be excited in the UV range, which leads to more efficient excitation of QDs, the 10^5 times longer excited state lifetimes of the lanthanide donors proved to be the key to unlocking QD acceptor based FRET. Time-gated detection after a sufficient delay time after the pulsed excitation allowed efficient detection of both lanthanide donor FRET-quenching and QD acceptor FRET-sensitization. (ii) Bioluminescent and chemiluminesent molecules as donors do not require light

excitation. If bioluminescent or chemiluminescent molecules are used as donors in FRET, the phenomena are now referred to as bioluminescence or chemiluminescence resonance energy transfer (BRET or CRET), respectively. In 2006, Rao *et al.* demonstrated QDs acceptor-based BRET. They showed that mutagenically optimized Rluc and QDs can be used as BRET donor-acceptor for multicolor imaging in vitro and in deep tissues in living mice.[62] In the same year, Ren *et al.* demonstrated an efficient CRET between luminol and QDs and showed potential application of multiple QDs acceptors with different color to multiplex analysis.[63] (iii) UCNP with higher energy visible PL can be excited using low energy NIR by sequential absorption of two or more photons. Therefore, direct QD excitation can also be avoided by using upconverting NPs as donors. It should be noted that FRET between UCNPs and QDs is not the most advantageous situation since the NPs usually possess relatively large size as compared to the usual FRET range of ca. 1 to 10 nm. Thus, in UCNP-to-QD FRET, only the lanthanide ions close to the surface can participate in FRET to the QD, whereas the ions close to the center of the UCNP usually remain unquenched.[64] In order to generate efficient FRET, it is necessary to design UPNCs with efficient surface-emitting lanthanide ions.

QD as FRET relay

QDs can serve as relay. In this case, the QD is used simultaneously as a donor and an acceptor, and can transfer energy provided by an initial donors to an acceptor. The advantage of QD as relay is that the color multiplexing can be achieved with a single QD. **Figure 2.8** presents a full FRET relay cycle (*e.g.*, *m*Tb-QD-*n*A647) after a pulsed excitation. Both Tb and QD can be excited by pulsed UV light directly, whereas the A647 (assuming no direct excitation) remains in its ground state. In this situation, FRET2 (QD-to-A647) occurs and followed by A647 PL emission, while the FRET1 is forbidden. Then Tb still remains in excited state due to the long lifetime (~ms), in which the QD and A647 decay to their ground states. FRET1 (Tb-to-QD) will then occur followed by another FRET2 (FRET-sensitized QD to A647). Such kind of QD as relay based FRET systems have already been developed for enzymatic and hybridization assay or for the design of molecular logic gates. [65]–[68] In this thesis, we are interested the mechanism and application

of QD as relay based system, and previous studies about these systems are listed in **Table 2.2**.

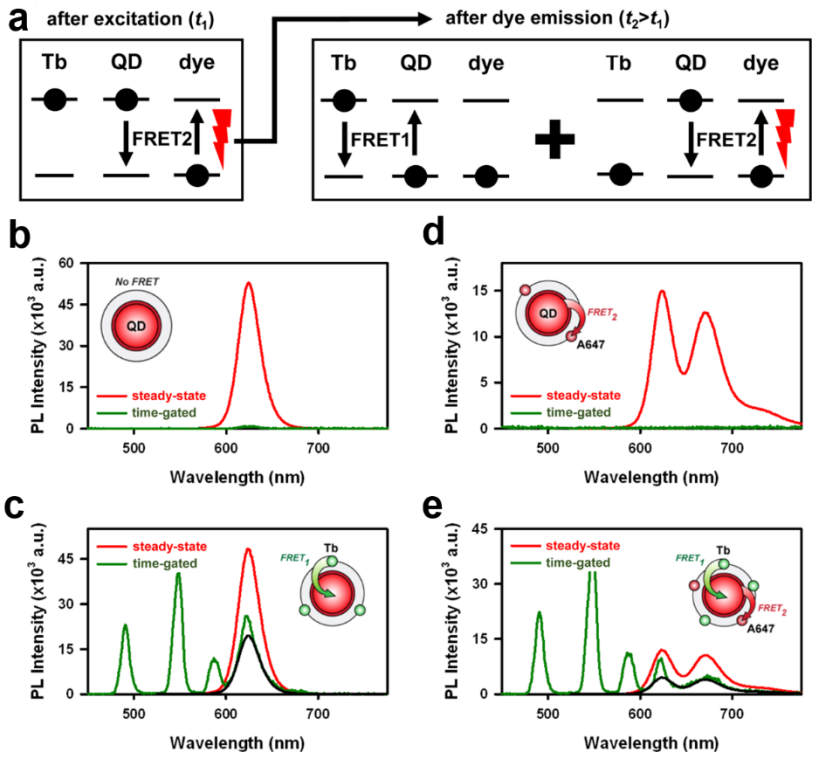

Figure 2.8. (a) Schematic presentation of FRET (arrows) and radiative (flashes) transitions and excited and ground state situations for a full FRET relay cycle after pulsed excitation. Steady-state (red) and time-gated (green, 55 µs) PL spectra of **(b)** pure QDs, **(c)** *m*Tb-QD (time-gated FRET1 from Tb to QD), **(d)** *n*A647-QD (steady-state FRET2 from QD to A647), and **(e)** *m*Tb-QD-*n*A647 (FRET relay).The black spectra show scaling of the steady-state PL spectrum to fit the time-gated PL spectrum. (Adapted from reference [3],[65]. Copyright 2017 American Chemical Society)

Table 2.2. QD as relay based multiple (*m*) donors and multiple (*n*) acceptors systems.

Acceptor	*n*	Donor	*m*	Application	Mechanism investigated	Ref.
IRD700	/	PDFD(polymer), QD615	/	detection of DNA hybridization	yes	[69]
A647	0~15	Tb	0~20	monitoring protease activity and nucleic acid hybridization	yes	[65]
A647	0~5	Tb	0~10	multiplexed protease sensing	no	[66]
A647	0~25	Tb	0~25	complex logic functions	yes	[67]
A555/Cy3/A594	0~8	Ru-phen	0~12	detection of the proteolytic activity of trypsin	yes	[70]
A647	0~20	Tb	0~45	sensitive intra- and extracellular fluorescence imaging	no	[68]

2.3 Luminescent lanthanides

Lanthanides are a series of 15 metal elements located at the sixth period and IIIB group in the periodic table, ranging from lanthanum to lutetium, with the electronic configuration of $[Xe]4f^{n-1}5d^{0-1}6s^2$ (n = 1−15), and are also referred as the f-block elements. Trivalent lanthanide ions (Ln^{3+}) are the most stable oxidation state of lanthanide cations, except for Ce^{4+}, Tb^{4+}, and Yb^{2+}, for which the f orbitals are empty, half-, or full-occupied, respectively.[71] Due to specific electronic configurations, Ln show similar chemical properties. Ln^{3+} ions possess intrinsic luminescence that originates from f−f electronic transitions, the 4f orbitals do not directly participate in chemical bonding due to shielding by the 5s and 5p orbitals, which minimizes the influence of external ligand fields, leading to sharp-band emissions.[72] **Figure 2.9** show the ground and excited states of the Ln^{3+} ions, where radiative transition between the energy levels occurs to give rise to luminescent lanthanide ions. As it can be observed for the Ln^{3+} ions on the periphery (Ce^{3+}, Pr^{3+}, Nd^{3+}, Pm^{3+}, Ho^{3+}, Er^{3+}, Tm^{3+}, and Yb^{3+}), the energy gaps are relatively small between adjacent levels, while the central metals (Sm^{3+}, Eu^{3+}, Gd^{3+}, Tb^{3+}, Dy^{3+}) exhibit larger energy gaps. As a result, f-f emission lines cover the entire spectrum from UV (Gd^{3+}) to visible (e.g., Pr^{3+}, Sm^{3+}, Eu^{3+}, Tb^{3+}) and NIR (e.g., Pr^{3+}, Nd^{3+}, Er^{3+}, Yb^{3+}).[73] In addition, Ln^{3+} ions possess significant paramagnetic properties due to unpaired electrons in 4f orbitals (except La^{3+} and Lu^{3+}). Unlike their chemical properties, the magnetic moments and magnetic susceptibilities of Ln^{3+} differ dramatically along the series.[74]

The studies on lanthanide elements date back to the 18th century. With the development of lanthanide chemistry for more than two centuries, these elements have found a wealth of applications, ranging from high-tech products to health and medical utilization.[75],[76] Particularly, there has been a steady increase in the theoretical and experimental studies of luminescent lanthanide complex and lanthanide nanoparticle over the past decade, principally due to an increasing demand for photoluminescence and related applications, including electronic

display, document security, optical data storage, biological labeling, and imaging.[73],[77]–[82] The discussion below will review the luminescence mechanism and design of luminescent lanthanide complexes (LLCs) **(2.3.1)** and upconverting nanoparticle (UCNP) **(2.3.2)**, and examine how lanthanide serves as FRET donor **(2.3.3)**.

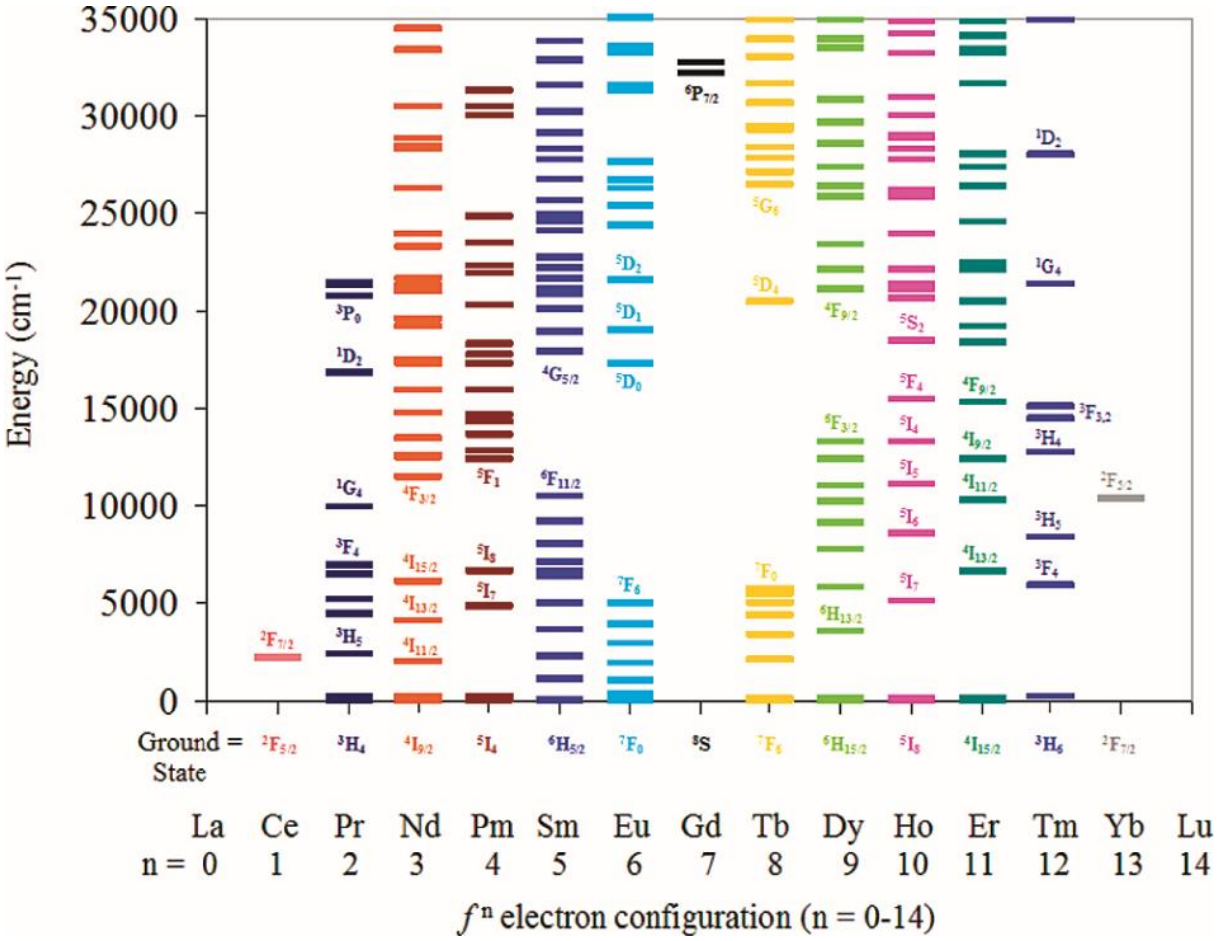

Figure 2.9. A summary of ground and excited energy levels of Ln^{3+} ions series. (Reproduced from reference [72]. Copyright 2009 American Chemical Society)

2.3.1 Luminescent lanthanide complexes and nanoparticles

Luminescent lanthanide complexes (LLCs)

The unique luminescence properties of lanthanides come from transitions involving a redistribution of electrons within 4f orbitals because of the effective shielding by 6s and 5p orbitals. Since the transitions within 4f orbitals are in violation of the Laporte rule which states that electronic transitions that conserve parity, either symmetry or antisymmetry with respect to an inversion center are

forbidden, lanthanide ions display extremely long luminescent lifetimes and very small molar absorption coefficients (<10 M^{-1} cm^{-1}).[83] In order to get more excited, lanthanide ions usually require indirect excitation, which means the emissive states of lanthanides are populated through energy transfer from a sensitizing antenna. As illustrated in **Figure 2.10 (a)**, the general architecture of luminescent lanthanide complexes (LLCs) consists of the Ln^{3+} center surrounded by a moiety that coordinates the central ion (lanthanide ion carrier chelate) and equipped with a sensitizing chromophore moiety (antenna ligand). The chelate serves to prevent the release of free Ln^{3+} ions and to protect the Ln^{3+} ions from quenching from vibrational energy dissipation by oscillators like O–H of water. For the antenna effect, a simplified Jablonski diagram shows the main energy migration pathways, the antenna harvests energy through high molar absorption to the ligand singlet excited state ($S_0 \rightarrow S_1$), and is generally assumed to first undergo intersystem crossing to the triplet state ($S_1 \rightarrow T_1$), followed by population of excited states of Ln^{3+} through energy transfer from T_1 state of the ligand, and finally characteristic luminescent emission from the Ln^{3+} ion. A large ligand-induced Stokes shift should exist between ligand absorption and lanthanide emission in order to prevent back energy transfer which results in low quantum yields and short, temperature-dependent lifetimes.[73] **Figure 2.10 (b)** shows the transitions between the well-defined J-levels (degenerated from the electronic configuration based on Coulomb interaction and spin-orbit coupling) of Tb^{3+} and Eu^{3+}.

The overall quantum yield, Φ_{Ln}^{L}, of a lanthanide complex is given by **Equation 2.13**:

$$\Phi_{Ln}^{L} = \frac{I_{Ln}(E)}{I_{L}(A)} = \eta_{sens}\, \Phi_{Ln}^{Ln} \qquad (2.13)$$

Where $I_{Ln}(E)$ is the number of photons emitted by the Ln metal ion, $I_{L}(A)$ is the number of photons absorbed by the ligand, Φ_{Ln}^{Ln} is the intrinsic quantum yield of the Ln metal ion, η_{sens} represents the sensitization efficiency.

Based on **Equation 2.13**, the Φ_{Ln}^{L} can be improved by tuning the following two factors: η_{sens} and Φ_{Ln}^{Ln}. A higher η_{sens} value can be achieved by the antenna ligand with a higher intramolecular energy transfer rate, and a higher Φ_{Ln}^{Ln} can be improved by optimized Ln^{3+} ion carrier chelate which protect the ions from the

quenching effects of the aqueous matrix, and thus minimizes the non-radiative processes. **Figure 2.11** represents the Tb complex (Lumi4-Tb) based on 2-hydroxyisophthalamide ligands we used in this thesis bearing maleimide functional groups and having a molar absorption coefficient of ca. 26000 M^{-1} cm^{-1} at 340 nm.

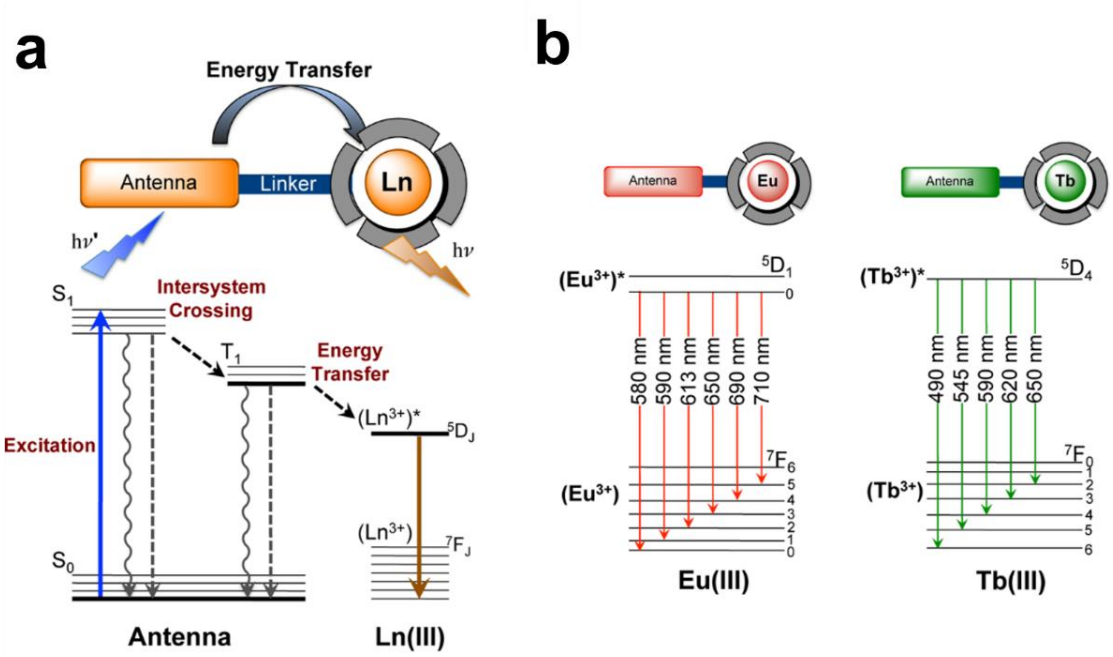

Figure 2.10. (a) Simplified Jablonski diagram for the antenna effect and the scheme of lanthanide complexes (the Ln center surrounded by a chelate and equipped with a sensitizing antenna). **(b)** Commonly observed emission wavelengths of europium (red) and terbium (green) complexes. (Reproduced from reference [84]. Copyright 2014 American Chemical Society)

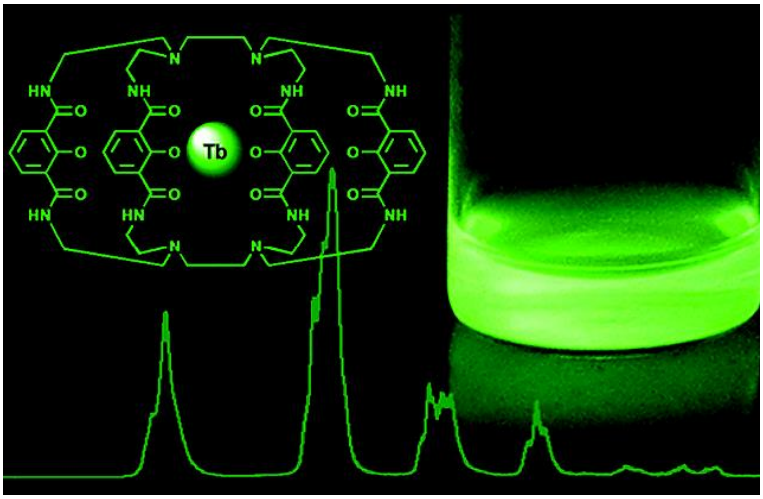

Figure 2.11. Cage-like structure of the ligand for photon harvesting of the Lumi4-Tb complex used in this thesis. (Reproduced from reference [85]. Copyright 2011 American Chemical Society)

Upconverting nanoparticles (UCNPs)

Luminescence usually follows Stokes' law which states that emitted photons have a smaller energy than excitation photons. In 1966, Auzel suggested that energy transfer can take place between neighboring Ln^{3+} ions that are both in their excited states by sequential energy transfer process, which is more efficient than excited-state absorption (or 2-step absorption). In this process, two (or more) low-energy photons are combined resulting in the emission of one higher-energy photon, known as upconversion emission.[86]

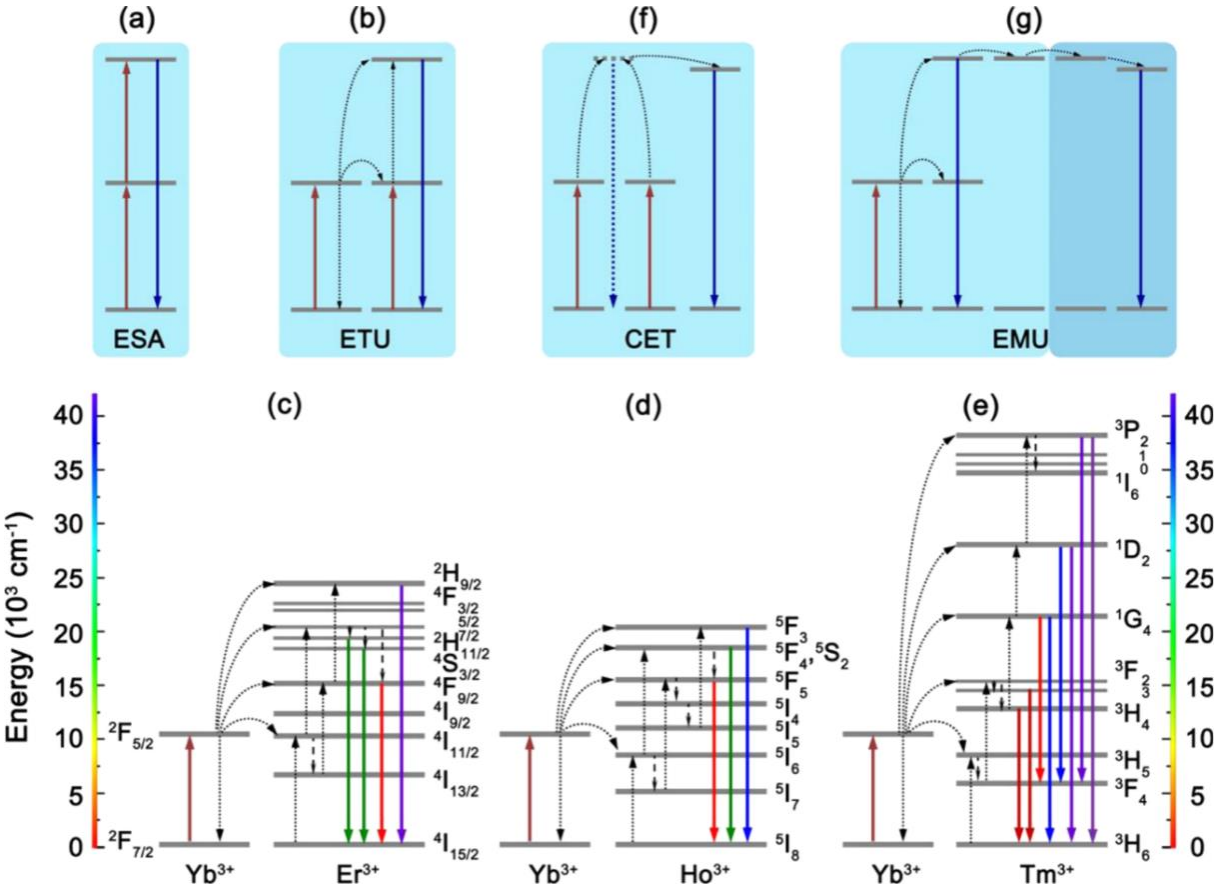

Figure 2.12. Principal UC mechanisms of Ln^{3+}: **(a)** ESA, **(b)** ETU, and UC energy transfer diagrams in **(c)** Yb^{3+}–Er^{3+}, **(d)** Yb^{3+}–Ho^{3+}, and **(e)** Yb^{3+}–Tm^{3+} pairs, **(f)** CET, **(g)** EMU. (Reproduced from reference [87]. Copyright 2015 American Chemical Society)

As illustrated in **Figure 2.12**, upconversion (UC) emissions of Ln^{3+} generally can be divided into the following types of energy transfer pathways: excited-state absorption (ESA), energy transfer upconversion (ETU), cooperative transfer upconversion (CTU), and energy migration-mediated upconversion (EMU). In the case of ESA, excitation takes the form of the sequential absorption of two or more

low-energy photons in a single Ln^{3+}. For ETU processes, each of two neighboring Ln^{3+} ions (sensitizer and activator) can absorb a pump phonon of the same energy, and then transfer the contained to the emitting Ln^{3+} ions (activator) leading to emission at shorter wavelength. UC efficiency of ETU process was strong influenced by the average distance between the neighboring dopant ions which was determined by the dopant concentration. Yb^{3+} is an ideal sensitizer and can effectively transfer its energy to activator ions such as Er^{3+}, Ho^{3+}, or Tm^{3+} by ETU due to a relatively large absorption coefficient at 980 nm (around 10-12 $M^{-1}cm^{-1}$).[88] Nd^{3+} can also be used as a sensitizer when excited at its absorption maximum around 800 nm for a series of lanthanide activators (Er^{3+}, Ho^{3+}, or Tm^{3+}).[89]–[91] CTU is a process involving the interaction of three Ln^{3+} ion centers. Two Ln^{3+} ions generally are the same type (sensitizer), and both can absorb a pump photon to the excited state, and then interact with the third Ln^{3+} ions (activator) simultaneously, cooperatively transfer the contained energy, and excite the third Ln^{3+} to a higher state. Compared with ETU process, the UC efficiency of CTU is very low due to the absence of a long-lived intermediate energy state of the activator. EMU process was suggested by Liu and co-corkers in 2011, four types of Ln^{3+} centers, including sensitizer, accumulator, migrator, and activator, are incorporated into different parts of core/shell nanostructure with precisely defined concentration. A sensitizer ion first transfers its excitation energy to an accumulator ion. Subsequently, the energy transfers from the excited state of the accumulator to a migrator ion, followed by the migration of excitation energy via the migrator ion sublattice through the core–shell interface. Finally, the migrating energy is trapped by the activator ion, resulting in UC emission.[92]

2.3.2 Lanthanide complexes as FRET donor

LLCs-based donors have many advantages, and the most important property of lanthanide-based donors for FRET is their long luminescence decay time reaching up to several milliseconds[3],[93],[94], which means that the excited-state lifetimes of most lanthanide-based donors are several orders of magnitude larger than those of any other acceptor. In 1993, Mathis demonstrated LLCs can be used as energy donors in a homogeneous FRET immunoassay,[95] and since then Tb and Eu based

LLCs have been used much as FRET-donors. Depending on the design of FRET systems, FRET acceptors such as organic dyes fluorescent proteins, or QDs can be paired with LLCs as donor. As mentioned in **Section (2.2.3)**, LLCs/UCNP-to-QD based FRET configurations can inhibit or decrease direct excitation of the QDs. A clear evidence for LLCs-to-QD based FRET configurations was demonstrated by Hildebrandt and Charbonnière.[60],[61] Due to the large difference in D and A excited state lifetimes, the FRET-sensitized lifetime of A is the same as the FRET-quenched lifetime of the lanthanide donor.[2] As shown in **Figure 2.13**, the higher the FRET efficiency, the lager the required difference between τ_A and τ_D. For the case of 95% FRET efficiency, $\tau_A = 0.1\tau_D$ already shows clear differences in the slope of decay curve of τ_{AD} and τ_{DA}. As a result, the use of donors with $\tau_D \gg \tau_A$ allows the replacement of τ_{DA} by τ_{AD}, and **Equation 2.10** (**Section 2.1.1**) can be rewritten as **Equation 2.14**:

$$E_{FRET} = 1 - \frac{\tau_{DA}}{\tau_D} = 1 - \frac{\tau_{AD}}{\tau_D} \tag{2.14}$$

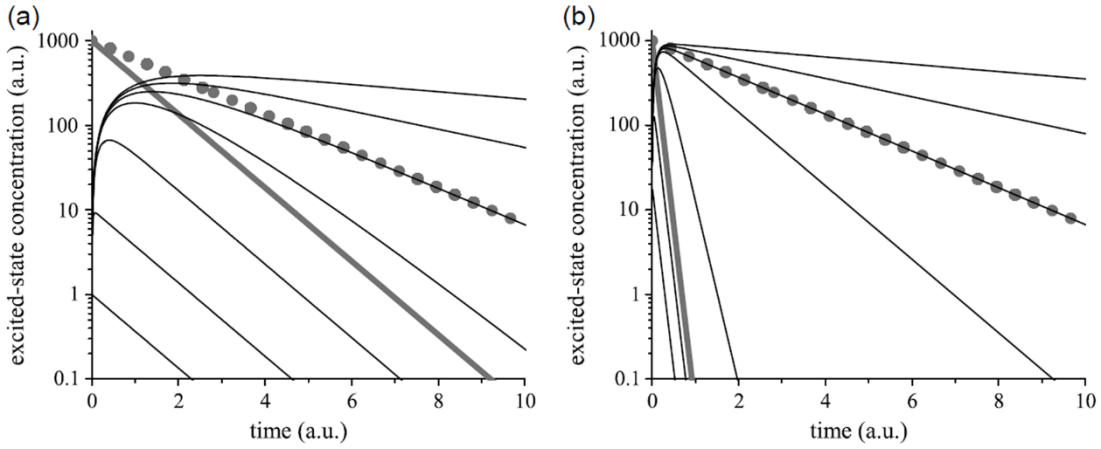

Figure 2.13. Time-resolved decay curves of A with τ_A = 0.001, 0.01, 0.1, 0.5, 1, 2, and 5 τ_D(black curves from bottom to top) for E_{FRET} =50% **(a)** and 95% **(b)**. Pure donor decays (τ_D, dotted gray curves) and FRET quenched donor decays (τ_{DA}, gray curves) are shown for comparison. (Reproduced from reference [2]. Copyright 2013 Wiley-VCH Verlag GmbH & Co. KGaA)

Therefore, by choosing an acceptor with emission at a wavelength region void of donor emission, and using pulsed excitation and time-gated detector for a short delay time and gate width (time-gated measurement, detail in **Section 2.4.1**), the acceptor detection channel becomes a "FRET-proof" channel, which means the sensitized acceptor signal completely arises from FRET pairs, and is independent of concentration effects and incomplete binding.

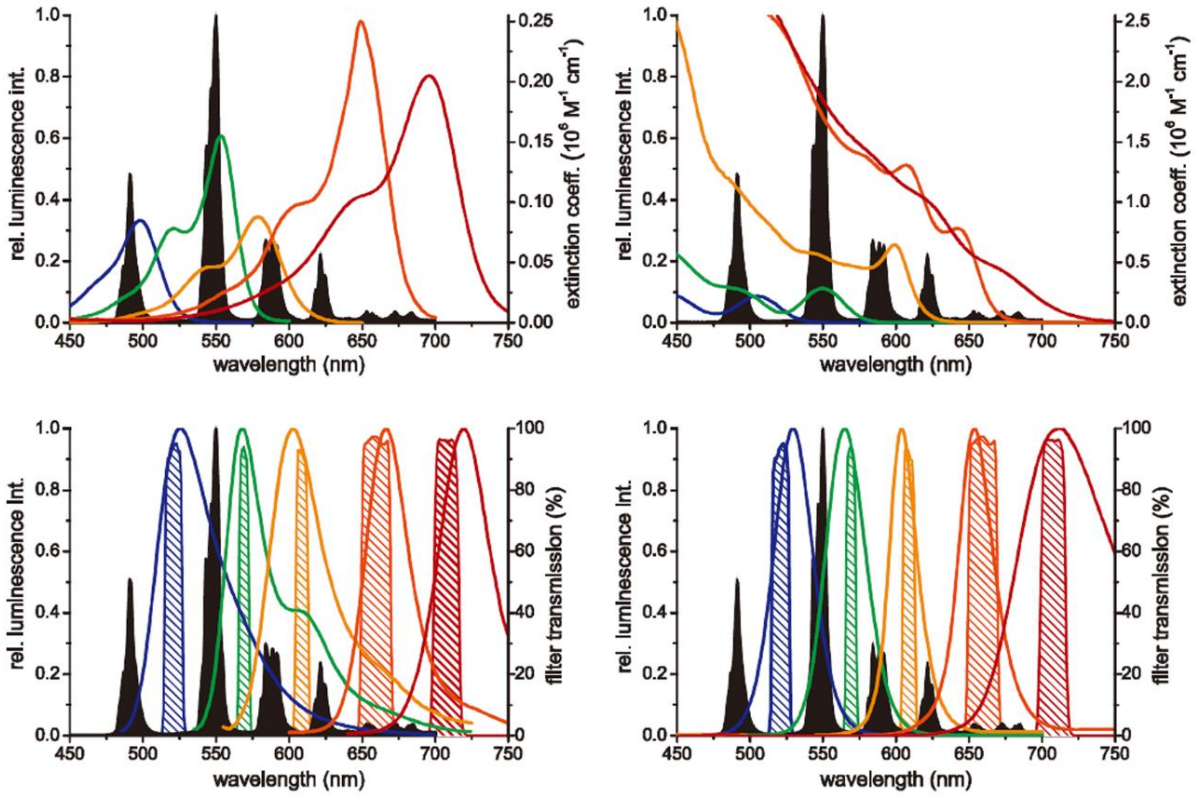

Figure 2.14. LTC as donor based multiplexed FRET. **Top:** Broad spectral overlap between LTC emission and the absorption of several different acceptors. **Bottom:** Well-separated PL spectra of LTC emission bands allows the detection of different acceptors with very low LTC background (represented by the shaded bandpass filter transmission spectra). LTC PL spectra in black. Left (organic dyes): Oregon Green (blue), AlexaFluor555 (green), AlexaFluor568 (orange), Cy5 (red) and AlexaFluor700 (wine); right (QDs): QD525 (blue), QD565 (green), QD605 (orange), QD655 (red), and QD705 (wine). (Reproduced from reference [94]. Copyright 2014 Elsevier)

In addition, multiple narrow and well-separated PL spectra of LLCs provides the possibility of multiplexing with several different FRET acceptors.[94] And some of LLCs PL spectra (*e.g.*, luminescent Tb complex (LTC)) are in a wavelength region where many fluorophores are excellent absorbers and therefore lead to relatively large spectral overlap integrals. For example, Förster distances of up to 11 nm can be achieved by using LTC-to-QD D–A pairs.[96] It should be noted that for the calculation of Förster distances of LLCs donors based FRET, the QY of donor is the QY of the Ln^{3+} ion (Φ_{Ln}^{Ln}) and not the QY of the complete LLCs (Φ_{Ln}^{L}) (calculated by **Equation 2.13**) because the Φ_{Ln}^{Ln} determines the strength of the donor's electric field, thus, LLCs with high Φ_{Ln}^{Ln} can be designed for achieving large Förster distance and efficient FRET. As shown in **Figure 2.14**, by choosing several different acceptors with emission at a wavelength region between or beyond the LTC PL bands, LTC as donor based multiplexed FRET can be achieved by using

QDs and organic dyes. Compared to LTC-organic dyes, the board and continuous absorption spectrum and high molar absorption coefficient of QD lead to larger overlap integrals and Förster distances between LTC-QD D-A pairs. Moreover, spectral separations of LTC-QDs are more efficient due to narrow, size- and symmetric emission spectra of QD acceptor. It should be noted that several organic dyes emit in the same detection region, which lead to spectral crosstalk for LTC-organic dyes multiplexing. This unavoidable spectral overlap requires mathematical correction in order to achieve efficient multiplexing.

Another advantage (or comfortable aspect) of LTC donors (also for Eu complexes) is that they most often possess unpolarized emission, which can greatly reduce the uncertainty of the orientation factor κ^2. Due to their multiple transition dipole moments, LTC can server as randomized donors and the orientation factor κ^2 will be limited to values between 1/3 and 4/3 even with an acceptor having a fixed orientation.[94] In this situation, simply assuming $\kappa^2 = 2/3$ results in error in R_0 less than 12% due to the sixth root dependence.

2.4 Fluorescent dyes

Fluorescent dyes are widely used in fluorescent labelling of biomolecules because of their high quantum yields, solubility, and particularly commercial availability. Fluorescent dyes functionalized with N-hydroxysuccinimide (NHS) ester, maleimide, hydrazide, or amine group are available from commercial sources and easy for bioconjugation.[97] **Figure 2.15** shows the fluorescence spectra regions of commercial dye families that cover the UV-vis-IR range. However, they usually have a high rate of photobleaching, are sensitive to environment and can self-quench at high concentration (self-aggregation). All dye families are typically characterized by closely spaced, broad absorption/emission profiles (small Stokes shift),[97],[98] which usually lead to direct excitation of the acceptor for FRET application. Since fluorescent dyes as FRET acceptor/multi acceptors have been discussed in **Section (2.2.3)**, this section will focus on the dye aggregates **(2.5.1)** and homo FRET of fluorescent dyes **(2.5.2)**.

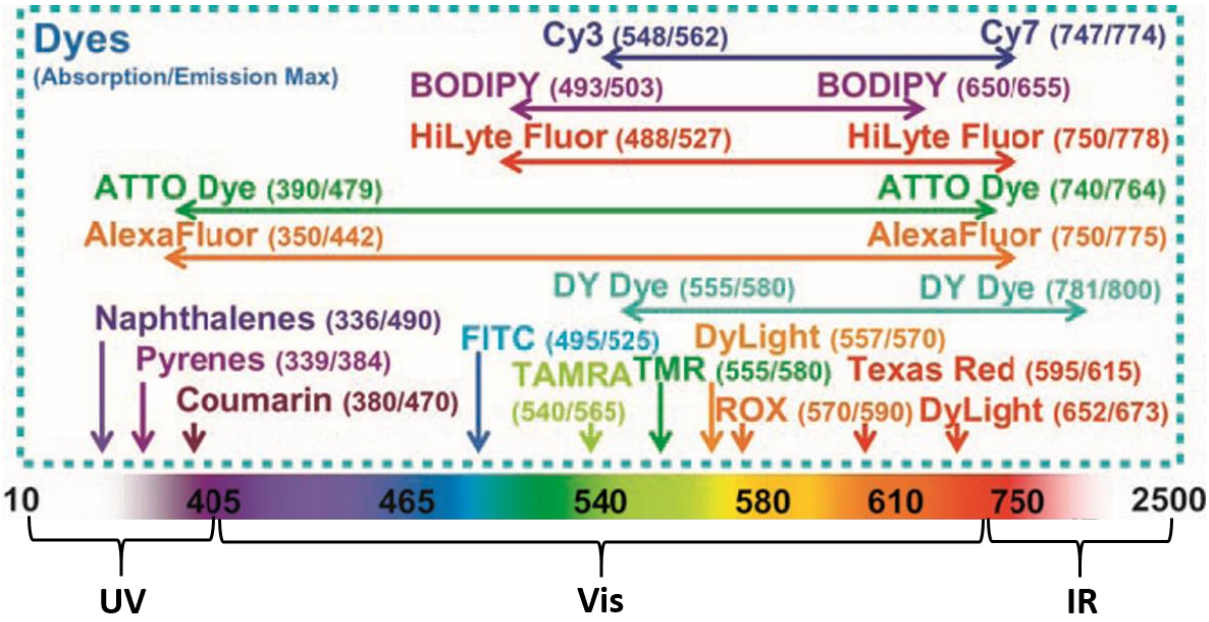

Figure 2.15. Examples of available fluorescent dye families. (Adapted from reference [97]. Copyright 2006 Wiley-VCH Verlag GmbH & Co. KGaA)

2.4.1 Dye aggregates

For FRET application, large surface area of nanoparticle based donor enable to assemble multiple acceptors, and also can facilitate the formation of aggregates of acceptor organic dyes. In general, dye aggregates are classified on the basis of the spectral shift. For some dye aggregates, the absorption maximum is blue-shifted and bandwidth increases as compared to the monomer, termed as H-aggregates.[99] In contrast, the absorption maximum is red-shifted and exhibits very narrow peak with respect to that of the monomer, termed as J-aggregates.[100] J-aggregates possess a bent or head-to-tail structure and usually show higher fluorescence intensity than that of the monomer, while H-aggregates exhibit non-fluorescence with the exception of a few examples.[101] It can be explained by exciton theory of Kasha, as illustrated in **Figure 2.16**, the dye molecule is regarded as a point dipole and the excited state of the dye aggregate splits into two levels through the interaction of transition dipoles. For H-aggregates, molecular dimers stacked "side-by-side" exhibit a blue-shifted absorption maximum and suppressed radiative decay rate, while for J-aggregates, molecular dimers stacked "head-to-tail" exhibit a red-shifted absorption maximum and enhanced radiative decay rate.[102]

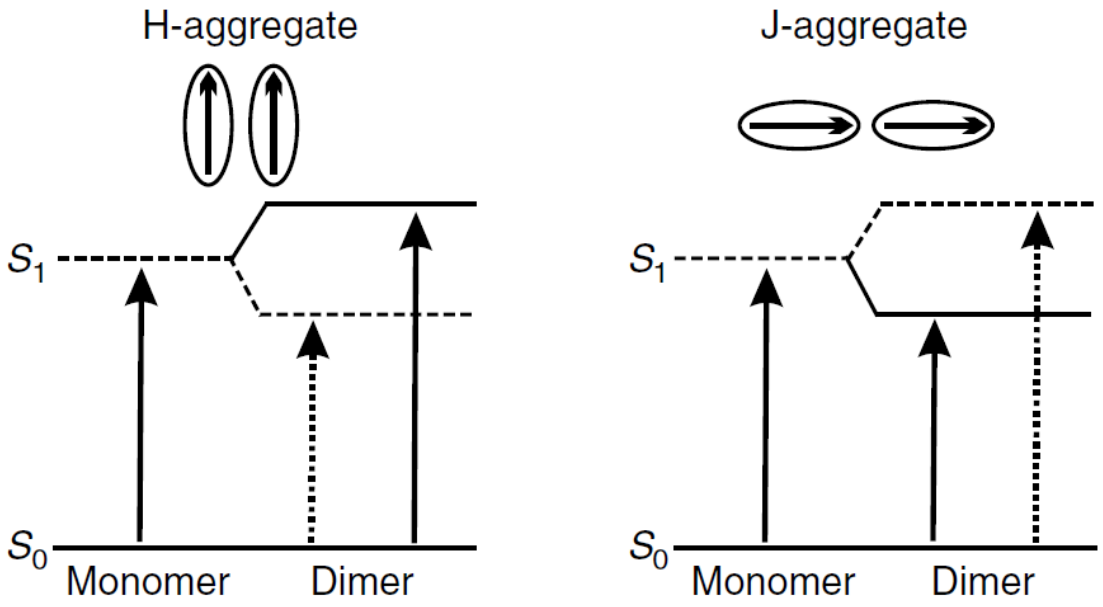

Figure 2.16. Simplified schematic of exciton theory to explain the different absorption and fluorescence behaviors of H-aggregates and J-aggregates. (Reproduced from reference [99]. Copyright 2011 Wiley-VCH Verlag GmbH & Co. KGaA)

Algar *et al.* reported the formation of H-aggregates on the surface of the QDs as the *n* increased in a QD-multiple (*n*) dyes FRET system. The formation of non-fluorescent dimers led to two hetero-FRET pathways: from the QD to fluorescent monomeric dyes or non-fluorescent dimeric dyes.[56] As a result, the sensitized dye PL did not correspond to the QD donor quenching. Bawendi and co-workers reported the QD/J-aggregates can combine the broad UV absorption of QDs with the ultra-narrow emission band of J-aggregates due to efficient FRET from the QDs to the J-aggregates with essentially complete quenching of the QD and sensitizing of the J-aggregates fluorescence,[103]–[105] which could be potentially applied for biological multiplexing. Consequently, the formation of such aggregates can strongly modify optical absorption and the fluorescence spectra, which is both a limitation and an opportunity for FRET application.

2.4.2 Homo FRET

FRET does not necessarily require two different fluorophores as a D–A pair. In particular, fluorescent dyes usually have a significant overlap of their absorbance and emission spectra due to their small Stokes shift. In principle, such a fluorophore can transfer its excitation energy to a neighboring molecule of the

same species, which is referred as homo-FRET.[99] Typically, this phenomenon does not lead to changes in PL lifetime, the steady-state intensity or a shift in the emission spectrum, and such a bi-directional energy transfer can be monitored only by fluorescence anisotropy.[106]–[108] Fluorescence anisotropy (A) can be calculated using **Equation 2.15**: [1]

$$A = \frac{I_{\parallel} - I_{\perp}}{I_{\parallel} + 2I_{\perp}} \tag{2.15}$$

Where $I_{\parallel}$ and $I_{\perp}$ represent the intensities of emission polarizer that is oriented parallel and perpendicular to the direction of the polarized excitation, respectively.

For randomly oriented transition dipoles in the absence of FRET, A equals 0.4. When homo-FRET occurs, A will decrease and close to 0 due to depolarization process.[99] FRET efficiency based on fluorescence anisotropy can be calculated using **Equation 2.16**:[99]

$$E_{\mathrm{FRET}} = 1 - \frac{A_{\mathrm{FRET}}}{A_0} \tag{2.16}$$

Where A_{FRET} and A_0 are the fluorescence anisotropy in the presence and absence of energy transfer, respectively.

However, in multi-dye systems (dye aggregates) the increased homo-FRET (more random migration steps) leads to a higher probability that the exciton encounters a trap state (dark dye or H-dimer), which resulted in both PL intensity and lifetime quenching.[1],[56],[109]–[112] In this thesis, we also observed quenching of Cy5.5 PL intensity caused by combination of the formation of non-fluorescent H-dimers and multiple homo-FRET steps between Cy5.5 dyes, which increased the probability of the migrating exciton to get dissipated in the Cy5.5 dimer "trap states".

2.5 Gold nanoparticles

Gold nanoparticles (AuNPs) possess unique physical and chemical properties that make them excellent candidates for fabricating biosensors.[113] (i) AuNPs with high stability can be synthesized under mild condition. (ii) Similar to other nanoparticles, large surface area of Au NPs offer a suitable platform for multifunctionalization.[114] (iii) The properties of AuNPs can be tuned by varying their size, shape, and the surrounding chemical environment (*e.g.*, ligand,

magnetic fields and electrolyte ions).[115],[116] (iv) Small AuNPs (or Au clusters diameter ≤ 3 nm) exhibit broad absorption and distinct fluorescence due to quantum confinement effects, while lager AuNPs have strong plasmon absorption bands and non-fluorescence. In this section, we will focus on surface plasmon resonance **(2.5.1)** and nanosurface energy transfer theory **(2.5.2)**.

2.5.1 Surface plasmon resonance

The SPR is the result of the collective oscillation of the conduction electrons across the nanoparticle due to the resonant excitation by the incoming photons.[113] For AuNPs, the resonance condition is satisfied at visible wavelengths, therefore leading to its deep-red color in water.[117] The main characteristics of SPB are including: (i) The surface plasmon band (SPB) decreases with decreasing size and is absent for AuNPs with core diameter less than 2 nm. (ii) the SPR is influenced not only by size but also by solvent, ligand, interparticle distance, and temperature.[113] (iii) The SPR frequency is sensitive to the proximity of other nanoparticles. Therefore, the aggregation of nanoparticles results in significant red-shifting (from ~520 to ~650 nm) and broadening in the SPB, changing the solution color from red to blue due to the interparticle plasmon coupling.[118] For application of energy transfer, large AuNPs can serve as excellent acceptor, because they have strong SPB that can overlap with the donor (*e.g.*, QD) emission. For biosensing based on QD quenching by AuNP, emission of QD is often tuned to align with absorption of AuNP to increase quenching efficiency.[119] However, it should be noted that this strong absorption can also lead to inner filter effects (reabsorption of QD emitted light by the AuNPs or absorption of QD excitation light by the AuNPs).[3]

2.5.2 Nanosurface energy transfer theory

Metal nanoparticles (*e.g.*, Au nanoparticles (AuNPs)) provide strong fluorescence quenchers when paired with dyes,[120]–[124] QDs,[125]–[129] fluorescent proteins,[130] or lanthanide complexes,[131] and the extent of energy transfer quenching exceed the range stipulated by FRET.[132] The energy transfer mechanism to AuNPs has been discussed within the concepts of nanosurfaces.

Nanosurface energy transfer (NSET) is a dipole-surface energy transfer process involving molecular dipole and nanometal surface, which can be distinguished from FRET by the efficiency equations. In addition, there is no overlap integral to calculate. Persson has been a leader in advancing theories of molecular de-excitation by metal surfaces.[133] Based on the model suggested by Persson, the NSET model was proposed by Strouse and coworkers.[121]–[123],[134],[135] They suggested a R^{-4} distance dependence for the energy transfer rate, which significantly increases (about two fold) the distance range of FRET. In detail, Persson's surface damping model was applied to molecular dipole quenching of NSET model, which was based on the conservation of momentum during electron-hole pair formation via the near field of an electric dipole.[133] Basically, the electric field of a separate dipole does not provide the required momentum for direct exciton formation, so the process must occur simultaneously with the electron scattering process. Persson recognizes two main sources of scattering: the bulk scattering (electron-electron, electron-phonon, electron-defect etc.) process involves interactions on the over the integrated volume of the crystal, resulting in a R^{-3} distance dependence. However, scattering from surface potential involves integration on the plane and produces R^{-4} distance dependence.

NSET transfer rate is given by **Equation 2.17**:[123]

$$k_{\mathrm{NSET}} = 0.225 \frac{c^3}{\omega_{\mathrm{D}}^2 \omega_{\mathrm{F}} k_{\mathrm{F}} R^4} \frac{\Phi_{\mathrm{D}}}{\tau_{\mathrm{D}}} \tag{2.17}$$

where c is the speed of light, ω_{D} is the angular frequency ($\omega = 2\pi c\lambda^{-1}$) for the donor, ω_{F} is the angular frequency for bulk gold, k_{F} is the Fermi vector for bulk gold, R is the donor-acceptor distance, Φ_{D} is the donor quantum yield, and τ_{D} is luminescence decay time of the donor. Similar to the Förster distance R_0 in FRET theory, a distance of 50% NSET efficiency can be defined by replacing k_{NSET} with $1/\tau_{\mathrm{D}}$, and R_0^{NSET} can be calculated by **Equation 2.18**:

$$R_0^{\mathrm{NSET}} = \left(0.225 \frac{c^3 \Phi_{\mathrm{D}}}{\omega_{\mathrm{D}}^2 \omega_{\mathrm{F}} k_{\mathrm{F}}}\right)^{1/4} \tag{2.18}$$

NSET has emerged as an energy transfer principle that can measure biomolecular interactions over distances up to 50 nm and thereby more than double the range of FRET.[125] Research showed that NSET model was in good agreement with the experimental data of small size AuNPs (below 3 nm) by using dyes and quantum

dots (QDs) as donors because they do not have any plasmon bands.[123],[134],[135] NSET behavior with energy transfer efficiencies independent of the NP size or number of donors was also demonstrated for larger size AuNPs.[120],[128],[130],[132] However, NSET studies have focused on the interaction of AuNPs with organic dyes and QDs. In this thesis, we will investigate the interaction of AuNPs with luminescent lanthanide complexes.

2.6 Time-resolved measurement

Time-resolved (TR) measurements are widely used in fluorescence spectroscopy, particularly for studies of biological macromolecules and cellular imaging because they contain more information than steady-state data.[1] For instance, the precision of the imaging and quantification analysis are influenced by the variation of excitation laser power and probe concentration in steady-state measurement, while fluorescence lifetimes of probe are typically independent of the probe concentration.[136] Moreover, when there is spectral overlap between probes and autofluorescence or the emission from two or more probes, it is difficult to recognize the signal of interest based on the steady-state data. In contrast, time-resolved measurement can distinguish these probes from autofluorescence or each other based on their different decay rates.[83] Furthermore, in order to obtain high-quality time-resolved photoluminescence images of biological samples, luminophores are required to possess a luminescence lifetime that is sufficiently long compared to that of autofluorescence in biological sample. Lanthanides complexes and nanoparticles are famous for their long luminescence lifetimes (up to ms) and have been mentioned in **Section (2.3.1)**. Other luminophores such as transition-metal complexes, doped-quantum dots (d-dots), lattice-strained QDs (LS-QDs), carbon dots, metal nanoclusters, and persistent nanoparticles have also been reported to exhibit long luminescence lifetimes and be suitable for time-resolved luminescence measurements. The lifetime ranges of different classes of luminophores are listed in **Table 2.3**. The discussion below will focus on the time-gated measurement **(2.4.1)**, lifetime measurement **(2.4.2)**, and application of time-resolved measurement **(2.4.3)**.

Table 2.3. PL lifetime ranges of different classes of long lifetime luminophores.

Luminophores	Maximum lifetimes
lanthanide chelates[86]	μs~ms
lanthanide-doped nanocrystals[137]	μs~ms
transition-metal complexes[138]	hundreds ns ~ μs
doped-QDs (*e.g.*, Mn,[139] Cu,[140] Ni,[141] and Yb[142])	hundreds ns ~μs
lattice-strained QDs[143],[144]	hundreds ns
carbon dots[145]	~s
metal nanoclusters[146],[147]	~μs
persistent nanoparticles[148]	~days

2.6.1 Time-gated measurement

Standard luminescence analysis and microscopy techniques are based on variation of PL intensity with specific wavelength bands, which is indicative of the presence of a specific analyte or the occurrence of an event. However, for applications such as analyte in low concentration and rare-event detection, the luminescence signal is difficult recognized from naturally occurring autofluorescent substances.[149] Time-gated (TG) measurement in combination with luminescent probes with relatively long emission lifetimes can efficiently solve this problem. As shown in **Figure 2.17**, in a typical TG measurement, the luminescent probe is excited by a pulsed light, and exhibits relatively long decay time. The detector starts to work after a delay time in which short-lived autofluorescence fades. Thus, only long-lived events will be detected in the signal collection window. These signals can be distinguished from short-lived background even if they are low intensity, which significantly enhances the detection sensitivity.[83]

Recently, the application of TG microscopy imaging has been expanded in bioimaging and sensing for different purposes. As mentioned in Section **(2.3.2)**, in a FRET system with a long lifetime LLCs-based donor, time-gated measurement efficiently suppressed the fluorescence from directly excited acceptors.[68],[96] And the decay time of FRET-sensitized acceptor PL can be precisely tuned and

designed as single nanoparticle barcoding.[44][150] Combination of TG measurement with stimulated emission depletion (STED) microscopy opened up new approaches for designing probe of STED microscopy.[151] In addition, TG measurement can be extended to the second biological window (1000-1350 nm),[152]–[154] which could provide much higher signal-to-noise ratio and penetration depth in vivo imaging than that within the first biological window (700−950 nm).[155],[156] In this thesis, TG measurement was employed to regionalize the lifetime codes.

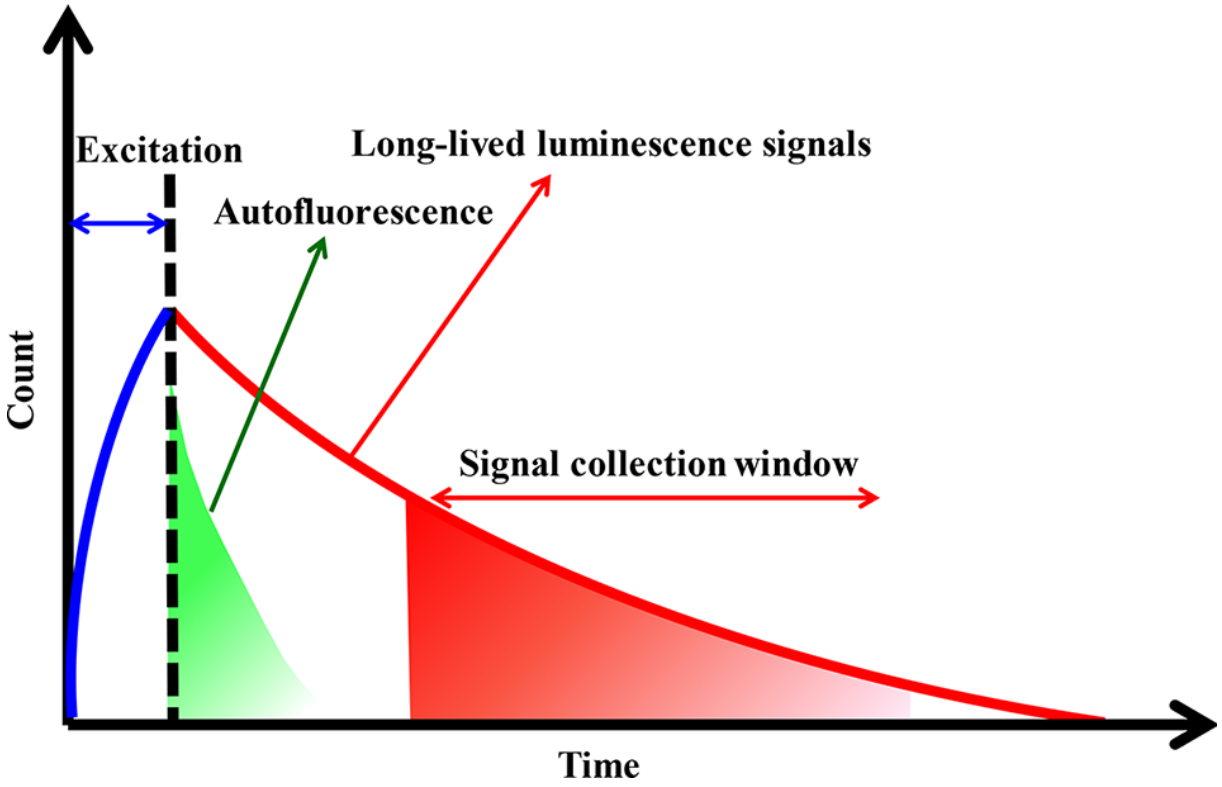

Figure 2.17. Principle of TG measurement. (Reproduced from reference [83]. Copyright 2015 American Chemical Society)

2.6.2 Lifetime measurement

TG measurement provides the intensity information of the photons collected in gate width. In contrast, lifetime measurement analyzes the luminescence lifetime of a probe. The time-domain and frequency-domain are two dominant methods for measuring time-resolved fluorescence. For the time-domain method, as illustrated in **Figure 2.18 a**, the sample is excited with a pulse of light much shorter than the decay time τ of the sample. The time dependent intensity decay is measured

following the pulsed excitation, and can be descripted as a function of time (**Equation 2.19)**:

$$I = \sum_i A_i e^{-\frac{t}{\tau_i}} \tag{2.19}$$

Where I is the luminescence intensity, A_i is the amplitude for different I, and τ_i is the different decay times. It should be noted that the shape of the excitation pulse and how this pulse is detected by the instrument are not negligible in the case of short lifetime sample (in the nanosecond range), and a deconvolution of the instrument response function (IRF) to the measured fluorescence decay curve is necessary in order to extract the "true" lifetime.[1]

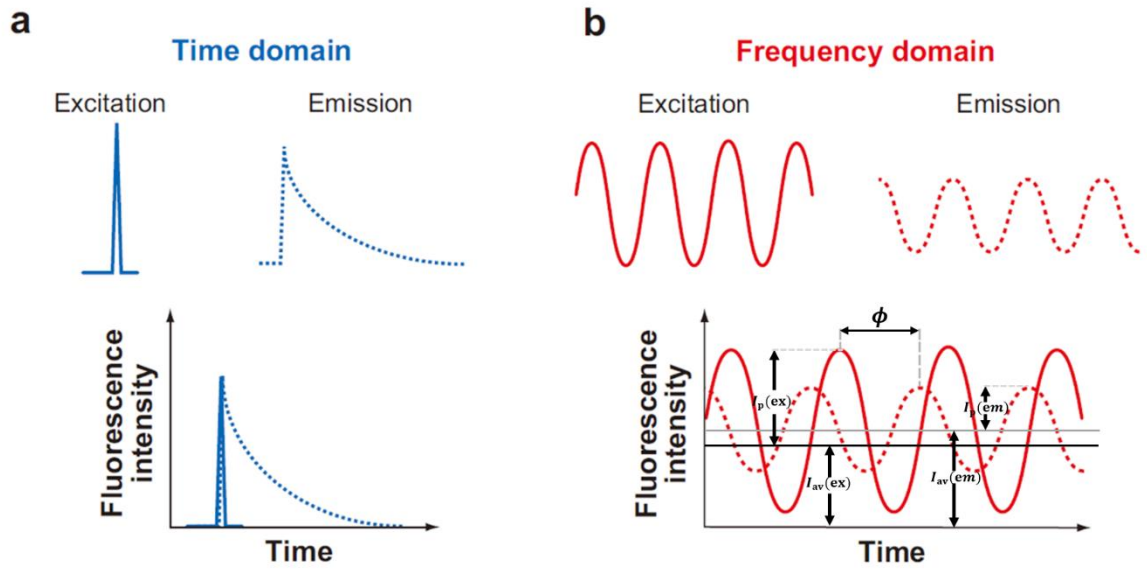

Figure 2.18. Principles of fluorescence lifetime measurement. **(a)** Time domain method, **(b)** Frequency domain method (Adapted from reference [157]. Copyright 2006 Annual Reviews)

For the frequency domain method, as illustrated in **Figure 2.18 b**, the sample is excited with intensity-modulated (typically sinusoidal modulation) light (*e.g.*, $I = I_{\mathrm{av}}(\mathrm{ex}) + I_{\mathrm{p}}(\mathrm{ex})\cos(\omega t)$) with a frequency, which is typically in the same range as the reciprocal of the luminescence decay time of the sample. Then the emission light (*e.g.*, $I = I_{\mathrm{av}}(\mathrm{em}) + I_{\mathrm{p}}(\mathrm{em})\cos(\omega t - \phi)$) will have the same frequency, the phase shift (ϕ) between excitation and emission lights is used to calculate the luminescence decay times and can be descripted as **Equation 2.20**:

$$\phi = \tan^{-1}\left(\frac{\sum_i(\alpha_i\omega\tau_i^2)/(1+\omega^2\tau_i^2)}{\sum_i(\alpha_i\tau_i)/(1+\omega^2\tau_i^2)}\right) \tag{2.20}$$

Moreover, the lifetime of the fluorophore also causes a decrease in the peak-to-peak

intensity of the emission relative to that of the excitation. The demodulation is usually expressed as modulation ratio ($M = \left[I_{\mathrm{p}}(\mathrm{em})/I_{\mathrm{av}}(\mathrm{em})\right]/\left[I_{\mathrm{p}}(\mathrm{ex})/I_{\mathrm{av}}(\mathrm{ex})\right]$), and can also be used to calculate the lifetime. The relation between modulation ratio and luminescence decay times can be descripted as **Equation 2.21**:

$$M = \sqrt{\frac{\left[\left(\sum_i(\alpha_i\omega\tau_i^2)/\left(1+\omega^2\tau_i^2\right)^2+\sum_i(\alpha_i\tau_i)/\left(1+\omega^2\tau_i^2\right)^2\right)\right]}{(\sum_i\alpha_i\tau_i)^2}} \tag{2.21}$$

In this thesis we chose to use the time-domain method for temporal characterization. Depending on the lifetime of the fluorophore, the photons arriving at the detector can be counted by several techniques such as steady-state photon counting, gated photon counting, multichannel scalers (MCS), and time correlated single photon counting (TCSPC).[158] Based on the TCSPC, fluorescence lifetime imaging microscopy (FLIM) maps lifetime spatial distribution in cells, tissues, and small animal modes, where all photons are collected for calculation of lifetimes and signals of probe and autofluorescence are distinguished based on their different decay rates in each pixel.[158] FLIM is mainly used to image viscosity, temperature, pH, refractive index, ion and oxygen concentrations at the cellular level[159] or fabricate two dimensional codes.[140] Recently, the application of FLIM has been expanded to tissues, organs, and laboratory animals.[160]–[162]

Both TG measurement and lifetime measurement can obtain high quality imaging with minimized autofluorescence interference. TG measurement is more suitable for long lifetime probes with significant intensity response to analyses, while lifetime measurement has higher resolution in time domain, and suitable for relatively short lifetime (ns~μs), because lifetime measurement requires a very long photon acquiring duration.

2.6.3 Time to multiplex

Optical multiplexing typically requires a matrix of optical codes, ideally carried by nano/micro-sized objects, such as nanoparticles or microbeads. It provides many advantages for biomedicine, optical data storage, document security.[137],[154],[163],[164] In biomedicine, multiplexing refers to high-throughput technologies, which can simultaneously identify and quantify multiple

distinctive species.[165],[166] In optical data storage, multiplexing is aim to increase the storage capacity within spatially limited memory elements.[163],[167] In document security, the purpose of multiplexing is to prevent forgery, tampering or counterfeiting.[137] Luminescent nanoparticles based encoding is an important technology for optical multiplexing, and the most commonly used encoding principle is based on color, polarization, lifetime, and intensity. In 2001, Nie *et al.* fabricated a diverse array of barcoding by mixing different color and intensity levels of QDs in microbeads.[164] Since then, the spectroscopic encoding of microbeads based on QD color and intensity has been regarded as one of the most promising approaches due to its flexible encoding and convenient decoding.[168] However, intensity-bases encoding requires the precise control of concentration. In 2014, Chen *et al.* suggested that the lifetime of QDs can be regarded as an excellent parameter for designing optical encoding, and fabricated NIR-emitting two-dimensional(2D) codes based on multi-lifetime and multi-color.[140] As shown in **Figure 2.19**, NIR-emitting QDs with long lifetime (up to 1 μs) were synthesized by doping Cu into the lattice-strained core/shell nanostructure, and embedded into microbeads to fabricate NIR-emitting 2D codes. FLIM and multispectral imaging system were employed to recognize the codes. Lu *et al.* also realized that lifetimes can become a new dimension for optical encoding. They prepared UCNPs with a wide tunable lifetime range (μs-ms) and named them "τ dots".[137] **Figure 2.20** shows that tunable lifetime of UCNPs were achieved with stepwise varied Tm^{3+} concentrations in $NaYF_4$ host nanocrystals. In this case, energy transfer from the sensitizer to the activator ion at varying sensitizer-activator distances provides lifetime tunability. And they also demonstrated that these τ dots can be used in lifetime-encoded document security and photonic data storage. In a traditional luminescence imaging, only a complex picture can be observed, while in time-resolved imaging, the three patterns with different lifetime can be distinguished. Recently, Fan *et al.* reported that lifetime-engineering nanoparticles can unlock multiplexing *in vivo* imaging in the second biological window.[154] They shift the wavelength range of lifetime tunable nanoparticles to NIR, enabling them to reach deeper penetration depths.

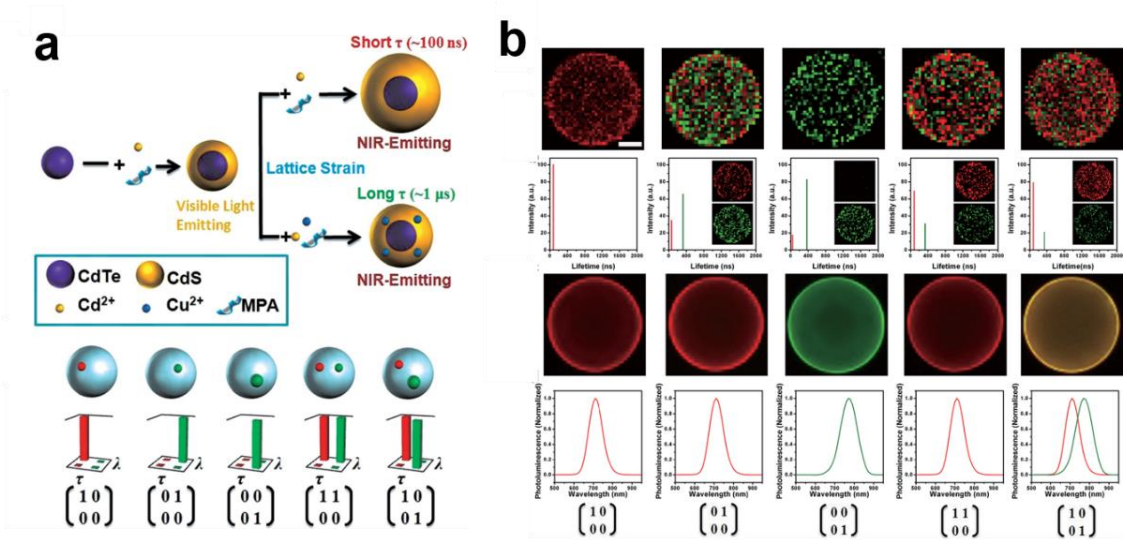

Figure 2.19. (a) Synthesis of NIR-emitting QDs with tunable lifetime and principle of 2D encoding based on color(λ) and lifetime(τ). Large spheres represent microbeads, in which small colored spheres represent QDs (red: short τ, green: long τ, the size of spheres represents the different color). **(b)** Decoding using FLIM and multispectral imaging system (from top to bottom: FLIM images, lifetime distribution (inset: unmixed FLIM images), merged multispectral images, and emission spectra. Scale bar: 10 μm).(Adapted from reference [140]. Copyright 2014 Wiley-VCH Verlag GmbH & Co. KGaA)

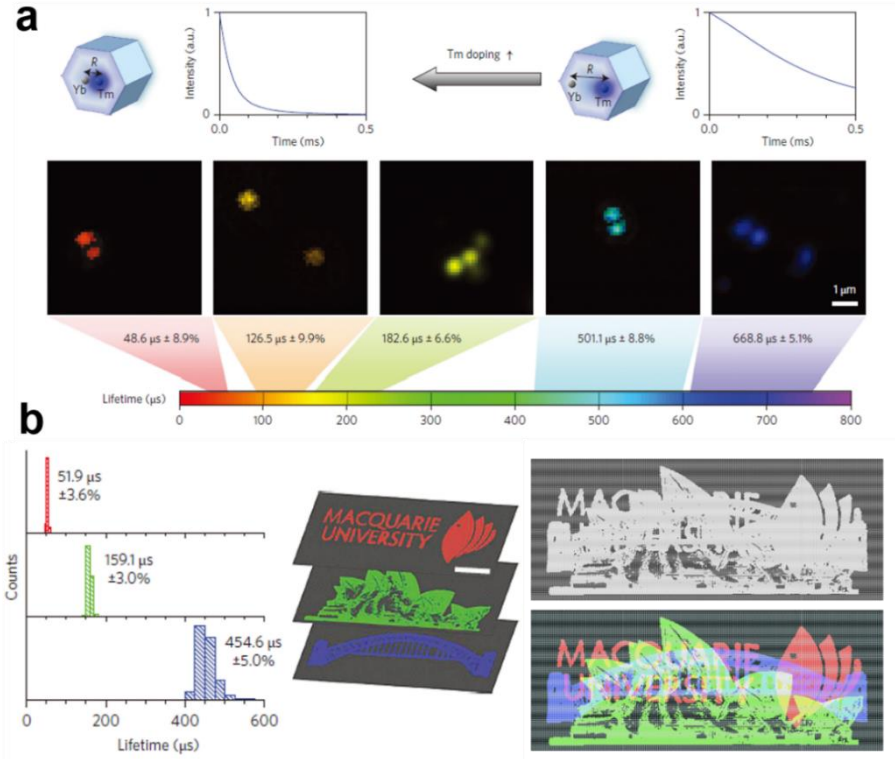

Figure 2.20. (a) Scheme for lifetime tuning of UCNPs and time-resolved confocal images for "τ dots". **(b)** Demonstration of lifetime-encoded document security and optical data storage (Intensity-based luminescence imaging only gives a complex picture, while time-resolved scanning separates the patterns based on the lifetime components of every pixel). (Adapted from reference [137]. Copyright 2014 Nature Publishing Group)

3. Lanthanides complex to QD FRET based cell barcoding

C. Chen, L. Ao, Y.-T. Wu, V. Cifliku, M. Cardoso Dos Santos, E. Bourrier, M. Delbianco, D. Parker, J. Zwier, L. Huang, and N. Hildebrandt. Single-Nanoparticle Cell Barcoding by Tunable FRET from Lanthanides to Quantum Dots. *Angewandte Chemie International Edition* **2018**, *57*, 13686-13690.

3.1 Introduction

Optical encoding has great potential for nanomedicine, diagnostics, biosensing, document security, and optical data storage.[137],[163],[164],[168] Such barcoding has exploited both the emission color[164],[169] and the excited-state lifetime[140],[144],[170] components of PL. The majority of encoding approaches applied mixing of different luminescent molecules or nanoparticles in microspheres[140],[164],[170] or cells.[144],[169],[171] Using individual dyes or nanoparticles (e.g., QDs)[172],[173] for optical encoding is limited by the spectral overlap of their PL spectra and the concentration-dependence of PL intensity. Concentration-independent PL lifetime-multiplexing with individual nanoparticles has also been demonstrated. One concept used upconversion nanoparticles (UCNPs) with varying co-doping concentrations of Yb^{3+} and Tm^{3+} ions, but only for proof-of-concept biosensing and security printing,[137] most probably due to the limited brightness of UCNPs.[174] Individual QDs were also used for PL lifetime tuning through bandgap engineering, including increasing the particle size,[175] introducing various dopants,[140],[161] and fabricating the nanostructure with lattice-strain.[143],[144] Unfortunately, these methods led to the change of PL wavelengths and thus, color could not be used as an independent parameter, which is a prerequisite for combining both color and lifetime into higher-order multiplexing. A facile and robust strategy to prepare lifetime-tunable QDs that are independent of PL color would significantly advance this endeavor.

Förster resonance energy transfer (FRET) is a strongly distance-dependent interaction within a luminescent donor-acceptor pair and the donor-acceptor

distance defines the PL lifetime of the donor. A FRET pair of lanthanide (e.g., Eu^{3+} or Tb^{3+}) donors and QD acceptors is of particular interest for multiplexed biosensing, because lanthanides possess very long PL lifetimes and QDs provide color-tunability and narrow PL emission.[3],[93],[94],[176] Due to the large difference between the PL lifetimes of lanthanides (~ms) and QDs (~ns), the FRET-sensitized lifetime of the QD acceptor is the same as the FRET-quenched lifetime of the lanthanide donor.[94] Therefore, shorter (or longer) lanthanide-QD distances lead to shorter (or longer) PL lifetimes of both lanthanide and QD.

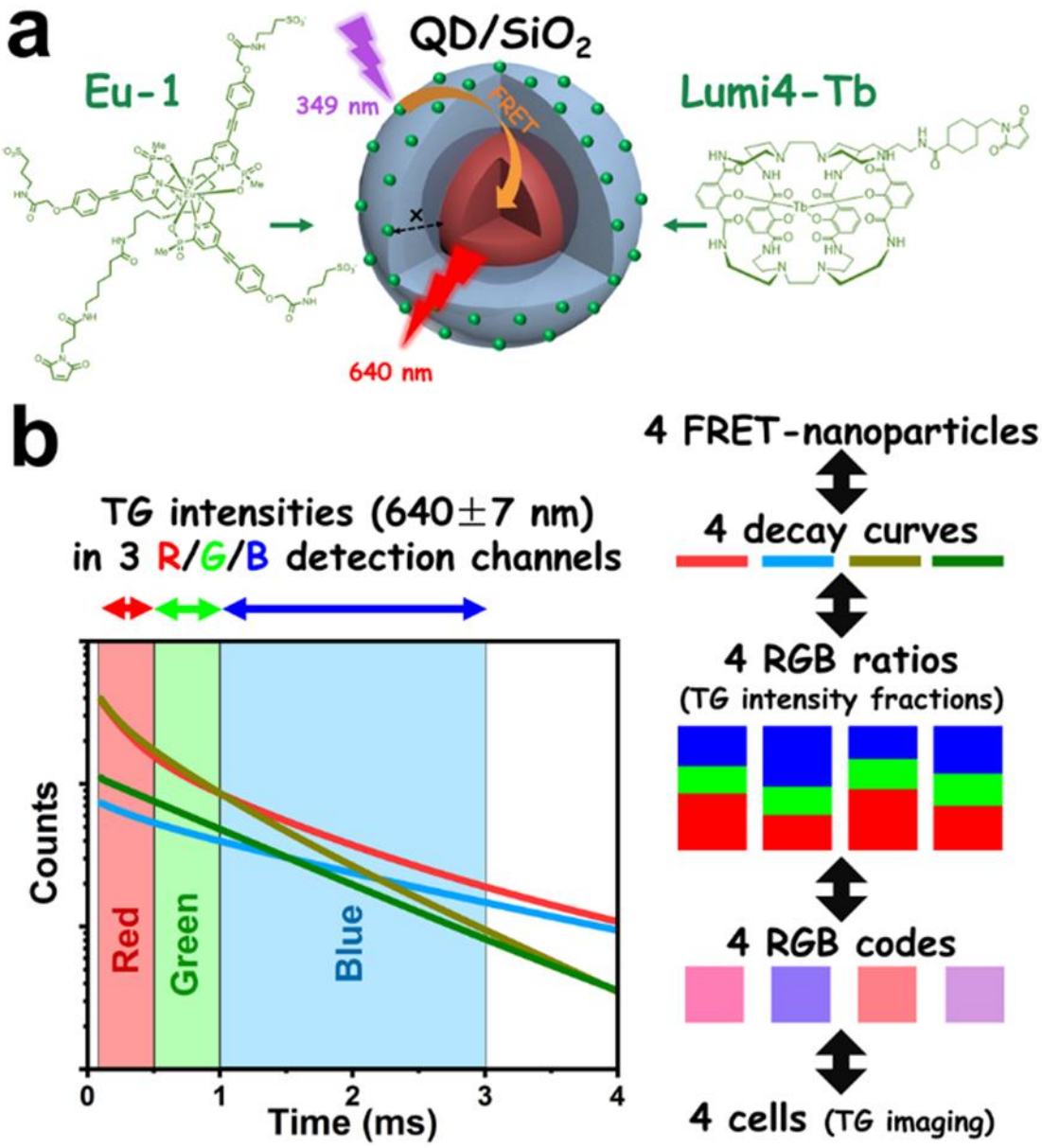

Figure 3.1 (a) QDs with SiO_2 coatings of different thicknesses (x=6 or 12 nm) functionalized with Eu-1 or Lumi4-Tb for single-wavelength temporal PL barcoding. **(b)** The RGB encoding principle based on three distinct TG PL intensity fractions for each of the four FRET-specific PL decays.

In this Chapter, we demonstrate that such a distance tuning approach can be used within one single nanoparticle by direct attachment of the lanthanides to QD-coatings with different thicknesses and that these individual lanthanide-coated QD nanohybrids can be used for encoding of different cells via TG temporal multiplexing. As a prototypical system for FRET lifetime encoding via individual nanoparticles (**Figure 3.1a**), SiO_2-coated QD with tunable shell thicknesses (6 and 12 nm) was synthesized. Then, lanthanide complexes (Tb-Lumi4 or Eu-1)[85],[177],[178] with long PL-lifetimes (~ms) were attached on the surface of SiO_2 shells. Based on the different thicknesses of SiO_2 shell, different PL decay times were obtained due to distance-dependent Lan-to-QD FRET. Distance-tuned PL decay times were selected for well-defined single nanoparticle codes. The principle of time-gated RGB encoding was illustrated in **Figure 3.1b**, based on the crossing of time-resolved decay curve between each single nanoparticle codes, three time-gated ranges were chosen and defined as red, green, and blue color, respectively. With the comparing and analysis of PL time-gated PL integral intensity in each channel, the RGB color images for each single nanoparticle code was obtained. Furthermore, the living cells encoding was demonstrated by incubating as-prepared single nanoparticle codes with the HeLa cells. To recognize the living cell codes, time-gated fluorescence microscopy system was employed. As a result, we could define the encoded cells according to the PL lifetime parameter in the QD acceptor detection channels.

3.2 Materials and methods

3.2.1 Materials

Terbium (III) chloride hexahydrate (99.999% trace metals basis), Poly (ethylene glycol) nonylphenyl ether (NP-5), tetraethyl orthosilicate (TEOS) and (3-mercaptopropyl) trimethoxysilane (MPS) were purchased from Sigma-Aldrich. Cyclohexane, chloroform, ethanol, ammonia aqueous solution (28%) were purchased from Sinopharm Chemical Reagent Co., Ltd. (Shanghai, China). CdSe/CdS/ZnS QDs with emission maximum at 620 nm were purchased from Poly OptoElectronics Co., Ltd. Black Costar Half Area 96 well microtitration plates

were purchased from Corning Inc. (Corning, NY, USA), Lumi4 functionalized to maleimide were provided by Lumiphore Inc. (Berkeley, CA, USA). Eu-1-Maleimide were provided by Cisbio.

3.2.2 Synthesis of QD embedded silica nanpspheres

The QDs embedded silica nanospheres were synthesized by a reverse microemulsion approach. Typically, the glass bottlecontaining 30 mL of cyclohexane was added with 3.95 mL of NP-5 and stirred for 15 min. The above solution was mixed with 300 µL of ammonia aqueous solution followed by stirring for another 15 min to form the reverse microemulsion. The mixture was subsequently added to 200 µL of QDs chloroform solution (10 mg/mL), followed by the injection of TEOS to start the silica encapsulation. After stirring at room temperature for 18 h, the QDs embedded silica nanospheres were precipitated by adding ethanol followed by centrifugation. The products were washed with ethanol for several times and finally dispersed in 20 mL of ethanol. To form the silica shell thickness of 6 nm and 12 nm, TEOS volumes of 60 µL and 260 µL were employed, respectively.

3.2.3 Synthesis of mercapto-terminated silica nanospheres

For the grafting of mercapto-groups onto silica surface, the above QDs embedded silica nanospheres in 20 mL of ethanol was added 500 µL of ammonia and 100 µL of MPS, followed by vigorous stirring at room temperature for 12 h. The final product was harvested by centrifugation, washed thoroughly with ethanol and redispersed in 2 mL water.

3.2.4 Estimation of molar concentration of QD/SiO_2

We assume that the nanonaterials have the same density as the according bulk materials. For the CdSe/CdS/ZnS QD, the density of CdSe, CdS, and ZnS are 5.816 g/cm^3, 4.82 g/cm^3, and 4.09 g/cm^3, respectively. The radius of QD is about 3.5 nm according the HRTEM. We assume the radius of CdSe core is 1.8 nm, the thickness of CdS and ZnS shell are 1.16 nm and 0.54 nm, respectively. Then we can obtain the density of the QD, which is nearly 5.223 g/cm^3 (**Equations 3.1** and **3.2**).

According the density and volume of single QD and Avogadro constant, we can obtain the molecular weight of QD, which is nearly 570000. The yield of synthetic QD/SiO_2 can be estimate to 70%. Finally, the molar concentration of QD/SiO_2 should be nearly 1.23 μM.

$$V = \frac{4}{3}\pi r^3 \quad (3.1)$$

$$\rho = \frac{m}{V} \quad (3.2)$$

3.2.5 Formation of mTb-QD/SiO_2 donor-acceptor assemblies

Lumi4-Mal was dissolved to 3.8 mM in anhydrous DMF. 5.25 μL of Lumi4-Mal (3.8 mM), 162.5 μL of QD/SiO_2 (6 nm or 12 nm, 1.23 μM), and 232.25 μL of Tris-HCl buffer at pH 7.5 (50 mM) were mixed in 0.5 mL eppendorf tube (Lumi4: QD/SiO_2=100:1). The mixtures in alu foil were incubated for 3 h at room temperature. Intelli Mixer was employed for prewetting tubewalls by rotating the tube. Then the product was harvested by centrifugation (8000 r.p.m, 20 min) and redispersed in 400 μL Tris-HCl buffer at pH 7.5 (50 mM). The number of Lumi4 per QD/SiO_2 was confirmed by absorbance spectrum (75 Lumi4 per QD/SiO_2 (6 nm) and 87 Lumi4 per QD/SiO_2 (12 nm)). For the formation of 100Tb-QD/SiO_2 donor-acceptor assemblies, Tb^{3+} was dissolved to 100 μM in pure water. For the 200 nM 100Tb-QD/SiO_2 codes, 80 μL of Lumi 4-QD/SiO_2 (500 nM), 40 μL of Tb^{3+}, and 80 μL of Tris-HCl buffer at pH 7.5 (50 mM) were mixed in 0.5 mL eppendorf tube (Tb: Lumi4: QD/SiO_2 (6 nm) = 100:75:1 and Tb: Lumi4: QD/SiO_2 (12 nm) =100:87:1).

3.2.6 Formation of Eu-QD/SiO_2 donor-acceptor assemblies

Eu-1-Mal was dissolved to 0.1 mM in pure water. 100 μL of Eu-1-Mal, 40.6 μL of QD/SiO_2, and 359.4 μL Tris-HCl buffer at pH 7.5 (50 mM) were mixed in 1 mL eppendorf tube (Eu-1-Mal: QD/SiO_2=200:1). The mixtures were incubated for 3 h at room temperature. An Intelli Mixer (ELMI) was employed to prewet the wall of the tube. Then the product was collected by centrifugation (8000 r.p.m, 20 min) and redispersed in 500 μL Tris-HCl buffer at pH 7.5 (50 mM). The number of Eu-1 per QD/SiO_2 was confirmed by absorbance spectrum (175 Eu-1 per QD/SiO_2 (6 nm) and 180 Eu-1 per QD/SiO_2 (12 nm)).

3.2.7 Cell culture

Human cervical carcinoma (HeLa) cells were purchased from American Type Culture Collection (CCL-2). Cells were grown in Dulbecco's modified eagle medium (DMEM, Sigma-Aldrich, D6546), supplemented with 10% fetal bovine serum (FBS, Sigma-Aldrich, F0804), 1% antibiotics (Pen Strep, Sigma-Aldrich, P4333) and 2 mM L-glutamine (Sigma-Aldrich, G7513) at 37°C and 5% CO_2. The cells were passaged with trypsin-EDTA 0.05%.

3.2.8 Living cell encoding.

HeLa cells were seeded at $3x10^5$ cells in 8-chamber glass slide (Nunc® Lab-Tek® II Chamber Slide™, 155409) and incubated at 37°C and 5% CO_2 overnight. The following day, the cells were washed with 1xPBS (Sigma-Aldrich, P4417) and incubated with a complete culture medium (10% FBS, 1% Pen Strep and 2 mM L-glutamine). Solution of Tb-QD/SiO_2 (6 nm), Tb-QD/SiO_2 (12 nm), Eu-QD/SiO_2 (6 nm), and Eu-QD/SiO_2 (12 nm) in Tris-HCl buffer at pH 7.5 (50 mM) were sonicated for 15 minutes and added at 20 nM into previously prepared slide with cells. Cells were incubated at 37°C and 5% CO_2 for 2h. For mixing, the cells which incubated with Tb-QD/SiO_2 (6 nm), Tb-QD/SiO_2 (12 nm), Eu-QD/SiO_2 (6 nm), and Eu-QD/SiO_2 (12 nm) were washed by 1XPBS, trypsinized then seeded on the Poly-L-lysine (Thermofisher, P4707) coated slide. Images of living cell encoding were acquired using a wide-field, TG luminescence inverted microscope (Olympus IX71) that uses a UV laser (349 nm, 100 Hz, Nd:YLF, Triton, Spectra Physics) for pulsed excitation and an intensified CCD camera (ICCD, PI-MAX3, Princeton Instruments) for gated detection. QD PL signals were detected using a 639±10 nm bandpass filter. Acquisition settings (Winview software controlling the camera) were adjusted to optimal conditions regarding RGB ratio and were fixed to a delay time of 50 µs (after the excitation pulse) and a gate width of 450 µs (red window - R), a delay time of 500 µs and a gate width of 500 µs (green window - G), and a delay time of 1 ms and a gate width of 2 ms (blue window - B). *ImageJ* was used to assign red, green, or blue color to the three detection windows and define a common intensity range (same minimum and maximum values for all windows).

3.2.9 Cytotoxicity Measurements

The cytotoxicity of QD/SiO_2 (6 nm and 12 nm) were evaluated by MTT viability assay on various cells. Both tumor cells (HeLa, MDA-MB231) and normal cells (293T) were cultured in DMEM medium supplemented with 10% (v/v) FBS, 1% (v/v) penicillin, and 1% (v/v) streptomycin under 37 °C within a humidified atmosphere of 5% CO_2. The HeLa, MDA-MB231 and 293T cells were seeded in 96-well plates with a seeding density of 5×10^3 cell/well, respectively. After 24 h incubation, the medium was removed and replaced with fresh medium containing QD/SiO_2 with various concentrations (0, 25, 50, 100, 200, 400, 800 nM). After 24 h incubation, the standard MTT assay was carried out to evaluate the cell viability.

3.2.10 Analytical methods

Structural characterization of the QD/SiO_2 was carried out using a FEI Tecnai G2 F20 S-Twin high-resolution transmission electron microscope (HR-TEM) operating at 200 kV. Absorption spectra were acquired using a Lambda 35 UV/Vis spectrophotometer (Perkin Elmer). Steady state PL spectra were acquired using a Xenius fluorescence plate reader (SAFAS). For the measurement of the PL decay curves of the Tb or Eu to QD/SiO_2, an EI fluorescence plate reader (Edinburgh Instruments, UK) with 4000 detection bins of 2 µs integration time was used. A nitrogen laser (LTB, Berlin, Germany) was used for excitation (337.1 nm, 20 Hz, 600 flashes). (494/20) nm, (567/15) nm, and (640/14) nm bandpass filter were used for analyzing the Tb, Eu, and QD PL, respectively. For the measurement of the PL decay curves of the pure QD/SiO_2 (6 nm) and QD/SiO_2 (12 nm), a SuperChrome sources (Fianium, UK) was used for excitation (480 ± 15 nm, 5 MHz, Laser Power: 200). (640/14) nm bandpass filter were used for analyzing. The data were fit with FAST software version 3.1 (Edinburgh Instruments, UK). All assays were measured in black 96-well microtiter plates with an optimal working volume of 150 µL.

3.2.11 FRET calculation

For FRET model, the overlap integral (J) and Förster distance (R_0) were calculated using **Equations 3.3** and **3.4**:

$$J = \int \bar{I}_{\mathrm{D}}(\lambda)\varepsilon_{\mathrm{A}}(\lambda)\lambda^4 \mathrm{d}\lambda \tag{3.3}$$

where $\bar{I}_{\mathrm{D}}(\lambda)$ is the area-normalized emission spectrum of donor, $\varepsilon_{\mathrm{A}}(\lambda)$ is the molar absorptivity spectrum of the acceptor in $M^{-1}cm^{-1}$, and λ is the wavelength in nm.

$$R_0 = 0.0211[\kappa^2 \Phi_{\mathrm{D}}(n)^{-4} J(\lambda)]^{1/6} \quad \text{(in nm)} \tag{3.4}$$

where κ^2 is orientation factor (κ^2=2/3 due to dynamic averaging of Tb/Eu-NP donor-acceptor systems), Φ_{D} is quantum yield of the donor, and n=1.35 is the refractive index of the surrounding medium. The molar extinction coefficients $\varepsilon_{\mathrm{QD/SiO_2}}(\lambda)$ for QD/SiO_2 with different shell thicknesses were calculated with estimated molar concentration and absorbance spectra.

Due to the strong difference in their intrinsic PL lifetimes in Ln-to-QD FRET, the FRET-sensitized PL decay time of QD adapts to the FRET-quenched PL decay time of Ln (τ_{AD}=τ_{DA}). Thus, the FRET efficiency (E_{FRET}) can be determined by **Equation 3.5**:

$$E_{\mathrm{FRET}} = 1 - \frac{\tau_{\mathrm{AD}}}{\tau_{\mathrm{D}}} \tag{3.5}$$

The Ln-to-QD distance (R) was calculated using **Equation 3.6**:

$$R = R_0 \left(\frac{\tau_{\mathrm{DA}}}{\tau_{\mathrm{D}} - \tau_{\mathrm{DA}}}\right)^{1/6} \tag{3.6}$$

3.2.12 Multi-exponential PL decay analysis.

We analyzed the data with multiexponential decays. This analysis has been shown to lead to a coherent picture of FRET in Tb-nanoparticle assemblies. It is based on fitting the decay curves were fitted using a multiexponential PL intensity decay function (**Equation 3.7**).

$$I = A\,[\sum \alpha_{\mathrm{ADi}*} \exp(-t/\tau_{\mathrm{ADi}})] + B \exp(-t/\tau_{\mathrm{D}}) \tag{3.7}$$

where A is the total amplitude and $\alpha_{\mathrm{ADi}*}$ are the amplitude fractions ($\sum \alpha_{\mathrm{ADi}*} = 1$) of the different FRET contributions with FRET-sensitized PL decay times τ_{ADi}. Amplitude B and decay time τ_{D} correspond to the contribution of unquenched Tb donor PL (due to spectral crosstalk in the QD detection channel). The amplitudes must be further corrected by FRET rates (**Equation 3.8**) to take into account the FRET efficiency-dependent excitation of the acceptor (**Equation 3.9**).[2] PL decay time averaging was then performed using amplitude weighted average decay times (**Equation 3.10**).

$$k_{\mathrm{FRETi}} = \frac{1}{\tau_{\mathrm{ADi}}} - \frac{1}{\tau_{\mathrm{D}}} \tag{3.8}$$

$$\alpha_{\mathrm{AD}i} = \frac{{}^{\alpha_{\mathrm{AD}i*}}/_{k_{\mathrm{FRET}i}}}{\Sigma\left({}^{\alpha_{\mathrm{AD}i*}}/_{k_{\mathrm{FRET}i}}\right)} \tag{3.9}$$

$$\tau_{\mathrm{AD}} = \sum a_{\mathrm{ADi}}\tau_{\mathrm{ADi}} \tag{3.10}$$

3.3 Results and discussion

3.3.1 Characterization of Ln (Tb/Eu)-QD assemblies

High resolution transmission electron microscopy (HRTEM, **Figure 3.2**) showed nearly monodisperse QDs with clearly defined SiO_2 nanoshells of 6 nm and 12 nm thicknesses. Absorption and emission spectra of Lumi4-Tb, Eu-1, QD/SiO_2 (6 nm) and QD/SiO_2 (12 nm) were presented in **Figure 3.3a**. Both lanthanide complexes were excitable in the 300 to 400 nm wavelength region and their PL spectra overlapped well with the QD absorption spectra for efficient FRET (**Figure 3.3b**). Photophysical and FRET parameters for the different single luminophores and the donor-acceptor combinations are listed in **Table 1**. Although the PL emission wavelength of QDs before and after SiO_2 coating did not change (**Figure 3.3a**), the extinction coefficient of QD/SiO_2 significantly increased with increasing shell thickness due to a better protection of the QD from the environment. The spectral overlap integral (J) and Förster distance (R_0) of each individual FRET-pair were calculated. The R_0 was increasing from 9.7 nm and 8.6 nm to 10.7 nm and 9.2 nm for Tb-QD and Eu-QD, respectively (**Table 3.1**). The maleimide functional Lumi4 and Eu-1 were conjugated with acceptor through sulfhydryl on the surface of SiO_2 shell. UV-vis absorbance spectra were employed to calculate the number of lanthanide donors per QD acceptor. The absorbance spectra (**Figure 3.4**), which presented linear combinations of QD-SiO_2 and the lanthanide complexes, resulted in labeling ratios of ~75 Lumi4-Tb per QD/SiO_2(6 nm), ~87 Lumi4-Tb per QD/SiO_2(12 nm), ~175 Eu-1 per QD/SiO_2(6 nm), and ~180 Eu-1 per QD/SiO_2(12 nm). Approximate double amounts for Eu-1 were used to account for the lower brightness (lower extinction coefficient at the microscopy excitation wavelength of 349 nm and lower quantum yield) of Eu-1 compared to Lumi4-Tb. Due to the long PL lifetime of lanthanides, one QD can be sensitized by FRET from several lanthanide donors and therefore an increasing number of donors increases the

overall brightness of FRET-sensitized QD emission.

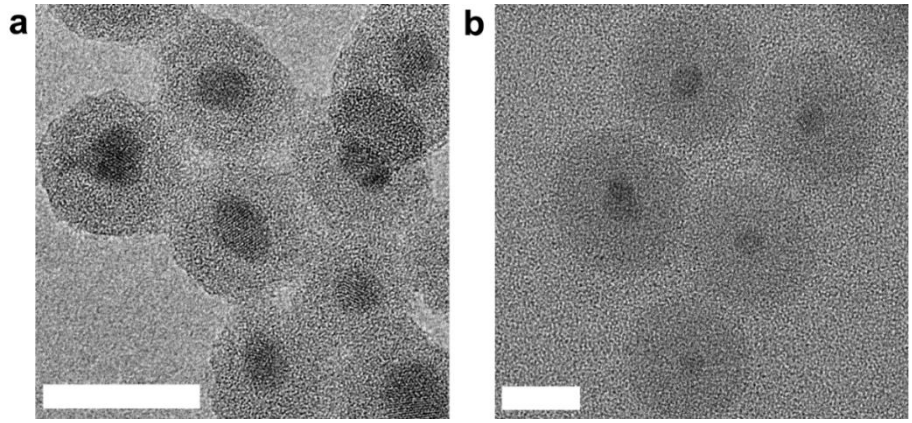

Figure 3.2. HRTEM of **(a)** QD/SiO_2 (6 nm) and **(b)** QD/SiO_2 (12 nm). Scale bar: 20 nm.

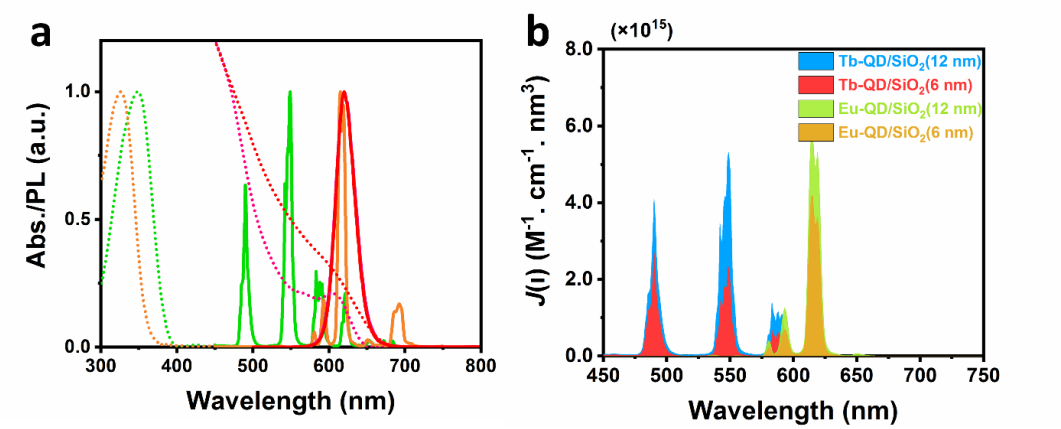

Figure 3.3. (a) Absorbance (dashed lines) and PL emission spectra (solid lines) for the Lumi4-Tb (green), Eu-1 (orange), QD/SiO_2 (6 nm) (pink), and QD/SiO_2 (12 nm) (red). **(b)** Spectral overlap functions for the Tb-QD/SiO_2 (12 nm), Tb-QD/SiO_2 (6 nm), Eu-QD/SiO_2 (12 nm), Eu-QD/SiO_2 (6 nm) FRET pairs.

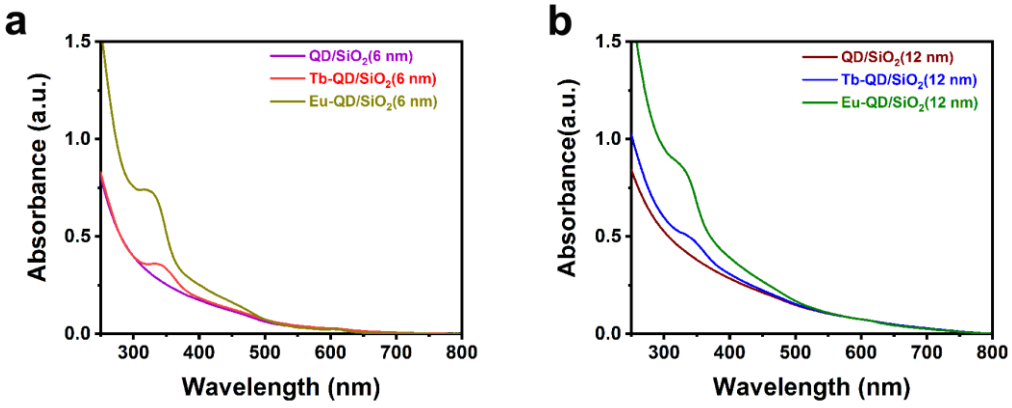

Figure 3.4. Absorbance spectra (in water) for the **(a)** QD/SiO_2 (6 nm) and **(b)** QD/SiO_2 (12 nm) before and after conjugating with Lumi4-Tb and Eu-1

Table 3.1 Optical characteristics of Tb, Eu, and QD/SiO_2 with their FRET pairs.

	ε_{max} (M^{-1} cm^{-1}) [λ_{max}]	Φ_{Ln3+}	Emission Filter (nm)[a]	τ [b]
Lumi4-Tb	26,000 [340 nm]	0.79	490/20	2.7 ms
Eu-1	58,000 [330 nm]	0.48	567/15	1.1 ms
QD/SiO_2 (6 nm)	485,000 [610 nm]	/	640/14	~12 ns
QD/SiO_2 (12 nm)	680,000 [610 nm]	/	640/14	~11 ns

FRET pair (D → A)	J (M^{-1}. cm^{-1}. nm^4)	R_0 (nm)	τ_{ave} (ms)[c]
Tb → QD/SiO_2(6 nm)	6.1×10^{16}	9.7	0.74
Tb → QD/SiO_2(12 nm)	1.1×10^{17}	10.7	1.82
Eu → QD/SiO_2(6 nm)	4.8×10^{16}	8.6	0.61
Eu → QD/SiO_2(12 nm)	7.3×10^{16}	9.2	1.09

(a) See **Figure 3.6a** for filter spectra. Lumi4-Tb and Eu-1 filters were selected to measure their bluest emission bands with the least possible overlap with the QD emission band. QD filter was selected to avoid overlap with Tb and Eu PL. (b) See **Figure 3.6b** for PL decay curves. (c) Amplitude averaged decay time that takes into account the complete decay curves, which contain FRET-quenched and unquenched (lanthanide complexes that do not participate in FRET) components. FRET-quenched average decay times, FRET efficiencies, and donor-acceptor distances can be found in **Table 3.2**.

Due to the different distances (6 nm or 12 nm) and different R_0 values (between 8.6 and 10.7 nm, **Table 3.1**), the PL lifetimes (τ) of Lumi4-Tb (2.7 ms) and Eu-1(1.1 ms) were quenched to different extents. Because of the much shorter PL lifetime of the QDs (ns) compared to the lanthanide complexes (ms), the FRET-quenched PL decay times of the lanthanides equaled the FRET-sensitized PL decay times of the QDs.[3] Therefore, FRET led to distinct and long-lived QD decays (**Figure 3.5**) with average decay times (τ_{ave}) between 0.61 ms and 1.82 ms (**Table 3.1**) for the four lanthanide-QD FRET nanoparticles. Steady-state PL spectra also showed increased lanthanide PL quenching with decreasing shell thickness (**Figure 3.6**). Based on the PL decay curves, we also calculated FRET efficiencies and donor acceptor distances. With the fixed component of donor contribution, the average lifetime of acceptors in Tb-QD/SiO_2 (6 nm), Tb-QD/SiO_2 (12 nm), Eu-QD/SiO_2 (6 nm), and Eu-QD/SiO_2 (12 nm) were 0.75, 1.27, 0.52, and 0.74 ms, respectively. The energy transfer efficiencies were calculated as 0.72 (Tb-QD/SiO_2 (6 nm)), 0.53 (Tb-QD/SiO_2 (12 nm)), 0.53 (Eu-QD/SiO_2 (6 nm)), and 0.33 (Eu-QD/SiO_2 (12 nm)). With the R_0 for each FRET-pair as calculated above, Tb-to-QD distances of R = 8.6 nm (6 nm SiO_2 shell) and R = 10.5 nm (12 nm SiO_2 shell), and Eu-to-QD distances of R = 8.4 nm (6 nm SiO_2 shell) and R = 10.4 nm (12 nm SiO_2 shell) were obtained, respectively. The results from Ln-to-QD with 6 nm SiO_2 shell were in very good agreement and very well in line with the estimated average distance of the lanthanide complex conjugated randomly over the surface of SiO_2 shell. However,

the results from Ln-to-QD with 12 nm SiO_2 shell led to the deduction that a significant fraction of Tb and Eu must be positioned inside the 12 nm SiO_2 shell. This conclusion is not unrealistic because both the porosity of the outer SiO_2 layers and the non-spherical shape on the entire QD can lead to closer and further distances than estimated by the ideal spherical model.

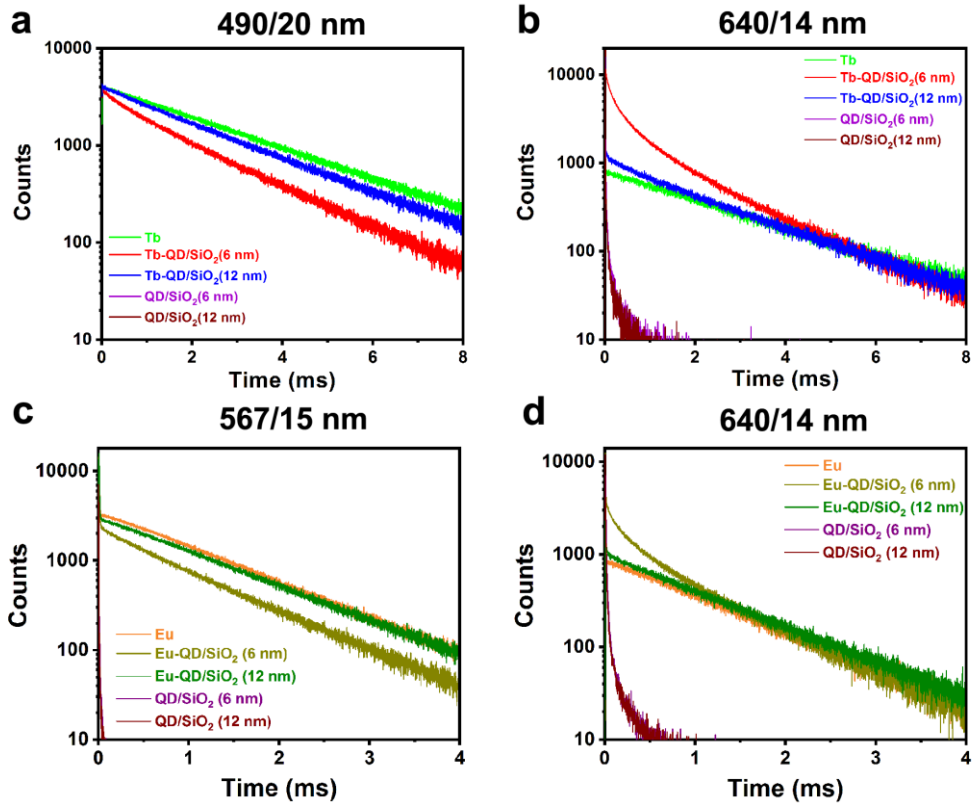

Figure 3.5. (a) Tb donor PL decay curve, **(b)** QD acceptor PL decay curve of Tb-QD/SiO_2 FRET-pairs. **(c)** Eu donor PL decay curve, **(d)** QD acceptor PL decay curve of Eu-QD/SiO_2 FRET-pairs.

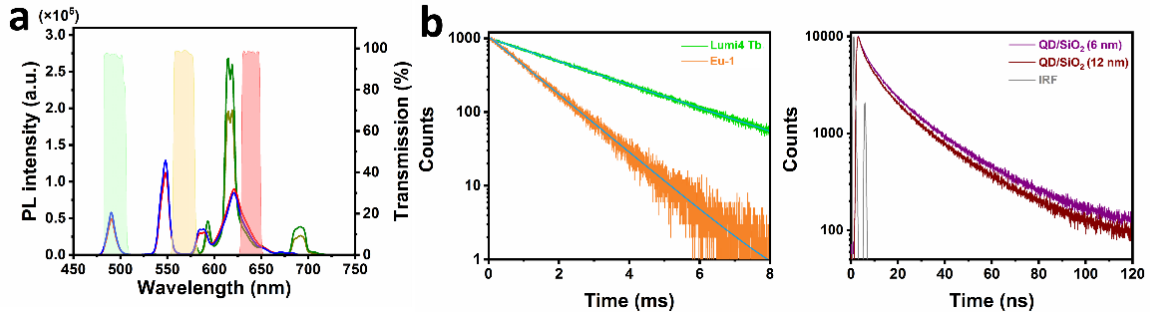

Figure 3.6. **(a)** Steady-state PL spectra of Tb-QD/SiO_2 (6 nm) (red), Tb-QD/SiO_2 (12 nm) (blue), Eu-QD/SiO_2 (6 nm) (yellow), and QD/SiO_2 (12 nm) (green). (Filter green: 490/20 nm, filter yellow: 567/15 nm, and filter red: 640/14 nm). **(b)** Time-resolved PL decay curves of (left) pure Lumi4-Tb-Mal and Eu-1-Mal (in water) and (right) pure QD/SiO_2 (6 nm) and QD/SiO_2 (12 nm). (IRF: Instrument response function.)

Table 3.2. PL decay time fitting and analysis parameters, and RGB ratio calculation in QD acceptor channel for four well-defined codes (0.1 ms-8 ms for Tb-QD/SiO_2, and 0.1 ms-4 ms for Eu-QD/SiO_2).

Codes	Tb-QD/SiO_2 (6 nm)	Tb-QD/SiO_2 (12 nm)	Eu-QD/SiO_2 (6 nm)	Eu-QD/SiO_2 (12 nm)
$A\alpha_{AD1*}$	1920	92	850	29
α_{AD1*}	0.555	0.234	0.324	1.000
τ_{AD1} (ms)	0.19	0.25	0.12	0.74
k_{FRET1}	4.89	3.63	7.42	0.44
α_{AD1}	0.17	0.03	0.06	1.00
$A\alpha_{AD2*}$	1540	301	1770	/
α_{AD2*}	0.445	0.766	0.676	/
τ_{AD2} (ms)	0.86	1.30	0.54	/
k_{FRET2}	0.79	0.40	0.94	/
α_{AD2}	0.83	0.97	0.94	/
B	439	346	1234	715
τ_D (ms)	2.7	2.7	1.1	1.1
χ^2	1.164	1.201	1.138	1.160
τ_{AD}(ms)[a]	0.75	1.27	0.52	0.74
E_{FRET}[b]	72%	53%	53%	33%
R(nm)[c]	8.6	10.5	8.4	10.4
TG intensity(0.05-0.5 ms)	594320	144800	620500	422300
TG intensity(0.5-1 ms)	289130	116410	307880	305280
TG intensity(1-3 ms)	419120	250080	333020	450680
RGB ratio	(46%/22%/32%)	(28%/23%/49%)	(49%/24%/26%)	(36%/26%/38%)

(a) Amplitude-averaged PL decay of only the first two decay components, which were caused by FRET-quenching. The third decay component (2.7 ms and 1.1 ms, respectively) results from unquenched lanthanide PL, which is still present (spectral crosstalk) in the QD detection channel. (b) Calculated using **Equation 3.5**. (c) Calculated using **Equation 3.6**.

3.3.2 Living cell encoding

The principle of TG RGB encoding is illustrated in **Scheme 1b**. Based on the intersections of the four distinct PL decay curves (**Figure 3.7a**), three temporally distinct TG PL intensity detection windows were selected and defined as red (R), green (G), and blue (B), respectively. One PL intensity (integrated over the time interval of the detection channel) is recorded for each channel. The different shapes of the decay curves (different PL lifetimes) result in distinct PL intensity combinations of the three detection channels R, G, and B. Thereby, each FRET-

nanoparticle can be identified by a unique RGB ratio (ratios of TG PL intensities: R/(R+G+B), G/(R+G+B), and B/(R+G+B); **Figure 3.7b** and **Table 3.2**). TG imaging uses the same three TG detection windows as de-fined by the decay curves and each camera pixel records three time-dependent intensities (R, G, and B) for each image. *ImageJ* was used to assign red, green, or blue color to the three detection channels and define a common intensity range (same minimum and maximum values for all channels). The resulting overlay images provide RGB codes (be-tween 0 and 255 for R, G, and B) for each pixel, which can then be transferred into RGB ratios and directly related to the four different FRET-nanoparticles. As a first evaluation of biocompatibility, the stability of the RGB codes was analyzed for the four different nanoparticles incubated in PBS buffer at different pH (5.3, 6.8, and 7.5) for 2h and 4h. TG PL intensity ratios of each code were nearly invariant (**Figure 3.8a**), which provided first good evidence concerning compatibility of our temporal PL encoding approach with live cell imaging.

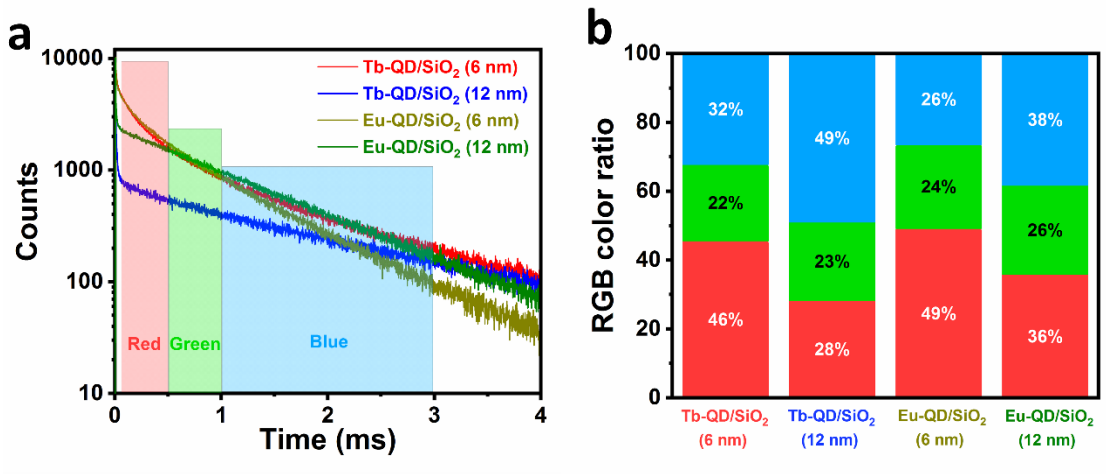

Figure 3.7. (a) QD acceptor PL decay curves of each single nanoparticle code. **(b)** TG PL intensity (RGB) ratio of each single nanoparticle code calculated from the TG intensities in the red, green, and blue TG detection windows in a.

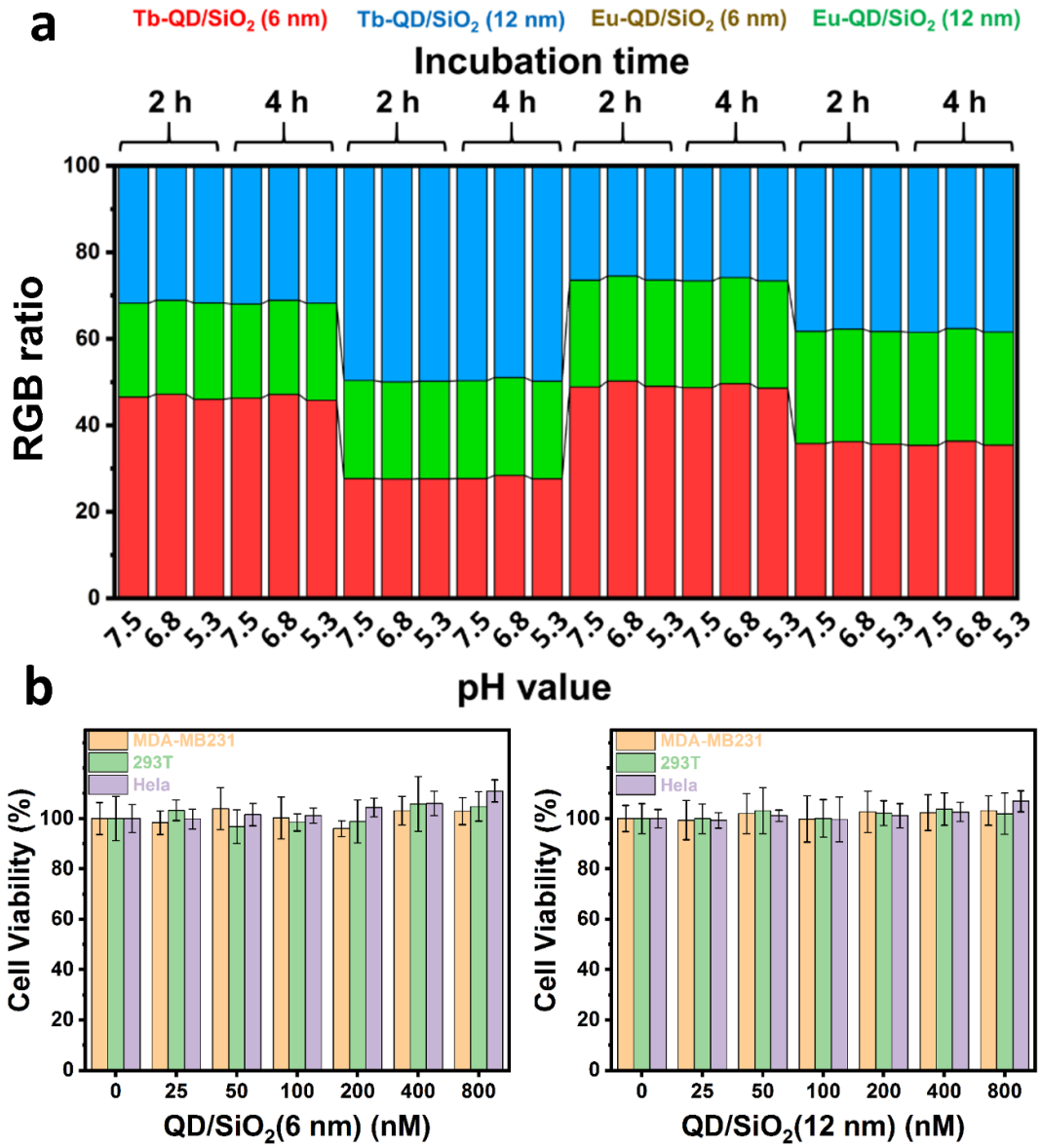

Figure 3.8. (a) Stability of RGB color of the single nanoparticle codes in PBS buffer with different pH. **(b)** Cell viability data of MDA-MB231, 293T, and Hela cells incubated with **(left)** QD-SiO_2 (6 nm) and **(right)** QD-SiO_2 (12 nm) after 24 hours in various concentration (0, 25, 50, 100, 200, 400 and 800 nM).

To demonstrate the actual application for live cell imaging, HeLa cells were incubated with Tb-QD/SiO_2 (6 nm), Tb-QD/SiO_2 (12 nm), Eu-QD/SiO_2 (6 nm), and Eu-QD/SiO_2 (12 nm), respectively. Although adequately coated and biocompatible QDs have been used in many biological imaging applications in vivo and in vitro, their toxicity remains an important subject of discussion.[173] Cell viability tests (MTT assays) with QD concentrations up to 800 nM (the concentration used for imaging experiments was only 20 nM) for both QD/SiO_2 (6 nm) and QD/SiO_2

(12 nm) revealed no significant cytotoxicity (**Figure 3.8b**). To encode the cells incubated with a specific nanoparticle, we used a TG microscopy imaging system with pulsed laser excitation at 349 nm and time-gated detection of the QD PL by an intensified CCD camera.[179] In general, TG microscopy in the micro and millisecond range can be realized on any standard fluorescence microscope that is equipped with pulsed excitation (e.g., LEDs, lasers, flash lamps, mechanical choppers) and time-gated detection (e.g., intensified cameras, scanning photon detectors, mechanical choppers).[180],[181] As defined before in the PL decay experiments, TG windows of 0.05-0.5 ms (R), 0.5-1 ms (G), and 1-3 ms (B) were selected for TG image encoding (**Figure 3.9**). After merging the images from the three TG detection windows (overlay), the RGB color images were obtained. Each code was determined according to RGB color selection and was consistent with the previously calculated results obtained by PL decays. Noteworthy, the different RGB colors could be readily distinguished by the naked eye (**Figure 3.9**).

To emphasize the capability of these codes to distinguish cells in more complex environments, four differently encoded HeLa cells were mixed and cultured on the same microscopy slide. As shown in **Figure 3.10**, single-color (one excitation and one emission wavelength) TG imaging could efficiently distinguish the four types of cells within the same field of view. Again, the four RGB codes can be already distinguished by the naked eye (**Figure 3.10d**). However, for clarity and taking into account the different color impressions from screen to screen and from screen to paper, we retrieved the RGB codes from color selection within the overlay image and marked the different cells with colored arrows in the bright field images (**Figure 3.10e**). We noted that the RGB color of each code in this rather complex mixing environment exhibited less blue, which we assigned to quenching effects during the 8 h incubation time. Still, we could clearly distinguish the encoded cells via the ratios of TG PL intensities. Finally, to demonstrate the independence of PL intensity and probe concentration, different encoding nanoparticles were incubated at distinct concentration with HeLa cells and afterwards the cells were mixed. Adjusting brightness and contrast within the same field of view also allowed us to distinguish cells with significantly different PL intensities (**Figure 3.11**).

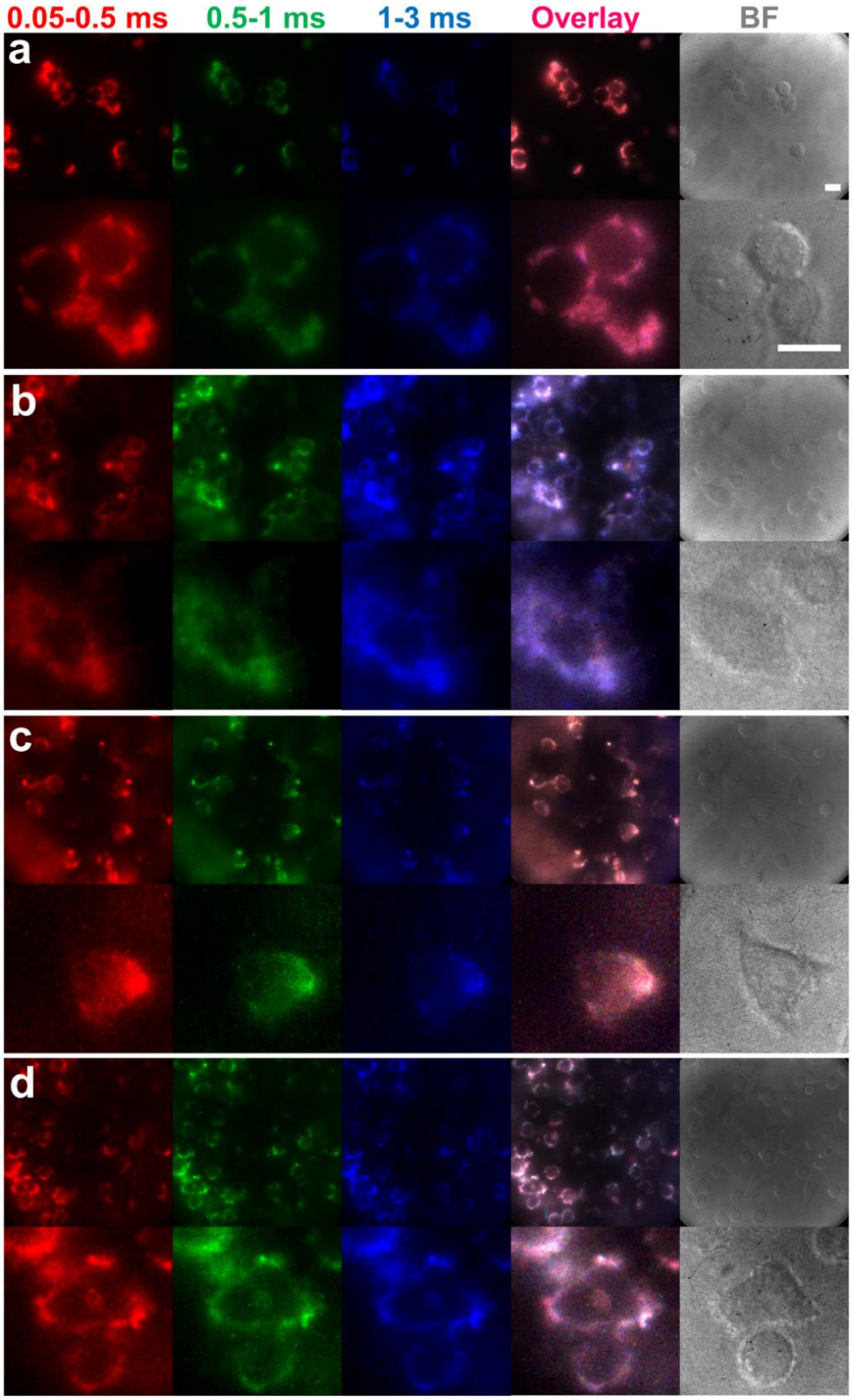

Figure 3.9. TG PL images (top panels) and high resolution TG PL images (bottom panels) in different temporal detection windows (time-ranges on top), their overlay, and bright field (BF) images of HeLa cells labeled with individual nanoparticle codes. **(a)** Tb-QD/SiO_2 (6 nm), **(b)** Tb-QD/SiO_2 (12 nm), **(c)** Eu-QD/SiO_2 (6 nm), **(d)** Eu-QD/SiO_2 (12 nm). Scale bar (top right): 20 µm; λ_{ex}: 349 nm; λ_{em}: 640 nm.

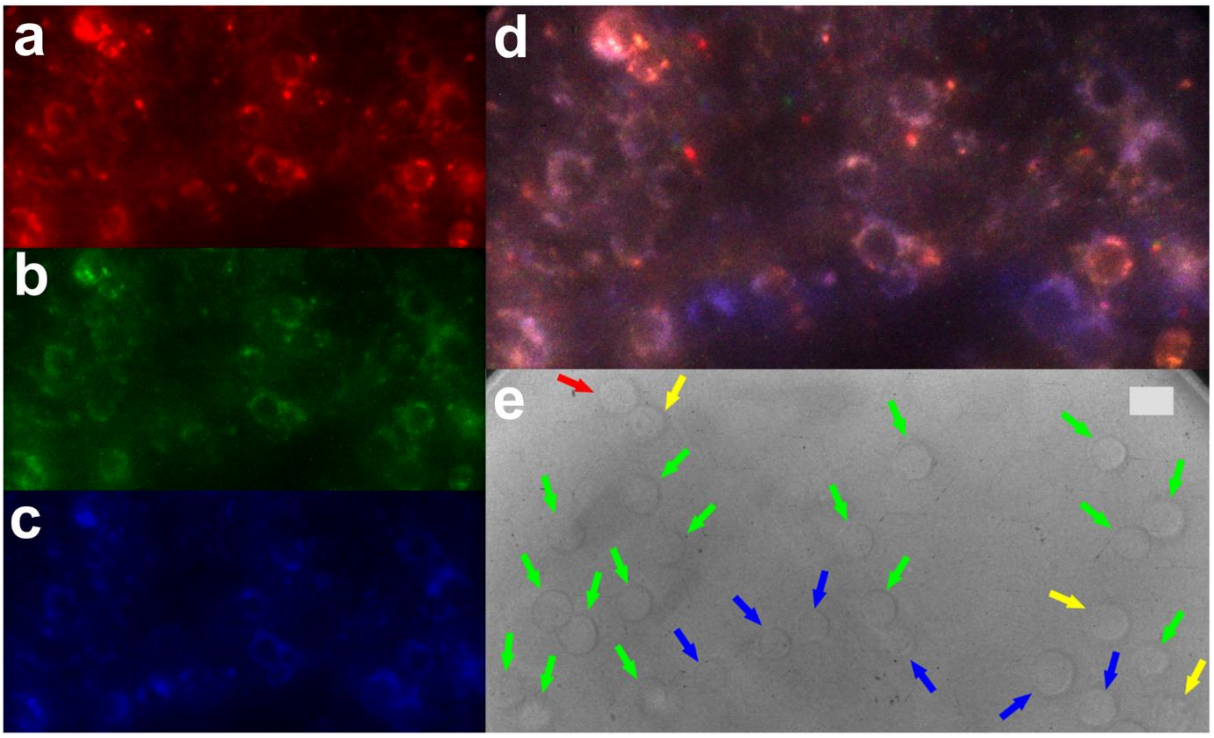

Figure 3.10. TG PL images of differently encoded HeLa cells. **(a)** 0.05-0.5 ms; **(b)** 0.5-1 ms; **(c)** 1-3 ms; **(d)** overlay; **(e)** bright field-red arrow: Tb-QD/SiO_2 (6 nm), blue arrows: Tb-QD/SiO_2 (12 nm), yellow arrows: Eu-QD/SiO_2 (6 nm), green arrows: Eu-QD/SiO_2 (12 nm). Scale bar (in e): 20 μm; λ_{ex}: 349 nm; λ_{em}: 640 nm.

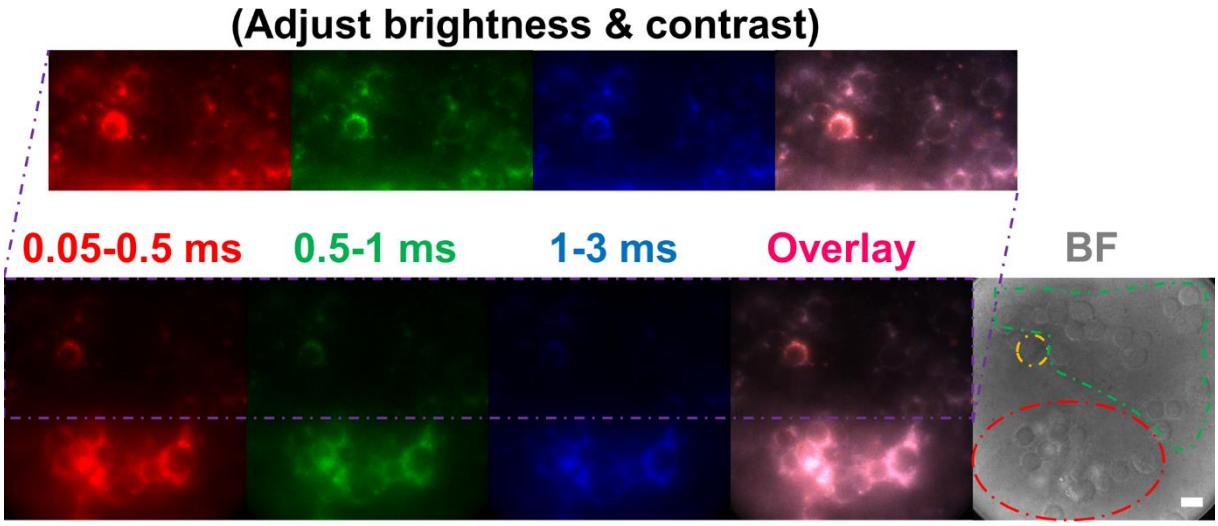

Figure 3.11. Time-gated PL images of Hela cells labeled with different single nanoparticle codes at different concentrations (red dot-dashed area: Tb-QD/SiO_2 (6 nm), yellow dot-dashed area: Eu-QD/SiO_2 (6 nm), green dot-dashed area: Eu-QD/SiO_2 (12 nm). Scale bar: 20 μm.

3.4 Conclusion

In summary, we have developed and applied a single-wavelength, single-

nanoparticle encoding system composed of QD cores with lanthanide-functionalized SiO_2 shells. Our TG-FRET barcoding technique was accomplished by precise distance control between lanthanide donors and QD acceptors, which, in turn, led to distinct PL decay curves. TG PL detection in three specific time windows allowed us to create distinct RGB codes for each encoding nanoparticle, which were used to label live cells. Individual and mixed cells could be distinguished by the predefined RGB codes in the same field of view using TG PL imaging. Our encoding approach was independent of PL intensity and nanoparticle concentration and was shown to be stable at different pH over several hours of incubation. While our study used two different QD coating thicknesses and two different lanthanide complexes to create four different codes, more variations could be used to extend the coding range by additional lifetimes. Although a larger lifetime difference will always lead to a better distinction, the curves of Eu-QD/SiO_2 (6 nm) and Tb-QD/SiO_2 (6 nm) are very similar with an average lifetime difference of only ca. 20% (0.61 and 0.74 ms, *cf.* **Table 3.1**) but can still be distinguished very efficiently. A 20% difference between all lifetimes and a minimum lifetime of ca. 10 % of the one of Lumi4-Tb (2.7 ms) would allow for 14 different codes (lifetimes of 0.25, 0.30, 0.36, 0.44, 0.52, 0.63, 0.75, 0.90, 1.09, 1.30, 1.56, 1.88, 2.25, and 2.70 ms). If the coding system of interest requires more than 20% lifetime difference, the FRET multiplexing range can be extended by other means, e.g., by a combination of the spectral and temporal multiplexing components or by multistep FRET processes, in which the QD is used both as acceptor (to a Tb complex) and donor (to a dye). Such approaches have already been used in solution to quantify multiple DNAs by spectrotemporal multiplexing[182] or for the design of sophisticated molecular logic gates[67],[183] Taking into account that lanthanide-to-QD FRET can be applied to many different QD colors,[93],[184]–[186] our single nanoparticle encoding strategy shows the potential of extending to higher-order spectrotemporal PL barcoding and thereby significantly advancing the possibilities of fluorescent encoding.

4. FRET-modulated multi-hybrid nanoparticles for brightness-equalized barcoding

C. Chen, B. Corry, L. Huang, N. Hildebrandt. FRET-Modulated Multihybrid Nanoparticles for Brightness-Equalized Single-Wavelength Barcoding. *Journal of the American Chemical Society* **2019**, *141*, 11123-11141.

4.1 Introduction

The combination of unique photophysical properties and large surface-to-volume ratios have made semiconductor quantum dots (QDs) to one of the most versatile types of donors and acceptors for FRET.[3] Although QD-FRET biological applications range from *in-vitro* diagnostic assays over molecular logic gates to *in-vivo* imaging with various combinations of donors and/or acceptors interacting with many different QDs, the full extent of how the number of donors and acceptors assembled or co-assembled to a single QD regulate the different FRET pathways has not yet been investigated and understood. Different types of multiple acceptors attached to a central QD have been used for showing the increasing FRET efficiency with the number of acceptors, and such concepts have been frequently exploited for various biosensing applications.[21], [61] , [62]–[69], [70]–[72] The investigation and application of multiple donors interacting with a central QD for an increased probability of QD-sensitization via FRET but unchanged FRET efficiency has been limited to lanthanide complexes.[61],[94],[185],[187]–[193] Few studies have also investigated and applied the co-assembly of several lanthanide FRET donors and dye FRET acceptors,[65]–[68],[183] or the combination of FRET to dyes and charge transfer with ruthenium complexes on one QD.[70] However, none of these studies has systematically investigated all different combinations with a broad range of numbers of donors and acceptors and compared the experimental results with theoretical modelling. Such an extensive investigation would not only contribute to a full understanding of such complicated multi donor-

acceptor energy transfer pathways on nanoparticles but also open the opportunity to use the models for calculating desired photophysical properties adapted to advanced fluorescence biosensing applications such as multiplexed or encoded detection.

Optical multiplexing or barcoding based on nanoparticles, FRET, or their combination provides many advantages for biological sensing and imaging, optical data storage, and document security.[44],[137],[163],[164],[194] Encoding based on QDs attracted considerable attention due to their unique optical properties.[65],[140],[164],[171],[184],[185],[195] QD emission spectra are narrow and tunable throughout the visible and near-infrared wavelength range. Moreover, their absorption spectra are extremely broad and thus, several QDs with different emission colors can be excited with the same wavelength for spectral multiplexing.[17],[173],[196]–[198] An important drawback for quantitative biosensing and imaging is the significant difference in brightness when exciting different QDs by the same wavelength.[199] Smith *et al.* [200] used distinct core/shell/shell structures to overcome the mismatch of extinction coefficients of different QDs and to equalize their brightness over a wavelength range between *ca.* 500 and 800 nm.[199] Despite the similar brightness of these QDs, they still require the detection of different wavelengths for multiplexing or barcoding.

One way to use only a single emission wavelength is the exploitation of PL lifetimes for multiplexing.[44],[137],[144],[170],[182],[184],[201]–[204] Owing to their extremely long PL lifetimes and their multiple narrow emission bands, fluorophores based on lanthanides are particularly well suited for multiplexed detection or optical barcoding.[44],[182],[184],[204]–[208] The PL lifetimes of lanthanide complexes can be tuned over a broad temporal range and long donor-acceptor distances by combination with suitable FRET acceptors, such as organic dyes or QDs.[44],[182],[184],[204],[209],[210] Moreover the use of such emitting acceptors allows for using the FRET-sensitized acceptor PL as a single-wavelength readout, which we recently applied for single-wavelength optical barcoding in cellular imaging.[44] Similar to the excitation-dependent brightness of QDs, one important drawback of temporal optical barcoding via time-gated (TG) FRET codes is the significant variation in brightness of the different codes, which can be in the

order of 10 to 100 fold, depending on the selection of the distinguishable temporal coding windows. Multiple Tb donors and dye acceptors co-assembled to the same QD and a precise control of PL lifetimes and intensities have the potential to be used for designing multi-hybrid nanoparticles with brightness-equalized single-wavelength PL emission for temporal optical barcoding applied to single-contrast imaging. Thus, an extensive analysis of a multitude of donor-acceptor combinations on the same QD for a precise understanding of how the different FRET pathways lead to controlled photophysical properties is not only of fundamental interest for multi-donor-acceptor FRET on nanoparticle surfaces. It also provides the necessary knowledge of optimizing such multi-FRET nanoparticles for advanced multiplexed biosensing in both fluorescence spectroscopy and microscopy.

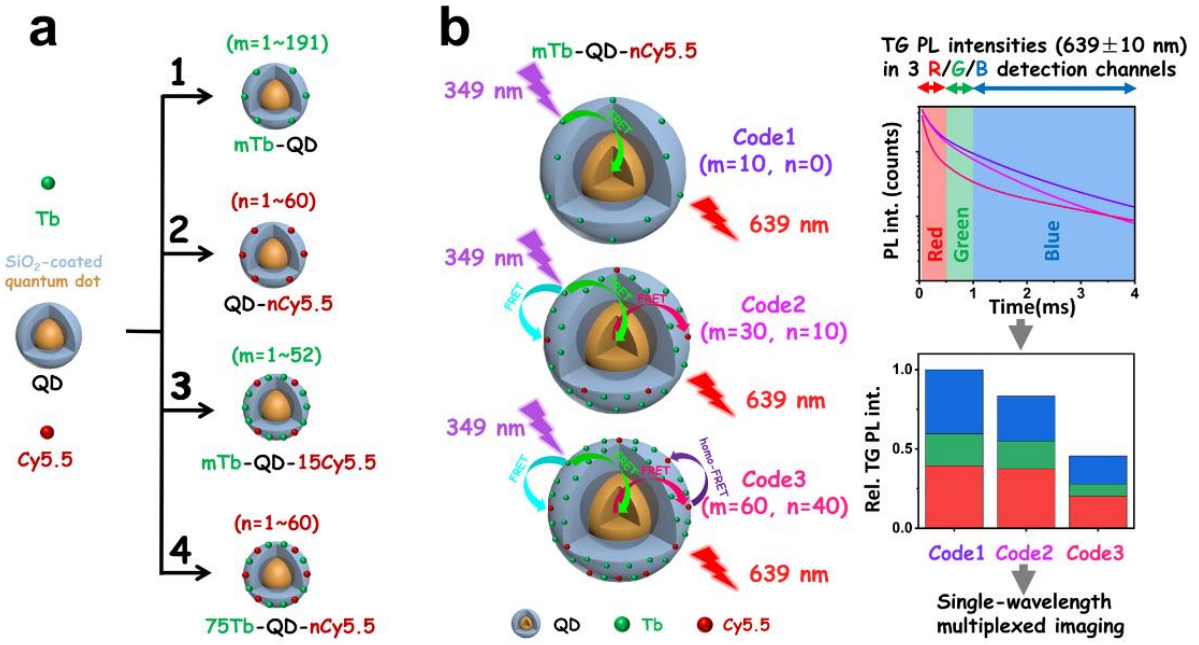

Figure 4.1. Concept of FRET-modulated multi-hybrid NPs. **(a)** Schematic illustration of the four multi-donor-acceptor FRET systems. **(b)** Design and principle of brightness-equalized multi-hybrid NP for PL lifetime barcoding.

In this Chapter, we investigated four kinds of *m*Tb-QD-*n*Cy5.5 FRET system, as illustrated in **Figure 4.1a**. The multiple-donors system (***m*Tb-QDs**) contained increasing numbers of m = 1 to 191 Tb per QD. The multiple-acceptors system (**QD-*n*Cy5.5**) contained increasing numbers of n = 1 to 60 Cy5.5 per QD. Based on the results from these two systems, we then prepared two different systems

containing both multiple donors and acceptors (***m*Tb-QD-*n*Cy5.5**), one with a fixed number of n = 15 Cy5.5 per QD and an increasing number of m = 1 to 52 Tb per QD and another with a fixed number of m = 75 Tb per QD and an increasing number of n = 1 to 60 Cy5.5 per QD. The extensive characterization of the same Tb-QD-dye FRET system at a myriad of different configurations with steady-state and time-resolved spectroscopy and Monte-Carlo simulations (MCS) not only allowed us to gain a deeper understanding of such multi-FRET nanosystems but also to fine-tune the ingoing and outgoing FRET contributions for an ultimate control of PL intensities and lifetimes. This strategy permitted us to design multi-hybrid NPs with distinct PL lifetimes for optical RGB barcoding and the unique feature of equalized PL brightness while using only a single excitation and a single emission wavelength (**Figure 4.1b**). Direct applicability to multiplexed fluorescence microscopy was demonstrated by doping three differently coded multi-hybrid NPs in microbeads. The different FRET microbeads (mixed on one microscope slide) could be easily distinguished within a single field of view by single-excitation and single-emission wavelength TG PL imaging on a standard wide-field microscope. Our results demonstrate that a combination of experimental and modeling approaches can provide a deeper fundamental understanding of even very complicated FRET systems, including various hetero-FRET, homo-FRET, and dimer-induced self-quenching pathways, with multiple donor-acceptor interactions at high densities on NP surfaces. This knowledge can be used to design advanced optical biosensing and imaging methods that are not accessible by simple FRET systems.

4.2 Materials and methods

4.2.1 Materials

Terbium(III) chloride hexahydrate (99.999% trace metals basis), Poly(ethylene glycol) nonylphenyl ether (NP-5), tetraethyl orthosilicate (TEOS) and (3-mercaptopropyl) trimethoxysilane (MPS) were purchased from Sigma-Aldrich. Cyanine5.5 maleimide was purchased from Lumiprobe Inc. (Berkeley, CA, USA). Cyclohexane, chloroform, ethanol, ammonia aqueous solution (28%) were

purchased from Sinopharm Chemical Reagent Co., Ltd. (Shanghai, China). CdSe/CdS/ZnS QDs with emission maximum at 620 nm were purchased from Poly OptoElectronics Co., Ltd. Black Costar Half Area 96 well microtitration plates were purchased from Corning Inc. (Corning, NY, USA), and Lumi4 functionalized to maleimide were provided by Lumiphore Inc. (Berkeley, CA, USA).

4.2.2 Synthesis of QDs embedded silica nanospheres

The QDs embedded silica nanospheres were synthesized by a reverse microemulsion approach. Typically, the glass bollte containing 30 mL of cyclohexane was added with 3.95 mL of NP-5 and stirred for 15 min. The above solution was mixed with 300 µL of ammonia aqueous solution followed by stirring for another 15 min to form the reverse microemulsion. The mixture was subsequently added with 200 µL of QDs chloroform solution (10 mg/mL), followed by the injection of 140 µL of TEOS to start the silica encapsulation. After stirred at room temperature for 18 h, the QDs embedded silica nanospheres were precipated by adding ethanol followed by centrifugation. The products were washed with ethanol for several times and finally dispersed in 20 mL of ethanol.

4.2.3 Synthesis of mercapto-terminated silica nanospheres

For the grafting of mercapto-groups onto silica surface, the above QDs embedded silica nanospheres in 20 mL of ethanol was added with 500 µL of ammonia and 100 µL of MPS, followed by vigorous stirring at room temperature for 12 h. The finally product was harvested by centrifugation, washed with ethanol thoroughly and redispersed in 2 mL water.

4.2.4 Estimation of molar concentrations of QD/SiO_2

We assumed that the nanomaterials have the same density as the corresponding bulk materials. For the CdSe/CdS/ZnS QD, the density of CdSe, CdS, and ZnS are 5.816 g/cm^3, 4.82 g/cm^3, and 4.09 g/cm^3, respectively. The radius of QD is approximately 3.5 nm according HR-TEM. The radius of the CdSe core and the thicknesses of the CdS and ZnS shell were estimated to 1.8 nm, 1.16 nm, and 0.54 nm, respectively. These assumptions led to a QD density of 5.22 g/cm^3 (**Equations**

4.1 and **4.2**). Using the density and volume of a single QD and Avogadro's constant, we obtained the molecular weight of QDs, which was ~570,000. The yield of synthetic QD/SiO_2 was approximately 70%, which resulted in a final molar concentration of 1.23 μM QD/SiO_2.

$$V = \frac{4}{3}\pi r^3 \tag{4.1}$$

$$\rho = \frac{m}{V} \tag{4.2}$$

4.2.5 Photoluminescence quantum yield determination

The PL QY of as-prepared QD/SiO_2 was determined using Qdot™ 605 ITK™ Streptavidin Conjugate Kit (Invitrogen™) as a standard (λ_{ex}=480 nm, Φ_s=0.76). The PL QY was calculated according to the following **Equation 4.3**:

$$\Phi_x = \Phi_s \left(\frac{A_s}{A_x}\right)\left(\frac{lnt_x}{lnt_s}\right)\left(\frac{\eta_x}{\eta_s}\right)^2 \tag{4.3}$$

Where Φ is the PL QY, *lnt* is the area under the emission peak, *A* is the absorbance at the excitation wavelength, and η is the refractive index of the solvent. The subscripts s and x denote the respective values of the standard and QD/SiO_2.

4.2.6 Determination of Tb^{3+} to Lumi4-ligand ratio for ~100% coordination

For the titration experiment, the initial solution contained 4 μL of Lumi4-Mal (0.38 mM) and 0.5 μL of $TbCl_3$ (0.6 mM) in 1.5 mL of water (Lumi4-Mal/Tb = 1/0.2). Then 0.5 μL of $TbCl_3$ (0.6 mM) were added stepwise to the solution while stirring until at Lumi4-Mal/Tb ratio of 1/4 was reached. The PL intensity of each point was recorded at 550 nm.

4.2.7 Formation of FRET system 1 (*m*Tb-QD)

For ~191 Lumi4 per QD, 42 μL of Lumi4-Mal (3.8 mM in anhydrous DMF), 162.5 μL of QD (1.23 μM), and 195.5 μL of Tris-HCl buffer at pH 7.5 (50 mM) were mixed in a 0.5 mL Eppendorf tube (molar ratio of Lumi4/QD = 800:1). For ~136 Lumi4 per QD, 10.5 μL Lumi4-Mal (3.8 mM in anhydrous DMF), 162.5 μL QD (1.23 μM), and 227 μL Tris-HCl buffer at pH 7.5 (50 mM) were mixed in a 0.5 mL Eppendorf tube (molar ratio of Lumi4/QD = 200:1). For ~50 Lumi4 per QD, 3.7 μL of Lumi4-

Mal (3.8 mM in anhydrous DMF), 162.5 µL of QD (1.23 µM), and 233.8 µL of Tris-HCl buffer at pH 7.5 (50 mM) were mixed in a 0.5 mL Eppendorf tube (molar ratio of Lumi4/QD = 70:1). The mixtures were incubated for 3 h at room temperature with the tube covered in aluminum foil and rotating with an Intelli Mixer (ELMI). Then the product was collected by centrifugation (10,000 r.p.m, 10 min) and redispersed in 400 µL Tris-HCl buffer at pH 7.5 (50 mM). The number of Lumi4 per QD was determined by UV/Vis and TG PL spectroscopy. For the formation of *m*Tb-QD FRET assemblies with constant QD concentration, we used two different constant concentrations of Lumi4-QD (0.5 nM and 5 nM). Tb^{3+} was used at concentrations of 0.5 µM and 5 µM in pure water. For the 20 to 1000 Tb per QD in solution series, a QD concentration of 0.5 nM (in Tris-HCl buffer at pH 7.5, 50 mM) was used. For the total measuring volume of 150 µL, 15 µL of QD solutions (5 nM) were mixed with 135 µL of solutions containing increasing amounts (3, 7.5, 15, 22.5, 30, 37.5, 45, 52.5, 60, 67.5, 75, 82.5, 90, 97.5, 105, 112.5, 120, 135 µL of Tb^{3+} (0.5 µM) and 15 µL of Tb^{3+} (5 µM)) in pure water. The mixtures were incubated while slowly shaking for 1 h at room temperature. For the 0 to 300 Tb per QD in solution series, a QD concentration of 5 nM (in Tris-HCl buffer at pH 7.5, 50 mM) was used. For the total measuring volume of 150 µL, 15 µL of QD solutions (50 nM) were mixed with 135 µL of solutions containing increasing amounts (0, 1.5, 3, 7.5, 15, 30, 75 µL of Tb^{3+} (0.5 µM) and 15, 22.5, 30, 37.5, 45 µL of Tb^{3+} (5 µM)) in pure water. The mixtures were incubated while slowly shaking for 1 h at room temperature. For the 0 to 300 Tb per QD in solution series, a QD concentration of 5 nM (in Tris-HCl buffer at pH 7.5, 50 mM) was used. For the total measuring volume of 150 µL, 15 µL of QD solutions (50 nM) were mixed with 135 µL of solutions containing increasing amounts (0, 1.5, 3, 6, 12, 15, 22.5, 30, 45, 60, 75, 90 µL of Tb^{3+} (0.5 µM) and 10.5, 12, 13.5, 15, 22.5, 30, 37.5, 45 µL of Tb^{3+} (5 µM)) in pure water. The mixtures were incubated while slowly shaking for 1 h at room temperature.

4.2.8 Formation of FRET system 2 (QD-*n*Cy5.5)

Cy5.5-Mal (4.54 mM) in anhydrous DMF was diluted to 4.54 µM in pure water. QD was diluted to 500 nM in Tris-HCl buffer at pH 7.5 (50 mM). For the formation of

QD-*n*Cy5.5 donor-acceptor assemblies, we used constant concentrations of QD (50 nM) for all experiments. For the total incubation volume of 200 µL, 20 µL of QD solutions (500 nM) were mixed with 180 µL of solutions containing increasing amounts (2.2, 4.4, 8.8, 17.6, 22, 33, 44, 66, 88, 110, 132 µL) of Cy5.5 (4.54 µM) in Tris-HCl buffer at pH 7.5 (50 mM). The mixtures were incubated for 3 h at room temperature with the tube covered in aluminum foil and rotating with an Intelli Mixer. For the total measuring volume of 150 µL, 150 µL of above mixtures were used for steady state PL experiments, while 15 µL of above mixtures mixed with 135 µL pure water were used for time-resolved (time-correlated single photon counting – TCSPC) PL experiments.

4.2.9 Formation of FRET system 3 (*m*Tb-QD-15Cy5.5)

For the total incubation volume of 400 µL, 6.6 µL of Cy5.5-Mal (0.454 mM), 5.2 µL of Lumi4-Mal (3.8 mM), 162.5 µL of QD (1.23 µM), and 225.7 µL of Tris-HCl buffer at pH 7.5 (50 mM) were mixed in a 0.5 mL Eppendorf tube. The mixtures were incubated for 3 h at room temperature with the tube covered in aluminum foil and rotating with an Intelli Mixer. Then the product was collected by centrifugation (10,000 r.p.m, 10 min) and redispersed in 400 µL pure water. The number of Cy5.5 and Lumi4 per QD was confirmed by UV/Vis spectroscopy. For the formation of *m*Tb-QD-15Cy5.5 FRET assemblies, we used constant concentrations of QD-15Cy5.5 (5 nM) for the experiments. Solutions of 50 nM QD-15Cy5.5 and 0.5 µM 5 µM, and 50 µM Tb^{3+} in pure water were used. For the total incubation volume of 150 µL, 15 µL of QD-15Cy5.5 solutions (50 nM) were mixed with 135 µL of solutions containing increasing amounts (1.5, 3, 6, 12, 15, 22.5, 30, 45, 60, 75, 90 µL) of 0.5 µM Tb^{3+}, (10.5, 12, 13.5, 15, 22.5, 30, 37.5, 45, 60, 75, 90 µL) of 5 µM Tb^{3+} and (10.5, 12, 13.5, 15 µL) of 50 µM Tb^{3+} in pure water. The mixtures were incubated while slowly shaking for 1 h at room temperature.

4.2.10 Formation of FRET system 4 (75Tb-QD-*n*Cy5.5)

For the total incubation volume of 400 µL, 5.2 µL of Lumi4-Mal (3.8 mM), 162.5 µL of QD (1.23 µM), and 232.3 µL of Tris-HCl buffer at pH 7.5 (50 mM) were mixed in a 0.5 mL Eppendorf tube. The mixtures were incubated for 3 h at room

temperature with the tube covered in aluminum foil and rotating with an Intelli Mixer. Then the product was collected by centrifugation (10,000 r.p.m, 10 min) and redispersed in 400 µL Tris-HCl buffer at pH 7.5 (50 mM). The number of Lumi4 per QD was confirmed by UV/Vis spectroscopy. For the formation of 75Tb-QD, 2.44 µL of Tb^{3+} (5 mM) were added (molar ratio of Tb^{3+} per QD = 150:1). For the formation of 75Tb-QD-*n*Cy5.5 FRET assemblies, the total incubation volume of 200 µL contained 20 µL of 75Tb-QD (500 nM) and 180 µL of solutions containing increasing amounts (2.2, 4.4, 8.8, 17.6, 22, 33, 44, 66, 88, 110, 132 µL) of 4.54 µM Cy5.5 in Tris-HCl buffer at pH 7.5 (50 mM). The mixtures were incubated for 3 h at room temperature with the tube covered in aluminum foil and rotating with an Intelli Mixer. For the total measuring volume of 150 µL, 150 µL of above mixtures (50 nM) were used for steady state PL experiments, while 15 µL of above mixtures diluted with 135 µL of pure water were used for time-resolved (multi-channel scaling) experiments.

4.2.11 Fabrication of FRET-modulated multi-hybrid nanoparticles for brightness-equalized single-wavelength barcoding.

For the total incubation volume of 400 µL of *m*Tb-QD, 2.6 µL of Lumi4-Mal (3.8 mM), 81.3 µL of QD (1.23 µM), and 316.1 µL of Tris-HCl buffer at pH 7.5 (50 mM) were mixed in a 0.5 mL Eppendorf tube. For the total incubation volume of 400 µL of *m*Tb-QD-10Cy5.5, 2.2 µL of Cy5.5-Mal (0.454 mM), 2.6 µL of Lumi4-Mal (3.8 mM), 81.3 µL of QD (1.23 µM), and 313.9 µL of Tris-HCl buffer at pH 7.5 (50 mM) were mixed in a 0.5 mL Eppendorf tube. For the total incubation volume of 400 µL of *m*Tb-QD-40Cy5.5, 8.8 µL of Cy5.5-Mal (0.454 mM), 2.6 µL of Lumi4-Mal (3.8 mM), 81.3 µL of QD (1.23 µM), and 307.3 µL of Tris-HCl buffer at pH 7.5 (50 mM) were mixed in a 0.5 mL Eppendorf tube. The mixtures were incubated for 3 h at room temperature with the tubes covered in aluminum foil and rotating with an Intelli Mixer. Then the products were collected by centrifugation (10,000 r.p.m, 10 min) and redispersed in 400 µL pure water. The number of Cy5.5 and Lumi4 per QD were confirmed by UV/Vis and TG PL spectroscopy. For formation of *m*Tb-QD-*n*Cy5.5 FRET assemblies with n = 0, 10, or 40, Lumi4-QD-*n*Cy5.5, solutions of 50

nM and Tb^{3+} solutions of 0.05 µM, 0.5 µM, and 5 µM in pure water were used. For the total incubation volume of 150 µL, 15 µL of QD-*n*Cy5.5 solutions (50 nM) were mixed with 135 µL of solutions containing increasing amounts (15, 30, 60 µL) of 0.05 µM Tb^{3+}, (12, 15, 22.5, 30, 45, 60, 75, 90 µL) of 0.5 µM Tb^{3+}, and (10.5, 12, 13.5, 15, 22.5, 30, 37.5, 45 µL) of 5 µM Tb^{3+} in pure water. The mixtures were incubated while slowly shaking for 1 h at room temperature.

4.2.12 Microbeads encoding

For brightness-equalized microbeads encoding, solutions of 10Tb-QD, 30Tb-QD-10Cy5.5, and 60Tb-QD-40Cy5.5 were selected. For each microbead encoding, 5 µL of microbeads (Pierce Iminobiotin Agarose Microbead, Thermo Scientific) were mixed with 100 µL (50 nM) of each single-nanoparticle code. After purification by centrifugation, the microbeads were dispersed in 200 µL pure water in an 8-chamber glass slide (Nunc® Lab-Tek® II Chamber Slide™, 155409) for imaging. Images of microbeads encoding were acquired using a wide-field, TG luminescence inverted microscope (Olympus IX71) that uses a UV laser (349 nm, 100 Hz, Nd:YLF, Triton, Spectra Physics) for pulsed excitation and an intensified CCD camera (ICCD, PI-MAX3, Princeton Instruments) for gated detection. QD PL signals were detected using a 639±10 nm bandpass filter. Acquisition settings (Winview software controlling the camera) were adjusted to optimal conditions regarding RGB ratio and were fixed to a delay time of 50 µs (after the excitation pulse) and a gate width of 450 µs (red window - R), a delay time of 500 µs and a gate width of 500 µs (green window - G), and a delay time of 1 ms and a gate width of 3 ms (blue window - B). *ImageJ* was used to assign red, green, or blue color to the three detection windows and define a common intensity range (same minimum and maximum values for all windows).

4.2.13 Analytical Methods

Structural characterization of the QD/SiO_2 was carried out using a FEI Tecnai G2 F20 S-Twin high-resolution transmission electron microscope (HR-TEM) operating at 200 kV. Absorption spectra were acquired using a Lambda 35 UV/Vis spectrophotometer (Perkin Elmer). Steady-state PL spectra were acquired using a

Xenius fluorescence spectrometer (SAFAS). PL decay curves of FRET system 1 (*m*Tb-QD), FRET system 3 (*m*Tb-QD-15Cy5.5), and FRET system 4 (75Tb-QD-*n*Cy5.5) were recorded in multi-channel scaling mode with a time-resolved fluorescence plate reader (Edinburgh Instruments) with 4000 detection bins of 2 µs integration time. A nitrogen laser (LTB) was used for excitation (337.1 nm, 20 Hz, 600 flashes). 494/20 nm (Semrock), 640/14 nm (Semrock), and 707/16 nm (Delta) bandpass filters were used for analyzing the Tb, QD, and Cy5.5 PL, respectively. For the measurement of the PL decay curves of FRET system 2 (QD-*n*Cy5.5), a SuperChrome supercontinuum source (Fianium) was used for excitation (480 ± 15 nm, 5 MHz, indicated laser power: 255) and the time-resolved fluorescence plate reader (Edinburgh Instruments) was used in TCSPC mode. 640/14 nm and 707/16 nm bandpass filters were used for analyzing the QD and Cy5.5 PL, respectively. PL decay data was fit with FAST software version 3.1 (Edinburgh Instruments). All samples were measured in black 96-well microtiter plates with an optimal working volume of 150 µL.

4.2.14 FRET calculation

The overlap integral (J) and Förster distance (R_0) were calculated using **Equations 4.4** and **4.5**.

$$J = \int \bar{I}_{\mathrm{D}}(\lambda)\varepsilon_{\mathrm{A}}(\lambda)\lambda^4 \mathrm{d}\lambda \tag{4.4}$$

where $\bar{I}_{\mathrm{D}}(\lambda)$ is the area-normalized emission spectrum of the donor, $\varepsilon_{\mathrm{A}}(\lambda)$ is the molar absorptivity spectrum of the acceptor in $\mathrm{M^{-1}cm^{-1}}$, and λ is the wavelength in nm.

$$R_0 = 0.0211[\kappa^2 \Phi_{\mathrm{D}}(n)^{-4} J(\lambda)]^{1/6} \quad \text{(in nm)} \tag{4.5}$$

where κ^2 is orientation factor (κ^2=2/3 due to dynamic averaging within all FRET pairs as justified by the flexible attachment of Tb and Cy5.5 to the SiO_2 coating, the isotropic emission of Tb and QD, and the long PL lifetimes), Φ_{D} is quantum yield of the donor, and n=1.35 is the refractive index of the surrounding medium. The molar extinction coefficients for QD/SiO_2 were calculated using molar concentration (known from the synthesis) and measured absorbance spectra. The molar extinction coefficients for Cy5.5 and Tb were provided by the suppliers.

Relative energy transfer rates were calculated using **Equation 4.6**, where τ_{D} is the

unquenched donor lifetime, $R_{0,n}$ is the Förster distance for the FRET pathway, and the donor-acceptor distance R was assumed to be constant between different pathways.

$$\frac{k_1}{k_2} = \frac{\tau_{D,1}{}^{-1}\left[\frac{R_{0,1}}{R}\right]^6}{\tau_{D,2}{}^{-1}\left[\frac{R_{0,2}}{R}\right]^6} = \frac{\tau_{D,2}}{\tau_{D,1}}\left[\frac{R_{0,1}}{R_{0,2}}\right]^6 \tag{4.6}$$

In the case of Tb-to-QD FRET (due to the strong difference in their intrinsic PL lifetimes – *cf.* **Table 4.1**), the FRET-sensitized PL decay time of QD adapts to the FRET-quenched PL decay time of Tb ($\tau_{AD} = \tau_{DA}$). Thus, the FRET efficiency can be determined by **Equation 4.7**.

$$E_{FRET} = 1 - \frac{\tau_{AD}}{\tau_D} \tag{4.7}$$

where τ_{AD} is the average PL decay time of the *m*Tb-QD FRET system and τ_D is the average PL lifetime of Tb alone.[94]

The Tb-to-QD distance was calculated using **Equation 4.8**.

$$R = R_0\left(\frac{\tau_{AD}}{\tau_D - \tau_{AD}}\right)^{1/6} \tag{4.8}$$

The theoretical probability of FRET-sensitized emission from one QD sensitized by *m* equidistant Tbs on its surface can be calculated by **Equation 4.9**.[94]

$$P = 1 - (1 - E_{FRET})^m \tag{4.9}$$

In the case of QD-to-Cy5.5 FRET, the FRET efficiencies were calculated using PL decay times (**Equation 4.10**) and intensities (**Equation 4.11**).

$$E_{FRET} = 1 - \frac{\tau_{DA}}{\tau_D} \tag{4.10}$$

where τ_{DA} is the average PL lifetime of the QD-*n*Cy5.5 FRET system and τ_D is the average PL lifetime of QD alone.

$$E_{FRET} = 1 - \frac{I_{DA}}{I_D} \tag{4.11}$$

where I_{DA} is the PL peak intensity of the QD-*n*Cy5.5 FRET system and I_D is the PL peak intensity of QD alone.

In the case of FRET from one QD to *n* equidistant Cy5.5 dyes on its surface, the FRET efficiency can be calculated by **Equation 4.12**.[2],[3],[8]

$$E_{FRET} = \frac{n{R_0}^6}{n{R_0}^6 + R^6} \tag{4.12}$$

4.2.15 Multi-exponential PL decay analysis

PL decay curves of FRET-sensitized QD or Cy5.5 PL were fit using a multiexponential PL intensity decay function (**Equation 4.13**).

$$I = A\,[\sum \alpha_{\mathrm{ADi}*} \exp(-t/\tau_{\mathrm{ADi}})] + B \exp(-t/\tau_{\mathrm{D}}) \quad (4.13)$$

where A is the total amplitude and $\alpha_{\mathrm{ADi}*}$ are the amplitude fractions ($\sum \alpha_{\mathrm{ADi}*} = 1$) of the different FRET contributions with FRET-sensitized PL decay times τ_{ADi}. Amplitude B and decay time τ_{D} correspond to the contribution of unquenched Tb donor PL (due to spectral crosstalk in the QD detection channel). The amplitudes must be further corrected by FRET rates (**Equation 4.14a**) to take into account the FRET efficiency-dependent excitation of the acceptor (**Equation 4.14b**).[2] PL decay time averaging was then performed using amplitude weighted average decay times (**Equation 4.14c**).

$$k_{\mathrm{FRETi}} = \frac{1}{\tau_{\mathrm{ADi}}} - \frac{1}{\tau_{\mathrm{D}}} \quad (4.14a)$$

$$\alpha_{\mathrm{ADi}} = \frac{{}^{\alpha_{\mathrm{ADi}*}}/_{k_{\mathrm{FRETi}}}}{\Sigma\left({}^{\alpha_{\mathrm{ADi}*}}/_{k_{\mathrm{FRETi}}}\right)} \quad (4.14b)$$

$$\tau_{\mathrm{AD}} = \sum a_{\mathrm{ADi}} \tau_{\mathrm{ADi}} \quad (4.14c)$$

PL decay curves of FRET-quenched QD PL were fit using a multiexponential PL intensity decay function (**Equation 4.15**).

$$I = C\,[\sum \gamma_{\mathrm{DAi}} \exp(-t/\tau_{\mathrm{DAi}})] \quad (4.15)$$

where C is the total amplitude and γ_{DAi} are the amplitude fractions ($\sum \gamma_{\mathrm{DAi}} = 1$) of the different FRET contributions with FRET-quenched PL decay times τ_{DAi}. PL decay time averaging was performed using amplitude weighted average decay times (**Equation 4.16**).

$$\tau_{\mathrm{DA}} = \sum \gamma_{\mathrm{DAi}} \tau_{\mathrm{DAi}} \quad (4.16)$$

4.3 Results and discussion

4.3.1 Design and preparation of the multi-hybrid FRET nanoparticles

The central nanoscaffold of the multi-hybrid nanoparticles were SiO_2-coated QDs (the entire QD/SiO_2 is denoted as "QD" throughout the manuscript – *cf.* **Figure 4.1**), which consisted of a *circa* 7 nm diameter CdSe/CdS/ZnS core/shell/shell QD

emitting at 620 nm and a 7±2 nm thick SH-functionalized SiO_2 shell (*cf.* **Figure 4.2**). Control over the number of Tb donors and/or Cy5.5 acceptors (*cf.* **Figure 4.3** for chemical structures) assembled to the central QD was extremely important for an extensive characterization of FRET over a large range of numbers of Tb and Cy5.5 per QD. Both, Tb and Cy5.5 contained maleimide groups for attachment to the SH-functionalized SiO_2 shells of the QDs. The separation of absorption (via the Lumi4 ligand) and emission (via the central Tb^{3+} ion) of the supramolecular Lumi4-Tb complex (the entire complex is denoted as "Tb" throughout the manuscript – *cf.* **Figure 4.1**) provided a particular advantage because without the central Tb^{3+} ion the ligands were not luminescent and could not contribute to FRET. Thus, we could conjugate a constant number of ligands (between *ca.* 50 and 190) per QD, which was quantified by UV/Vis absorption and time-gated PL spectroscopy (**Figure 4.4**), and add the Tb^{3+} ions in a second step via addition of $TbCl_3$ to the ligand-coated QDs. The advantage of this two-step procedure was the much simpler control of the number of actual Tb donors (addition of Tb^{3+} that coordinates to the Lumi4 ligand) with only one QD-functionalization and separation step (attachment of maleimide-activated ligand to the thiols of the QD SiO_2 shell and separation of free ligands). Only a Tb^{3+} ion coordinated inside a ligand (and neither the Tb^{3+} nor ligand alone) resulted in a functional luminescent Tb donor on the QD and thus, the number of Tb per QD could be simply adjusted and calculated via the concentrations of $TbCl_3$ and QD and taking into account a ratio of ~1.5 Tb^{3+} per Lumi4 ligand (because coordination by titration is not quantitative). This ratio of 100% Tb coordination into the ligand was determined by titrating $TbCl_3$ into a solution of Lumi4 ligands and measuring the Tb PL intensity (at 550 nm) upon ligand excitation (at 337 nm). PL saturation occurred at 1.5±0.2 Tb^{3+} per ligand (**Figure 4.5**). Therefore, the amount of *m* Tb per QD equaled the amount of Tb^{3+} in solution divided by 1.5. The amount of *n* Cy5.5 per QD was calculated by the respective concentrations of Cy5.5 and QD used for fabricating the QD-Cy5.5 assemblies and assuming a ~100 % attachment efficiency (all maleimide-functionalized Cy5.5 added to a QD solution attached to the QD surface). The ~100% surface functionalization efficiency was confirmed by measuring the Cy5.5 and QD concentrations of QD-*n*Cy5.5 conjugates (after separation of QD-*n*Cy5.5

from eventually free Cy5.5) by UV/Vis spectroscopy (**Figure 4.6**).

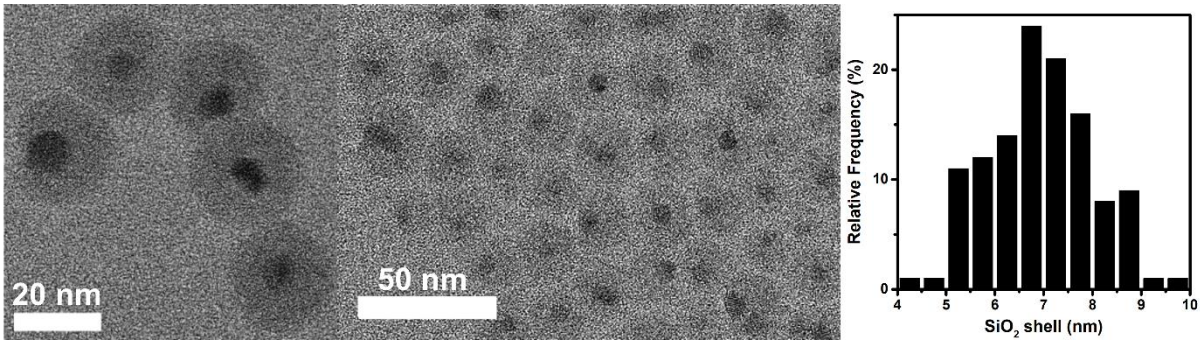

Figure 4.2. TEM images of QD/SiO_2 NPs and determination of SiO_2 shell thickness of 7±2 nm (calculated from 96 QD/SiO_2 NPs from the right TEM image).

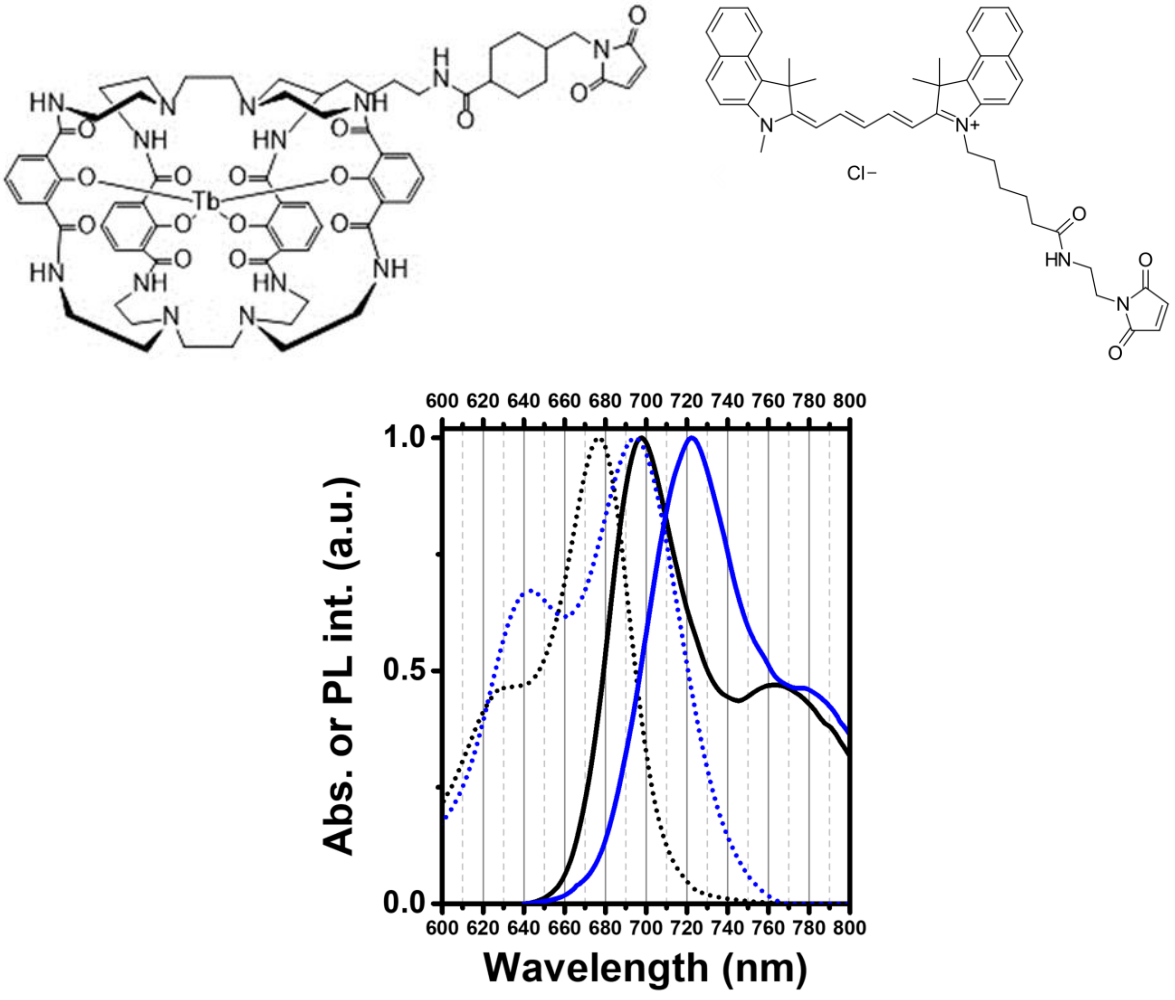

Figure 4.3. Chemical structures of maleimide-functionalized Lumi4-Tb **(top left)** and Cyanine5.5 **(top right)** and changes in absorption (dotted) and PL (straight) spectra of Cyanine5.5 in water (black) and attached to QDs in Tris-HCl buffer at pH 7.5 **(bottom)**. The spectra of Lumi4-Tb do not change upon attachment to QDs.

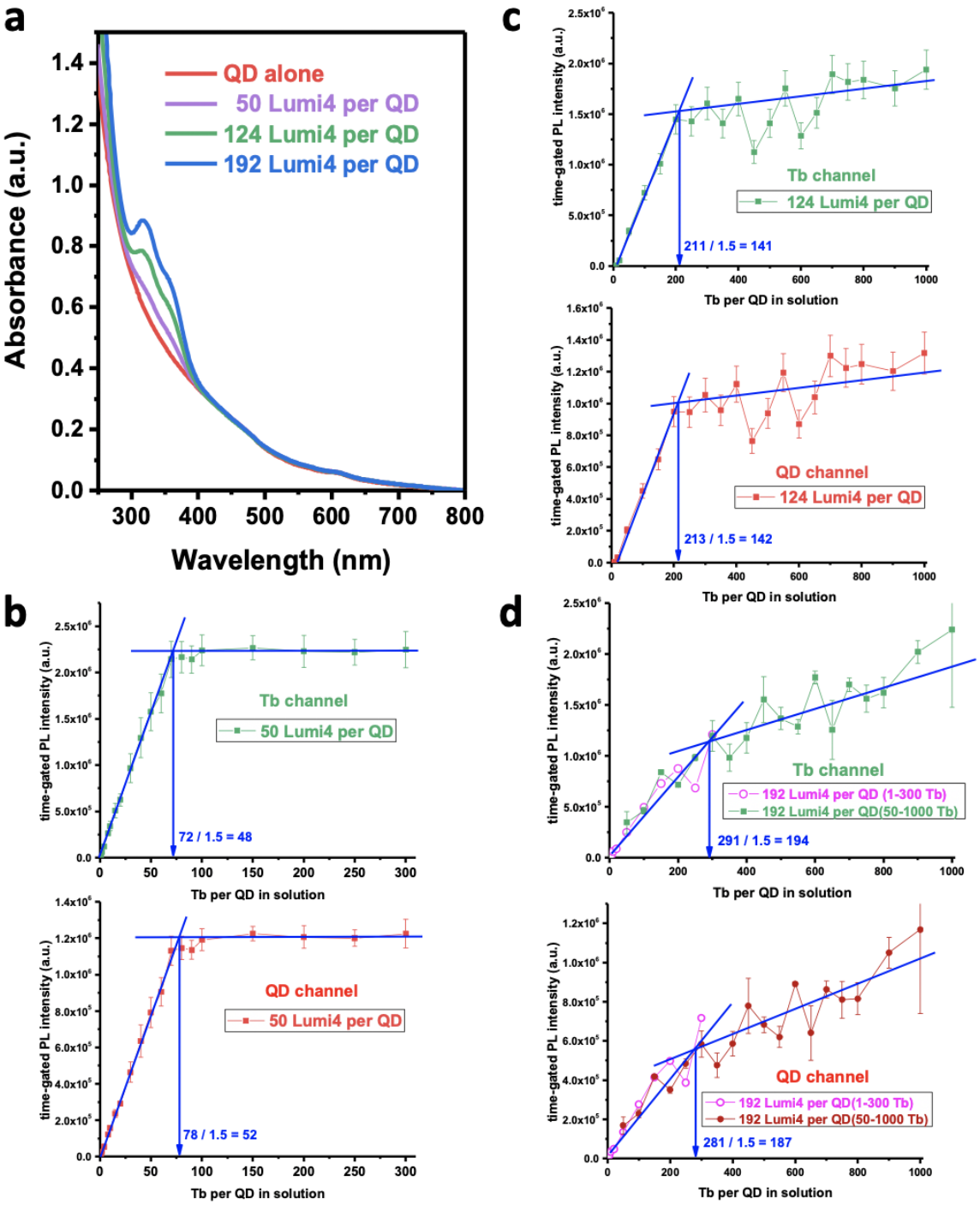

Figure 4.4. Absorption **(a)** and PL (**b to d** – TG Tb PL in the top graphs and TG QD PL in the bottom graphs) spectra used to analyze the number of Lumi4 ligands per QD. Absorption spectra use the difference between Lumi4-coated QDs and pure QDs and the extinction coefficients of Lumi4 (at 340 nm) and QD (at 610 nm) to calculate the Lumi4 per QD ratios (given inside the graph). The same samples were used for PL titration experiments (Tb^{3+} ions were added to the Lumi4-coated QDs) and the saturation points of the Tb and QD PL curves were divided by 1.5 (saturation of Lumi4 with Tb^{3+} - cf. Figure S4) to verify the number of Lumi4 per QD. Both approaches were used to estimate Lumi4 per QD ratios (average ± 10%) of 50±5, 136±14, and 191±19, respectively.

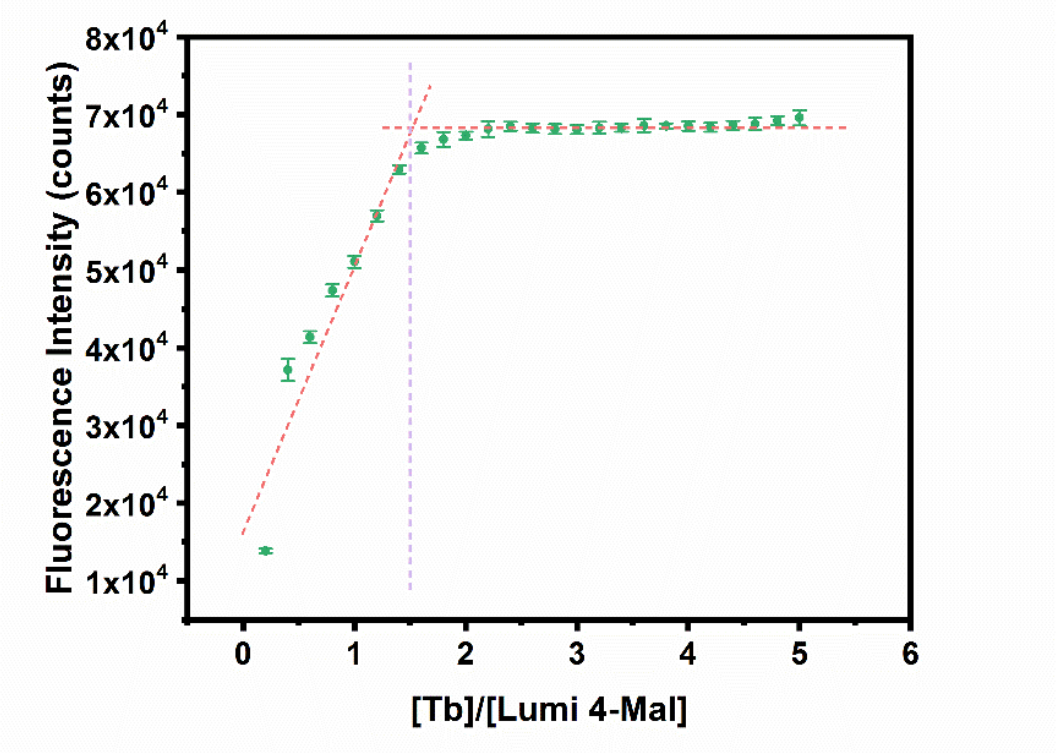

Figure 4.5. Titration experiment of Tb^{3+} coordination into the Lumi4-maleimide ligand.

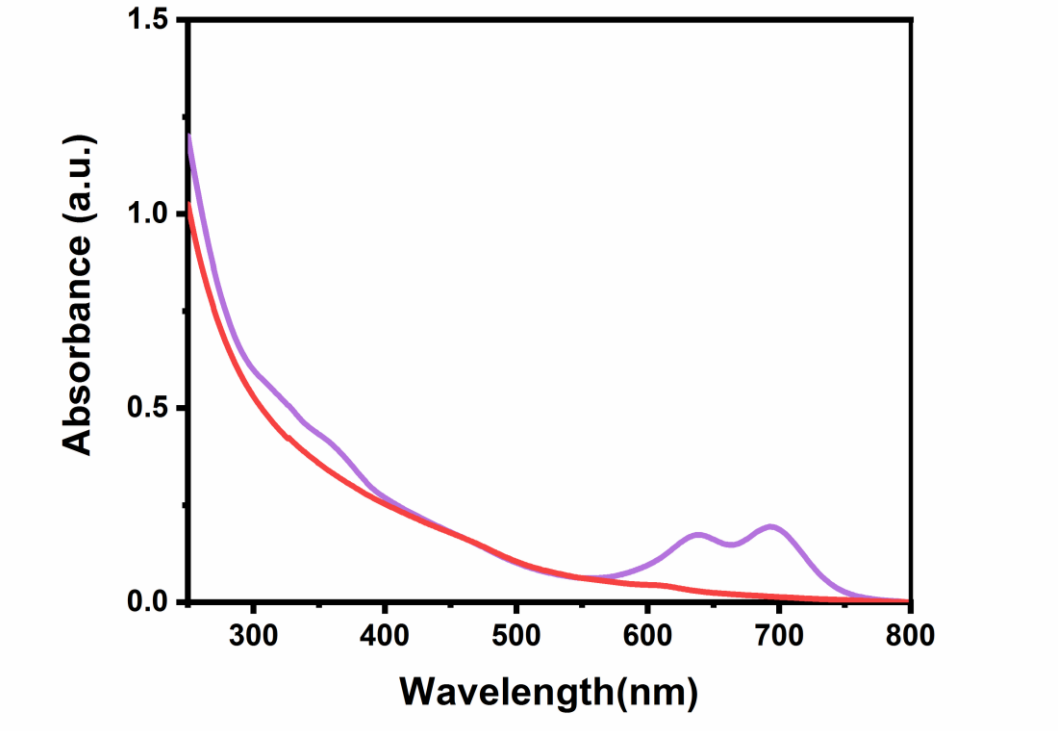

Figure 4.6. Absorption spectra of QD (red) and 52±7 Lumi4 and 15±2 Cy5.5 per QD (purple). We note that Cy5.5 has a weak absorption at 340 nm ($\varepsilon_{Cy5.5} \leq 10{,}000\ M^{-1}cm^{-1}$), which was subtracted when calculating the number of Lumi4 per QD on *m*Tb-QD-*n*Cy5.5 nano-hybrids.

Table 4.1. Photophysical properties of the FRET compounds within the multi-hybrid FRET NPs.

Fluorophore	ε_{max} (M^{-1} cm^{-1}) [λ_{max}]	Φ	Filter (nm)	lifetime
Tb	26,000 [340 nm]	0.79±0.08	494±12	2.7±0.1 ms
QD	501,000 [610 nm]	0.20±0.05	639±10	7.0±1.2 ns
Cy5.5	209,000 [694 nm]	0.20±0.05	708±8	~1 ns
FRET pair	J (M^{-1}. cm^{-1}. nm^4)		R_0 (nm)	
Tb → QD	$6.0±0.6\times 10^{16}$		9.7±0.7	
QD → Cy5.5	$1.3±0.1\times 10^{16}$		6.0±0.4	
Tb → Cy5.5	$2.5±0.3\times 10^{15}$		5.7±0.4	
Cy5.5 → Cy5.5	$1.6±0.2\times 10^{16}$		6.2±0.4	
QD → QD	$4.6±0.5\times 10^{16}$		7.4±0.5	
Cy5.5 → QD	$1.2±0.1\times 10^{13}$		1.9±0.1	

Notes: ε and Φ of Tb and Cy5.5 were provided by the suppliers. ε and Φ of QD were calculated using **Equations 4.1**, **4.2**, and **4.3**. J was calculated using **Equation 4.4**. R_0 was calculated using **Equation 4.5**.

4.3.2 Photophysical characterization of the multi-hybrid FRET nanoparticles

The absorption and PL emission spectra of Tb, QD, and Cy5.5 (**Figure 4.7a**) show spectral overlap between the different luminescent components. Thus, spectral overlap integrals (J) and Förster distances (R_0) were calculated for each individual FRET pair (**Figure 4.7b** and **Table 4.1**). Details and equations concerning the calculations are given in the Experimental Section (**Equations 4.1** to **4.5**). The large Förster distance for the initial Tb-QD FRET pair (R_0 = 9.7±0.7 nm) was caused by the very strong absorption of the QD across the almost entire PL emission range of the Tb donor. However, also the other FRET pairs showed significantly large Förster distances of 5.7±0.4 nm (Tb-Cy5.5), 6.0±0.4 nm (QD-Cy5.5), and 6.2±0.4 nm (Cy5.5-Cy5.5). Even QD-QD (R_0 = 7.4±0.5 nm) and Cy5.5-QD (R_0 = 1.9±0.1 nm) could function as FRET pairs. However, QDs were not in close enough distance to each other to engage in FRET and the Cy5.5-QD Förster distance was too short for efficient FRET. It is important that the initial FRET step from Tb to QD is much more efficient than FRET from Tb to Cy5.5 (~24-fold higher FRET rate when considering equal distances between Tb and QD and Tb

and Cy5.5 – **Equation 4.6**, Experimental Section) to avoid significant energy transfer from Tb to Cy5.5 even at high loading ratios. Another FRET pathway to take into account is homo-FRET between Cy5.5 dyes at high loading ratios. Both Tb-to-Cy5.5 and Cy5.5-to-Cy5.5 FRET were taken into consideration for the Monte-Carlo simulations. Other important PL properties of the FRET nano-hybrids were the molar absorptivities or extinction coefficients (ε), PL quantum yields (Φ), PL lifetimes (τ), and band pass wavelength ranges of the filters used for detecting Tb, QD, and Cy5.5 PL (**Table 4.1** and **Supporting Figure 4.8 and 4.9**).

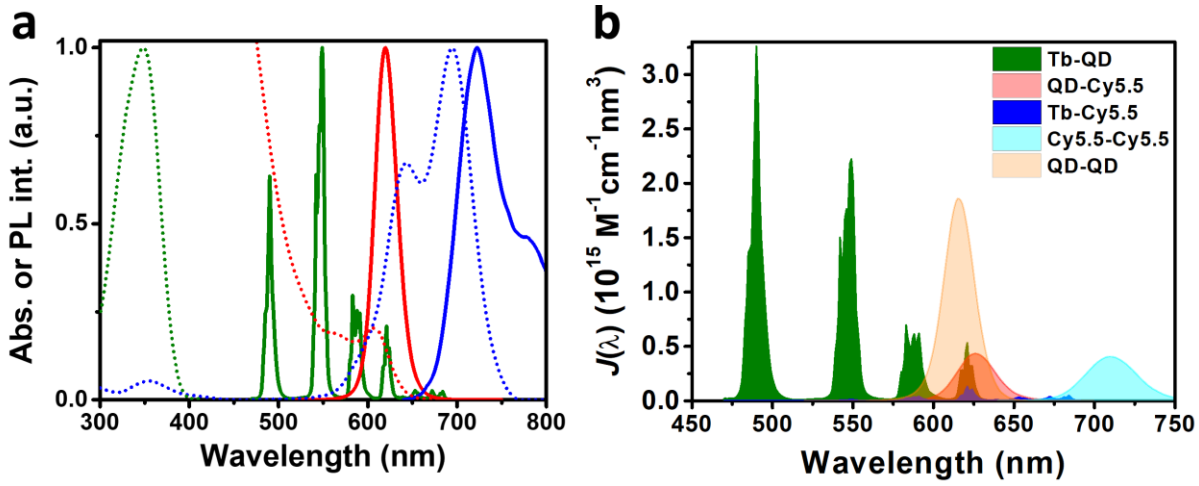

Figure 4.7. **(a)** Absorption (dashed lines) and PL (solid lines) spectra of Tb (green), QD (red), and Cy5.5 (blue). **(b)** Spectral overlap functions for the Tb–QD, QD–Cy5.5, Tb-Cy5.5, Cy5.5-Cy5.5, QD-QD, and Cy5.5-QD FRET pairs.

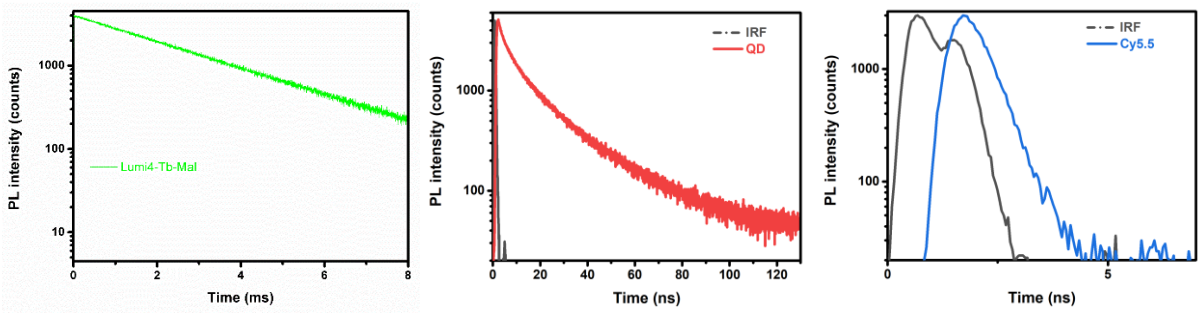

Figure 4.8. PL decay curves of Tb (left, $\langle\tau\rangle$ ~ 2.7 ms, λ_{ex} = 337.1 nm, λ_{em} = 494±12 nm), QD (center, $\langle\tau\rangle$ ~ 8 ns, λ_{ex} = 480 nm, λ_{em} = 639±10 nm) and Cy5.5 (right, $\langle\tau\rangle$ ~ 1 ns, λ_{ex} = 660 nm, λ_{em} = 708±8 nm). IRF: Instrument response function.

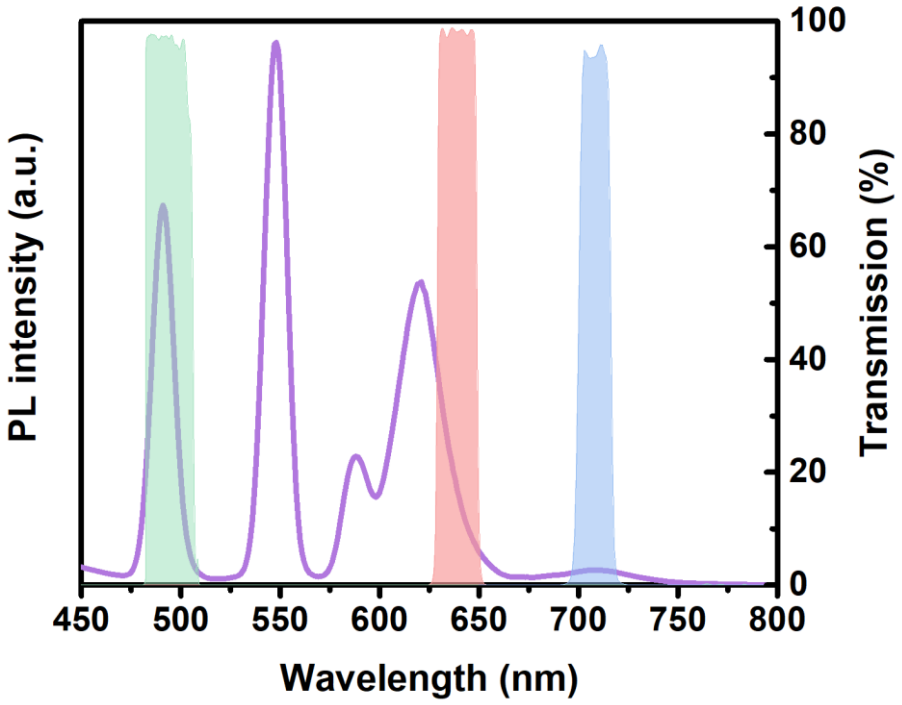

Figure 4.9. Spectra of band pass filters for Tb (green), QD (red), and Cy5.5 (blue) and a representative Tb-QD-Cy5.5 PL emission spectrum (purple).

4.3.3 FRET system 1: *m*Tb-QD

The unique feature of this FRET system was the ability to first conjugate the antenna ligands to the QD and then add Tb^{3+} ions in different amounts, thereby investigating a very large range of Tb donor per QD acceptor ratios (*m*). To estimate a maximum loading ratio of Lumi4 ligands per QD, we prepared three batches with 70:1, 200:1, and 800:1 molar ratios of ligand per QD, which resulted in 50±5, 136±14, and 191±19 Lumi4 per QD (**Figure 4.4**), respectively. Owing to the strong decrease of labeling efficiencies of 71 % and 68 % for the first two batches to 24 % for the third batch, we did not further increase the initial molar ratio and used these three batches (with 191 Lumi4 per QD as maximum labeling ratio) for the *m*Tb-QD FRET investigations. PL titration experiments (**Figure 4.4b to d**) of the Lumi4 coated QDs with Tb^{3+} ions revealed that the lowest labeling ratio (50 Lumi4 per QD) resulted in complete saturation of the PL upon saturation of the ligands with Tb ions, whereas the samples with 136 and 191 Lumi4 per QD showed a continuous (linear) increase of PL intensities even after saturation. This phenomenon was stronger for the samples with 191 Lumi4 per QD and was

attributed to a more difficult complete saturation of the Lumi4 ligands, which were attached at high density to the QDs.

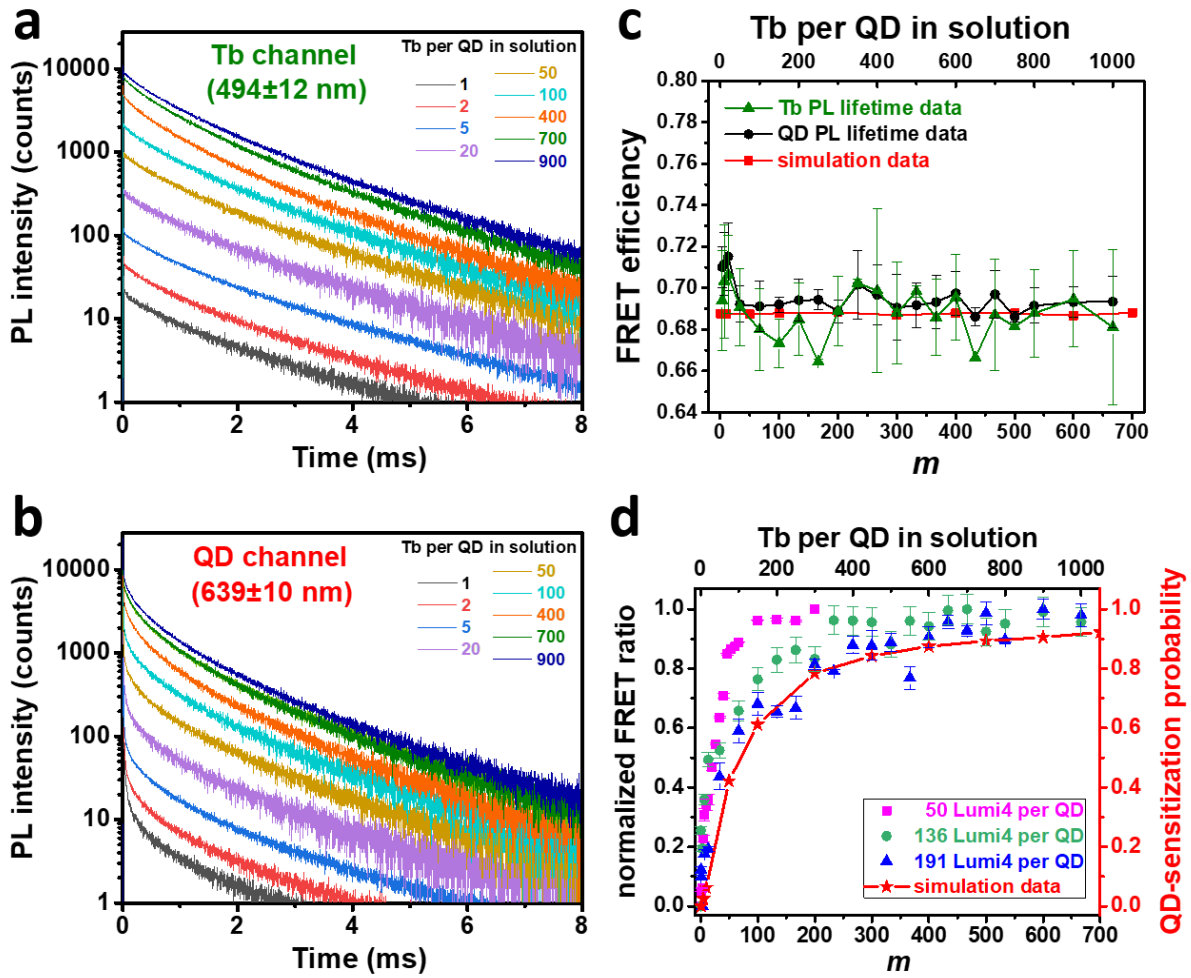

Figure 4.10. FRET system 1 (*m*Tb-QD): Selected PL decay curves (*cf.* **Appendix Figure 7.2** for all curves) of Tb FRET donor **(a)** and QD FRET acceptor **(b)** at different Tb per QD ratios (only the curves for 191 Lumi4 ligands per QD are shown). **(c)** FRET efficiency as function of *m* for experimental (determined by PL decay times from experiments with 136 and 191 Lumi4 ligands per QD – **Appendix Tables 7.1 and 7.2**) and simulation (MCS) results. **(d)** TG (0.1–0.9 ms) intensity ratios (normalized FRET ratio: $y_m(\text{norm}) = [y_m - y(\text{min})] / [y(\text{max}) - y(\text{min})]$) as function of *m* for experimental (with 50, 136, and 191 Lumi4 ligands per QD) and simulation (MCS) results. Note: *m* corresponds to "Tb per QD in solution" divided by 1.5, which is the necessary ratio of Tb^{3+} ions per Lumi4 ligand to accomplish ~100% Tb^{3+}-to-ligand coordination (*cf.* **Figure 4.5**).

Time-resolved PL spectroscopy was used to analyze the FRET-quenched Tb donor (**Figure 4.10a**) and FRET-sensitized QD acceptor (**Figure 4.10b**) emission with increasing *m*. The addition of Tb^{3+} to Lumi4 ligand coated QD led to Tb per QD ratios between 1 to 1000 (Tb per QD in solution), which corresponded to $m = 1$ to 670 when taking into account the ~1.5 Tb^{3+} per Lumi4 ligand (corresponding to 0.67 to 667 Tb per QD) necessary to accomplish ~100% of Tb^{3+} coordination (*cf.*

Figure 4.5). Although *m* ranged from 1 to 670, the PL saturated at approximately 1.5 times the number of ligands (**Figures 4.4b** to **d**), which means that the actual maximum amount of luminescent Tb (Tb^{3+} coordinated to the Lumi4 ligand) on the QD was limited by the number of ligands. Addition of Tb^{3+} beyond ligand saturation did not lead to a further increase of the PL intensity (or only small continuous increase due to a more difficult ligand saturation for the two systems with 136 and 191 ligands – *vide supra*). Because the concentrations of Tb increased and the concentration of QDs was constant, both PL intensities of Tb and QD increased with increasing *m*. PL decay time analysis (**Appendix Table 7.1 and 7.2**) revealed a constant FRET efficiency of E_{FRET} = 0.69±0.03 for all *m*, which was in almost perfect agreement with the MCS results (**Figure 4.10c**), and an average Tb-QD distance (**Equation 4.8**) of 8.5±0.6 nm. The independence of E_{FRET} from the number of donors is in agreement with previously proposed theoretical approaches.[4],[6],[7]

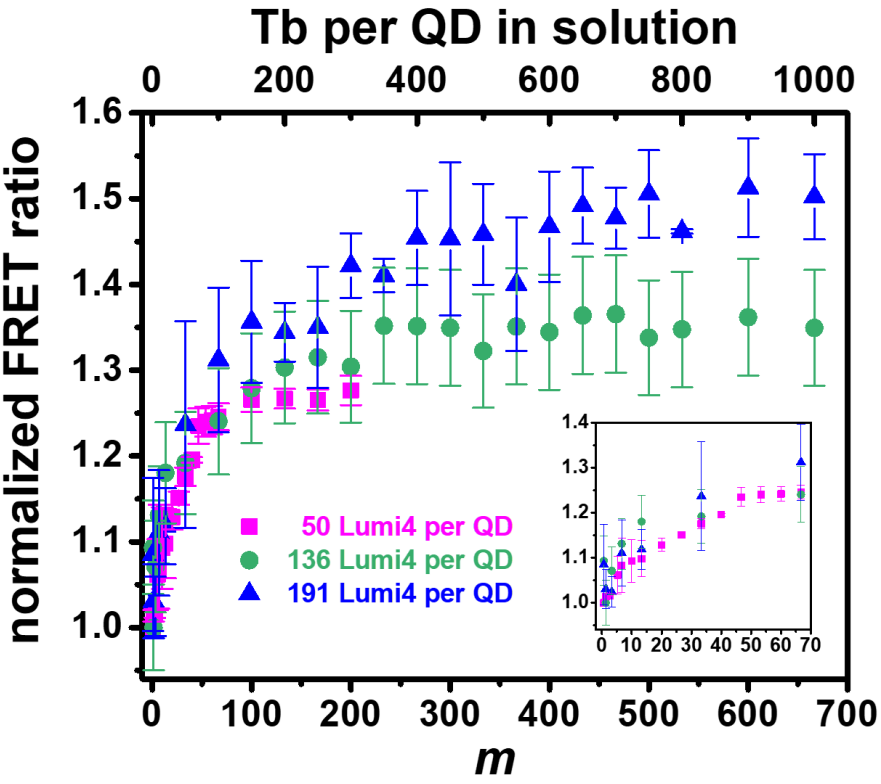

Figure 4.11. FRET system 1 (mTb-QD): Time-gated (0.1–0.9 ms) intensity ratios ((normalized FRET ratio: $y_m(\text{norm}) = y_m / y(\text{min})$) as function of *m* (with 50, 136, and 191 Lumi4 ligands per QD). Inset shows the region of m<70. Note: *m* corresponds to "Tb per QD in solution" divided by 1.5, which is the necessary ratio of Tb^{3+} ions per Lumi4 ligand to accomplish ~100% Tb^{3+}-to-ligand coordination (*cf.* **Figure 4.5**).

A probably even more interesting aspect in these multiple-donor/single-acceptor systems is the amount of FRET-sensitized acceptor PL because this purely FRET-dependent signal (whereas donor quenching can have other causes than FRET) is extremely useful for quantitative sensing. Taking into account the almost 10^6-fold difference in Tb and QD PL lifetimes (**Table 4.1**), it should be possible that one central QD accepts energy sequentially from many Tb donors because the de-excitation of the QD after each FRET-sensitization by another Tb would be almost instantaneous (compared to the long excited states of Tb). If, in addition, all Tb on the QD are assumed to be excited (*i.e.*, all Tb on the QD surface can be excited by the same light pulse), the probability of QD sensitization (using $E_{FRET} = 0.69$) would be $P > 0.99$ after only $m = 4$ (**Equation 4.9**, Experimental Section). This, in turn, would mean that the ratio of QD and Tb PL intensities (FRET-sensitized QD PL normalized per m) should show a steep increase for $m \leqslant 4$ (increase of P from 0.8 to 0.99) and a less steep and linear increase for $m > 4$ (constant P of ~100 % and constant E_{FRET} of ~69 %). In contrast to these purely theoretical assumptions, MCS can take into account the geometrical conditions (the number of Tb, the QD surface, the necessary excitation volume to excite all Tb on the QD surface), the sample excitation conditions (density of excitation energy), the extinction coefficient of the Tb donors, the FRET efficiency, and the quantum yield of the QD acceptors, all of which play an important role for FRET-sensitized acceptor emission. The MCS data (red curve in **Figure 4.10d**) predicted a much shallower increase of the probability of FRET-sensitized QD PL as a function of m, which levels off between $m \sim 100$ to 300 (probability between ~60 % and 85 %) and saturates after $m \sim 600$ (probability > 90 %). Our experimental data (**Figure 4.10d**) followed extremely well these MCS predictions. For comparison with the probability from MCS, the FRET-ratios were normalized between 0 (for the lowest FRET-ratio) and 1 (for the highest FRET-ratio). This normalization approach allowed us verify experimentally if the simulated onset of FRET saturation would really occur between $m \sim 100$ to 300 (as predicted by MCS). The samples with 50 Lumi4 per QD (magenta data points in **Figure 4.10d**) cannot reach such high values of m and thus, the highest intensity of FRET-sensitized QD PL occurred already at $m \sim 100$ with the onset of FRET saturation at $m \sim 50$, as expected from

the limited number of ligands. The FRET ratios of the 136 Lumi4 per QD samples (green data points in **Figure 4.10d**) already approach the MCS data but still saturation occurs at lower *m*. For the highest possible ligand coating of 191 Lumi4 per QD (blue data points in **Figure 4.10d**) the experimental data overlaps very well with the MCS data, which confirmed the predicted onset of FRET saturation. Normalizing the FRET-ratio to the lowest FRET-ratio (lowest *m*) also confirmed that the initial relative FRET-sensitization (below Tb saturation for all samples) was similar for all Lumi4 per QD ratios (**Figure 4.11**). The agreement of MCS simulation and experimental results underlines the importance of taking into account the excitation energy and the coverage of Tb on the QD surface and that the simple theoretical model is not sufficient to correctly describe the FRET-sensitized acceptor PL.

4.3.4 FRET system 2: QD-*n*Cy5.5.

To investigate the single-donor/multiple-acceptors FRET system, up to 60 Cy5.5 were conjugated to the SiO_2 shell of the QD (*vide supra*). Both steady-state (PL spectra) and time-resolved (PL decays) spectroscopy of QD and Cy5.5 were used to analyze FRET. QD donor PL lifetimes (**Figure 4.12a** and **Appendix Table 7.3**), Cy5.5 acceptor PL lifetimes (**Figure 4.12b**), and QD PL intensities (**Figure 4.12c** and **Appendix Table 7.4**) clearly decreased with increasing *n* due to FRET quenching. The corresponding FRET efficiencies (**Equations 4.10** and **4.11**, Experimental Section) showed a steep increase from 1 to 10 Cy5.5 per QD followed by a saturation for larger *n* (**Figure 4.12e**). This experimental data was in excellent agreement with theoretical calculation (**Equation 4.12**) and MCS (**Figure 4.12e**) and led to an average donor-acceptor distance of $R = 7.9 \pm 0.6$ nm (**Appendix Table 7.5**), which was in good agreement with the average donor-acceptor distance found for FRET system 1 ($R = 8.5 \pm 0.6$ nm), as expected due to the similar attachment of Tb and Cy5.5 to the SiO_2 shell of the QD. The somewhat longer distance for system 1 could be caused by the slightly larger structure of the Lumi4 complex compared to the Cy5.5 dye (*cf.* **Figure 4.3**). When taking into account that the optically active CdSe core of the QD (approximated as a sphere) has a radius of 1.8 nm, the total CdSe/CdS/ZnS has a radius of 3.5 nm, and the

SiO_2 shell has a thickness of 7±2 nm, the Tb donors and Cy5.5 acceptors should be positioned on the surface of a sphere with a radius of 9.4±1.5 nm and 8.8±1.5 nm, respectively (**Figure 4.13**). These distance estimations lead to the deduction that a significant fraction of Tb and Cy5.5 must be positioned inside the SiO_2 shell. This conclusion is not unrealistic because both the porosity of the outer SiO_2 layers and the non-spherical shape on the entire QD can lead to closer and further distances than estimated by the ideal spherical model.

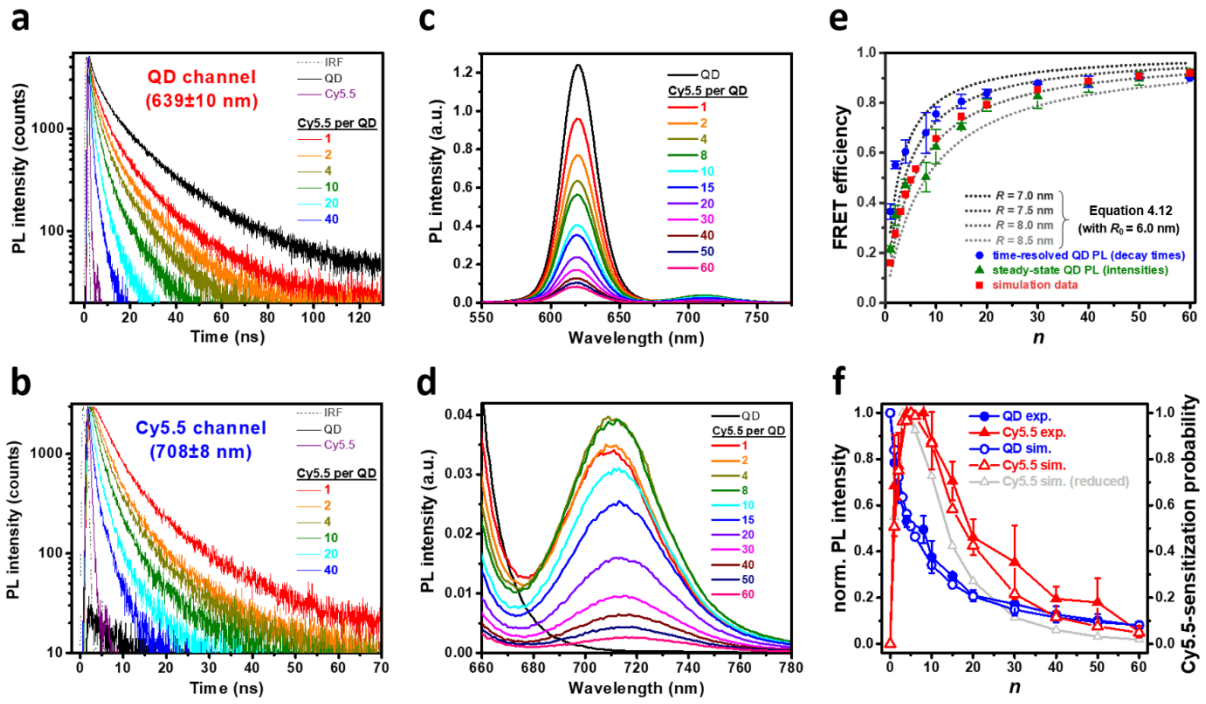

Figure 4.12. FRET system 2 (QD-*n*Cy5.5): Selected PL decay curves (*cf.* **Appendix Figure 7.3** for all curves) of **(a)** QD FRET donor and **(b)** Cy5.5 FRET acceptor. Steady-state FRET-quenching of **(c)** QD donor PL and (d) FRET-sensitization of Cy5.5 PL (enlargement of Cy5.5 contribution from the spectra in **(c)**). **(e)** FRET efficiencies as a function of n calculated theoretically (gray dotted curves), from QD PL decays (**(a)** and **Appendix Table 7.3**), from QD PL intensities (**(c)** and **Appendix Table 7.4**), and MCS. **(f)** FRET-quenched QD PL intensity (blue) and FRET-sensitized Cy5.5 PL intensity (red) as a function of n for experimental (full symbols) and MCS data (hollow symbols). The gray curve presents a reduced MCS model that did not take into account the decreasing spectral overlap with increasing n.

Similar to FRET system 1, it is interesting and important to analyze and understand the FRET-sensitized PL of the Cy5.5 acceptor. In most studies concerning FRET from a QD donor to many dye acceptors on its surface, the QD PL quenching is very strong and follows the theoretical prediction, whereas the sensitized dye PL is quite weak and does not correspond to the QD donor quenching. In our study (**Figures 4.12c** and **d**, which is a zoom into the Cy5.5 PL

band from **Figure 4.12c**), we found the same behavior of strong QD PL quenching and weak sensitized Cy5.5 PL. In agreement with the increasing FRET efficiencies (**Figure 4.12e**), the QD PL intensities decreased with increasing n, which was also found for the MCS results (blue curves in **Figure 4.12f**). The Cy5.5 PL intensities showed a strong initial increase from $n = 0$ to ~ 4, remained constant until $n \sim 8$, and then decreased steadily up to $n = 60$ (**Figure 4.12f**). The reasons for the strong PL intensity decrease with increasing n (for $n > 8$) can be dye aggregation or homo-FRET between the dyes. The formation of non-fluorescent dye dimers (H-dimers) on macromolecules,[211] proteins,[109] or QDs[56] was already related to self-quenching of dyes. Similar to these studies, the Cy5.5 absorption spectra showed an increase of the hypsochromic shoulder with increasing n (**Figure 4.14**), which is characteristic of H-dimers.[99] On the other hand, the increase was rather weak, which means that only a small fraction of dyes formed non-fluorescent dimers. This finding is reasonable because the dyes were directly attached to the SiO_2 coating of the QDs without further linkers or biomolecules (*e.g.*, peptides or DNA), which should limit dye-dye dimerization and favor monomeric dyes. Therefore, a large fraction of the strong PL intensity decrease of ~95 % from $n = 8$ to $n = 60$ must have been caused by homo-FRET. Homo-FRET does not lead to changes in PL lifetime or intensity and such non-directional energy migration between identical dyes can only be detected by fluorescence anisotropy.[106]–[108] On the other hand, the migration of an exciton in a random manner over many dye-to-dye homo-FRET steps increases the probability (compared to a stationary exciton) of encountering a dark or trap state (*e.g.*, a non-fluorescent H-dimer), which leads to fluorescence quenching. In multi-dye systems (densely packed or aggregated dyes) both PL intensity and lifetime quenching were found.[1],[56],[109]–[112] Our MCS approach, which simulated exciton per exciton, included the possibility of Cy5.5-to-Cy5.5 homo-FRET and an increasing probability of energy dissipation (or trap state encounter) with an increasing amount of Cy5.5-to-Cy5.5 FRET events. The MCS model accounted for two additional properties of our FRET system. First, the Cy5.5 distance from the QD center was 8.5±1.5 nm whereas the average QD-Cy5.5 donor-acceptor distance was 7.9±0.6 nm (*vide supra*). Thus, the actual Cy5.5-to-Cy5.5 distance was larger than on the simulated 7.9 nm sphere, which was taken

into account by reducing the Cy5.5-Cy5.5 Förster distance from R_0 = 6.2 nm to R_0 = 5.8 nm in the MCS model. Second, the blue shift (hypsochromic shoulder increases and bathochromic peak decreases) of the Cy5.5 absorption and red shift of the Cy5.5 emission (**Figure 4.12d**) with increasing n resulted in a decreasing spectral overlap with increasing n. In the model, each energy transfer event involves some degree of energy loss making future transfer more difficult due to worsening the spectral overlap. The MCS kept track of how many times a packet of energy had undergone homo-FRET and reduced the transfer probability for future homo-FRET by 50 %. Although reduced overlap effect has little influence for small number of n, it is more significant for larger n (gray compared to red simulation curves in **Figure 4.12f**), for which the chance of multiple homo-FRET events is greater. The MCS results were in excellent agreement with the experimental data (red curves in **Figure 4.12f**). Förster distance, sphere radius, and probability of trap state encounter per homo-FRET step could be easily changed in the MCS input parameters and allowed to evaluate the influence of these properties on the probability of FRET-sensitized Cy5.5 emission (**Figure 4.15**). The comparison of experimental and simulation data for up to 60 dyes per QD explained very well the quenching of FRET-sensitized acceptor PL at high loading ratios by a combination of homo-FRET and non-radiative deactivation by non-fluorescent h-dimers and is an important result for a better understanding of such multiple-acceptor FRET systems.

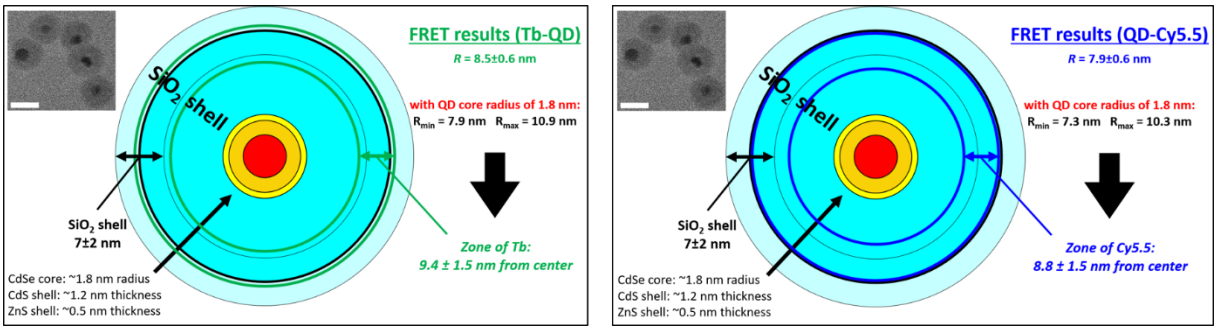

Figure 4.13. Estimation of Tb donor and/or Cy5.5 acceptor positions on the SiO_2-coated CdSe/CdS/ZnS QD when approximated as an ideal spherical model and taking into account the results from Tb-to-QD and QD-to-Cy5.5 FRET.

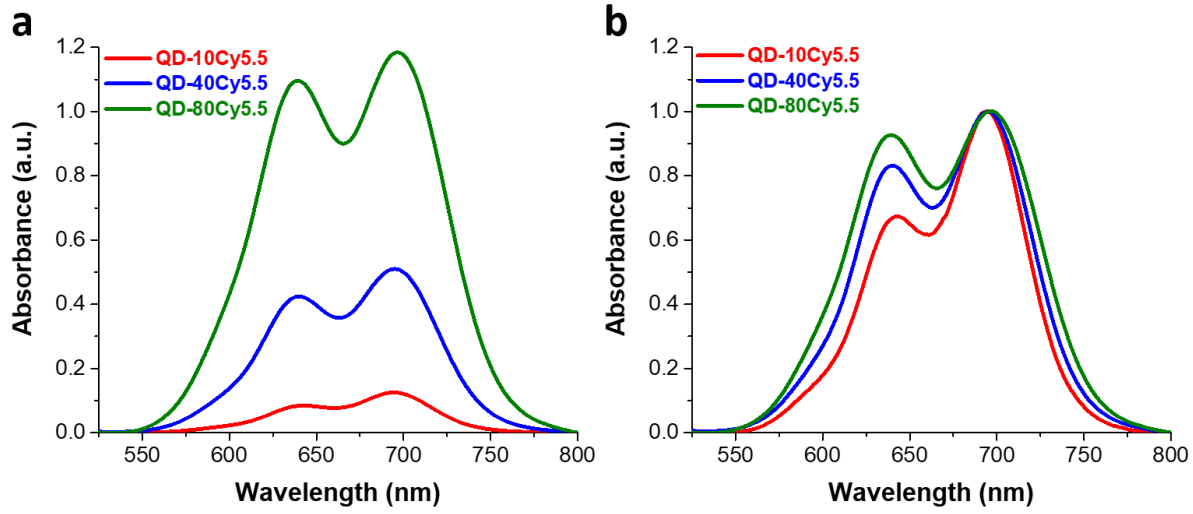

Figure 4.14. Absorption spectra (relative intensities in **(a)** and intensity-normalized to the red peak in **(b)**) of Cy5.5 for 10, 40, and 80 Cy5.5 per QD.

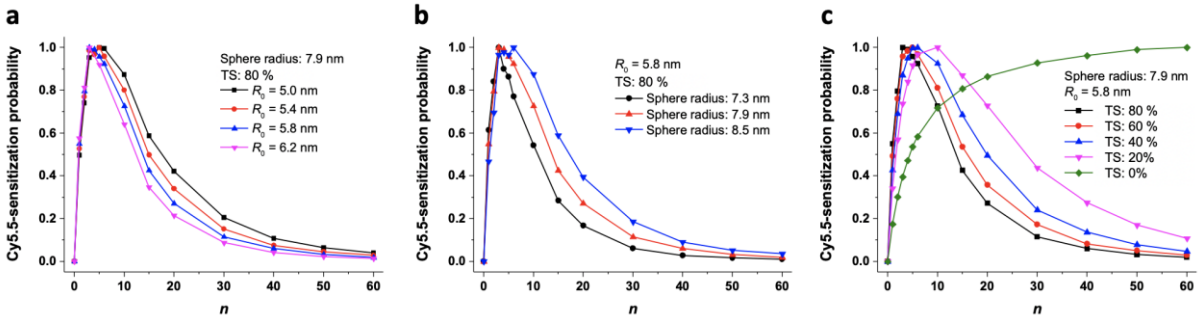

Figure 4.15. FRET system 2 (QD-*n*Cy5.5): MCS results showing the probability of FRET-sensitized Cy5.5 PL as a function of *n* for **(a)** changing R_0 (Cy5.5-Cy5.5 Förster distance), **(b)** changing sphere radius (sphere on which surface the Cy5.5 dyes are situated), and **(c)** changing probability of trap state encounter (TS). Only a 0% probability of trap state encounter allows for a constant increase in Cy5.5 sensitization with increasing *n*.

4.3.5 FRET system 3: *mTb*-QD-15Cy5.5

The full versatility of a QD-based FRET system can be exploited when both Tb donors and dye acceptors are conjugated to the same QD. In this case, predictions of how the different FRET pathways (Tb-to-QD, QD-to-dye, Tb-to-dye, dye-to-dye) interact and how varying amounts of Tb donors and dye acceptors can be used to tune the PL properties (PL lifetimes and intensities at different emission wavelengths) are even more difficult than for the systems with only one FRET pair (systems 1 and 2). As a first possibility of a central QD with multiple donors and acceptors on its surface, we investigated a system with a variable amount of *m* Tb donors and constant amount (15) of Cy5.5 acceptors. Experimentally, this FRET

system 3 was realized by co-labeling 52±7 Lumi4 ligands and 15±2 Cy5.5 on the SiO_2 coating of the QDs. Similar to FRET system 1, the varying amount of Tb (*m*) was accomplished by adding increasing amounts of Tb^{3+} ions to the Lumi4-QD-15Cy5.5 conjugates (Tb per QD-15Cy5.5 in solution) and taking into account a 1.5 Tb/Lumi4 saturation to calculate *m*.

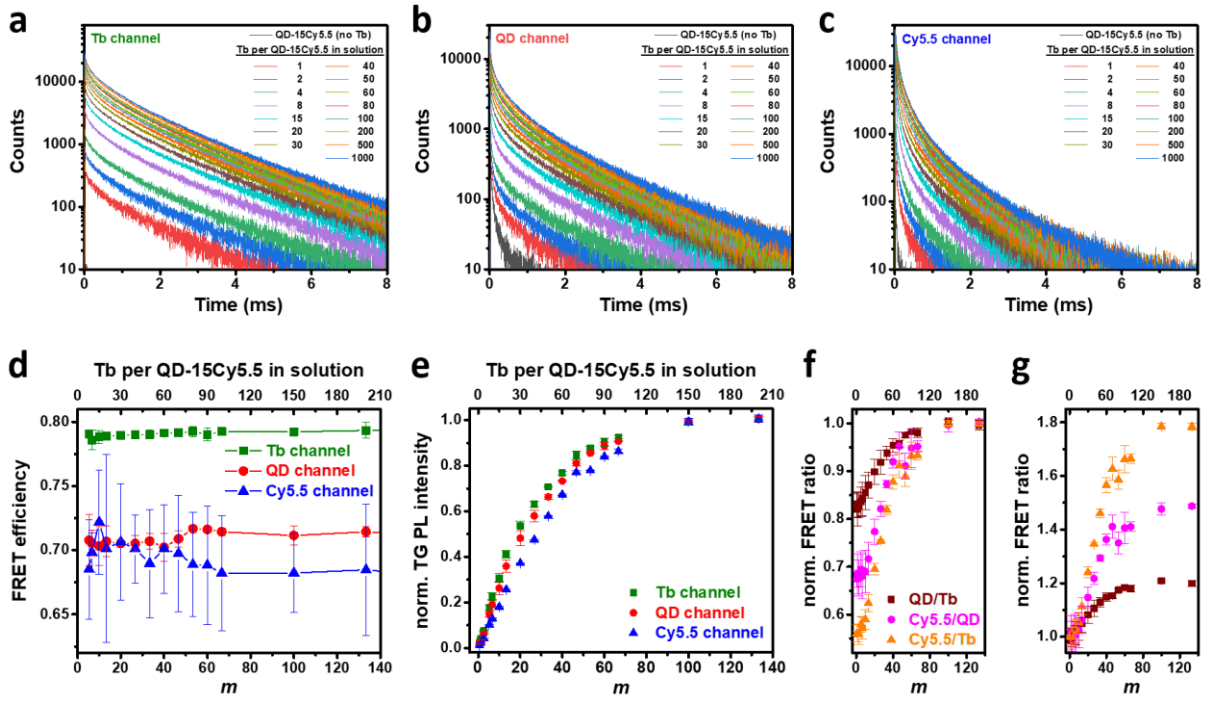

Figure 4.16. FRET system 3 (*m*Tb-QD-15Cy5.5): Selected PL decay curves (*cf.* **Appendix Tables 7.6** to **7.8** for complete data) of Tb FRET donor **(a)**, QD FRET acceptor/donor **(b)**, and Cy5.5 FRET acceptor **(c)** at different Tb per QD-15Cy5.5 ratios. **(d)** FRET efficiencies as function of *m* determined by PL decay times of the Tb initial donor (green), the QD acceptor/donor (red), and the Cy5.5 final acceptor (blue). **(e)** TG (0.1–0.9 ms) intensities (normalized intensity: $y_m(\text{norm}) = [y_m - y(\text{min})] / [y(\text{max}) - y(\text{min})]$) as function of *m* for Tb, QD, and Cy5.5. FRET ratios of TG PL intensities of QD and Tb (brown), Cy5.5 and QD (magenta), and Cy5.5 and Tb (orange) as a function of *m* and normalized to unity for the maximum FRET ratio **(f)** or at the smallest value of *m* **(g)**.

One interesting feature of this FRET system is the possibility to study it from three independent perspectives, namely the Tb, QD, and Cy5.5 PL. When comparing the PL decays for these three detection channels for varying amounts of Tb (**Figures 4.16a** to **c**), it becomes clear that the long PL lifetime of FRET-quenched Tb can be used to FRET-sensitize Cy5.5 via the central QD. The PL decay becomes faster for each step (from Tb to QD to Cy5.5), which shows that the first FRET-sensitization (from Tb-to-QD) is reutilized for a second FRET sensitization (from QD-to-Cy5.5). The average PL decay times of Tb, QD, and Cy5.5 (**Appendix Tables 7.6** to **7.8**) were used to calculate the FRET efficiencies of the subsequent FRET steps

(**Figure 4.16d**). Tb PL led to a constant value of E_{FRET} = 0.79±0.01 for all m, which is *circa* 10% higher than for system 1 (*cf.* **Figure 4.10c**). This increased FRET efficiency can be explained by the additional quenching of Tb by Cy5.5 (R_0 = 5.7±0.4 nm, *cf.* **Table 4.1**) when they are both attached to the same QD. The FRET efficiency in the QD channel was also constant with E_{FRET} = 0.71±0.02, which was only 2% higher than for system 1. In this case, the average FRET-sensitized lifetime could be corrected by the FRET-rates of the two contributing FRET lifetimes (**Equations 4.14a** and **b**), which suppressed the additional quenching effect by FRET from QD-to-Cy5.5. Indeed, if only the apparent FRET-quenched lifetimes were taken into account (without k_{FRET} correction), the FRET efficiency would be around 81% (**Figure 4.17**), as expected from the additional QD-to-dye FRET pathway. Analyzing the Cy5.5 time-resolved PL led to a constant FRET efficiency of E_{FRET} = 0.70±0.07 for all m, which was in good agreement with FRET system 2 (E_{FRET}~0.7 for n = 15, *cf.* **Figure 4.12e**). The different FRET efficiencies found for this mTb-QD-15Cy5.5 FRET system confirmed the findings of FRET systems 1 and 2 and that their FRET properties can be combined into one multi-donor-acceptor QD-FRET approach.

Similar to FRET systems 1 and 2, an interesting aspect from the application point of view is the investigation of FRET-sensitized PL intensities and FRET intensity ratios. In addition to the distinct PL decays for Tb, QD, and Cy5.5 (**Figures 4.16a** to **c**) upon single-wavelength excitation of the initial Tb donor, tunable TG PL intensities of Tb, QD, and Cy5.5 by a varying amount of Tb (m) would present an interesting lever to adapt such multi-hybrid FRET NPs for brightness-equalized spectrotemporal barcoding. **Figure 4.16e** shows that the TG PL intensity of FRET-quenched Tb (as a function of m) was transferred to both FRET-sensitized QD and FRET-sensitized Cy5.5 and could be tuned in the entire range of 1 to 52 Tb (52±7 Lumi4 ligands per QD). The FRET-ratios (sensitized TG PL intensities of QD and Cy5.5 divided by the donor intensities for each m) normalized to the maximum or minimum values (**Figure 4.16f** and **g**) showed the strongest relative FRET sensitization from end-to-end (Cy5.5/Tb ratio) followed by the second (Cy5.5/QD ratio) and the first (QD/Tb ratio) FRET steps, which provides another possibility for adapting and/or optimizing sensitivities or limits of detection for multiplexed

biosensing applications. Although the experimental results of FRET system 3 make sense when taking into account the findings for system 1 and 2, it would have been interesting to use MCS for comparison. Unfortunately, our current MCS model cannot properly account for long lifetime donors because it (and other MCS codes) tests for available acceptors at the time of excitation rather than at the time of de-excitation. This is due to the fact that the time of de-excitation is itself dependent of the number of locations of available acceptors. The simplification is valid for short lifetime donors and can be accounted for in system 1 by appropriately choosing the laser irradiance, but does not lead to reasonable results in this situation, in which the number of donors varies and dye acceptors are co-assembled. One of our future objectives will be the adaption of the MCS model to the complicated properties of this long lifetime multi-donor-acceptor QD FRET system.

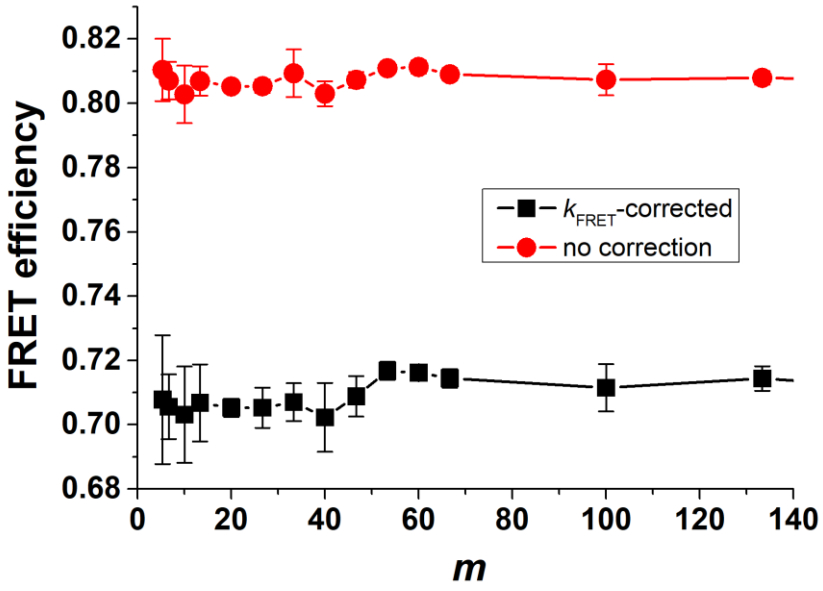

Figure 4.17. FRET system 3 (*m*Tb-QD-15Cy5.5): FRET efficiencies calculated with apparent average PL decay time (without correction of amplitudes by k_{FRET} - red) and FRET average PL decay time (correction of amplitudes by k_{FRET} - black) of FRET-sensitized QD acceptor PL (*cf.* **Appendix Table 7.7**).

4.3.6 FRET system 4: 75*Tb*-QD-*n*Cy5.5

Instead of changing the number of initial Tb donors, another possibility of tuning the Tb-to-QD-to-dye FRET system is to change the number of final dye acceptors while leaving the number of Tb donors constant. Experimentally, this FRET

system 4 was realized by pre-labeling 75±9 Lumi4 ligands on the SiO_2 coating of the QDs and saturating them with Tb^{3+} ions to accomplish a constant amount of 75±9 Tb per QD. These 75Tb-QD conjugates were then labeled with increasing amounts (n = 1 to 60) of Cy5.5 dyes. Similar to system 3, we could investigate FRET from three different emitters (Tb, QD, and Cy5.5).

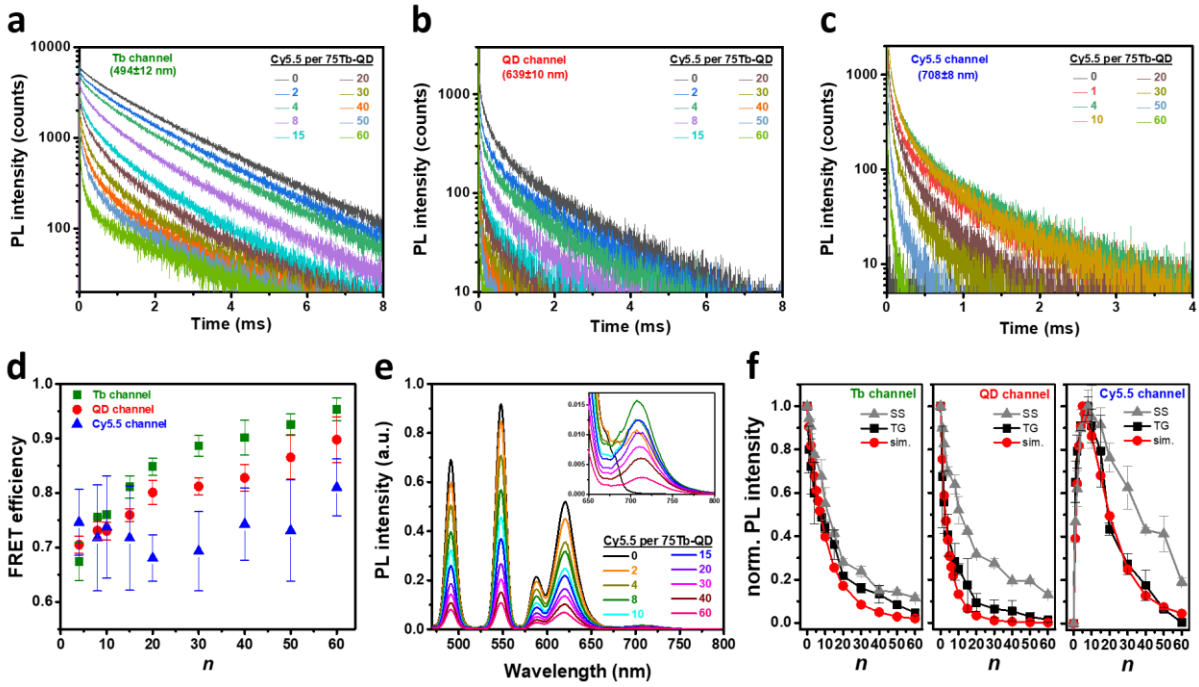

Figure 4.18. FRET system 4 (75Tb-QD-*n*Cy5.5): Selected PL decay curves (*cf.* **Appendix Tables 7.9** to **7.11** for complete data) of **(a)** Tb FRET donor (time scale 0 to 8 ms), **(b)** QD FRET acceptor/donor (time scale 0 to 8 ms) and **(c)** Cy5.5 FRET acceptor (time scale 0 to 4 ms) at different Cy5.5 per 75Tb-QD ratios. **(d)** FRET efficiencies as function of n determined by PL decay times of the Tb initial donor (green), the QD acceptor/donor (red), and the Cy5.5 final acceptor (blue). **(e)** Steady-state PL spectra (inset is a zoom into the Cy5.5 PL) of the different 75Tb-QD-*n*Cy5.5 assemblies. **(f)** Normalized (to unity at the highest value) PL intensities of Tb, QD, and Cy5.5 (from left to right) as a function of n (TG: 0.1–0.9 ms using the PL decay curves in **(a)** to **(c)**; SS: steady-state using the PL spectra from e; sim: MCS data).

In contrast to system 3, for which m (amount of Tb) was varied and thus the FRET efficiency did not change, the increase of n (amount of Cy5.5) led to an increasing FRET efficiency, as expected from system 2. This behavior can readily be witnessed in the PL decay curves of all three detection channels, which change significantly in lifetime and intensity (**Figures 4.18a to c**). When considering all four possible FRET pathways (Tb-QD, Tb-Cy5.5, QD-Cy5.5, and Cy5.5-Cy5.5) independently, the MCS results show a constant FRET efficiency for Tb-QD (as expected from system 1) and increasing FRET efficiencies for the other three pathways (as

expected from system 2) with increasing *n* (**Figure 4.19**). In the experiments, all FRET pathways influenced the PL decays of the different emitters and thus, the FRET efficiencies (as calculated by PL decay time analysis – **Appendix Tables 7.9** to **7.11**) became convolutions of those FRET pathways. Because Tb was only FRET-quenched (initial donor), increasing FRET efficiencies with increasing *n* became most obvious (green data points in **Figure 4.18d**) and were caused by a constant FRET efficiency for Tb-QD and an increasing FRET efficiency for Tb-Cy5.5 FRET. For QD PL (acceptor to Tb and donor to Cy5.5), the FRET efficiencies also increased but less steep compared to Tb-QD (red data points in **Figure 4.18d**), which was in agreement with the MCS results that showed a steeper increase for Tb-Cy5.5 compared to QD-Cy5.5 (**Figure 4.19**). The Cy5.5 is the most complicated case because Cy5.5 is an acceptor for Tb and QD and a donor to other Cy5.5 acceptors (homo-FRET), the latter leading to significant PL quenching at high numbers of *n* (*cf.* system 2). MCS results (**Figure 4.19**) suggested a convolution of increasing FRET efficiencies for all three pathways. Taking into account that two are energy inputs (Tb-Cy5.5 and QD-Cy5.5) and one is an energy output and input (Cy5.5-Cy5.5), predictions of the overall FRET efficiency are difficult. The experimental results (blue data points in **Figure 4.18d**) did not show a clear trend but rather a more or less constant FRET efficiency around 0.73±0.10 caused by the convolution of the ingoing and outgoing FRET efficiencies for Cy5.5. Although a precise interpretation of the FRET efficiencies as in system 3 was not possible for system 4, the results still confirmed the findings and expectations from FRET systems 1 and 2 and from the MCS for each distinct FRET pathway. Moreover, the modification of *n* clearly resulted in a significant and tunable change of the PL decays in the different detection channels, which is very advantageous for temporal barcoding (*vide infra*).

Another interesting aspect of this FRET system 4 was the possibility of analyzing the influences of the different FRET pathways on the PL intensities, which should decrease for Tb and QD and increase and then decrease for Cy5.5 (homo-FRET) with increasing *n*, when taking into account the previous results of system 1 and 2. Experimentally, we analyzed TG PL intensities (0.1–0.9 ms) from the PL decay curves (**Figures 4.18a** to **c**) and steady-state (SS) PL intensities (**Figure 4.18e**)

for Tb, QD, and Cy5.5 as a function of *n* and compared the results to MCS (**Figure 4.18f**). As expected, both TG and SS experimental and MCS results showed decreasing PL intensities for Tb and QD and an initially strongly increasing followed by a decreasing PL intensity for Cy5.5. While the Tb donor MCS data could be well reproduced by both TG and SS PL intensity data, the more complicated PL cases of QD and Cy5.5, who acted as both acceptors and donors, clearly showed that TG PL was much better suited to analyze the development of PL intensities as a function of *n*. The reason for the better fit of TG and MCS data for the QD and Cy5.5 channels is most probably related to the selective energy pathway for TG detection. In steady state, both Tb and QD excitation lead to PL because short PL lifetimes (from direct QD excitation) and long PL lifetimes (from Tb excitation and FRET to QD and Cy5.5) cannot be distinguished. In TG detection, only the long-lifetime PL components are taken into account and thus the short-lifetime QD-to-Cy5.5 FRET is not detected. To show that the decreasing PL intensities for high values of *n* in the Cy5.5 channel (**Figure 4.18f right**) were really caused by energy loss due to non-radiative decay after each Cy5.5-to-Cy5.5 step (*cf.* system 2), we recorded the PL intensities of Cy5.5 as a function of *n* for different excitation wavelengths, such that Tb, QD, or Cy5.5 were selectively excited, and compared the results to MCS (**Figure 4.20**). The same PL intensity quenching behavior, no matter if Cy5.5 was excited via Tb-to-QD-to-Cy5.5 or QD-to-Cy5.5 FRET or directly by the excitation source, for both experimental and MCS results clearly confirmed our results from system 2 and the interpretation that homo-FRET between many dyes with non-unity quantum yield leads to significant PL intensity quenching due to non-radiative decay. The different increases and decreases of PL intensities as a function of *n* in the different detection channels could also be used for tuning the different FRET ratios both in intensity and direction (increase or decrease with *n* –**Figure 4.21**), which could again be very beneficial for designing multiplexed sensing applications or molecular logic gates.[67],[183]

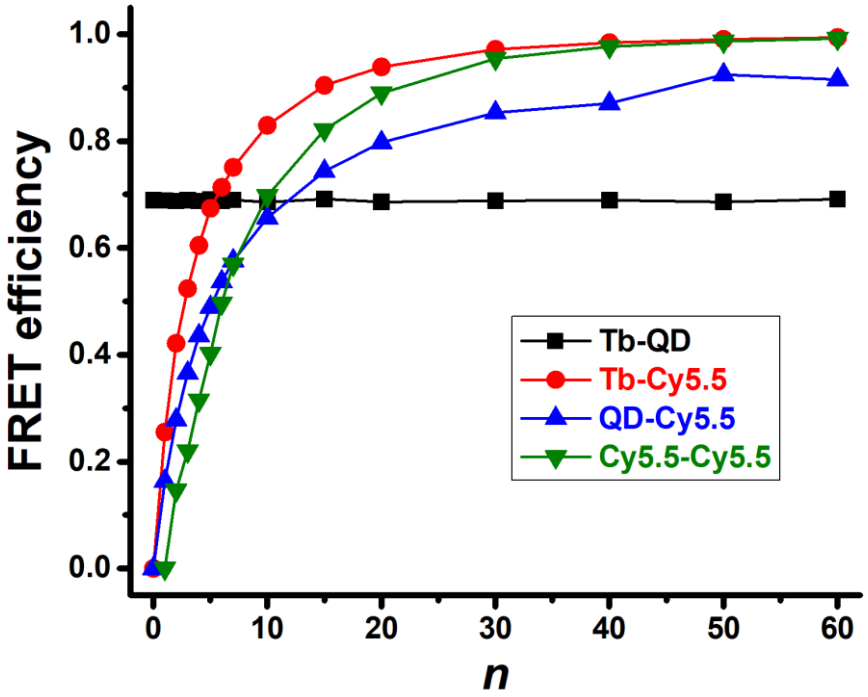

Figure 4.19. FRET system 4 (75Tb-QD-*n*Cy5.5): Simulated (MCS) FRET efficiencies for each possible FRET pathway. All different FRET pathways were calculated without the influence of the others.

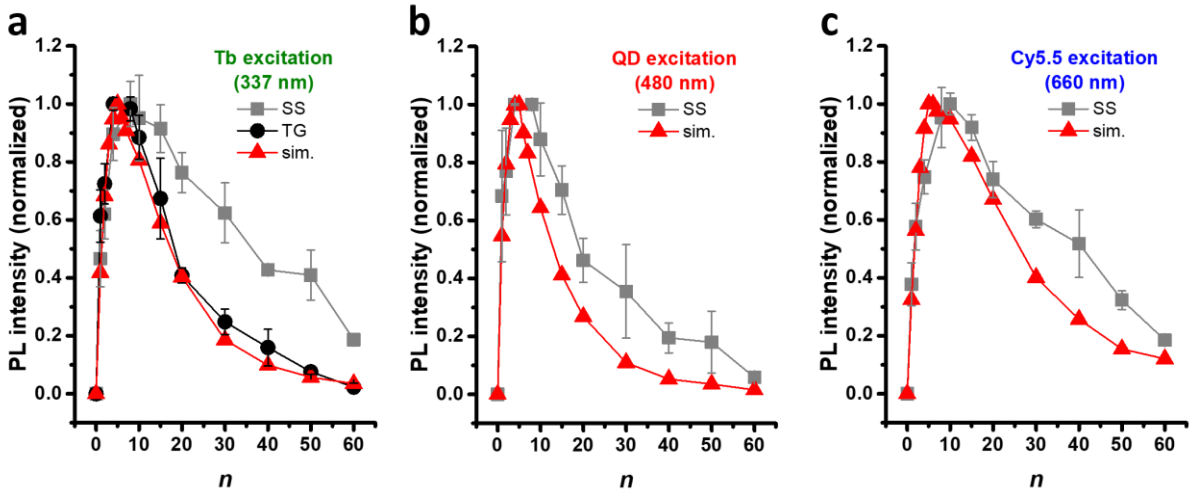

Figure 4.20. FRET system 4 (75Tb-QD-*n*Cy5.5): PL intensities (SS and TG experimental and MCS results) of Cy5.5 upon excitation of Tb **(a)**, QD **(b)**, and Cy5.5 **(c)**. Excitation of QD and Cy5.5 could not be measured with TG detection because of the short PL lifetimes (ns range).

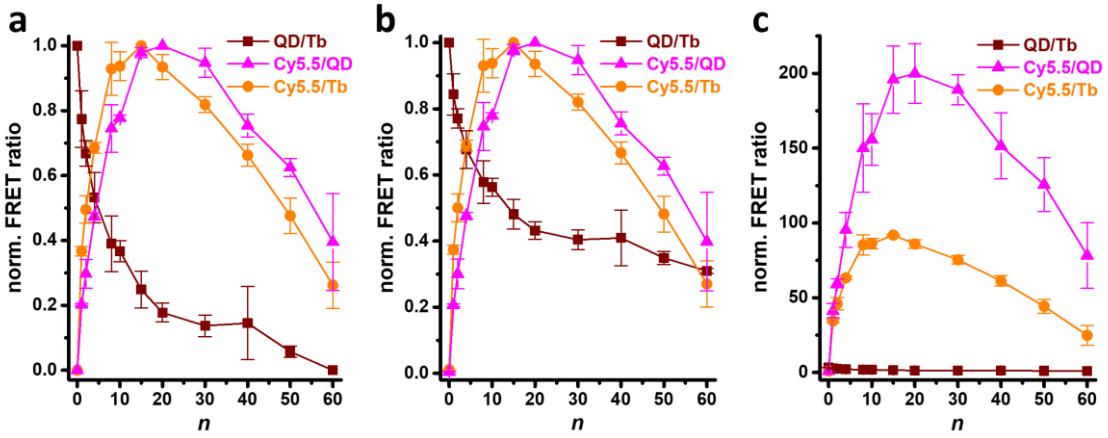

Figure 4.21. FRET system 4 (75Tb-QD-nCy5.5): FRET ratios of different TG (0.1 – 0.9 ms) PL intensities (QD/Tb, Cy5.5/QD, and Cy5.5/Tb) normalized between 0 and 1 **(a)**, to unity for the highest FRET ratio **(b)**, or to unity for the lowest FRET ratio **(c)**.

4.3.7 Brightness-equalized barcoding

The importance of such multi-donor-multi acceptor FRET QDs is not limited to a better fundamental understanding of the underlying FRET pathways. In fact, the knowledge of how to adjust the PL lifetimes and intensities in the three different detection channels can be exploited to design powerful tools for optical barcoding. Based on the *m*Tb-QD-*n*Cy5.5 systems, brightness-equalized lifetime-barcoding multi-hybrid FRET NPs can be designed by optimized numbers of Tb donors (*m*) and Cy5.5 acceptors (*n*). As our results from the different FRET systems showed, the intensity in the QD channel can be tuned by *m* without significantly altering the lifetime (*cf.* **Figures 4.10b** and **4.16b**), whereas the lifetime can be tuned by *n* (*cf.* **Figures 4.12** and **4.18b**). Thus, TG PL intensity barcoding by distinct PL decays, which we previously demonstrated for different lanthanide donors attached to QD acceptors at variable brightness,[44] can possibly advance to a next level, namely single-wavelength barcoding at similar intensity levels. To select the optimal combinations of *m* and *n* for distinct codes at similar brightness, we prepared three types of samples with different amounts of Lumi4 ligands and Cy5.5 (60Lumi4-QD, 60Lumi4-QD-10Cy5.5, and 60Lumi4-QD-40Cy5.5 – **Figure 4.22**) and measured the TG PL intensities in the three detection channels as a function of *m* (**Figure 4.23**). Because the quenching of both QD PL intensity by the Cy5.5 acceptors could be compensated by increasing amounts of Tb donors without altering significantly the PL lifetime, both lifetime and intensity of the

multi-hybrid FRET NPs could be tuned independently.

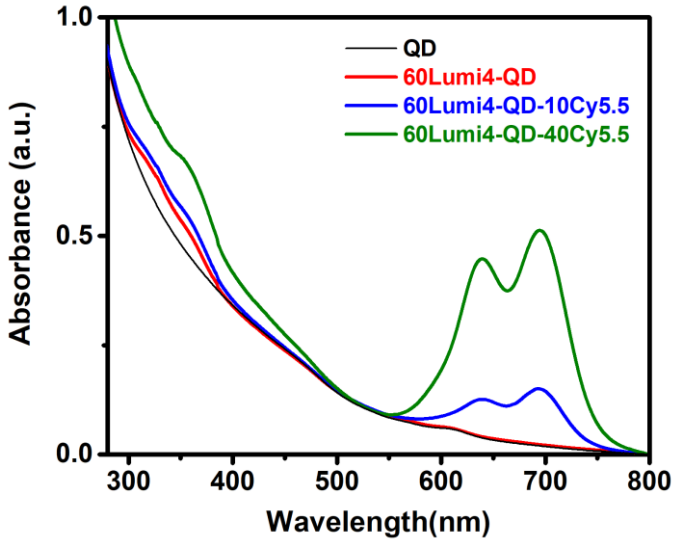

Figure 4.22. Absorption spectra of QD with different amounts of Lumi4 and Cy5.5. Note that Cy5.5 possesses absorption bands in the UV (*cf.* **Figure 4.7a**), which makes a precise quantification of Lumi4 per QD rather difficult. Taking into account a conjugation efficiency of ~70% and the PL results from **Figure 4.23**, we assumed 60±10 Lumi4 per QD for all three conjugates.

To demonstrate the capability of brightness-equalized PL barcoding, we selected the three NP systems "10Tb-QD", "30Tb-QD-10Cy5.5", and "60Tb-QD-40Cy5.5" and the three TG PL detection windows 0.05-0.5 ms, 0.5-1 ms, and 1-4 ms, which were decoded as red (R), green (G), and blue (B) (**Figure 4.24a**). This approach did not only allow us to accomplish three distinct RGB codes but also to reduce the brightness mismatch to 1.2 fold between code1 and code2 and 2.2 fold between code1 and code3 (**Figure 4.24b**). In contrast, lifetime tuning alone, as shown in FRET system 4 with a constant amount of 75 Tb per QD (**Figure 4.18b**), resulted in up to 12 fold (code1/code2) and 74 fold (code1/code3) TG PL intensity differences. To verify that deviations in the number of Tb donors (m), which could be caused by the uncertainties in Lumi4 ligand conjugation and/or the coordination of Tb^{3+} inside the ligands, do not cause deviations in the specific RGB codes, we evaluated the stability of the code as a function of m for the three different multi-hybrid FRET NPs (**Figure 4.25**). All codes were extremely stable and only deviated significantly for low values of m in system mTb-QD-40Cy5.5. These values were much lower than the selected m = 60 and did therefore not interfere with the code stability.

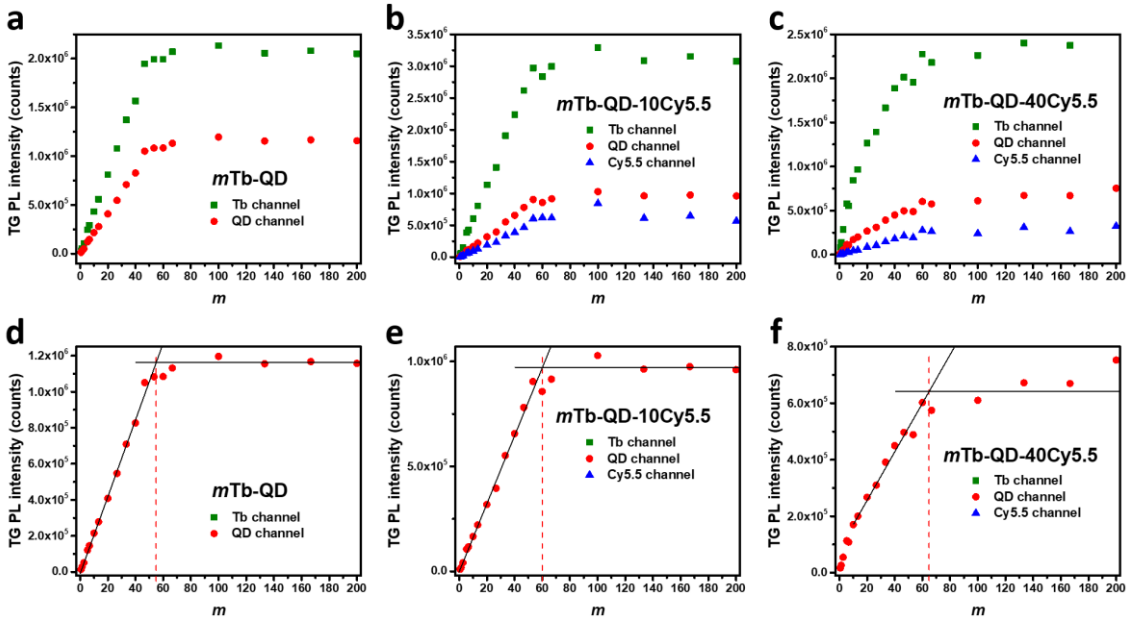

Figure 4.23. Time-gated intensities (range: 0.1-0.9 ms) of *m*Tb-QD (**a** and **d**), *m*Tb-QD-10Cy5.5 (**b** and **e**), and *m*Tb-QD-40Cy5.5 (c and f) in the different detection channels (**a** to **c**) and in only the QD detection channel (**d** to **e**) for estimating the Lumi4 per QD/SiO_2 ratio (60±10) and for a better visualization of the sensitivity (slope of the curves) of TG PL intensity as a function of *m*.

To actually apply the FRET barcodes for imaging, we prepared microbeads doped with the different multi-hybrid FRET NPs and obtained three distinct spectrotemporally coded beads (code 1 to 3). Each batch of encoded microbeads was dispersed on a microscopy coverslip and imaged with a TG microscopy imaging system using pulsed laser excitation at 349 nm and TG of the QD PL by an intensified CCD camera.[44] Using the previously defined TG detection windows R, B, and G (**Figure 4.24a** and **b**), we acquired three different images that were color-coded and overlaid to produce the final RGB-encoded image (**Figure 4.24c**). Each code was determined according to the RGB ratio using *ImageJ* and were consistent with the previously calculated results from PL decay analysis (**Figures 4.24a** and 4.24**b**). Although an RGB-analysis via *ImageJ* (or any other image software) is more precise (**Table 4.2**) and colors may appear different depending on the used monitor or printer, the three distinct RGB colors in the overlay images (**Figure 4.24c**) can be readily distinguished by the naked eye. To emphasize the capability of barcoding in more complex environments, the three differently encoded microbeads were mixed on the same microscopy slide. As shown in **Figure 4.24d**, single-color (one excitation and one emission wavelength) TG imaging could efficiently distinguish the three types of microbeads within the

same field of view. Again, the three RGB colors are readily distinguishable in the overlay images and distinction via the RGB ratio from *ImageJ* was very simple (**Table 4.2**). An important feature of the different codes was their similar brightness, which circumvented any contrast adaption and made the barcoding even simpler to apply.

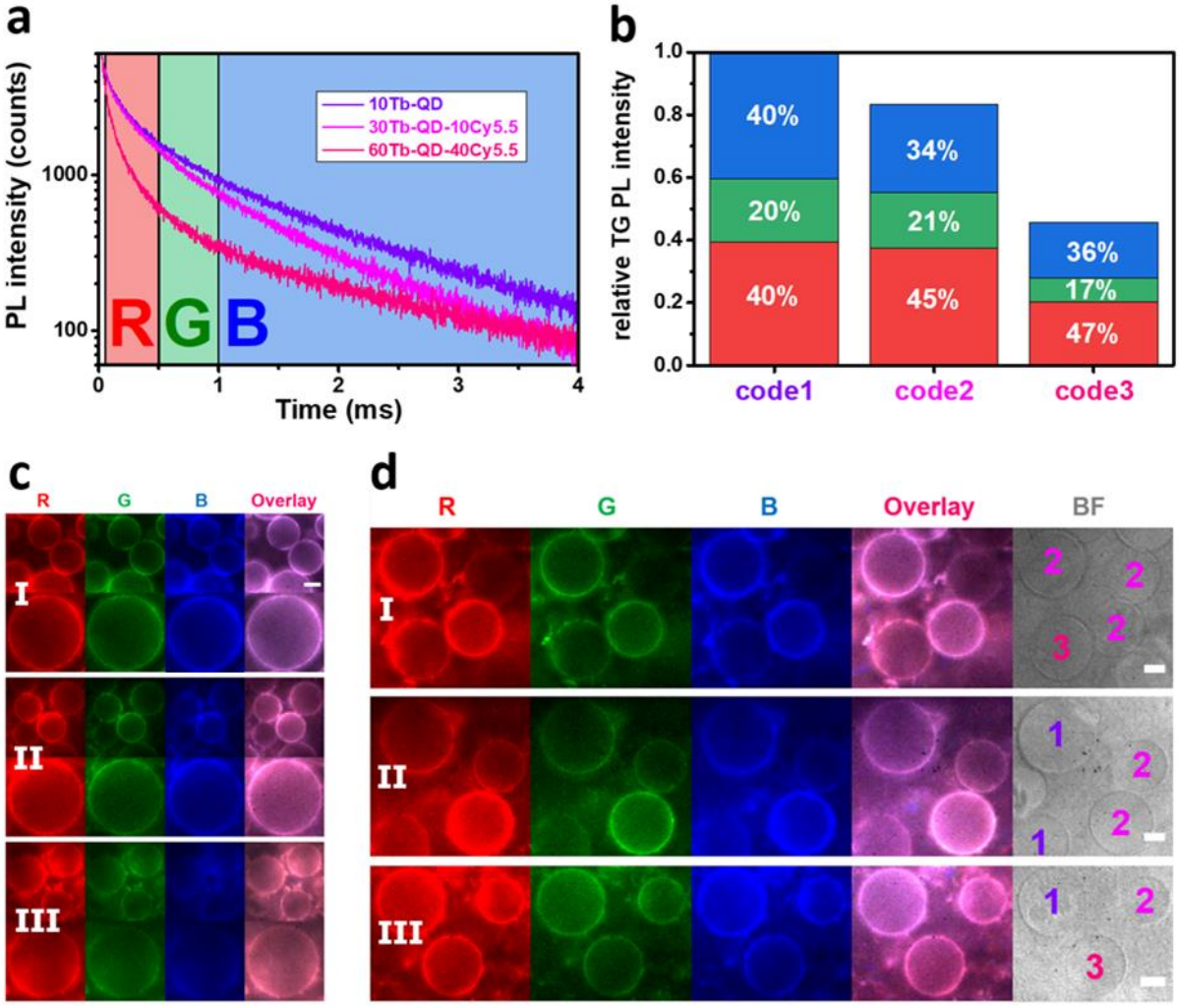

Figure 4.24. (a) PL decays of the three multi-hybrid NPs selected for optical barcoding. The TG PL intensities in the detection windows from 0.05 to 0.5 ms, 0.5 to 1 ms, and 1 to 4 ms were used for RGB encoding. **(b)** RGB ratios of the TG intensities from the different PL decay curves in a. Three codes with distinct ratios and the same order of brightness (maximum of 2-fold difference) were accomplished. **(c)** TG PL images (single R, G, and B detection channel and RGB code in overlay) of several beads (top) and single beads (bottom – amplification of top images) doped with 10Tb-QD (I), 30Tb-QD-10Cy5.5 (II), and 60Tb-QD-40Cy5.5 (III). Scale bar (top right): 50 µm; λ_{ex} = 349 nm; λ_{em} = 639±10 nm. **(d)** TG PL images of differently encoded beads mixed on the same microscopy slide and imaged in one field of view. For easier distinction (colors appear different depending on the screen/print version) the codes are also shown in the bright field (BF) images on the right. Scale bars (right): 50 µm; λ_{ex} = 349 nm; λ_{em} = 639±10 nm. Determination and assignment of the codes via RGB analysis is shown in **Table 4.2**.

Table 4.2. Brightness-equalized single-wavelength barcoding: Determination and assignment of the three different codes.

SPECTROSCOPY RESULTS (Figure 4.24 a/b)					R %	G %	B %	DETERMINE CODE
					0.40	0.20	0.40	
					0.45	0.21	0.34	
					0.47	0.17	0.36	
MICROSCOPY RESULTS FOR EACH CODE								
Figure	**Sample**	**R value**	**G value**	**B value**	**R %**	**G %**	**B %**	
4.24cI	**Top bead 1**	109	54	124	0.38	0.19	0.43	
	Top bead 2	110	53	121	0.39	0.19	0.42	
	Top bead 3	146	73	158	0.39	0.19	0.42	
	Top bead 4	155	77	163	0.39	0.20	0.41	
	Bottom bead	124	60	134	0.38	0.20	0.42	
				mean	0.39	0.19	0.42	
				SD	0.005	0.005	0.008	
Code 1					39±1%	19±1%	42±1%	
4.24cII	**Top bead 1**	148	59	117	0.46	0.18	0.36	
	Top bead 2	114	43	88	0.46	0.18	0.36	
	Top bead 3	166	70	134	0.45	0.19	0.36	
	Bottom bead	163	68	131	0.45	0.19	0.36	
				mean	0.45	0.18	0.36	
				SD	0.008	0.006	0.002	
Code 2					45±1%	18±1%	36±1%	
4.24cIII	**Top bead 1**	138	61	89	0.48	0.21	0.31	
	Top bead 2	192	86	119	0.48	0.22	0.30	
	Top bead 3	149	66	95	0.48	0.21	0.31	
	Bottom bead	156	69	96	0.49	0.21	0.30	
				mean	0.48	0.21	0.30	
				SD	0.003	0.002	0.005	
Code 3					48±1%	21±1%	31±1%	
FINAL CODES (Spectroscopy and Microscopy)								
Code 1					40±2%	18±2%	42±2%	
Code 2					44±2%	19±2%	36±2%	
Code 3					48±2%	19±3%	33±3%	
BARCODING (find codes in unknown samples)								
Figure	**Sample**	**R value**	**G value**	**B value**	**R %**	**G %**	**B %**	**ASSIGN CODE**
4.24dI	**Top left**	170	74	154	0.43	0.19	0.38	2
	Top right	139	56	121	0.44	0.18	0.38	2
	Bottom left	157	59	120	0.47	0.17	0.36	3
	Bottom right	184	78	157	0.44	0.19	0.37	2
4.24dII	**Top left**	116	47	125	0.40	0.16	0.44	1
	Top right	119	49	108	0.43	0.18	0.39	2
	Bottom left	169	73	171	0.41	0.18	0.41	1
	Bottom right	206	94	180	0.43	0.19	0.38	2
4.24dIII	**Top left**	207	102	109	0.40	0.20	0.40	1
	Top right	217	91	188	0.44	0.18	0.38	2
	Bottom	173	58	130	0.48	0.16	0.36	3

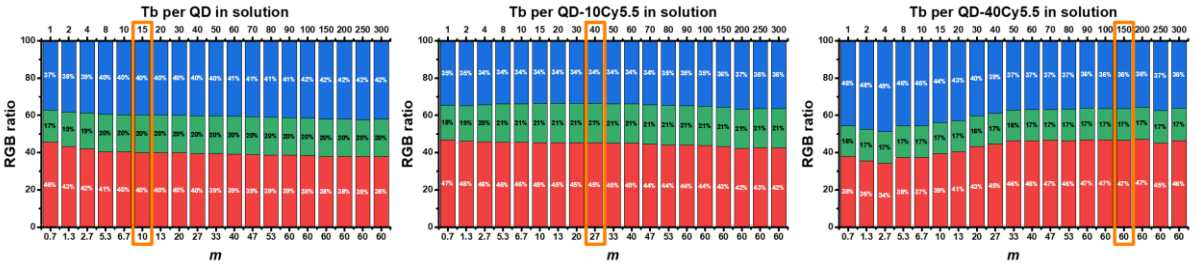

Figure 4.25. TG PL intensity (RGB) ratios of each multi-hybrid nanoparticle as a function of *m* (calculated from the TG intensities in the red (0.05-0.5 ms), green (0.5-1 ms), and blue (1-4 ms) TG detection windows shown in **Figure 4.24a**). The selected codes for barcoding (highlighted by orange frames) were in regions were the changes with *m* were negligible. Because the number of Lumi4 ligands per QD was 60, the maximum number of *m* was also 60 (ligand saturation).

4.4 Conclusion

We have extensively analyzed the photophysical properties of a single QD surrounded by up to 191 Tb donors and up to 60 Cy5.5 acceptors in all possible combinations. By separating the *m*Tb-QD-*n*Cy5.5 FRET-modulated multi-hybrid NPs into four distinct systems (*m*Tb-QD, QD-*n*Cy5.5, *m*Tb-QD-15Cy5.5, and 75Tb-QD-*n*Cy5.5) and combining steady-state and time-resolved spectroscopy with MCS, we were able to decipher the single contributions of all FRET pathways. Tb-to-QD FRET possessed a constant FRET efficiency and FRET-sensitized QD PL increased with *m* until a maximum loading of *circa* 200 Tb per QD was reached. However, this increase was less steep than expected from a purely theoretical estimation, which assumes that all Tb donors can sensitize the QD acceptor in a sequential manner without competition and/or experimental limitations. These restrictions could be very well modeled with MCS, which confirmed the experimental results. The FRET efficiency of QD-to-Cy5.5 FRET increases with *n*, which confirmed that FRET efficiency depends only on the number of acceptors and not the number of donors. Because of the many Cy5.5 FRET acceptors, we could show a steep increase of FRET-sensitized Cy5.5 PL for small values of *n*, followed by a constant decrease until $n = 60$. This decrease was mainly caused by combination of the formation of non-fluorescent H-dimers and multiple homo-FRET steps between Cy5.5 dyes, which increased the probability of the migrating exciton to get dissipated in the Cy5.5 dimer "trap states". The *m*Tb-QD-*n*Cy5.5 systems showed a convolution of Tb-to-Cy5.5 (co-assembled on the QD surface), Tb-

to-QD, QD-to-Cy5.5, and Cy5.5-to-Cy5.5 FRET. When n was constant, the FRET efficiency of all FRET steps was independent of m and the sensitization of QD by Tb could be used to further sensitize Cy5.5. When m was constant, Tb-to-Cy5.5, QD-to-Cy5.5, and Cy5.5-to-Cy5.5 FRET efficiencies increased with increasing n. Tb and QD PL intensities decreased with increasing n, whereas Cy5.5 PL increased for small n and then decreased for larger n (due to increased PL quenching caused by increased energy migration via homo-FRET). TG PL intensity detection of the long-lived PL (from the initial Tb donor with > 2 ms PL lifetime) provided more consistent results with MCS because TG could distinguish QD-to-Cy5.5 FRET originating from FRET-sensitized QDs and from directly excited QDs, which was not the case for steady-state PL detection.

Knowing the different FRET pathways and their dependence of m and n allowed us to tune both the PL intensity and lifetime of QD PL by adjusting m and n. This lever of independently tuning the intensity and shape (lifetime) of the QD PL decay curves was used to design brightness-equalized long-lifetime QDs with the possibility of RGB-encoded PL by TG intensity detection in three distinct time windows. The encoding strategy was applied to multiplexed imaging with single excitation and emission wavelengths and without the necessity of contrast adjustment for the differently encoded signals in the same field of view. The profound knowledge about multi-donor-multi-acceptor QD FRET and the demonstration of its application for single-wavelength optically-encoded multiplexed imaging demonstrate the level of sophistication such complicated FRET systems can contribute to fluorescence biosensing and imaging in case their properties are well understood. We anticipate that our results will find application in other fields of advanced optical barcoding such as multiplexed *in-vitro* diagnostics and cellular biology, security labeling, optical encryption, data storage, and molecular computing.

5. Energy transfer from Tb donors to AuNPs

C. Chen, C. Midelet, S. Bhuckory, N. Hildebrandt, and M. H. V. Werts. Nanosurface Energy Transfer from Long-Lifetime Terbium Donors to Gold Nanoparticles. *The Journal of Physical Chemistry C* **2018**, *122*, 17566-17574.

5.1 Introduction

The application of excitation energy transfer has expanded the applicability of luminescent probe methodologies in biochemistry, clinical diagnostics, and biomolecular imaging.[212]–[214] The understanding of energy transfer mechanism between donors and acceptors plays a fundamental role in developing and optimizing biosensing technologies. Förster resonance energy transfer (FRET) is the best-known energy transfer mechanism and has been confirmed for pairs of small donor and acceptor molecules. It predicts the energy transfer efficiency to be inversely proportional to the sixth power of the distance between the donor and acceptor.[8] This energy transfer occurs at intermolecular distances in the small window between approximately 1 and 20 nm,[2] a range that is ideally suited for observing dynamic biomolecular interactions, involving proteins, nucleic acids, cell membranes, and other biological systems.[215] However, many biomolecular processes take place over longer distances and their dynamic interactions are difficult to follow by FRET. Thus, investigating and understanding longer-range energy transfer processes and using them for biosensor development is highly desirable.

Theorized by Persson and Lang,[133] nanosurface energy transfer (NSET) has emerged as an energy transfer mechanism that can measure biomolecular interactions over distances up to 50 nm and thereby more than double the range of FRET.[125] Similar to FRET, NSET is a nonradiative dipole-dipole energy transfer but in contrast to FRET (in which both donor and acceptor are considered as point dipoles) the acceptor is a nanometric surface modeled as a collection of many dipoles. In NSET, the efficiency is inversely proportional to the fourth power

of the distance between the donor and the acceptor surface of a metallic nanoparticle (in most cases AuNPs).[126],[135] Research showed that NSET model was in good agreement with the experimental data on small size AuNPs (below 3 nm) in combination with organic dyes and quantum dots (QDs) as donors.[123],[134],[135] NSET behavior with energy transfer efficiencies independent of the NP size or number of donors was also demonstrated for larger size AuNPs.[120],[128],[130],[132] However, in other studies reporting about biosensors that use PL quenching by AuNPs, the underlying energy transfer mechanism is assumed to be FRET[216],[217] or is not specified.[218],[219]

Studies of the NSET mechanism have focused on the interaction of AuNPs with organic dyes and QDs but have as yet not used luminescent lanthanide complexes as the energy donor. Whereas hybrid nanomaterials incorporating luminescent lanthanide ions and plasmonic AuNPs have been reported in the literature,[220]–[222] a quantitative experimental study on the applicability of NSET *versus* FRET mechanisms in these materials has not been carried out. Compared with fluorescent molecular energy transfer donors, lanthanide ions offer some distinctive features such as long excited-state lifetimes (in the micro- to millisecond range) and multiple narrow emission bands in the visible region of the spectrum.[94] Thus, the investigation of lanthanide-to-AuNP energy transfer with AuNPs of different sizes has the potential to provide new insight for the debate on whether FRET or NSET is the cause of AuNP-based PL quenching.

In the chapter, we investigated the energy transfer interactions of Tb-conjugated sAv with biotinylated AuNPs with diameters of 5, 30, 50, and 80 nm (**Figure 5.1**). Resonant light scattering spectroscopy (RLS) and time-resolved PL spectroscopy were applied to characterize the different Tb-sAv-biot-AuNP assemblies at various donor/acceptor ratios. PL decays of many Tb-sAv-biot-AuNP assemblies at different concentrations and with AuNPs of all three sizes were studied by multi-exponential PL decay analysis and streched-exponential (Kohlrausch law) and the energy transfer efficiencies were found to be independent of the AuNP size. NSET theory provided excellent agreement between the time-resolved PL results and the Tb-to-AuNP distances within the different Tb-sAv-biot-AuNP assemblies, whereas application of FRET theory led to unrealistically long Förster distances and Tb-

AuNP distances without any correlation between the different AuNP sizes. Our results strongly suggest that energy transfer between Tb and AuNPs is of NSET type, which is a very important finding for understanding and designing AuNP-based biosensors and assemblies of AuNPs with photoluminescent units.

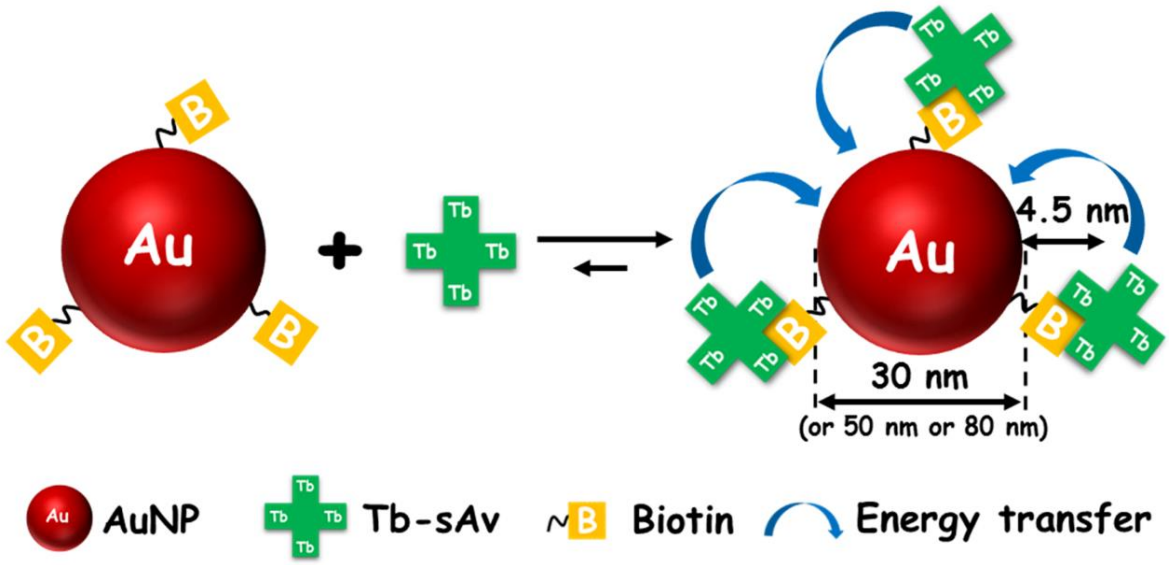

Figure 5.1. Schematic representation (not to scale) of the assemblies of Tb-labeled sAv (Tb-sAv) and biotinylated AuNPs (biot-AuNPs), in which excitation energy transfer occurs. For clarity only 3 biotins are shown. The actual number of biotins attached to the surface of each AuNP was determined to be ca. 25, 900, 2500, and 6400 for the 5, 30, 50, and 80 nm diameter AuNPs, respectively. A distance of 4.5 nm was estimated by a radius of 3 nm for sAv (size of sAv in the solid state: 5.4 nm x 5.8 nm x 4.8 nm in the solid state)[223] plus 1.5 nm for the biotin and linker attached to the AuNP.

5.2 Materials and methods

5.2.1 Materials

The biot-AuNPs were purchased from Sigma-Aldrich (5, 30, 50, and 80 nm diameter, biotin-terminated PEG mol. wt. 5000, dispersion in H_2O). For the measurements of 5 nm, 30 nm and 50 nm Au NPs, 2 mM Tris-HCl (pH 8.5) was used as a solvent, for the measurements of 80 nm Au NPs, pure water was used as a solvent. Black Costar Half Area 96 well microtiter plates were purchased from Corning Inc. (Corning, NY, USA), and Tb complexes (Lumi4-Tb) functionalized to sAv at a ratio of 4 Tb/sAv were provided by Lumiphore Inc. (Berkeley, CA, USA).

5.2.2 Optimization of buffer conditions

Optical extinction and light scattering spectra were measured on solutions of the biot-AuNPs in a selection of aqueous buffers. These spectroscopic measurements enabled to determine the long-term stability of biot-AuNPs in these buffers. Colloidal stability is a requirement for reliable results when forming donor-acceptor assemblies. Aggregation of instable AuNPs would lead to clearly observable changes in the optical spectra. Light scattering spectroscopy is particularly sensitive towards even slight changes in the chemical environment of plasmonic AuNPs.[224],[225] From these measurements (see Figure S1 to S3), it was concluded that 2 to 4 mM Tris-HCl buffer at pH 8.5, and pure water were the most suitable media for the experiments. An alternative buffer, phosphate-buffered saline (10 mM phosphate, pH 7.2, 137 mM NaCl, 2.7 mM KCl) also yielded stable nanoparticle solutions (no shift of the localized surface plasmon resonance maximum) but led to more pronounced "sticking" of the biot-AuNPs to the spectroscopic cell walls.

5.2.3 Formation of Tb/AuNP donor-acceptor assemblies

We used different but constant concentrations of Tb-sAv for the experiments with each of the three AuNPs. To these constant concentrations of Tb-sAv, increasing amounts of biot-AuNPs were added, such that the fraction of biot-AuNPs (x) was given per 6 Tb-sAv for 5 nm biot-AuNPs (25/4 = 6; 25 biotins on 4 sAv binding sites), per 225 Tb-sAv for 30 nm biot-AuNPs (900/4 = 225), per 625 Tb-sAv for 50 nm biot-AuNPs (2500/4 = 625), and per 1600 Tb-sAv for 80 nm biot-AuNPs (6400/4 = 1600). Tb-sAv was dissolved to 20.7 µM in anhydrous DMF, which corresponded to 82.8 µM of Tb (conjugation ratio of 4 Tb/sAv). For 5 nm biot-AuNPs, Tb-sAv was diluted to 2.73 nM in pure water. For the total measuring volume of 150 µL, 50 µL of Tb-sAv solutions were mixed with 100 µL of biot-AuNP solutions containing increasing amounts (0, 1, 5, 10, 20, 30, 40, 50, 60, 70, 80 µL) of 5 nm biot-AuNPs (9.09 nM) in 2 mM Tris-HCl buffer at pH 8.5. The mixtures were incubated for 2 h at 37° C. For 30 nm biot-AuNPs, Tb-sAv was diluted to 1.33 nM in pure water. For the total measuring volume of 150 µL, 50 µL of Tb-sAv solutions were mixed with 100 µL of biot-AuNP solutions containing increasing

amounts (0, 1, 2, 5, 10, 20, 30, 40, 50, 60, 80 µL) of 30 nm biot-AuNPs (29.6 pM) in 2 mM Tris-HCl buffer at pH 8.5. The mixtures were incubated for 2 h at 37° C. For 50 nm biot-AuNPs, Tb-sAv was diluted to 0.65 nM in pure water. For the total measuring volume of 150 µL, 50 µL of Tb-sAv solutions were mixed with 100 µL of biot-AuNP solutions containing increasing amounts (0, 1, 2, 5, 10, 20, 30, 40, 50, 60, 80 µL) of 50 nm biot-AuNPs (5.3 pM) in 2 mM Tris-HCl buffer at pH 8.5. The mixtures were incubated for 2 h at 37° C. For 80 nm biot-AuNPs, Tb-sAv was diluted to 0.72 nM in pure water. For the total measuring volume of 150 µL, 50 µL of Tb-sAv solutions were mixed with 100 µL of biot-AuNP solutions containing increasing amounts (0, 1, 2, 5, 10, 20 µL) of 80 nm biot-AuNPs (2.24 pM) in pure water. The mixtures were incubated while shaking slowly overnight at room temperature.

5.2.4 Analytical Methods

Extinction spectra were acquired using a Lambda 35 UV/Vis spectrophotometer from Perkin Elmer or on a modular fiber-based spectrometer system (OceanOptics LS-1 white light source and USB4000- VIS-NIR CCD spectrometer). Resonant light scattering spectroscopy (RLS) of the AuNP and AuNP-Tb-sAv solutions was performed using a fibre-coupled incandescent white light source (AvaLight-HAL-(S)-mini) and an OceanOptics QE65000 spectrograph, at right angle, using our published method,[224]–[226] A 200x diluted Ludox solution[227] in 50 mM aqueous NaCl was used as the reference. The corrected light scattering spectra represent the relative light scattering cross sections as a function of wavelength.

In the kinetics experiments probing the stability of the biot-AuNP solutions and the binding of Tb-sAv to biot-AuNP, corrected light scattering spectra were recorded at evenly spaced time intervals (rate typically 1 spectrum per 10 s). The position of the maximum of the resonant light scattering band $\lambda_{\max}^{\mathrm{RLS}}$ in each recorded spectrum was determined by fitting a parabola through the data points in a narrow spectral window ($\Delta\lambda$ = 10 nm) around the numerical maximum. The maximum of the parabola obtained from this first fit was then used as the center point for a second parabolic fit through the measured spectral data points over a narrow window ($\Delta\lambda$ = 10 nm), from which a refined determination of the position

of the maximum was deduced. This procedure yielded stable and reproducible measurement of the position of the resonant light scattering maximum λ_{max}^{RLS} and mitigates problems due to noise on the measured spectrum.

For the measurement of the PL decay curves of the Tb to AuNPs, an EI fluorescence plate reader (Edinburgh Instruments, UK) was used. For the multichannel scaler, 4000 detection bins of 2 µs integration time were used. A nitrogen laser (LTB, Berlin, Germany) was used for excitation (337.1 nm, 20 Hz, 600 flashes). 494/20 nm bandpass filter was used for analyzing the Tb PL. The data were fit with FAST software version 3.1 (Edinburgh Instruments, UK). All assays were measured in black 96-well microtiter plates with an optimal working volume of 150 µL.

5.3 Results and discussion

5.3.1 Characterization of Tb-sAv-biot-AuNP assemblies

The number of binding sites for sAv on each nanoparticle is of the same order of magnitude as the number of biotins per particle. In principle, sAv can bind up to four biotins.[185] The number of biotins per biot-AuNP were given by the supplier as a number density of approximately 0.5/nm^2 at the AuNP surface. At the same time, the surface areas were given as 78.5, 2830, 7850, and 20100 nm^2 for the 5, 30 nm, 50 nm, and 80 nm AuNPs, respectively, which led to 39 biotins per 5 nm AuNP, 1415 biotins per 30 nm AuNP, 3925 biotins per 50 nm AuNP, and 10050 biotins per 80 nm AuNP. Because no explanation of this estimation was provided, we applied our own estimation based on the number of Au surface atoms, which we calculated to be 500 for 5 nm biot-AuNPs, 18000 for the 30 nm biot-AuNPs, 50000 for the 50 nm biot-AuNPs, and 128000 for the 80 nm biot-AuNPs. Assuming the number of available biotins on the surface to be ca. 5% of the number of Au surface atoms led to 25 biotins per 5 nm biot-AuNP, 900 biotins per 30 nm biot-AuNP, 2500 biotins per 50 nm biot-AuNP, and 6400 biotins per 80 nm biot-AuNP, which were in good agreement with the estimates of the supplier. Taking into account that four biotins from the biot-AuNP will be able to bind one sAv, and ignoring any steric effects, the number of sAv that can bind to one nanoparticle is

anticipated to be 6 for 5 nm biot-AuNPs, 225 for 30 nm biot-AuNPs, 625 for 50 nm, and 1600 for 80 nm biot-AuNPs. PL titrations reported below enabled us to refine these estimates.

The interaction of Tb-sAv with biot-AuNPs was investigated by monitoring the light scattering spectra[224],[225] of the biot-AuNPs and introducing Tb-sAv into the solution. The light scattering spectra consist of the localized surface plasmon resonance of AuNPs, which is sensitive to the environment of the particles. In particular, immobilization of biomolecules at the nanoparticle surface leads to small changes (a few nm) in the position of the maximum of these resonance bands. Larger shifts of the plasmon maximum (> 10 nm) are in general the result of clustering of AuNPs into aggregates, which leads to strong coupling between the localized plasmon resonances of the individual particles[224],[225],[228],[229]. The particular sensitivity of the resonant light scattering spectrum towards the environment of the AuNPs provides a tool for monitoring the state of the biot-AuNPs when interacting with Tb-sAv.

Figure 5.2 shows the evolution of the wavelength of the maximum λ_{max} of the resonant light scattering spectrum of biot-AuNPs (30 nm, 50 nm, 80 nm diameter) over time, before and after adding Tb-sAv to the solution. The light scattering by 5 nm AuNPs is too weak and was not studied. The amount of Tb-sAv added was 25% and 200% of the amount needed to cover all binding sites on the AuNPs. The position of the maximum did not change over time before adding Tb-sAv, which was in line with the stability of the biot-AuNPs in the buffer. A prompt, small wavelength shift was observed in the light scattering resonance of the biot-AuNPs when Tb-sAv was added to the solution. Subsequently, there was virtually no evolution of λ_{max} at longer times after adding Tb-sAv. The observed evolution of λ_{max} is consistent with the binding of Tb-sAv to the biot-AuNPs. The absence of changes in λ_{max} after binding of Tb-sAv to the biot-AuNPs indicates that no significant clustering of Tb-sAv/biot-AuNPs into multi-AuNP aggregates occurred, and that under the experimental conditions the only donor-acceptor assemblies are based on single AuNPs.

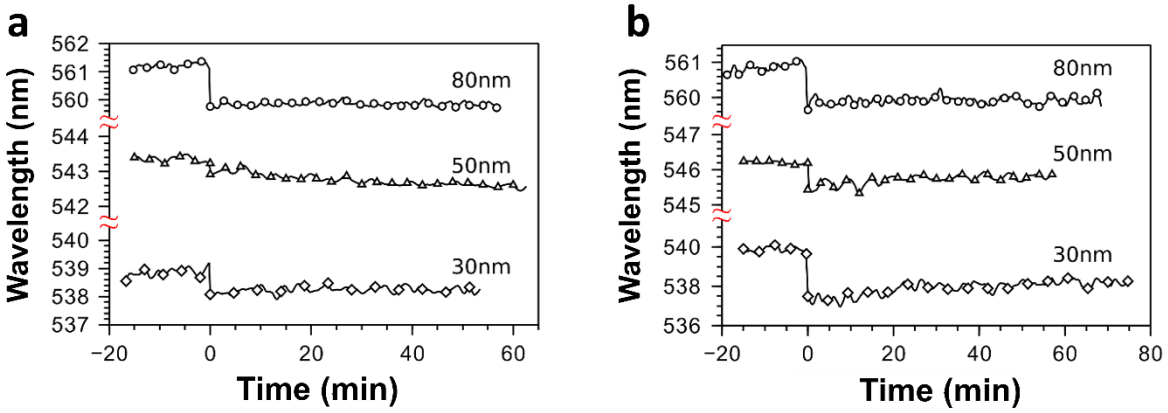

Figure 5.2. Wavelength evolution of the maximum of the resonant light scattering band of biot-AuNPs (30, 50 and 80 nm diameter AuNPs) as a function of time. At t = 0, Tb-sAv **(a)** 25% and **(b)** 200% with respect to biot-AuNP binding sites was added.

PL titration experiments (**Figure 5.3**) provided further insight in the interaction between Tb-sAv and biot-AuNPs. As the concentration of biot-AuNPs was increased in solutions of constant Tb-sAv concentration, the integrated time-gated Tb PL intensity decreased sharply (**Figure 5.3a**), until a certain concentration ratio, after which no further decrease took place. The decrease in overall intensity was accompanied by the appearance of a short PL decay component in the Tb PL decay curves (**Figure 5.3 b-d**), at the expense of the long-lived Tb decay from the initial Tb-sAv, which indicates energy transfer from Tb to AuNP.

The PL titration behavior can readily be interpreted in terms of the formation of Tb-sAv/biot-AuNP assemblies. Taking into account the results from the resonant light scattering spectroscopy, we can infer that these assemblies exist as isolated biot-AuNPs, bearing one or more Tb-sAv entities. The concentration ratio [biot-AuNP]/[Tb-sAv] beyond which the PL intensity remains constant, is the concentration ratio at which all (active) Tb-sAv are bound to biot-AuNP. This happened in all cases at approximately 3 times the initially estimated concentration of biot-AuNP necessary to bind all Tb-sAv. This common factor of 3 demonstrates the coherence in binding behavior of the four diameters of particles, since the initial estimates were based on the same assumptions for each particle diameter. According to the PL titrations, the binding capacity was 2, 75, 208, and 533 Tb-sAv per biot-AuNP, for 5 nm, 30 nm, 50 nm, and 80 nm AuNPs, respectively. Using the surface areas of the different AuNPs (*vide supra*) and the

size of sAv in the solid state (5.8 nm x 5.4 nm x 4.9 nm),[223] which would lead to a surface footprint of 24.6 nm^2 (π x 2.9 nm x 2.7 nm), the possible coverage of sAv per AuNP would be 3 (5 nm AuNPs), 115 (30 nm AuNPs), 319 (50 nm AuNPs), and 817 (80 nm AuNPs). When taking into account the curved surface of the AuNPs, the hydration layer of sAv, and possible sterical hindrance in sAv binding to biot in very close proximity, the 35% lower values determined by PL titration are in good agreement with the geometrical binding conditions. At [biot-AuNP]/[Tb-sAv] ratios below the equivalence point, biot-AuNPs carried the maximum number of Tb-sAv. At excess of biot-AuNP, the number of Tb-sAv per biot-AuNP decreased.

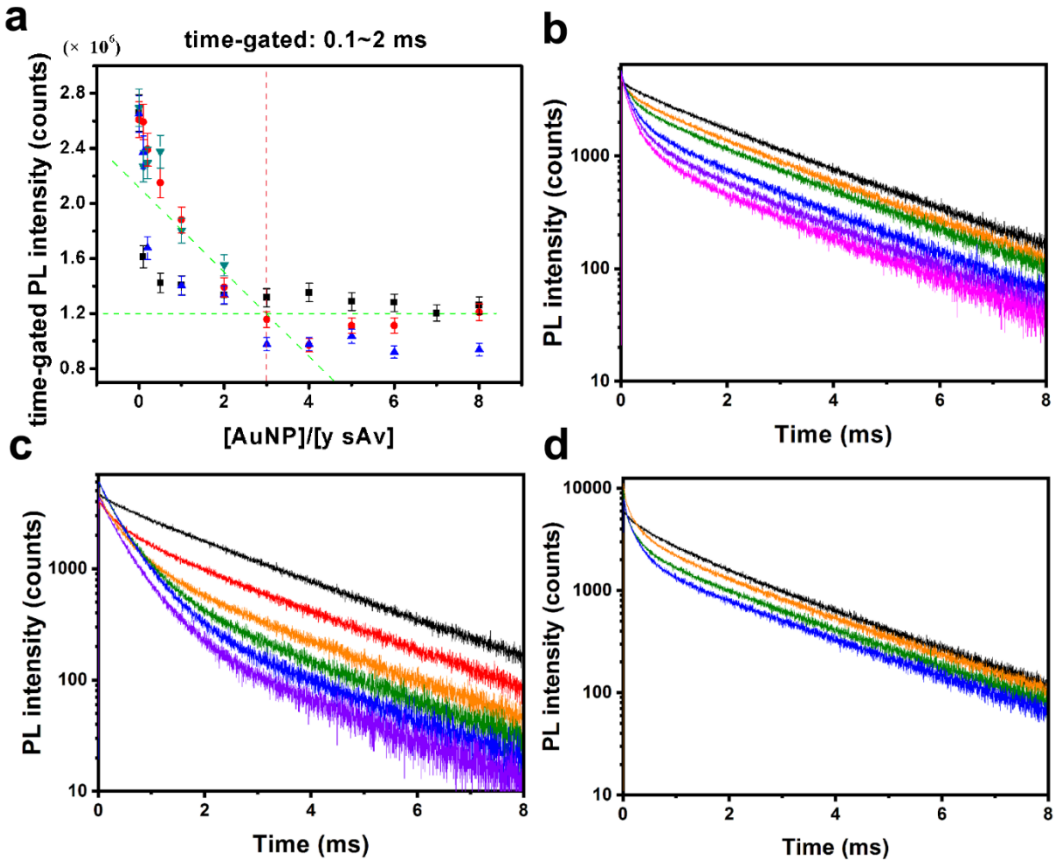

Figure 5.3. PL titration of Tb-sAv with biot-AuNP **(a)** Integrated time-gated (0.1 – 2 ms) PL intensities of the PL decay curves (black: 5 nm biot-AuNPs; red: 30 nm biot-AuNPs; blue: 50 nm biot-AuNPs; green: 80 nm biot-AuNPs). Crossing of the green dotted lines (at 3 [biot-AuNP]/ [y Tb-sAv] with y = 6 for 5 nm biot-AuNPs, y = 225 for 30 nm biot-AuNPs, y = 625 for 50 nm biot-AuNPs, and y = 1600 for 80 nm biot-AuNPs) indicates the maximum number of Tb-sAv per biot-AuNP (6/3=2 for 5 nm biot-AuNPs, 225/3 = 75 for 30 nm biot-AuNPs, 625/3 = 208 for 50 nm biot-AuNPs, and 1600/3 = 533 for 80 nm biot-AuNP **(b-d):** Selected PL decay curves detected within the Tb donor channel for increasing ratios of (x biot-AuNPs) per (y Tb-sAv). **(b)** 30 nm biot-AuNPs with y = 225 Tb-sAv; **(c)** 50 nm biot-AuNPs with y = 625 Tb-sAv; **(d)** 80 nm biot-AuNPs with y = 1600 Tb-sAv. Black: x = 0; red: x = 0.2; orange: x = 0.5; green: x = 1; blue: x = 2; violet: x = 3; pink: x = 4.

5.3.2 Time-resolved PL decay analysis

We analyzed the data with multiexponential decays. The multiexponential analysis has previously been shown to lead to a coherent picture of LRET in Tb-nanoparticle assemblies. [189], [190] It is based on fitting the decay curves using a multiexponential PL intensity decay function (**Equation 5.1**):

$$I = \sum A_{\mathrm{i}} \exp(-t/\tau_{\mathrm{i}}) = A \sum \alpha_{\mathrm{i}} \exp(-t/\tau_{\mathrm{i}}) \tag{5.1}$$

where A is the total amplitude and α_{i} are the amplitude fractions ($\sum \alpha_{\mathrm{i}} = 1$). The averaging of the PL lifetime for the quenching process was performed using amplitude weighted average lifetimes (**Equation 5.2**):[230]–[232]

$$\langle \tau \rangle = \sum a_i \tau_i \tag{5.2}$$

The decay curve of pure Tb-sAv donor in buffer slightly deviates from mono-exponentially (**Figure 5.4a**), which can be attributed to the multiple Tb (~4) conjugation per sAv. The heterogeneity in the local environments, that the Tb experience at the different sAv sites give rise to a distribution of decay rates. It was better fitted with a double-exponential decay function, which led to the amplitude fractions α_{D1} and α_{D2}, the PL decay times τ_{D1} and τ_{D2} (with $\tau_{\mathrm{D2}} > \tau_{\mathrm{D1}}$) and the average PL decay time of the pure donor (in the absence of the acceptor) $\langle \tau_{\mathrm{D}} \rangle$. The quenched decay curves in the donor detection channel were fitted using a triple-exponential decay function, leading to the amplitude fractions $\alpha_{\mathrm{DA*1}}$, $\alpha_{\mathrm{DA*2}}$, and $\alpha_{\mathrm{DA*0}}$ and the PL decay times τ_{DA1}, τ_{DA2}, and τ_{DA0}, for which the third decay time component was fixed to $\tau_{\mathrm{DA0}} = \tau_{\mathrm{D2}}$ in order to take into account the emission of unquenched donors. For the calculation of the average donor decay time in the presence of the acceptor $\langle \tau_{\mathrm{DA}} \rangle$, only the first two amplitudes and decay times were used (as the third component represents unquenched donors). Therefore, the amplitude fractions must be redefined for these two decay times τ_{DA1} and τ_{DA2}. As the unquenched donor possesses two decay time components (τ_{D1} and τ_{D2}), $\langle \tau_{\mathrm{DA}} \rangle$ must be corrected for the shorter time component τ_{D1}. As this shorter decay time of the "pure" donor falls within the time-range of the quenched decay times, the use of an additional exponential for the fit procedure leads to inconsistent fit results. We therefore applied a correction factor z_{D} (the fraction of unquenched donors in the short time components), which is determined by comparing the

amplitude fractions of τ_{D2} and τ_{DA0} ($\tau_{DA0} = \tau_{D2}$) multiplied by the amplitude fraction (**Equation 5.3)** and which was shown to lead to consistent distance results for many different Tb-to-quantum dot FRET systems. [2],[94],[190]

$$z_D = \alpha_{D1}(\alpha_{DA*0}/\alpha_{D2}) \tag{5.3}$$

The average quenched decay time is then (with $\alpha_{DA1}+ \alpha_{DA2}=1$, **Equation 5.4**)

$$\langle\tau_{DA}\rangle = \frac{\alpha_{DA1}\tau_{DA1}+\alpha_{DA1}\tau_{DA1}-z_D\tau_{D1}}{1-z_D} \tag{5.4}$$

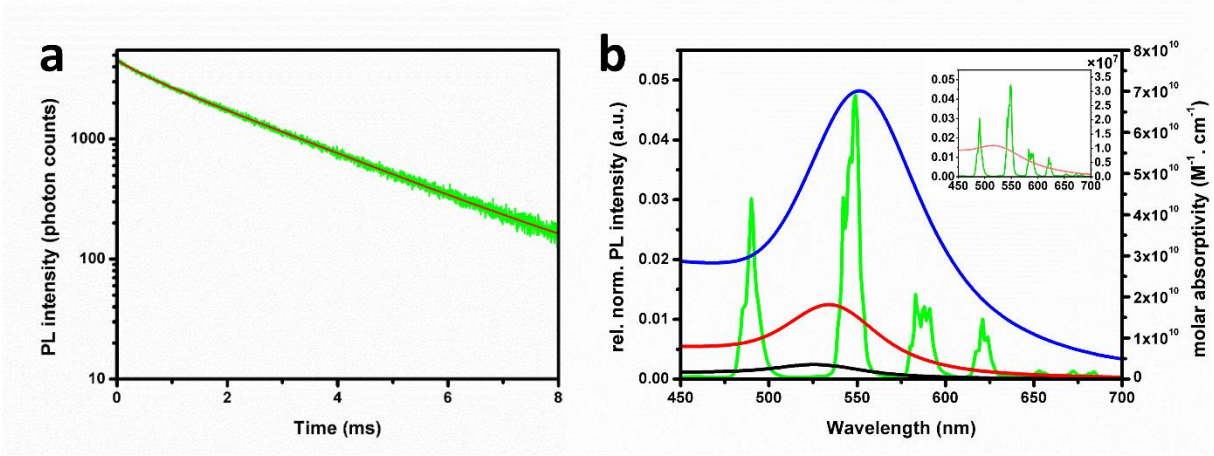

Figure 5.4. (a) PL decay (λ_{ex} = 337.1 nm; λ_{em} = 490/20 nm) of Tb-sAv in buffer (red) and fit (black) using multiexponential decays; yielding an average lifetime of $\langle\tau\rangle$ = 2.2 ms. **(b)** Overlap between absorption spectra of 30 nm (black), 50 nm (red), and 80 nm (blue) biot-AuNP acceptors and emission spectrum of the Tb-sAv donor (green) (inset: Overlap between absorption spectra of 5 nm biot-AuNP acceptor (red) and emission spectrum of the Tb-sAv donor (green)).

Table 5.1. Tb donor and Tb-sAv/biot-AuNP donor-acceptor decay times obtained from fits of decay models to the experimental Tb(III) luminescence decay. Uncertainties are reported as 95% confidence intervals.

	Kohlrausch decay model			Multi-exponential decay model		
AuNP diam. (nm)	$\langle\tau\rangle_D$ **(ms)**	$\langle\tau\rangle_{DA}$ **(ms)**	***E***	$\langle\tau\rangle_D$ **(ms)**	$\langle\tau\rangle_{DA}$ **(ms)**	***E***
5	2.17(±0.02)	0.80(±0.01)	0.63(±0.01)	2.15(±0.02)	0.81(±0.02)	0.62(±0.01)
30	2.23(±0.02)	0.19(±0.01)	0.91(±0.01)	2.20(±0.02)	0.31(±0.02)	0.86(±0.02)
50	2.20(±0.02)	0.46(±0.01)	0.79(±0.01)	2.19(±0.02)	0.47(±0.01)	0.79(±0.01)
80	1.66(±0.02)[a]	0.14(±0.02)	0.92(±0.02)	1.78(±0.02)	0.22(±0.03)	0.87(±0.02)

(a) Measurements for 80 nm biot-AuNPs were done in pure water instead of buffer; the donor lifetime is slightly shorter in this solvent.

Using this multi-exponential analysis, the average quenched decay times ($\langle\tau_{DA}\rangle$) were 0.81±0.02 ms, 0.31±0.02 ms, 0.47±0.01 ms, and 0.22±0.03 ms, and the energy

transfer efficiencies (E) were 0.62±0.01, 0.86±0.02, 0.79±0.01 and 0.87±0.02 for 5 nm, 30 nm, 50 nm, and 80 nm biot-AuNPs, respectively (**Appendix 7.4.2**). In addition to the multi-exponential analysis, the PL decay curves were also analyzed with a Kohlrausch decay model (**Appendix 7.4.3**). We found $\langle\tau\rangle_{DA}$ = 0.80±0.01 ms for 5 nm biot-AuNPs, $\langle\tau\rangle_{DA}$ = 0.19±0.01 ms for 30 nm biot-AuNPs, $\langle\tau\rangle_{DA}$ = 0.46±0.01 ms for 50 nm biot-AuNPs, and $\langle\tau\rangle_{DA}$ = 0.14±0.02 ms for 80 nm biot-AuNPs, with energy transfer efficiencies 0.63±0.01, 0.91±0.01, 0.79±0.01, and 0.9±0.02, respectively. The Kohlrausch analysis led to similar results as the multi-exponential analysis, indicating the consistency between the two models. The results of two analysis for all AuNP diameters studied are collected in **Table 5.1**. Finally, the energy transfer efficiencies, as well as the determined donor-acceptor distances are in close agreement between the multi-exponential and Kohlrausch decay models.

5.3.3 Energy transfer mechanism: FRET *vs* NSET

The energy transfer efficiencies indicate that PL quenching takes place by non-radiative energy transfer, and also that this quenching is incomplete, leaving some emission to be detected. Gold nanoparticles are known to be efficient quenchers for luminophores very close to their surface[233]–[236] and the mechanism for this quenching has been attributed to either FRET or NSET mechanisms.[9], [12], [15], [17], [19], [21], [23], [24], [213], [214], [233] We therefore subjected our PL decay time results to both FRET and NSET theory with the aim of contributing to the understanding of energy transfer processes in assemblies of photoluminescent entities and plasmonic nanoparticles, in particular to find out which theory, FRET of NSET, makes the best predictions about energy transfer in these systems. The long-lived PL emission from Tb enables a clear distinction of the Tb signal from other, short-lived background fluorescence, while still being subject to electric dipole-dipole energy transfer.[238]

For FRET model analysis, the overlap integral (J) and Förster distance (R_0) were calculated using **Equations 5.5** and **5.6**.

$$J = \int \bar{I}_D(\lambda)\varepsilon_A(\lambda)\lambda^4 d\lambda \quad (5.5)$$

where $\bar{I}_D(\lambda)$ is the area-normalized emission spectrum of donor, $\varepsilon_A(\lambda)$ is the molar

absorptivity spectrum of the acceptor in $M^{-1}cm^{-1}$, and λ is the wavelength in nm. **Figure 5.4 b** shows the intensity-normalized (area under the emission spectrum from 450 to 700 nm normalized to unity) PL spectrum of Tb donor and the absorption spectra of the differently sized biot-AuNP acceptors (5, 30, 50, and 80 nm).

$$R_0 = 0.0211[\kappa^2 \Phi_D (n)^{-4} J(\lambda)]^{1/6} \quad \text{(in nm)} \tag{5.6}$$

where κ^2 is orientation factor (κ^2=2/3 due to dynamic averaging as found for other Tb-NP donor-acceptor systems), [3],[94] Φ_D is Tb-centered quantum yield of the Tb donor (0.64), and n is the refractive index of the surrounding medium. The molar extinction coefficients $\varepsilon_{AuNP}(\lambda)$ for gold nanoparticles were obtained from the extinction cross sections calculated with analytic Mie expressions[239] evaluated using a Python computer program.[224]

Table 5.2. FRET model of resonance energy transfer from Tb to AuNPs.

AuNPs	5 nm	30 nm	50 nm	80 nm
κ^2:	2/3	2/3	2/3	2/3
Φ_D :	0.64	0.64	0.64	0.64
n (refractive index):	1.35	1.35	1.35	1.35
$J(\lambda)$ (M^{-1} cm^{-1} nm^4):	6.9 x 10^{17}	1.6 x 10^{20}	9.3 x 10^{20}	4.4 x 10^{21}
R_0 (nm):	14.1	34.8	46.8	60.7

Table 5.3. FRET model of resonance energy transfer from Tb to AuNPs (using the refractive index of Au).

AuNPs	5 nm	30 nm	50 nm	80 nm
κ^2:	2/3	2/3	2/3	2/3
Φ_D :	0.64	0.64	0.64	0.64
n (refractive index):	0.98	0.98	0.98	0.98
$J(\lambda)$ (M^{-1} cm^{-1} nm^4):	6.9 x 10^{17}	1.6 x 10^{20}	9.3 x 10^{20}	4.4 x 10^{21}
R_0 (nm):	17.4	43.1	57.9	75.1

Förster distances (R_0) were 14.1 nm, 34.8 nm, 46.8 nm, and 60.7 nm (for 30, 50, and 80 nm AuNPs, respectively) when using the refractive index of the aqueous buffer (**Table 5.2**) or 17.1 nm, 43.1 nm, 57.9 nm, and 75.1 nm, when using the refractive index of gold (**Table 5.3**). To fit the FRET model to different sizes of AuNPs, Wu *et al.* suggested to subtract the radius of the AuNPs from the R_0 values,[216] which would lead to 11.6 nm, 19.8 nm, 21.8 nm, and 20.7 nm when

using the refractive index of the aqueous buffer and 14.6 nm, 28.1 nm, 32.9 nm, and 35.1 nm when using the refractive index of gold. All R_0 values are far beyond the FRET range, which provides good evidence that the FRET mechanism is not operational here.

Table 5.4. Calculation of Tb-to-AuNP distance (*R*) with calculated Förster distances (R_0) and measured PL decays ($<\tau_{DA}>$ and $<\tau_D>$ obtained from the multi-exponential PL decay analysis).

	AuNP diameter (nm)	$<\tau_{DA}>$ (in ms)	$<\tau_D>$ (in ms)	R_0 (in nm)	R (in nm)	R (in nm) minus AuNP radius
n=1.35; R_0 with subtracted AuNP radius	5	0.81	2.15	11.6	10.7	
	30	0.31	2.20	19.8	14.6	
	50	0.47	2.19	21.8	17.5	
	80	0.22	1.78	20.7	15.1	
n=0.98; R_0 with subtracted AuNP radius	5	0.81	2.15	14.6	13.5	
	30	0.31	2.20	28.1	20.8	
	50	0.47	2.19	32.9	26.5	
	80	0.22	1.78	35.1	25.6	
n=1.35; full R_0 without subtraction	5	0.81	2.15	14.1	13.0	10.5
	30	0.31	2.20	34.8	25.7	10.7
	50	0.47	2.19	46.8	37.7	12.7
	80	0.22	1.78	60.7	44.2	4.2
n=0.98; full R_0 without subtraction	5	0.81	2.15	17.1	15.8	13.3
	30	0.31	2.20	43.1	31.8	16.8
	50	0.47	2.19	57.9	46.6	21.6
	80	0.22	1.78	75.1	54.7	14.7

Table 5.5. Calculation of Tb-to-AuNP distance (*R*) with calculated Förster distances (R_0) and measured PL decays ($<\tau_{DA}>$ and $<\tau_D>$ obtained from the analysis using the Kohlrausch decay law).

	AuNP diameter (nm)	$<\tau_{DA}>$ (in ms)	$<\tau_D>$ (in ms)	R_0 (in nm)	R (in nm)	R (in nm) minus AuNP radius
***n*=1.35; R_0 with subtracted AuNP radius**	5	0.80	2.17	11.6	10.6	
	30	0.19	2.23	19.8	13.3	
	50	0.46	2.20	21.8	17.5	
	80	0.14	1.66	20.7	13.9	
***n*=0.98; R_0 with subtracted AuNP radius**	5	0.80	2.17	14.6	13.3	
	30	0.19	2.23	28.1	18.9	
	50	0.46	2.20	32.9	26.4	
	80	0.14	1.66	35.1	23.6	
***n*=1.35; full R_0 without subtraction**	5	0.80	2.17	14.1	12.9	10.4
	30	0.19	2.23	34.8	23.4	8.4
	50	0.46	2.20	46.8	37.5	12.5
	80	0.14	1.66	60.7	40.8	0.8
***n*=0.98; full R_0 without subtraction**	5	0.80	2.17	17.1	15.6	13.1
	30	0.19	2.23	43.1	29.0	14.0
	50	0.46	2.20	57.9	46.4	21.4
	80	0.14	1.66	75.1	50.5	10.5

Within the FRET model, the Tb-AuNP distance (R) was calculated using **Equation 5.7**.[2]

$$R = R_0 \left(\frac{\tau_{DA}}{\tau_D - \tau_{DA}}\right)^{1/6} \quad (5.7)$$

As shown in **Table 5.4** and **5.5**, the calculated distances between Tb and the AuNP surface globally range from 4.2 nm to 54.7 nm (excluding an unrealistic 0.8 nm value). The calculated distances spans a very large distance range with almost all values far beyond a distance that could be attained by the dimensions of the streptavidin-biotin pair separating the Tb donors from the gold nanosurface. Moreover, these calculated distances do not show much consistency between the results for 5 nm, 30 nm, 50 nm and 80 nm particles.

For NSET analysis, the R_0^{NSET} was calculated by **Equation 5.8**. [123],[134]

$$R_0^{\mathrm{NSET}} = \left[0.225 \frac{\Phi_{\mathrm{D}}}{\omega_{\mathrm{D}}} \frac{1}{\omega_{\mathrm{F}} k_{\mathrm{F}}} c^3\right]^{1/4} \tag{5.8}$$

Where ω_{D} is the angular frequency of the donor electronic transition, ω_{F} and k_{F} are the angular frequency and the Fermi vector for bulk gold, respectively, and c is the speed of light. R_0^{NSET} was 7.2 nm for all three different sizes of AuNPs (**Table 5.6**), since it is independent of nanoparticle diameter (energy transfer to a surface).

Table 5.6. NSET model of resonance energy transfer from Tb to AuNPs

c (m/s):	3 x 10^8
Φ_{D}:	0.64
ω_{D} (s^{-1}):	3.8 x 10^{15}
ω_{F} (s^{-1}):	8.4 x 10^{15}
k_{F} (m^{-1})	1.2 x 10^{10}
R_0 (nm):	7.2

The Tb-AuNP distance (R) was calculated using Equation (5.9).[5]

$$R = R_0^{\mathrm{NSET}} \left(\frac{\tau_{\mathrm{DA}}}{\tau_{\mathrm{D}} - \tau_{\mathrm{DA}}}\right)^{1/4} \tag{5.9}$$

With the PL decay times for the donor and the donor–acceptor assemblies as determined above, and the R_0^{NSET} determined using the NSET theory, Tb–AuNP distances R were obtained and are collected in **Table 5.7**. All the distances found are in the 4.0–6.4 nm range and do not show a strong dependence on the acceptor AuNP diameter. Moreover, these distances are well in line with the estimated average distance of the Tb complexes conjugated randomly to the sAv binding via biotin to the surface of the AuNP (**Figure 5.1**).

Table 5.7. Tb-AuNP surface distances *R* calculated from the experimental luminescence decay times and the NSET theory. Decay times obtained using the Kohlrausch model can be compared to those obtained using multi-exponential model.

	Kohlrausch decay model		**Multi-exponential decay model**	
AuNP diam. (nm)	R/R_0^{NSET}	R (nm) [a]	R/R_0^{NSET}	R (nm) [a]
5	0.87 (±0.01)	6.3 (±0.6)	0.88 (±0.01)	6.4 (±0.7)
30	0.55 (±0.01)	4.0 (±0.4)	0.63 (±0.03)	4.5 (±0.3)
50	0.72 (±0.01)	5.2 (±0.5)	0.72 (±0.01)	5.2 (±0.6)
80	0.55 (±0.02)	4.0 (±0.4)	0.62 (±0.03)	4.5 (±0.5)

(a) Using R_0^{NSET} = 7.2(±0.7) nm, assuming 10% uncertainty on R_0^{NSET}

When considering the overall uncertainty on the donor–acceptor distances R derived from the experimental luminescence decay measurements, we distinguish two main sources of uncertainty, the first being the experimental error on the experimental decay times and the second being the uncertainty on the value on R_0^{NSET}. To separate these two contributions to the overall uncertainty, we have included the ratio R/R_0^{NSET} in **Table 5.7**. This ratio thus depends solely on the uncertainty of the experimental measurements, which is relatively small. The uncertainty on R_0^{NSET} was estimated to be 10% and represents a systematic uncertainty. The NSET model afforded a set of donor–acceptor distances that are similar for various AuNP diameters studied and consistent with the expected structure of Tb-sAv/biot-AuNP assemblies.

5.4 Conclusion

We have demonstrated efficient energy transfer between Tb donors and AuNP acceptors within different Tb-sAv/biot-AuNPs assemblies for AuNPs of 5nm, 30 nm, 50 nm, and 80 nm diameter. Characterization by RLS and time-resolved PL spectroscopy demonstrated the assembly of Tb-sAv to biot-AuNP with ratios up to 2 (5 nm AuNPs), 75 (30 nm AuNPs), 208 (50 nm AuNPs), and 533 (80 nm AuNPs) Tb-sAv per biot-AuNP, in good agreement with expectations based on the surface areas of the particles and the biotinylation density of the AuNPs. The stable Tb-sAv/biot-AuNP assemblies were investigated at different concentrations, Tb-sAv per biot-AuNP ratios, and AuNP sizes in aqueous solutions by time-resolved PL spectroscopy. The resulting PL decay curves were studied using both multi-exponential and Kohlrausch (stretched exponential) PL lifetime models, which yielded mutually consistent results. The analyses showed that energy transfer efficiencies were independent of the AuNP size. In contrast to FRET, NSET theory provided a coherent analysis of the experimental energy transfer results. The Tb donor to Au-NP surface acceptor distances determined based on NSET proved in excellent agreement with the structural conditions of the biotin-sAv binding on the AuNP surface. Our results present strong evidence favoring NSET over FRET as the operational energy transfer mechanism for the PL quenching of electric dipole emitters by AuNPs.

When comparing the quenching efficiencies predicted by NSET and by FRET, we find that NSET predicts less quenching for a given donor–acceptor distance, especially at shorter distance. This makes it more likely that fluorescence of fluorophores attached to plasmonic nanoparticles is partially retained and can still be useful for the detection of such assemblies. Moreover, successful design and optimization of biosensors such as "nano-flares"[218],[219] and molecular rulers[135] based on AuNP PL quenching is clearly dependent on the understanding of the underlying energy-transfer mechanism, to which our study has contributed important findings in favor of NSET.

6. Summary and outlook

This thesis presents the successful understanding and application of FRET modulated multi-hybrid nanoparticles based time-resolved multiplexing and the study of energy transfer mechanism from long lifetime Tb donors to AuNP. In a holistic approach, extensive spectroscopic analysis with Monte-Carlo simulations are combined to explain the interactions within multiple donor-acceptor FRET network, containing up to 191 lanthanide complexes and up to 60 fluorescent dyes attached to a single QD. And even highly complicated FRET nanosystems with up to four different hetero-FRET and homo-FRET pathways and non-fluorescent dimer formation concerning more than 100 participating donors and acceptors per one QD can be understood by time-resolved and steady-state PL spectroscopy and adequate modeling and simulation. Moreover, two strategies are developed for single-nanoparticle multiplexing. One is achieved by using different lanthanide donor and tunable D-A distance. Thus, tunable lifetime of QD can be obtained by attaching Tb or Eu complexes and well-defined silica shell, lead to single excitation, single wavelength, and single nanoparticle based live-cell barcoding. Another strategy is achieved by using multiple donors and acceptors. Multiple donors can enhance sensitizing QD PL without altering significantly the PL lifetime, while multiple acceptors change PL lifetime of QD, which means both lifetime and intensity of QD can be tuned independently. The control of such FRET-modulated multi-hybrid QDs can be used for designing a novel concept of optical multiplexing or barcoding, which has the potential to significantly advance multiplexed in-vitro diagnostics and cellular biology, security labeling, optical encryption, data storage, and molecular computing. Single-wavelength excitation and single-wavelength detection are employed to distinguish multiple FRET-encoded microbeads within a single microscopy image at constant contrast: Brightness-equalized single-color multiplexed imaging.

Due to the independent tunable color, lifetime and intensity in multi-hybrid QDs can be achieved by using different QDs, multiple and different donors, and multiple acceptors, we can fabricate 3D barcoding by combining three parameter and largely increase the information density of barcoding. Moreover, we can also

introduce polarization as a 4th dimension by using quantum rods (QRs). Furthermore, the enhanced single-nanoparticle barcoding can be functionalized with aptamer or cell-penetrating peptides which can uniquely identify and track targeted cells in different cells mixture.

The third study shows the NSET model provided excellent agreement between the Tb-to-AuNP surface distance estimated by the biotin-streptavidin interaction and calculated by the PL lifetime analysis. However, we only study the energy transfer mechanism in constant distance (~4.5 nm) between Tb and AuNP surface. In the case of large AuNP, the SPR may cause the energy transfer to varying degrees in different distance from the AuNP. In order to deeply understand the energy transfer phenomenon on the surface of AuNP, AuNP can be coated with silica shell before attaching with Tb donors.

7. Appendix

7.1 Abbreviations

A	acceptor
Abs.	absorption
biot	biotin
BRET	bioluminescence resonance energy transfer
BSA	bovine serum albumin
CB	conduction band
ChA	acceptor channel
ChD	donor channel
CRET	chemiluminescence resonance energy transfer
CTU	cooperative transfer upconversion
D	donor
d-dots	doped-quantum dots
DHLA	dihydrolipoic acid
DMF	dimethylformamide
DMEM	Dulbecco's modified eagle medium
DNA	deoxyribonucleic acid
ESA	excited-state absorption
EMU	energy migration-mediated upconversion

ETU	energy transfer upconversion
FBS	fetal bovine serum
FLIM	fluorescence lifetime imaging microscopy
FRET	Förster resonance energy transfer
FWHM	full-width-at-half-maximum
His6	hexahistidine
IR	infrared
IRF	instrument response function
Ln	lanthanides
LLCs	luminescent lanthanide complexes
LS	lattice strain
LTC	lanthanide terbium complex
MAA	mercaptoacetic acid
Mal	maleimide
MBP	maltose-binding protein
MCS	multichannel scalers
MMPs	matrix metalloproteinases
MPA	mercaptopropionic acid
MPS	(3-mercaptopropyl) trimethoxysilane
MUA	mercaptoundecanoic acid

NHS	N-hydroxysuccinimide
NIR	near infrared
NP	nanoparticle
NP-5	poly (ethylene glycol) nonylphenyl ether
NSET	nanosurface energy transfer
PBS	phosphate-buffered saline
PEG	poly(ethylene glycol)
PL	photoluminescence
PMT	photomultiplier tube
QD	quantum dot
QY	quantum yield
Ref.	reference
RET	resonance energy transfer
sAv	streptavidin
SET	surface energy transfer
SPB	surface plasmon band
SPR	surface plasmon resonance
STED	stimulated emission depletion
TCSPC	time-correlated single-photon counting
TEM	transmission electron microscopy

TEOS	tetraethyl orthosilicate
TG	time-gated
TR	time-resolved
UC	upconversion
UCNP	upconversion nanoparticle
UV	ultraviolet
VB	valence band
Vis	visible

7.2 Simulation methods

Monte-Carlo simulations were based on a previously published concept[4],[5] tailored to our specific system by modifying our exiFRET code,[6] most notably to enable FRET to occur between multiple fluorophore types including homo-FRET and to incorporate non-radiative de-excitation. In this approach, the fluorescence coming from a given configuration of fluorophores is calculated by modelling the evolution of a set of "excitons" generated by the adsorption of discrete incoming photons. These incoming photons cause the excitation of specific fluorophores for a period of time during which they cannot absorb another photon, but may become de-excited again either through the emission of a photon (fluorescence), non-radiative de-excitation, or else energy transfer to another fluorophore. The acceptor of an energy transfer event also remains excited for a period of time during which it is not available for further excitation, and itself can be de-excited through fluorescence, non-radiative de-excitation or further energy transfer. In the new scheme, all fluorophores can act as acceptors and a single exciton can participate in multiple energy transfer events.

The method proceeds as shown in **Figure 7.1**, which includes variations on our initially published approach.[5] We begin by generating coordinates of the fluorophores. In this case, the QD was assumed to be at the center of a spherical nanoparticle with the Tb and Cy5.5 distributed randomly on the surface of the sphere. From this, the distance between each pair of fluorophores and the transfer probability can be calculated. Next, a schedule of arrival times and targets of each incident photon are determined. This is based upon the irradiance of the laser specified assuming steady-state excitation. Photons are assumed to be absorbed by only one type of fluorophore chosen for each system to match wavelength of the incident laser, with the specific fluorophore determined randomly. Finally, each of the events following each incident photon are played out and the number of fluorescence, non-radiative de-excitation, and transfer events is recorded.

To do this last step, we first check that the donor is available for excitation of a photon from the laser. Then we calculate the rate of energy release using the lifetime of the fluorophore and the availability of all potential energy transfer

partners. Using this, the time at which the fluorophore de-excites can be derived using a randomized Monte-Carlo approach to select a time matching this release rate. Next, we use another Monte-Carlo step to determine if the fluorophore de-excites via non-radiative energy loss (based upon its quantum yield), fluorescence, or energy transfer. If the result is energy transfer, the time and target of transfer is inserted into the excitation schedule along with all the incident photons so that it can be played out in sequence with the others. Once all excitation events from the incident laser of energy transfer have been played out, we repeat the entire process with a new randomly generated configuration of fluorophores. Finally, once the desired number of configurations have been tested, the average number of fluorescence, energy transfer, and non-radiative de-excitation events from each fluorophore type for each configuration are output for analysis.

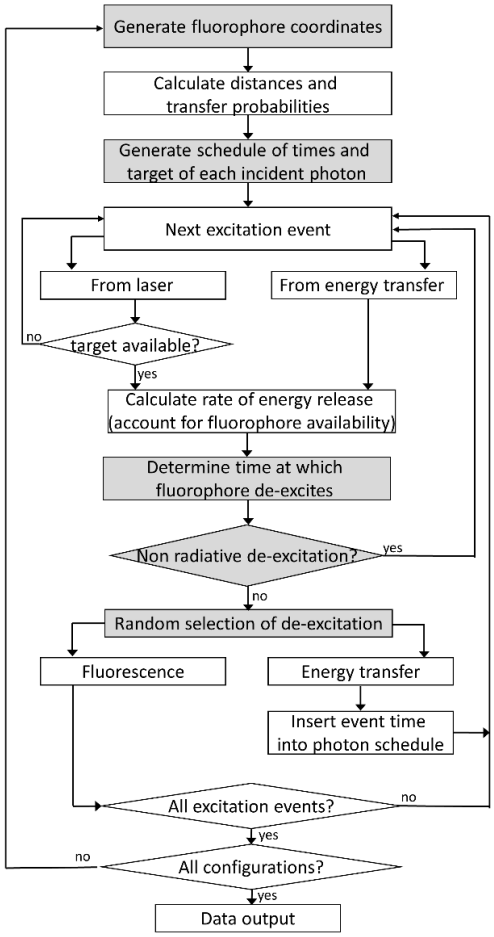

Figure 7.1. Flowchart of the steps involved in the Monte Carlo simulation scheme. Processes involving a random number generator are indicated by a shaded background.

In this work, we used 100 configurations and 10,000 incident photons for each data point shown in the MCS results. The size of the nanoparticles was determined by fitting the particle radius to match the experimental transfer efficiency for system 1. Because our simulation is designed for steady-state excitation, to emulate pulsed excitation in which all the incident photons arrive almost simultaneously, we fit the intensity ratio in **Figure 4.10d** at 200 Tb per QD to obtain the equivalent steady-state laser intensity to match the behavior of the pulsed system. An approximation in our method is that we determine all the available acceptors for energy transfer and thus whether the fluorophore de-excites via fluorescence, energy transfer, or non-radiative de-excitation at the time at which the donor fluorophore becomes excited. While this is suitable for the case of short lifetime donors under steady state excitation, it can break down for long lifetime donors as discussed in the thesis.

7.3 FRET-modulated multi-hybrid nanoparticles

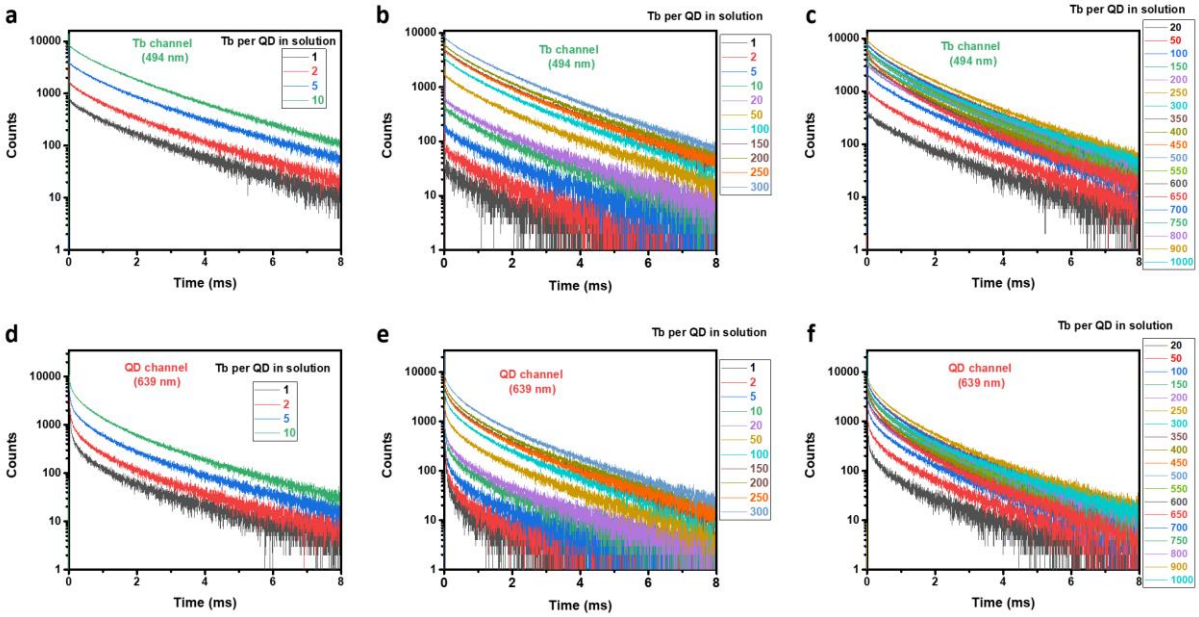

Figure 7.2. FRET system 1 (*m*Tb-QD): PL decays of Tb donor (**a**, **b**, and **c**) and QD acceptor (**d**, **e**, and **f**) at different ratios of Tb per QD. To accomplish a sufficient amount of PL photons for PL decay time analysis, excitation laser (337.1 nm) intensities and concentrations were adapted. Conditions are the same for **a** and **d**, **d** and **e**, and **c** and **f**, respectively. The selected curves in **Figure 4.10** show normalized PL decay curves from all three conditions (**a/d**, **b/e**, and **c/f**). Normalization was done by comparing the decay curves of overlapping ratios of Tb per QD in solution for the three different conditions.

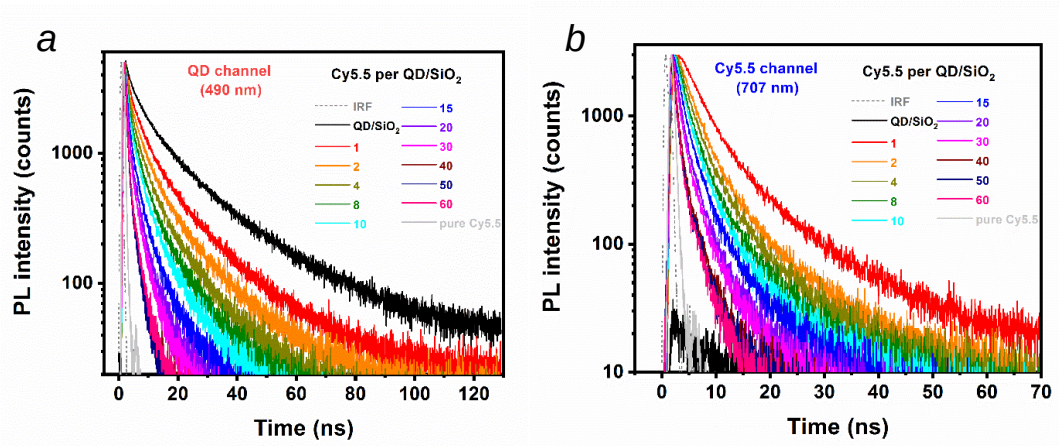

Figure 7.3. FRET system 2 (QD-*n*Cy5.5): PL decays of QD donor **(a)** and Cy5.5 acceptor **(b)** from FRET system 2 (QD-*n*Cy5.5) for increasing *n*.

Table 7.1. FRET system 1 (*m*Tb-QD): Results of PL decay fitting (PL decay curves shown in **Figure 7.2 d, e, and f** for **A**; decay curves for the fitting results in **B** and **C** were similar and are not shown) of FRET-sensitized QD acceptor PL using **Equations 4.13**, **4.14**, and **4.7**. Fit range: 0.1 to 8 ms.

A (191 Lumi4 per QD)

Experiment	c(QD)	Tb per QD in solution	$A\alpha_{AD1*}$	α_{AD1*}	τ_{AD1} (ms)	k_{FRET1}	α_{AD1}	$A\alpha_{AD2*}$	α_{AD2*}	τ_{AD2} (ms)	k_{FRET2}	α_{AD2}	B	τ_D (ms)	χ^2	τ_{AD}(ms)	E_{FRET}
1	5 nM	1	279	0.546	0.13	7.32	0.14	232	0.454	0.72	1.02	0.86	81	2.7	1.327	0.64	76%
		2	479	0.515	0.16	5.88	0.14	451	0.485	0.80	0.88	0.86	148	2.7	1.250	0.71	74%
		5	906	0.460	0.18	5.19	0.12	1063	0.540	0.83	0.83	0.88	349	2.7	1.222	0.75	72%
		10	1965	0.448	0.20	4.63	0.12	2417	0.552	0.87	0.78	0.88	715	2.7	1.162	0.79	71%
2	5 nM	2	44.3	0.572	0.12	7.96	0.17	33.2	0.428	0.63	1.22	0.83	11	2.7	1.244	0.54	80%
		5	69.1	0.522	0.12	7.96	0.13	63.2	0.478	0.70	1.06	0.87	21	2.7	1.333	0.63	77%
		10	133	0.502	0.16	5.88	0.13	132	0.498	0.82	0.85	0.87	39	2.7	1.393	0.74	73%
		20	178	0.504	0.19	4.89	0.14	175	0.496	0.89	0.75	0.86	50	2.7	1.302	0.80	71%
		50	481	0.480	0.20	4.63	0.13	521	0.520	0.91	0.73	0.87	125	2.7	1.241	0.82	70%
		100	928	0.461	0.21	4.39	0.13	1087	0.539	0.90	0.74	0.87	250	2.7	1.197	0.81	70%
		150	1420	0.461	0.20	4.63	0.12	1663	0.539	0.90	0.74	0.88	369	2.7	1.207	0.82	70%
		200	1646	0.451	0.20	4.63	0.12	2005	0.549	0.89	0.75	0.88	464	2.7	1.204	0.81	70%
		250	1362	0.475	0.21	4.39	0.13	1503	0.525	0.93	0.70	0.87	342	2.7	1.162	0.84	69%
		300	2399	0.459	0.21	4.39	0.12	2826	0.541	0.91	0.73	0.88	646	2.7	1.201	0.82	69%
3	0.5 nM	20	103	0.472	0.16	5.88	0.12	115	0.528	0.78	0.91	0.88	33	2.7	1.443	0.70	74%
		50	260	0.470	0.20	4.63	0.13	293	0.530	0.89	0.75	0.87	63	2.7	1.303	0.80	70%
		100	482	0.438	0.19	4.89	0.11	618	0.562	0.86	0.79	0.89	128	2.7	1.278	0.78	71%
		150	848	0.468	0.21	4.39	0.12	963	0.532	0.93	0.70	0.88	206	2.7	1.184	0.84	69%
		200	731	0.450	0.20	4.63	0.12	893	0.550	0.88	0.77	0.88	175	2.7	1.204	0.80	70%
		250	1009	0.461	0.22	4.18	0.13	1182	0.539	0.92	0.72	0.87	256	2.7	1.189	0.83	69%
		300	1027	0.464	0.22	4.18	0.13	1186	0.536	0.93	0.70	0.87	262	2.7	1.225	0.84	69%
		350	828	0.443	0.19	4.89	0.12	1042	0.557	0.85	0.81	0.88	190	2.7	1.249	0.77	71%
		400	1228	0.490	0.21	4.39	0.15	1276	0.510	0.87	0.78	0.85	190	2.7	1.269	0.77	71%
		450	1870	0.451	0.21	4.39	0.13	2275	0.549	0.87	0.78	0.87	394	2.7	1.248	0.79	71%
		500	1366	0.467	0.22	4.18	0.14	1560	0.533	0.89	0.75	0.86	251	2.7	1.204	0.80	70%
		550	1367	0.446	0.20	4.63	0.12	1700	0.554	0.87	0.78	0.88	283	2.7	1.226	0.79	71%
		600	1819	0.457	0.21	4.39	0.13	2165	0.543	0.87	0.78	0.87	378	2.7	1.257	0.78	71%
		700	1930	0.462	0.21	4.39	0.13	2247	0.538	0.87	0.78	0.87	352	2.7	1.218	0.78	71%
		800	1534	0.465	0.21	4.39	0.13	1765	0.535	0.90	0.74	0.87	325	2.7	1.240	0.81	70%
		900	2309	0.459	0.22	4.18	0.13	2719	0.541	0.90	0.74	0.87	481	2.7	1.206	0.81	70%
		1000	1560	0.474	0.21	4.39	0.14	1733	0.526	0.88	0.77	0.86	362	2.7	1.184	0.79	71%
															average	**0.77**	**71%**

B (191 Lumi4 per QD)

Experiment	c(QD)	Tb per QD in solution	$A\alpha_{AD1}$	α_{AD1*}	τ_{AD1} (ms)	k_{FRET1}	α_{AD1}	$A\alpha_{AD2}$	α_{AD2*}	τ_{AD2} (ms)	k_{FRET2}	α_{AD2}	B	τ_D (ms)	χ^2	τ_{AD}(ms)	E_{FRET}
1	5 nM	1	685	0.525	0.16	5.88	0.23	620	0.475	0.80	0.88	0.86	227	2.7	1.297	0.72	73%
		2	1080	0.485	0.17	5.51	0.22	1145	0.515	0.83	0.83	0.88	388	2.7	1.196	0.76	72%
		5	2467	0.420	0.19	4.89	0.21	3406	0.580	0.85	0.81	0.89	1020	2.7	1.182	0.80	70%
		10	4357	0.355	0.19	4.89	0.18	7919	0.645	0.88	0.77	0.92	2261	2.7	1.199	0.84	69%
2	5 nM	5	706	0.522	0.20	4.63	0.26	646	0.478	0.88	0.77	0.85	204	2.7	1.190	0.80	70%
		10	1419	0.477	0.19	4.89	0.24	1553	0.523	0.85	0.81	0.87	477	2.7	1.185	0.78	71%
		20	2224	0.444	0.20	4.63	0.23	2790	0.556	0.87	0.78	0.88	825	2.7	1.194	0.81	70%
		50	4879	0.349	0.19	4.89	0.18	9096	0.651	0.90	0.74	0.92	2318	2.7	1.240	0.87	68%
3	5 nM	5	98.5	0.520	0.12	7.96	0.20	90.8	0.480	0.72	1.02	0.88	26	2.7	1.342	0.66	76%
		10	174	0.494	0.15	6.30	0.21	178	0.506	0.80	0.88	0.88	52	2.7	1.400	0.74	73%
		20	242	0.460	0.15	6.30	0.20	284	0.540	0.80	0.88	0.89	83	2.7	1.334	0.74	72%
		50	732	0.467	0.19	4.89	0.23	837	0.533	0.88	0.77	0.88	236	2.7	1.166	0.82	70%
		100	1420	0.472	0.21	4.39	0.24	1589	0.528	0.91	0.73	0.87	426	2.7	1.171	0.84	69%
		150	2014	0.448	0.21	4.39	0.24	2478	0.552	0.89	0.75	0.88	645	2.7	1.149	0.83	69%
4	0.5 nM	50	413	0.447	0.18	5.19	0.21	510	0.553	0.87	0.78	0.89	123	2.7	1.303	0.81	70%
		100	402	0.445	0.18	5.19	0.21	502	0.555	0.88	0.77	0.89	119	2.7	1.249	0.82	69%
		150	805	0.451	0.19	4.89	0.22	978	0.549	0.89	0.75	0.89	251	2.7	1.232	0.83	69%
		200	611	0.435	0.19	4.89	0.22	793	0.565	0.87	0.78	0.89	204	2.7	1.257	0.82	70%
		250	824	0.428	0.19	4.89	0.22	1102	0.572	0.86	0.79	0.89	287	2.7	1.189	0.81	70%
		300	1284	0.458	0.21	4.39	0.24	1521	0.542	0.90	0.74	0.88	346	2.7	1.215	0.84	69%
		350	1015	0.432	0.19	4.89	0.22	1335	0.568	0.84	0.82	0.89	298	2.7	1.218	0.79	71%
		400	1220	0.447	0.21	4.39	0.23	1507	0.553	0.90	0.74	0.88	371	2.7	1.222	0.84	69%
		450	1232	0.459	0.22	4.18	0.24	1453	0.541	0.92	0.72	0.87	359	2.7	1.241	0.86	68%
		500	1420	0.455	0.22	4.18	0.24	1698	0.545	0.91	0.73	0.87	355	2.7	1.194	0.85	69%
		550	1105	0.464	0.22	4.18	0.25	1279	0.536	0.90	0.74	0.87	323	2.7	1.253	0.84	69%
		600	1806	0.462	0.22	4.18	0.25	2104	0.538	0.90	0.74	0.87	457	2.7	1.169	0.84	69%
		650	1501	0.453	0.21	4.39	0.24	1813	0.547	0.90	0.74	0.88	433	2.7	1.247	0.84	69%
		700	1579	0.456	0.21	4.39	0.24	1883	0.544	0.90	0.74	0.88	464	2.7	1.154	0.84	69%
		750	1851	0.472	0.22	4.18	0.25	2073	0.528	0.92	0.72	0.87	456	2.7	1.157	0.85	68%
		800	1735	0.451	0.21	4.39	0.24	2112	0.549	0.89	0.75	0.88	489	2.7	1.243	0.83	69%
		900	2020	0.466	0.22	4.18	0.25	2315	0.534	0.89	0.75	0.86	438	2.7	1.247	0.82	69%
		1000	2831	0.432	0.22	4.18	0.24	3729	0.568	0.90	0.74	0.88	929	2.7	1.285	0.85	69%
															average	**0.81**	**70%**

C (136 Lumi4 per QD)

Experiment	c(QD)	Tb per QD in solution	$A\alpha_{AD1}$	α_{AD1*}	τ_{AD1} (ms)	k_{FRET1}	α_{AD1}	$A\alpha_{AD2}$	α_{AD2*}	τ_{AD2} (ms)	k_{FRET2}	α_{AD2}	B	τ_D (ms)	χ^2	τ_{AD}(ms)	E_{FRET}
1	5 nM	2	555	0.554	0.14	6.77	0.22	447	0.446	0.78	0.91	0.86	130	2.7	1.632	0.70	74%
		10	1286	0.546	0.17	5.51	0.24	1068	0.454	0.87	0.78	0.85	299	2.7	1.262	0.78	71%
		20	2938	0.529	0.18	5.19	0.24	2614	0.471	0.87	0.78	0.86	712	2.7	1.287	0.79	71%
2	5 nM	5	106	0.628	0.12	7.96	0.22	62.9	0.372	0.74	0.98	0.83	33	2.7	1.471	0.64	76%
		10	150	0.588	0.14	6.77	0.22	105	0.412	0.82	0.85	0.85	53	2.7	1.311	0.73	73%
		50	704	0.576	0.17	5.51	0.23	519	0.424	0.95	0.68	0.86	249	2.7	1.230	0.85	68%
		100	1472	0.569	0.19	4.89	0.24	1117	0.431	0.97	0.66	0.85	535	2.7	1.263	0.87	68%
		200	2659	0.554	0.19	4.89	0.24	2141	0.446	0.96	0.67	0.85	962	2.7	1.224	0.87	68%
3	0.5 nM	20	110	0.593	0.14	6.77	0.22	75.5	0.407	0.83	0.83	0.85	29	2.7	1.149	0.73	73%
		50	506	0.558	0.18	5.19	0.24	401	0.442	0.94	0.69	0.86	172	2.7	1.240	0.85	69%
		100	1088	0.557	0.18	5.19	0.23	864	0.443	0.96	0.67	0.86	370	2.7	1.246	0.87	68%
		150	1552	0.554	0.18	5.19	0.24	1251	0.446	0.93	0.70	0.86	537	2.7	1.247	0.84	69%
		200	2232	0.546	0.19	4.89	0.24	1859	0.454	0.93	0.70	0.85	753	2.7	1.196	0.84	69%
		250	2144	0.537	0.18	5.19	0.23	1851	0.463	0.91	0.73	0.86	785	2.7	1.260	0.82	69%
		300	2443	0.545	0.19	4.89	0.24	2041	0.455	0.95	0.68	0.86	830	2.7	1.216	0.86	68%
		350	2272	0.552	0.19	4.89	0.24	1842	0.448	0.95	0.68	0.85	742	2.7	1.236	0.86	68%
		400	2562	0.539	0.19	4.89	0.24	2189	0.461	0.93	0.70	0.86	898	2.7	1.215	0.84	69%
		450	1858	0.560	0.19	4.89	0.24	1458	0.440	0.96	0.67	0.85	604	2.7	1.200	0.86	68%
		500	2143	0.542	0.19	4.89	0.24	1811	0.458	0.94	0.69	0.86	755	2.7	1.148	0.85	68%
		550	2754	0.546	0.19	4.89	0.24	2290	0.454	0.95	0.68	0.86	940	2.7	1.225	0.86	68%
		600	2069	0.548	0.18	5.19	0.24	1704	0.452	0.92	0.72	0.86	709	2.7	1.149	0.83	69%
		650	2486	0.555	0.19	4.89	0.24	1991	0.445	0.95	0.68	0.85	798	2.7	1.208	0.86	68%
		700	2931	0.534	0.19	4.89	0.24	2554	0.466	0.92	0.72	0.86	1047	2.7	1.222	0.83	69%
		750	2801	0.538	0.19	4.89	0.24	2406	0.462	0.93	0.70	0.86	969	2.7	1.235	0.84	69%
		800	2884	0.546	0.20	4.63	0.25	2396	0.454	0.95	0.68	0.85	971	2.7	1.190	0.86	68%
		900	2826	0.546	0.19	4.89	0.24	2353	0.454	0.94	0.69	0.85	937	2.7	1.230	0.85	69%
		1000	3068	0.546	0.19	4.89	0.24	2546	0.454	0.94	0.69	0.85	1037	2.7	1.197	0.85	69%
															average	0.82	70%

Note: Average values (and the resulting errors) of all three tables (each consisting of different experiments, as indicated by the different background colors) were used to calculate the FRET efficiencies presented in **Figure 4.10c** in the manuscript. Experiments shown in red font were not used for the calculations of the data in **Figure 4.10c** because the PL intensities were too low or the background of unquenched Tb PL was too high.

Table 7.2. FRET system 1 (*m*Tb-QD): Results of PL decay fitting (PL decay curves shown in **Figure 7.2 a, b, and c** for **A**; decay curves for the fitting results in **B** were similar and are not shown) of FRET-quenched Tb donor PL using **Equations 4.15**, **4.16**, and **4.10**. Fit range as indicated.

A (191 Lumi4 per QD)

Experiment	c(QD)	Tb per QD in solution	$A\alpha_{DA1*}$	α_{DA1*}	τ_{DA1} (ms)	$A\alpha_{DA2*}$	α_{DA2*}	τ_{DA2} (ms)	B	τ_D (ms)	χ^2	τ_{DA}(ms)	E_{FRET}	fit range
1	5 nM	1	143	0.290	0.30	350	0.710	1.10	214	2.7	1.345	0.87	68%	0.05-8ms
		2	288	0.263	0.29	807	0.737	1.10	439	2.7	1.327	0.89	67%	
		5	652	0.260	0.34	1859	0.740	1.10	1161	2.7	1.269	0.90	67%	
		10	1425	0.247	0.27	4338	0.753	1.10	2257	2.7	1.236	0.89	67%	
2	5 nM	2	55.2	0.543	0.01	46.4	0.457	0.78	24	2.7	1.333	0.36	87%	0.01-8ms
		5	30.3	0.233	0.19	100	0.767	0.98	51	2.7	1.569	0.80	71%	
		10	69.2	0.220	0.18	246	0.780	0.99	117	2.7	1.425	0.81	70%	
		20	91.3	0.199	0.15	367	0.801	0.98	162	2.7	1.403	0.81	70%	
		50	251	0.188	0.18	1082	0.812	1.00	409	2.7	1.314	0.85	69%	
		100	614	0.226	0.26	2105	0.774	1.10	731	2.7	1.320	0.91	66%	
		150	1040	0.258	0.33	2991	0.742	1.10	992	2.7	1.260	0.90	67%	
		200	1151	0.238	0.28	3690	0.762	1.10	1242	2.7	1.241	0.91	66%	
		250	925	0.247	0.33	2814	0.753	1.10	953	2.7	1.270	0.91	66%	
		300	1693	0.251	0.27	5048	0.749	1.10	1681	2.7	1.250	0.89	67%	
3	0.5 nM	20	74.4	0.241	0.11	234	0.759	0.94	100	2.7	1.484	0.74	73%	
		50	196	0.235	0.21	639	0.765	1.00	186	2.7	1.422	0.81	70%	
		100	421	0.243	0.23	1313	0.757	1.00	391	2.7	1.281	0.81	70%	
		150	582	0.212	0.22	2160	0.788	1.00	692	2.7	1.281	0.83	69%	
		200	601	0.232	0.23	1985	0.768	1.00	548	2.7	1.352	0.82	70%	
		250	789	0.231	0.26	2629	0.769	1.10	823	2.7	1.363	0.91	66%	
		300	803	0.227	0.22	2741	0.773	1.00	872	2.7	1.280	0.82	70%	
		350	861	0.270	0.26	2322	0.730	1.00	565	2.7	1.341	0.80	70%	
		400	1206	0.287	0.21	3003	0.713	0.95	639	2.7	1.352	0.74	73%	
		450	1798	0.269	0.24	4881	0.731	1.00	1174	2.7	1.273	0.80	71%	
		500	1204	0.254	0.25	3536	0.746	1.00	788	2.7	1.293	0.81	70%	
		550	1277	0.252	0.26	3783	0.748	1.00	862	2.7	1.319	0.81	70%	
		600	1845	0.282	0.23	4699	0.718	1.00	1129	2.7	1.318	0.78	71%	
		700	1875	0.275	0.25	4943	0.725	1.00	1080	2.7	1.308	0.79	71%	
		800	1384	0.260	0.24	3948	0.740	1.00	1084	2.7	1.243	0.80	70%	
		900	2164	0.275	0.26	5694	0.725	1.10	1398	2.7	1.348	0.87	68%	
		1000	1469	0.277	0.24	3836	0.723	1.00	1159	2.7	1.260	0.79	71%	
											average	**0.82**	**70%**	

B (191 Lumi4 per QD)

Experiment	c(QD)	Tb per QD in solution	$A\alpha_{DA1}$	α_{DA1*}	τ_{DA1} (ms)	$A\alpha_{DA2}$	α_{DA2*}	τ_{DA2} (ms)	B	τ_D (ms)	χ^2	τ_{DA}(ms)	E_{FRET}	fit range
1	5 nM	1	429	0.256	0.18	1249	0.744	0.99	808	2.7	1.284	0.78	71%	0.05-8ms
		2	717	0.235	0.19	2340	0.765	1.00	1431	2.7	1.216	0.81	70%	
		5	2008	0.241	0.23	6334	0.759	1.10	3521	2.7	1.235	0.89	67%	
		10	3528	0.228	0.15	11972	0.772	1.20	7852	2.7	1.216	0.96	64%	
2	5 nM	5	387	0.223	0.15	1348	0.777	0.95	720	2.7	1.283	0.77	71%	0.02-8ms
		10	1027	0.253	0.16	3034	0.747	0.99	1618	2.7	1.328	0.78	71%	
		20	1979	0.278	0.21	5137	0.722	1.10	2783	2.7	1.291	0.85	68%	0.01-8ms
		50	4984	0.272	0.13	13339	0.728	1.20	7268	2.7	1.212	0.91	66%	
3	5 nM	5	44	0.228	0.16	149	0.772	0.95	72	2.7	1.464	0.77	71%	0.02-8ms
		10	89	0.204	0.09	347	0.796	0.88	176	2.7	1.323	0.72	73%	
		20	160	0.228	0.13	543	0.772	0.95	264	2.7	1.353	0.76	72%	0.01-8ms
		50	434	0.203	0.19	1699	0.797	1.00	772	2.7	1.321	0.84	69%	
		100	913	0.227	0.26	3111	0.773	1.10	1307	2.7	1.250	0.91	66%	
		150	1478	0.247	0.27	4514	0.753	1.10	1847	2.7	1.213	0.90	67%	
4	0.5 nM	50	373	0.240	0.17	1178	0.760	0.96	440	2.7	1.368	0.77	71%	
		100	307	0.218	0.19	1102	0.782	1.00	397	2.7	1.298	0.82	69%	
		150	659	0.243	0.26	2058	0.757	1.10	829	2.7	1.282	0.90	67%	
		200	497	0.220	0.21	1758	0.780	1.00	673	2.7	1.308	0.83	69%	
		250	712	0.238	0.27	2283	0.762	1.10	885	2.7	1.261	0.90	67%	
		300	1157	0.253	0.23	3420	0.747	1.00	1191	2.7	1.264	0.81	70%	
		350	1001	0.261	0.26	2838	0.739	1.00	926	2.7	1.329	0.81	70%	
		400	1090	0.252	0.26	3243	0.748	1.10	1189	2.7	1.340	0.89	67%	
		450	1078	0.248	0.25	3267	0.752	1.10	1207	2.7	1.325	0.89	67%	
		500	1223	0.241	0.25	3855	0.759	1.00	1176	2.7	1.274	0.82	70%	
		550	1064	0.265	0.28	2958	0.735	1.10	1063	2.7	1.275	0.88	67%	
		600	1807	0.277	0.24	4710	0.723	1.10	1443	2.7	1.295	0.86	68%	
		650	1192	0.237	0.26	3831	0.763	1.10	1371	2.7	1.267	0.90	67%	
		700	1289	0.246	0.27	3950	0.754	1.10	1476	2.7	1.239	0.90	67%	
		750	1664	0.282	0.25	4235	0.718	1.10	1349	2.7	1.310	0.86	68%	
		800	1511	0.255	0.25	4407	0.745	1.10	1514	2.7	1.271	0.88	67%	
		900	2026	0.286	0.23	5068	0.714	1.00	1384	2.7	1.321	0.78	71%	
		1000	2764	0.285	0.26	6949	0.715	1.20	2736	2.7	1.266	0.93	65%	
											average	**0.85**	**69%**	

Note: Average values (and the resulting errors) of both tables (each consisting of different experiments, as indicated by the different background colors) were used to calculate the FRET efficiencies presented in **Figure 4.10c** in the manuscript. Experiments shown in red font were not used for the calculations of the data in **Figure 4.10c** because the PL intensities were too low or the background of unquenched Tb PL was too high.

Table 7.3. FRET system 2 (QD-*n*Cy5.5): Results of PL decay fitting (PL decay curves shown in **Figure 7.3a** for **A**; decay curves for the fitting results in **B** were similar and are not shown) of FRET-quenched QD donor PL in FRET system 2 (QD-*n*Cy5.5) using **Equations 4.15**, **4.16**, and **4.10**. Fit range: 0.1 to 8 ms.

A

Cy5.5 per QD	$C\gamma_{DA1}$	τ_{DA1} (ns)	$C\gamma_{DA2}$	τ_{DA2} (ns)	$C\gamma_{DA3}$	τ_{DA3} (ns)	χ^2	τ_{DA} (ns)	E_{FRET}
0	0.0164	24.91	0.031	7.99	0.044	1.77	1.031	8.0 (τ_D)	0%
1	0.0101	20.29	0.032	6.16	0.057	1.45	1.014	4.9	39%
2	0.0076	18.29	0.033	5.42	0.078	1.24	1.051	3.5	56%
4	0.0062	15.86	0.029	4.88	0.080	1.19	1.094	2.9	64%
8	0.0051	14.71	0.029	4.40	0.125	1.02	1.291	2.1	74%
10	0.0043	13.50	0.028	3.93	0.120	0.92	1.16	1.8	78%
15	0.0022	13.82	0.023	3.85	0.160	0.89	1.258	1.4	83%
20	0.0018	11.65	0.021	3.27	0.154	0.80	1.427	1.2	85%
30	0.0013	11.69	0.019	3.14	0.183	0.76	1.394	1.0	88%
40	0.0010	8.91	0.018	1.95	0.096	0.48	1.318	0.8	90%
50	0.0007	9.53	0.015	2.03	0.097	0.48	1.291	0.7	91%
60	0.0009	10.30	0.015	2.27	0.109	0.50	1.313	0.8	90%

B

Cy5.5 per QD	$C\gamma_{DA1}$	τ_{DA1} (ns)	$C\gamma_{DA2}$	τ_{DA2} (ns)	$C\gamma_{DA3}$	τ_{DA3} (ns)	χ^2	τ_{DA} (ns)	E_{FRET}
0	0.0139	22.12	0.028	6.71	0.049	1.23	1.071	6.1 (τ_D)	0%
1	0.0112	19.23	0.033	5.70	0.078	1.07	1.098	4.0	34%
2	0.0058	16.31	0.028	4.92	0.084	1.19	1.147	2.8	54%
4	0.0050	15.96	0.027	4.88	0.089	1.18	1.175	2.6	57%
8	0.0047	15.41	0.025	4.64	0.096	1.09	1.182	2.3	62%
10	0.0043	12.44	0.024	3.72	0.117	0.77	1.088	1.6	74%
15	0.0022	14.24	0.020	3.76	0.167	0.86	1.096	1.3	79%
20	0.0018	8.97	0.021	2.89	0.168	0.69	1.155	1.1	82%
30	0.0013	4.32	0.030	1.47	0.179	0.46	1.178	0.7	89%
40	0.0010	4.89	0.014	1.96	0.159	0.58	1.218	0.8	87%
50	0.0007	3.81	0.058	0.99	0.195	0.38	1.09	0.6	90%
60	0.0009	4.27	0.019	1.43	0.115	0.40	1.121	0.6	90%

Note: Average values (and the resulting errors) of both tables were used to calculate the FRET efficiencies presented in **Figure 4.12e**.

Table 7.4. FRET system 2 (QD-*n*Cy5.5): FRET efficiencies calculated by steady-state PL intensities (from PL spectra shown in **Figure 4.12c** for **A**; PL spectra for the results in **B** were similar and are not shown) using **Equation 4.11**.

A

Cy5.5 per QD	I_{DA}/I_D	E_{FRET}
0	1.000	0%
1	0.776	22%
2	0.620	38%
4	0.514	49%
8	0.455	54%
10	0.327	67%
15	0.285	72%
20	0.192	81%
30	0.139	86%
40	0.103	90%
50	0.085	92%
60	0.068	93%

B

Cy5.5 per QD	I_{DA}/I_D	E_{FRET}
0	1.000	0%
1	0.793	21%
2	0.679	32%
4	0.546	45%
8	0.538	46%
10	0.425	58%
15	0.303	70%
20	0.227	77%
30	0.207	79%
40	0.149	85%
50	0.121	88%
60	0.092	91%

Note: Average values (and the resulting errors) of both tables were used to calculate the FRET efficiencies presented in **Figure 4.12e**.

Table 7.5. FRET system 2 (QD-nCy5.5): Calculation of R using the FRET-efficiencies from **Tables 7.3** and **7.4** and **Equation 4.12** with an R_0 = 6.0 nm.

n	E_{FRET} (QD - τ)	ΔE_{FRET}	R_0	R (nm) (QD - τ)	ΔR (nm)	E_{FRET} (QD - *I*)	ΔE_{FRET}	R_0	R (nm) (QD - *I*)	ΔR (nm)
1	0.37	0.03	6.0	6.6	0.2	0.22	0.01	6.0	7.4	0.1
2	0.55	0.02	6.0	6.5	0.1	0.35	0.04	6.0	7.5	0.3
4	0.61	0.05	6.0	7.0	0.3	0.47	0.02	6.0	7.7	0.2
8	0.68	0.08	6.0	7.5	0.5	0.50	0.06	6.0	8.5	0.4
10	0.76	0.03	6.0	7.3	0.2	0.62	0.07	6.0	8.1	0.4
15	0.81	0.03	6.0	7.4	0.3	0.71	0.01	6.0	8.1	0.1
20	0.83	0.02	6.0	7.5	0.2	0.79	0.02	6.0	7.9	0.2
30	0.88	0.01	6.0	7.6	0.1	0.83	0.05	6.0	8.1	0.5
40	0.88	0.02	6.0	7.9	0.3	0.87	0.03	6.0	8.0	0.4
50	0.91	0.01	6.0	7.9	0.2	0.90	0.03	6.0	8.0	0.4
60	0.90	0.001	6.0	8.2	0.1	0.92	0.02	6.0	7.9	0.4
			average	**7.7**	**0.2**	***R* (mean) = 7.9±0.6 nm**			**8.1**	**0.4**

Note: Values shown in red font were not used for calculating the average distances because of the relatively high uncertainties caused by the low values of n, which lead to FRET efficiencies in the very steep part of the increasing FRET efficiency curve in **Figure 4.12e**.

Table 7.6. FRET system 3 (mTb-QD-15Cy5.5): Results of PL decay fitting (PL decay curves shown in **Figure 4.16a** for **A**; decay curves for the fitting results in **B and C** were similar and are not shown) of FRET-quenched Tb donor PL using **Equations 4.15**, **4.16**, and **4.10**. Fit range: 0.02 to 8 ms.

A

Tb per QD-15Cy5.5 in solution	$A\alpha_{DA1}$	τ_{DA1} (ms)	$A\alpha_{DA2}$	τ_{DA2} (ms)	B	τ_D (ms)	χ^2	τ_{DA}(ms)	E_{FRET}
1	154	0.097	176	0.9	62	2.7	1.622	0.50	81%
2	286	0.15	333	0.9	120	2.7	1.571	0.57	79%
4	537	0.13	644	0.9	225	2.7	1.454	0.56	79%
8	1251	0.14	1489	0.9	499	2.7	1.486	0.56	79%
10	1566	0.15	1834	1.0	603	2.7	1.508	0.58	78%
15	2161	0.14	2546	0.9	825	2.7	1.451	0.57	79%
20	3086	0.15	3489	1.0	1081	2.7	1.524	0.57	79%
30	4230	0.15	4524	1.0	1357	2.7	1.510	0.57	79%
40	5240	0.15	5417	1.0	1598	2.7	1.520	0.57	79%
50	6091	0.15	6156	1.0	6156	2.7	1.565	0.57	79%
60	6726	0.15	6764	1.0	1888	2.7	1.638	0.57	79%
70	7348	0.15	7542	1.0	2135	2.7	1.664	0.57	79%
80	7502	0.14	7791	1.0	2233	2.7	1.710	0.56	79%
90	7799	0.15	7989	1.0	2333	2.7	1.780	0.56	79%
100	7888	0.15	8194	1.0	2349	2.7	1.759	0.56	79%
150	8420	0.14	8937	1.0	2522	2.7	1.801	0.56	79%
200	8513	0.14	8964	1.0	2541	2.7	1.809	0.56	79%
250	8746	0.14	9363	1.0	2638	2.7	1.842	0.56	79%
300	9053	0.13	10035	0.9	2852	2.7	1.928	0.55	80%
400	9149	0.14	9969	1.0	2796	2.7	1.852	0.56	79%
500	9346	0.13	10271	0.9	2943	2.7	1.902	0.55	80%
600	9425	0.13	10433	0.9	2969	2.7	1.943	0.55	80%
700	9695	0.13	10814	0.9	3029	2.7	1.905	0.56	79%
800	9580	0.14	10574	0.9	2987	2.7	2.035	0.56	79%
900	9512	0.13	10675	0.9	3048	2.7	2.003	0.55	80%
1000	9814	0.13	11063	0.9	3169	2.7	2.051	0.56	79%
								average	**79%**

B

Tb per QD-15Cy5.5 in solution	$A\alpha_{DA1}$	τ_{DA1} (ms)	$A\alpha_{DA2}$	τ_{DA2} (ms)	B	τ_D (ms)	χ^2	τ_{DA}(ms)	E_{FRET}
1	131	0.1	152	0.81	56.8	2.7	1.572	0.48	82%
2	256	0.12	316	0.83	118	2.7	1.544	0.51	81%
4	507	0.15	570	0.92	201	2.7	1.473	0.56	79%
8	1195	0.15	1359	0.93	446	2.7	1.390	0.57	79%
10	1520	0.14	1787	0.91	598	2.7	1.377	0.56	79%
15	2103	0.14	2428	0.92	780	2.7	1.371	0.56	79%
20	2848	0.15	3190	0.93	999	2.7	1.369	0.56	79%
30	3900	0.15	4141	0.95	1243	2.7	1.409	0.56	79%
40	4559	0.15	4828	0.95	1421	2.7	1.352	0.56	79%
50	5143	0.15	5334	0.95	1552	2.7	1.355	0.56	79%
60	5641	0.15	5767	0.95	1670	2.7	1.402	0.55	79%
70	6179	0.15	6274	0.97	1771	2.7	1.312	0.56	79%
80	6420	0.15	6616	0.94	1914	2.7	1.337	0.55	80%
90	6579	0.15	6673	0.96	1936	2.7	1.366	0.56	79%
100	6933	0.15	6933	0.96	1999	2.7	1.349	0.56	79%
150	7402	0.15	7435	0.96	2112	2.7	1.403	0.56	79%
200	7434	0.14	7745	0.93	2229	2.7	1.331	0.54	80%
250	7657	0.14	7972	0.94	2241	2.7	1.387	0.55	80%
300	8055	0.14	8496	0.94	2402	2.7	1.359	0.55	80%
400	8258	0.14	8735	0.94	2466	2.7	1.381	0.55	80%
500	8451	0.14	8846	0.95	2489	2.7	1.430	0.55	79%
600	8423	0.14	8942	0.94	2502	2.7	1.395	0.55	80%
700	8996	0.14	9733	0.94	2682	2.7	1.419	0.56	79%
800	8985	0.14	9795	0.93	2740	2.7	1.366	0.55	80%
900	9026	0.14	9844	0.93	2768	2.7	1.422	0.55	80%
1000	9111	0.14	9887	0.93	2843	2.7	1.395	0.55	80%
								average	**80%**

C

Tb per QD-15Cy5.5 in solution	$A\alpha_{DA1}$	τ_{DA1} (ms)	$A\alpha_{DA2}$	τ_{DA2} (ms)	B	τ_{D} (ms)	χ^2	τ_{DA}(ms)	E_{FRET}
1	77.1	0.12	94.4	1.1	32.2	2.7	1.496	0.66	76%
2	159	0.1	182	0.9	67.7	2.7	1.554	0.50	81%
4	308	0.11	379	0.9	141	2.7	1.466	0.52	81%
8	545	0.13	724	0.9	262	2.7	1.457	0.57	79%
10	733	0.15	900	1.0	508	2.7	1.344	0.60	78%
15	1168	0.15	1426	0.9	496	2.7	1.403	0.58	78%
20	1432	0.14	1695	0.9	550	2.7	1.401	0.57	79%
30	2215	0.14	2625	0.9	893	2.7	1.466	0.57	79%
40	2315	0.15	2642	0.9	839	2.7	1.422	0.57	79%
50	3522	0.15	4007	1.0	1241	2.7	1.555	0.58	79%
60	3914	0.15	4313	1.0	1304	2.7	1.480	0.57	79%
70	4138	0.14	4557	0.9	1352	2.7	1.489	0.56	79%
80	4232	0.15	4593	1.0	1374	2.7	1.487	0.57	79%
90	4335	0.16	4709	1.0	1409	2.7	1.489	0.58	78%
100	5268	0.15	5478	1.0	1531	2.7	1.561	0.56	79%
150	5217	0.15	5612	1.0	1740	2.7	1.584	0.57	79%
200	5467	0.15	5878	1.0	1814	2.7	1.548	0.57	79%
250	5419	0.15	5830	1.0	1767	2.7	1.524	0.57	79%
300	4932	0.15	5294	1.0	1649	2.7	1.491	0.57	79%
								average	**79%**

Note: Average values (and the resulting errors) of all three tables were used to calculate the FRET efficiencies presented in **Figure 4.16d**. Experiments shown in red font were not used for the calculations of the data in **Figure 4.16d** because the PL intensities were too low or the background of unquenched Tb PL was too high.

Table 7.7. FRET system 3 (mTb-QD-15Cy5.5): Results of PL decay fitting (PL decay curves shown in **Figure 4.16b** for **A**; decay curves for the fitting results in **B and C** were similar and are not shown) of FRET-sensitized QD acceptor PL using **Equations 4.13**, **4.14**, and **4.7**. Green rows were used for calculating FRET-corrected FRET efficiencies (using **Equations 4.14**). Yellow rows were used to calculate apparent FRET-efficiencies (without correction for FRET rates). Comparison of both FRET efficiencies is shown in **Figure 4.17.** Fit range: 0.1 to 8 ms.

A

Tb per QD-15Cy5.5 in solution	$A\alpha_{AD1*}$	α_{AD1*}	k_{FRET1}	α_{AD1}	τ_{AD1} (ms)	$A\alpha_{AD2}$	α_{AD2*}	k_{FRET2}	α_{AD2}	τ_{AD2} (ms)	B	τ_D (ms)	χ^2	τ_{AD} (ms)	τ_{AD} (ms)	E_{FRET}	E_{FRET}
1	77.7	0.576	8.72	0.16	0.11	57.3	0.424	1.19	0.84	0.64	20.6	2.7	1.500	0.33	0.56	88%	79%
2	102	0.510	7.96	0.12	0.12	97.9	0.490	1.06	0.88	0.70	34	2.7	1.404	0.40	0.63	85%	77%
4	173	0.529	6.30	0.14	0.15	154	0.471	0.88	0.86	0.80	52.6	2.7	1.440	0.46	0.71	83%	74%
8	369	0.530	5.19	0.13	0.18	327	0.470	0.68	0.87	0.95	90.9	2.7	1.313	0.54	0.85	80%	69%
10	428	0.504	5.88	0.12	0.16	422	0.496	0.78	0.88	0.87	130	2.7	1.343	0.51	0.79	81%	71%
15	584	0.507	5.19	0.13	0.18	569	0.493	0.75	0.87	0.89	170	2.7	1.313	0.53	0.80	80%	70%
20	862	0.525	5.19	0.13	0.18	779	0.475	0.72	0.87	0.92	216	2.7	1.290	0.53	0.82	80%	70%
30	1131	0.510	5.19	0.13	0.18	1085	0.490	0.75	0.87	0.89	287	2.7	1.256	0.53	0.80	80%	70%
40	1412	0.521	4.89	0.14	0.19	1298	0.479	0.74	0.86	0.90	336	2.7	1.278	0.53	0.80	80%	70%
50	1683	0.558	5.19	0.15	0.18	1335	0.442	0.75	0.85	0.89	375	2.7	1.247	0.49	0.78	82%	71%
60	1880	0.524	4.89	0.14	0.19	1707	0.476	0.75	0.86	0.89	409	2.7	1.280	0.52	0.79	81%	71%
70	2111	0.529	4.89	0.15	0.19	1883	0.471	0.74	0.85	0.90	447	2.7	1.301	0.52	0.80	81%	70%
80	2150	0.508	5.19	0.14	0.18	2081	0.492	0.81	0.86	0.85	489	2.7	1.258	0.51	0.76	81%	72%
90	2280	0.510	5.51	0.13	0.17	2193	0.490	0.81	0.87	0.85	505	2.7	1.301	0.50	0.76	81%	72%
100	2311	0.520	4.89	0.14	0.19	2135	0.480	0.77	0.86	0.88	494	2.7	1.274	0.52	0.78	81%	71%
150	2553	0.516	4.89	0.15	0.19	2391	0.484	0.78	0.85	0.87	538	2.7	1.260	0.52	0.77	81%	71%
200	2548	0.518	4.89	0.15	0.19	2375	0.482	0.78	0.85	0.87	529	2.7	1.315	0.52	0.77	81%	71%
250	2670	0.522	4.89	0.15	0.19	2443	0.478	0.77	0.85	0.88	539	2.7	1.272	0.52	0.78	81%	71%
300	2852	0.516	4.89	0.15	0.19	2671	0.484	0.79	0.85	0.86	590	2.7	1.335	0.51	0.76	81%	72%
400	2865	0.518	4.89	0.15	0.19	2662	0.482	0.78	0.85	0.87	592	2.7	1.320	0.52	0.77	81%	71%
500	2898	0.510	4.89	0.14	0.19	2784	0.490	0.79	0.86	0.86	607	2.7	1.289	0.52	0.76	81%	72%
600	2995	0.518	4.89	0.15	0.19	2786	0.482	0.78	0.85	0.87	600	2.7	1.322	0.52	0.77	81%	71%
700	3100	0.514	4.89	0.15	0.19	2932	0.486	0.79	0.85	0.86	633	2.7	1.275	0.52	0.76	81%	72%
800	3046	0.517	4.89	0.15	0.19	2845	0.483	0.78	0.85	0.87	615	2.7	1.313	0.52	0.77	81%	71%
900	3013	0.510	5.19	0.14	0.18	2894	0.490	0.81	0.86	0.85	634	2.7	1.356	0.51	0.76	81%	72%
1000	3208	0.514	4.89	0.15	0.19	3038	0.486	0.79	0.85	0.86	648	2.7	1.328	0.52	0.76	81%	72%

B

Tb per QD-15Cy5.5 in solution	$A\alpha_{AD1*}$	α_{AD1*}	k_{FRET1}	α_{AD1}	τ_{AD1} (ms)	$A\alpha_{AD2}$	α_{AD2*}	k_{FRET2}	α_{AD2}	τ_{AD2} (ms)	B	τ_D (ms)	χ^2	τ_{AD} (ms)	τ_{AD} (ms)	E_{FRET}	E_{FRET}
1	96.5	0.648	7.96	0.21	0.12	52.5	0.352	1.12	0.79	0.67	43.3	2.7	1.479	0.31	0.56	88%	79%
2	125	0.592	6.77	0.16	0.14	86.3	0.408	0.90	0.84	0.79	29.2	2.7	1.483	0.41	0.69	85%	75%
4	191	0.584	5.88	0.16	0.16	136	0.416	0.79	0.84	0.86	48	2.7	1.582	0.45	0.75	83%	72%
8	349	0.519	5.51	0.13	0.17	323	0.481	0.79	0.87	0.86	97.2	2.7	1.392	0.50	0.77	81%	72%
10	440	0.520	5.19	0.14	0.18	406	0.480	0.78	0.86	0.87	128	2.7	1.346	0.51	0.77	81%	71%
15	581	0.501	5.51	0.13	0.17	579	0.499	0.81	0.87	0.85	166	2.7	1.278	0.51	0.76	81%	72%
20	791	0.514	5.19	0.13	0.18	748	0.486	0.75	0.87	0.89	205	2.7	1.314	0.53	0.80	81%	71%
30	1087	0.527	4.89	0.15	0.19	976	0.473	0.75	0.85	0.89	266	2.7	1.265	0.52	0.79	81%	71%
40	1247	0.508	5.19	0.13	0.18	1206	0.492	0.78	0.87	0.87	308	2.7	1.252	0.52	0.78	81%	71%
50	1453	0.519	5.19	0.14	0.18	1344	0.481	0.77	0.86	0.88	330	2.7	1.258	0.52	0.78	81%	71%
60	1569	0.523	4.63	0.15	0.2	1432	0.477	0.75	0.85	0.89	351	2.7	1.291	0.53	0.79	80%	71%
70	1696	0.511	5.19	0.14	0.18	1625	0.489	0.79	0.86	0.86	392	2.7	1.266	0.51	0.77	81%	72%
80	1824	0.516	5.19	0.14	0.18	1711	0.484	0.79	0.86	0.86	412	2.7	1.280	0.51	0.76	81%	72%
90	1859	0.513	5.19	0.14	0.18	1766	0.487	0.79	0.86	0.86	423	2.7	1.276	0.51	0.77	81%	72%
100	1935	0.513	5.19	0.14	0.18	1835	0.487	0.79	0.86	0.86	433	2.7	1.324	0.51	0.77	81%	72%
150	2135	0.518	5.19	0.14	0.18	1987	0.482	0.79	0.86	0.86	472	2.7	1.264	0.51	0.76	81%	72%
200	2175	0.517	4.89	0.15	0.19	2029	0.483	0.79	0.85	0.86	474	2.7	1.254	0.51	0.76	81%	72%
250	2229	0.515	5.19	0.14	0.18	2099	0.485	0.79	0.86	0.86	478	2.7	1.319	0.51	0.77	81%	72%
300	2373	0.517	4.89	0.15	0.19	2213	0.483	0.78	0.85	0.87	506	2.7	1.314	0.52	0.77	81%	71%
400	2486	0.519	4.89	0.14	0.19	2303	0.481	0.77	0.86	0.88	513	2.7	1.341	0.52	0.78	81%	71%
500	2465	0.511	4.89	0.14	0.19	2361	0.489	0.78	0.86	0.87	525	2.7	1.264	0.52	0.77	81%	71%
600	2509	0.508	5.19	0.14	0.18	2427	0.492	0.81	0.86	0.85	538	2.7	1.281	0.51	0.76	81%	72%
700	2758	0.511	4.89	0.14	0.19	2642	0.489	0.79	0.86	0.86	571	2.7	1.305	0.52	0.76	81%	72%
800	2753	0.512	5.19	0.14	0.18	2626	0.488	0.79	0.86	0.86	574	2.7	1.289	0.51	0.77	81%	72%
900	2814	0.519	4.89	0.15	0.19	2610	0.481	0.78	0.85	0.87	569	2.7	1.260	0.52	0.77	81%	71%
1000	2830	0.509	5.19	0.14	0.18	2734	0.491	0.81	0.86	0.85	595	2.7	1.328	0.51	0.76	81%	72%

C

Tb per QD-15Cy5.5 in solution	$A\alpha_{AD1*}$	α_{AD1*}	k_{FRET1}	α_{AD1}	τ_{AD1} (ms)	$A\alpha_{AD2}$	α_{AD2*}	k_{FRET2}	α_{AD2}	τ_{AD2} (ms)	B	τ_D (ms)	χ^2	τ_{AD} (ms)	τ_{AD} (ms)	E_{FRET}	E_{FRET}
1	52	0.591	10.50	0.15	0.092	36	0.409	1.32	0.85	0.59	13	2.7	1.348	0.30	0.51	89%	81%
2	65	0.533	9.63	0.12	0.1	57	0.467	1.14	0.88	0.66	20	2.7	1.350	0.36	0.59	87%	78%
4	114	0.553	6.30	0.13	0.15	92	0.447	0.79	0.87	0.86	30	2.7	1.390	0.47	0.76	83%	72%
8	170	0.482	6.77	0.10	0.14	183	0.518	0.85	0.90	0.82	58	2.7	1.350	0.49	0.75	82%	72%
10	223	0.515	5.19	0.13	0.18	210	0.485	0.72	0.87	0.92	65	2.7	1.339	0.54	0.83	80%	69%
15	338	0.510	4.89	0.13	0.19	325	0.490	0.69	0.87	0.94	96	2.7	1.328	0.56	0.84	79%	69%
20	375	0.474	6.30	0.11	0.15	416	0.526	0.83	0.89	0.83	125	2.7	1.402	0.51	0.76	81%	72%
30	625	0.502	5.51	0.12	0.17	621	0.498	0.75	0.88	0.89	184	2.7	1.267	0.53	0.80	80%	70%
40	661	0.510	5.51	0.12	0.17	634	0.490	0.74	0.88	0.90	173	2.7	1.303	0.53	0.81	80%	70%
50	1053	0.522	4.89	0.14	0.19	963	0.478	0.73	0.86	0.91	259	2.7	1.174	0.53	0.81	80%	70%
60	1168	0.529	4.89	0.14	0.19	1041	0.471	0.69	0.86	0.94	259	2.7	1.240	0.54	0.84	80%	69%
70	1192	0.516	5.19	0.13	0.18	1117	0.484	0.75	0.87	0.89	288	2.7	1.249	0.52	0.79	81%	71%
80	1211	0.503	5.51	0.13	0.17	1197	0.497	0.79	0.87	0.86	306	2.7	1.187	0.51	0.77	81%	71%
90	1249	0.502	5.51	0.13	0.17	1241	0.498	0.79	0.87	0.86	320	2.7	1.241	0.51	0.77	81%	71%
100	1505	0.508	5.19	0.14	0.18	1457	0.492	0.79	0.86	0.86	348	2.7	1.233	0.51	0.77	81%	72%
150	1562	0.516	4.89	0.14	0.19	1468	0.484	0.74	0.86	0.90	366	2.7	1.239	0.53	0.80	80%	70%
200	1659	0.515	4.89	0.14	0.19	1562	0.485	0.77	0.86	0.88	401	2.7	1.273	0.52	0.78	81%	71%
250	1654	0.524	4.63	0.15	0.2	1501	0.476	0.74	0.85	0.90	379	2.7	1.231	0.53	0.80	80%	71%
300	1503	0.523	4.89	0.14	0.19	1373	0.477	0.74	0.86	0.90	356	2.7	1.266	0.53	0.80	80%	70%

Note: Average values (and the resulting errors) of all three tables were used to calculate the FRET efficiencies presented in **Figure 4.16d**. Experiments shown in red font were not used for the calculations of the data in **Figure 4.16d** because the PL intensities were too low or the background of unquenched Tb PL was too high.

Table 7.8. FRET system 3 (mTb-QD-15Cy5.5): Results of PL decay fitting (PL decay curves shown in **Figure 4.16c** for **A**; decay curves for the fitting results in **B and C** were similar and are not shown) of FRET-sensitized Cy5.5 acceptor PL using **Equations 4.13**, **4.14**, and **4.7**. Fit range: 0.1 to 4 ms.

A

Tb per QD-15Cy5.5 in solution	$A\alpha_{AD1}$	α_{AD1*}	k_{FRET1}	α_{AD1}	τ_{AD1} (ms)	$A\alpha_{AD2}$	α_{AD2*}	k_{FRET2}	α_{AD2}	τ_{AD2} (ms)	$A\alpha_{AD3}$	α_{AD3*}	τ_{AD3} (ms)	χ^2	τ_{AD}(ms)	QD τ_D(ms)	E_{FRET} $\tau_{AD1\&2}$
1	47	0.31	75.13	0.04	0.013	72.4	0.48	5.35	0.96	0.14	31.2	0.21	0.7	1.429	0.13	0.56	76%
2	117	0.42	19.24	0.13	0.048	117	0.42	2.76	0.87	0.23	42.1	0.15	0.87	1.552	0.21	0.63	67%
4	198	0.44	12.88	0.21	0.07	171	0.38	2.94	0.79	0.23	81.2	0.18	0.86	1.374	0.20	0.71	72%
8	528	0.48	12.91	0.20	0.071	407	0.37	2.53	0.80	0.27	154	0.14	0.97	1.360	0.23	0.85	73%
10	627	0.46	14.11	0.18	0.065	527	0.39	2.57	0.82	0.26	200	0.15	0.93	1.261	0.23	0.79	71%
15	824	0.43	14.88	0.18	0.062	796	0.41	3.09	0.82	0.23	299	0.16	0.91	1.274	0.20	0.80	75%
20	1221	0.45	13.28	0.20	0.069	1089	0.40	2.95	0.80	0.24	419	0.15	0.89	1.223	0.21	0.82	75%
30	1747	0.44	13.67	0.20	0.067	1628	0.41	3.09	0.80	0.23	610	0.15	0.87	1.184	0.20	0.80	75%
40	2441	0.48	12.64	0.20	0.072	1949	0.38	2.60	0.80	0.26	727	0.14	0.9	1.145	0.22	0.80	72%
50	2879	0.46	13.42	0.19	0.068	2563	0.41	2.72	0.81	0.25	831	0.13	0.92	1.206	0.22	0.78	72%
60	3507	0.48	12.43	0.19	0.073	2839	0.39	2.44	0.81	0.27	922	0.13	0.93	1.179	0.23	0.79	71%
70	3750	0.45	12.83	0.19	0.071	3416	0.41	2.75	0.81	0.25	1138	0.14	0.89	1.173	0.22	0.80	73%
80	3831	0.46	12.57	0.19	0.072	3384	0.41	2.53	0.81	0.26	1111	0.13	0.91	1.225	0.23	0.76	70%
90	3933	0.44	12.97	0.18	0.07	3823	0.43	2.68	0.82	0.25	1203	0.13	0.9	1.282	0.22	0.76	71%
100	4282	0.46	12.80	0.18	0.071	3824	0.41	2.56	0.82	0.26	1189	0.13	0.92	1.201	0.23	0.78	71%
150	4920	0.46	12.40	0.18	0.073	4333	0.41	2.41	0.82	0.27	1384	0.13	0.91	1.215	0.23	0.77	70%
200	4701	0.43	12.99	0.17	0.07	4630	0.43	2.70	0.83	0.25	1478	0.14	0.89	1.166	0.22	0.77	72%
250	4605	0.43	13.42	0.17	0.068	4605	0.43	2.72	0.83	0.25	1498	0.14	0.87	1.175	0.22	0.78	72%
300	4817	0.43	13.18	0.17	0.069	4946	0.44	2.69	0.83	0.25	1535	0.14	0.89	1.236	0.22	0.76	71%
400	5155	0.46	12.22	0.18	0.074	4630	0.41	2.41	0.82	0.27	1481	0.13	0.9	1.158	0.23	0.77	70%
500	5019	0.43	13.18	0.15	0.069	5079	0.44	2.39	0.85	0.27	1575	0.13	0.9	1.126	0.24	0.76	69%
600	5162	0.44	12.79	0.17	0.071	5024	0.43	2.55	0.83	0.26	1532	0.13	0.91	1.190	0.23	0.77	70%
700	5274	0.43	12.77	0.17	0.071	5331	0.43	2.69	0.83	0.25	1718	0.14	0.89	1.245	0.22	0.76	71%
800	5321	0.45	12.04	0.19	0.075	4933	0.42	2.55	0.81	0.26	1561	0.13	0.9	1.173	0.23	0.77	71%
900	5142	0.44	12.57	0.17	0.072	4998	0.43	2.52	0.83	0.26	1605	0.14	0.89	1.169	0.23	0.76	70%
1000	5581	0.46	12.20	0.18	0.074	5111	0.42	2.39	0.82	0.27	1564	0.13	0.92	1.093	0.24	0.76	69%
																	72%

B

Tb per QD-15Cy5.5 in solution	$A\alpha_{AD1}$	α_{AD1*}	k_{FRET1}	α_{AD1}	τ_{AD1} (ms)	$A\alpha_{AD2}$	α_{AD2*}	k_{FRET2}	α_{AD2}	τ_{AD2} (ms)	$A\alpha_{AD3}$	α_{AD3*}	τ_{AD3} (ms)	χ^2	τ_{AD}(ms)	QD τ_D(ms)	E_{FRET} $\tau_{AD1\&2}$
1	26.3	0.21	45.82	0.04	0.021	68.9	0.55	5.35	0.96	0.14	29.5	0.24	0.72	1.359	0.13	0.56	76%
2	126	0.54	9.41	0.29	0.092	69.4	0.30	2.11	0.71	0.28	37.3	0.16	0.93	1.433	0.23	0.69	67%
4	197	0.43	13.59	0.20	0.067	185	0.40	3.21	0.80	0.22	75.5	0.17	0.87	1.516	0.19	0.75	75%
8	531	0.51	11.68	0.19	0.077	393	0.38	2.03	0.81	0.30	124	0.12	1.1	1.337	0.26	0.77	66%
10	644	0.48	13.41	0.18	0.068	515	0.38	2.41	0.82	0.27	192	0.14	0.97	1.332	0.23	0.77	70%
15	725	0.38	16.87	0.14	0.055	864	0.45	3.23	0.86	0.22	314	0.17	0.88	1.225	0.20	0.76	74%
20	1156	0.43	14.13	0.18	0.065	1105	0.41	2.91	0.82	0.24	409	0.15	0.89	1.203	0.21	0.80	74%
30	1957	0.50	12.81	0.20	0.071	1495	0.38	2.43	0.80	0.27	499	0.13	0.97	1.121	0.23	0.79	71%
40	2287	0.46	13.42	0.18	0.068	2049	0.41	2.56	0.82	0.26	644	0.13	0.95	1.165	0.23	0.78	71%
50	2932	0.49	13.22	0.19	0.069	2304	0.38	2.43	0.81	0.27	767	0.13	0.95	1.226	0.23	0.78	70%
60	3079	0.43	14.60	0.17	0.063	3004	0.42	2.89	0.83	0.24	1030	0.14	0.87	1.222	0.21	0.79	73%
70	3618	0.45	12.78	0.19	0.071	3286	0.41	2.70	0.81	0.25	1062	0.13	0.9	1.232	0.22	0.77	72%
80	3733	0.46	12.03	0.21	0.075	3172	0.39	2.69	0.79	0.25	1131	0.14	0.88	1.196	0.21	0.76	72%
90	3935	0.45	12.78	0.19	0.071	3610	0.41	2.69	0.81	0.25	1158	0.13	0.91	1.182	0.22	0.77	72%
100	3987	0.45	12.39	0.18	0.073	3651	0.41	2.54	0.82	0.26	1190	0.13	0.89	1.223	0.23	0.77	71%
150	4544	0.45	12.58	0.18	0.072	4203	0.42	2.54	0.82	0.26	1367	0.14	0.9	1.185	0.23	0.76	70%
200	4479	0.43	13.39	0.17	0.068	4404	0.43	2.69	0.83	0.25	1426	0.14	0.87	1.226	0.22	0.76	71%
250	4843	0.44	12.21	0.16	0.074	4849	0.44	2.40	0.84	0.27	1347	0.12	0.91	1.192	0.24	0.77	69%
300	4786	0.44	12.99	0.18	0.07	4660	0.42	2.70	0.82	0.25	1521	0.14	0.88	1.181	0.22	0.77	72%
400	4833	0.44	13.00	0.17	0.07	4776	0.43	2.56	0.83	0.26	1471	0.13	0.9	1.169	0.23	0.78	71%
500	5137	0.46	12.41	0.17	0.073	4706	0.42	2.41	0.83	0.27	1337	0.12	0.95	1.180	0.24	0.77	70%
600	4986	0.44	12.76	0.18	0.071	4860	0.42	2.68	0.82	0.25	1594	0.14	0.88	1.175	0.22	0.76	71%
700	5280	0.44	12.02	0.18	0.075	5086	0.43	2.54	0.82	0.26	1596	0.13	0.9	1.181	0.23	0.76	70%
800	5348	0.45	12.58	0.18	0.072	4916	0.42	2.54	0.82	0.26	1545	0.13	0.91	1.217	0.23	0.77	70%
900	5049	0.43	12.79	0.17	0.071	5051	0.43	2.55	0.83	0.26	1519	0.13	0.91	1.199	0.23	0.77	70%
1000	5282	0.44	12.38	0.18	0.073	5068	0.43	2.53	0.82	0.26	1557	0.13	0.91	1.197	0.23	0.76	70%
																	71%

C

Tb per QD 15Cy5.5 in solution	$A\alpha_{AD1}$	α_{AD1*}	k_{FRET1}	α_{AD1}	τ_{AD1} (ms)	$A\alpha_{AD2}$	α_{AD2*}	k_{FRET2}	α_{AD2}	τ_{AD2} (ms)	$A\alpha_{AD3}$	α_{AD3*}	τ_{AD3} (ms)	χ^2	τ_{AD}(ms)	QD τ_D(ms)	E_{FRET} $\tau_{AD1\&2}$
1	37.9	0.35	25.08	0.09	0.037	52.8	0.48	3.31	0.91	0.19	18.6	0.17	0.88	1.095	0.18	0.51	66%
2	67.4	0.33	35.35	0.08	0.027	96.6	0.48	4.20	0.92	0.17	38.9	0.19	0.82	1.274	0.16	0.59	73%
4	162	0.42	16.55	0.12	0.056	175	0.45	2.54	0.88	0.26	48.8	0.13	1.1	1.043	0.23	0.76	69%
8	369	0.48	12.55	0.17	0.072	310	0.40	2.11	0.83	0.29	96.3	0.12	1.1	1.140	0.25	0.75	66%
10	533	0.52	10.84	0.21	0.083	369	0.36	2.01	0.79	0.31	124	0.12	1.1	1.248	0.26	0.83	68%
15	897	0.52	11.64	0.19	0.078	639	0.37	1.94	0.81	0.32	193	0.11	1.1	1.364	0.27	0.84	68%
20	1109	0.55	10.31	0.20	0.086	713	0.35	1.62	0.80	0.34	202	0.10	1.2	1.374	0.29	0.76	62%
30	1717	0.53	11.10	0.20	0.081	1166	0.36	1.88	0.80	0.32	329	0.10	1.2	1.486	0.27	0.80	66%
40	1711	0.52	11.92	0.19	0.076	1241	0.38	1.99	0.81	0.31	344	0.10	1.1	1.385	0.27	0.81	67%
50	2767	0.55	10.53	0.20	0.085	1815	0.36	1.71	0.80	0.34	459	0.09	1.2	1.451	0.29	0.81	64%
60	2908	0.54	11.00	0.20	0.082	1974	0.37	1.84	0.80	0.33	502	0.09	1.2	1.433	0.28	0.84	66%
70	2949	0.54	10.65	0.20	0.084	2012	0.37	1.77	0.80	0.33	513	0.09	1.2	1.442	0.28	0.79	65%
80	3059	0.52	11.21	0.18	0.08	2206	0.38	1.83	0.82	0.32	575	0.10	1.1	1.460	0.28	0.77	64%
90	3298	0.54	10.47	0.20	0.085	2249	0.37	1.74	0.80	0.33	587	0.10	1.2	1.441	0.28	0.77	63%
100	3782	0.54	10.60	0.19	0.084	2647	0.38	1.73	0.81	0.33	627	0.09	1.2	1.386	0.28	0.77	63%
150	3915	0.53	10.52	0.19	0.085	2789	0.38	1.78	0.81	0.33	688	0.09	1.2	1.468	0.28	0.80	65%
200	4211	0.53	10.21	0.19	0.087	2971	0.38	1.66	0.81	0.34	701	0.09	1.2	1.437	0.29	0.78	63%
250	4265	0.53	10.51	0.19	0.085	2986	0.37	1.68	0.81	0.34	724	0.09	1.2	1.463	0.29	0.80	63%
300	3915	0.55	10.38	0.19	0.086	2635	0.37	1.61	0.81	0.35	612	0.09	1.2	1.428	0.30	0.80	62%
																	65%

Note: Average values (and the resulting errors) of all three tables were used to calculate the FRET efficiencies presented in **Figure 4.16d**. Experiments shown in red font were not used for the calculations of the data in **Figure 4.16d** because the PL intensities were too low or the background of unquenched Tb PL was too high.

Table 7.9. FRET system 4 (75Tb-QD-nCy5.5): Results of PL decay fitting (PL decay curves shown in **Figure 4.18a** for **A**; decay curves for the fitting results in **B** were similar and are not shown) of FRET-quenched Tb donor PL using Equations **4.15**, **4.16**, and **4.10**. Fit range: 0.01 to 8 ms.

A

Cy5.5 per 75Tb-QD	$A\alpha_{DA1}$	τ_{DA1} (ms)	$A\alpha_{DA2}$	τ_{DA1} (ms)	B	τ_{D} (ms)	χ^2	τ_{DA}(ms)	E_{FRET}
0	791	0.29	2936	1.40	2223	2.70	1.306	1.16	57%
1	850	0.23	2709	1.30	1934	2.70	1.318	1.04	61%
2	946	0.24	2639	1.30	1716	2.70	1.286	1.02	62%
4	1111	0.19	2421	1.20	1376	2.70	1.322	0.88	67%
8	1317	0.16	1908	1.00	781	2.70	1.391	0.66	76%
10	1332	0.15	1911	0.99	774	2.70	1.398	0.64	76%
15	1413	0.12	1314	0.85	427	2.70	1.451	0.47	83%
20	1482	0.11	1079	0.75	308	2.70	1.521	0.38	86%
30	1294	0.08	739	0.61	222	2.70	1.595	0.27	90%
40	1180	0.06	563	0.51	180	2.70	1.382	0.21	92%
50	1031	0.05	437	0.43	154	2.70	1.479	0.16	94%
60	707	0.03	220	0.26	126	2.70	1.426	0.09	97%

B

Cy5.5 per 75Tb-QD	$A\alpha_{DA1}$	τ_{DA1} (ms)	$A\alpha_{DA2}$	τ_{DA2} (ms)	B	τ_{D} (ms)	χ^2	τ_{DA}(ms)	E_{FRET}
0	1734	0.25	5005	1.50	2703	2.70	1.244	1.18	56%
1	1516	0.22	3482	1.30	2066	2.70	1.343	0.97	64%
2	1304	0.19	3077	1.20	1871	2.70	1.305	0.90	67%
4	1038	0.16	2330	1.20	1526	2.70	1.300	0.88	67%
8	1394	0.17	2060	1.00	791	2.70	1.435	0.67	75%
10	1877	0.15	2683	1.00	1067	2.70	1.387	0.65	76%
15	2467	0.14	2792	0.91	856	2.70	1.576	0.55	80%
20	1694	0.12	1465	0.81	433	2.70	1.495	0.44	84%
30	2010	0.10	1410	0.69	222	2.70	1.552	0.34	87%
40	2136	0.11	1310	0.68	321	2.70	1.598	0.33	88%
50	1593	0.08	821	0.55	238	2.70	1.538	0.24	91%
60	1259	0.06	540	0.42	199	2.70	1.453	0.17	94%

Note: Average values (and the resulting errors) of both tables were used to calculate the FRET efficiencies presented in **Figure 4.18d**. Experiments shown in red font were not used for the calculations of the data in **Figure 4.18d** because the PL intensities were too low or the background of unquenched Tb PL was too high.

Table 7.10. FRET system 4 (75Tb-QD-nCy5.5): Results of PL decay fitting (PL decay curves shown in **Figure 4.18b** for **A**; decay curves for the fitting results in **B** were similar and are not shown) of FRET-sensitized QD acceptor PL using **Equations 4.13**, **4.14**, and **4.7**. Green rows were used for calculating FRET-corrected FRET efficiencies (using **Equations 4.14**). Yellow rows were used to calculate apparent FRET-efficiencies (without correction for FRET rates). Fit range: 0.1 to 8 ms.

A

Cy5.5 per 75Tb-QD	$A\alpha_{AD1*}$	α_{AD1*}	k_{FRET1}	α_{AD1}	τ_{AD1} (ms)	$A\alpha_{AD2}$	α_{AD2*}	k_{FRET2}	α_{AD2}	τ_{AD2} (ms)	B	τ_D (ms)	χ^2	τ_{AD} (ms)	τ_{AD} (ms)	E_{FRET}	E_{FRET}
0	313	0.576	4.63	0.16	0.2	230	0.424	0.63	0.84	1.00	110	2.7	1.305	0.54	0.88	80%	68%
1	252	0.575	5.51	0.15	0.17	186	0.425	0.72	0.85	0.92	90	2.7	1.300	0.49	0.81	82%	70%
2	201	0.535	5.88	0.14	0.16	175	0.465	0.82	0.86	0.84	85	2.7	1.267	0.48	0.75	82%	72%
4	144	0.524	5.88	0.12	0.16	131	0.476	0.75	0.88	0.89	56	2.7	1.279	0.51	0.80	81%	70%
8	90	0.533	5.88	0.14	0.16	79	0.467	0.81	0.86	0.85	28	2.7	1.327	0.48	0.76	82%	72%
10	92	0.541	5.51	0.14	0.17	78	0.459	0.79	0.86	0.86	27	2.7	1.317	0.49	0.76	82%	72%
15	54	0.540	7.96	0.12	0.12	46	0.460	0.96	0.88	0.75	12	2.7	1.337	0.41	0.67	85%	75%
20	35	0.493	7.96	0.15	0.12	36	0.507	1.42	0.85	0.56	11	2.7	1.379	0.34	0.50	87%	82%
30	22	0.524	7.96	0.17	0.12	20	0.476	1.45	0.83	0.55	6.2	2.7	1.454	0.32	0.48	88%	82%
40	18	0.600	9.63	0.20	0.1	12	0.400	1.63	0.80	0.50	4.2	2.7	1.253	0.26	0.42	90%	84%
50	12	0.500	32.96	0.08	0.03	12	0.500	2.86	0.92	0.31	4.7	2.7	1.378	0.17	0.29	94%	89%
60	1	0.137	28.20	0.03	0.035	6.3	0.863	4.63	0.97	0.20	2.8	2.7	1.405	0.18	0.20	93%	93%

B

Cy5.5 per 75Tb-QD	$A\alpha_{AD1*}$	α_{AD1*}	k_{FRET1}	α_{AD1}	τ_{AD1} (ms)	$A\alpha_{AD2}$	α_{AD2*}	k_{FRET2}	α_{AD2}	τ_{AD2} (ms)	B	τ_D (ms)	χ^2	τ_{AD} (ms)	τ_{AD} (ms)	E_{FRET}	E_{FRET}
0	4383	0.533	4.89	0.13	0.19	3837	0.467	0.66	0.87	0.97	1542	2.7	1.231	0.55	0.87	79%	68%
1	4671	0.597	5.19	0.18	0.18	3149	0.403	0.79	0.82	0.86	998	2.7	1.308	0.45	0.73	83%	73%
2	3712	0.602	5.51	0.18	0.17	2450	0.398	0.82	0.82	0.84	789	2.7	1.349	0.44	0.72	84%	73%
4	2829	0.609	6.30	0.15	0.15	1815	0.391	0.73	0.85	0.91	747	2.7	1.221	0.45	0.79	83%	71%
8	1854	0.616	5.88	0.19	0.16	1157	0.384	0.85	0.81	0.82	280	2.7	1.271	0.41	0.70	85%	74%
10	2184	0.612	5.88	0.19	0.16	1386	0.388	0.85	0.81	0.82	346	2.7	1.277	0.42	0.70	85%	74%
15	1947	0.616	5.88	0.21	0.16	1212	0.384	0.96	0.79	0.75	249	2.7	1.307	0.39	0.63	86%	77%
20	908	0.623	6.30	0.22	0.15	550	0.377	1.06	0.78	0.70	113	2.7	1.330	0.36	0.58	87%	78%
30	839	0.647	6.77	0.24	0.14	458	0.353	1.14	0.76	0.66	79.5	2.7	1.421	0.32	0.54	88%	80%
40	958	0.674	6.30	0.28	0.15	464	0.326	1.17	0.72	0.65	71.8	2.7	1.416	0.31	0.51	88%	81%
50	423	0.667	7.32	0.28	0.13	211	0.333	1.42	0.72	0.56	46.3	2.7	1.419	0.27	0.44	90%	84%
60	232	0.652	9.63	0.26	0.1	124	0.348	1.85	0.74	0.45	35.6	2.7	1.402	0.22	0.36	92%	87%

Note: Average values (and the resulting errors) of both tables were used to calculate the FRET efficiencies presented in **Figure 4.18d**. Experiments shown in red font were not used for the calculations of the data in **Figure 4.18d** because the PL intensities were too low or the background of unquenched Tb PL was too high.

Table 7.11. FRET system 4 (75Tb-QD-nCy5.5): Results of PL decay fitting (PL decay curves shown in **Figure 4.18c** for **A**; decay curves for the fitting results in **B** were similar and are not shown) of FRET-sensitized Cy5.5 acceptor PL using **Equations 4.13**, **4.14**, and **4.7**. Fit range: 0.1 to 4 ms.

A

Cy5.5 per 75Tb-QD	$A\alpha_{AD1}$	α_{AD1*}	k_{FRET1}	α_{AD1}	τ_{AD1} (ms)	$A\alpha_{AD2}$	α_{AD2*}	k_{FRET2}	α_{AD2}	τ_{AD2} (ms)	$A\alpha_{AD3}$	α_{AD3*}	τ_{AD3} (ms)	χ^2	τ_{AD} (ms)	QD τ_D(ms)	E_{FRET} $\tau_{AD1\&2}$
0	\	\	\	\	\	\	\	\	\	\	\	\	\	\	\	0.88	\
1	378	0.53	19.17	0.20	0.049	241	0.34	3.11	0.80	0.23	95.5	0.13	1	1.369	0.19	0.81	76%
2	399	0.48	19.94	0.19	0.047	310	0.37	3.66	0.81	0.20	123	0.15	0.94	1.311	0.17	0.75	77%
4	595	0.50	21.48	0.20	0.044	420	0.36	3.75	0.80	0.20	164	0.14	0.88	1.334	0.17	0.80	79%
8	704	0.48	23.07	0.19	0.041	510	0.35	3.94	0.81	0.19	262	0.18	0.85	1.413	0.16	0.76	79%
10	652	0.52	21.41	0.23	0.044	436	0.35	4.24	0.77	0.18	155	0.12	0.8	1.396	0.15	0.76	80%
15	473	0.52	25.54	0.19	0.037	342	0.38	4.39	0.81	0.17	94.4	0.10	0.76	1.365	0.14	0.67	78%
20	399	0.56	24.30	0.20	0.038	250	0.35	3.86	0.80	0.17	63.6	0.09	0.72	1.258	0.14	0.50	71%
30	231	0.56	22.91	0.25	0.04	137	0.33	4.58	0.75	0.15	42.2	0.10	0.58	1.241	0.12	0.48	74%
40	114	0.43	39.28	0.15	0.024	121	0.45	7.61	0.85	0.10	32.1	0.12	0.46	1.019	0.09	0.42	79%
50	36.8	0.22	55.35	0.08	0.017	101	0.60	12.65	0.92	0.06	31.2	0.18	0.31	1.012	0.06	0.29	80%
60	35.9	0.75	28.23	1.00	0.03	\	\	\	\	\	11.9	0.25	0.18	0.984	0.03	0.20	85%

B

Cy5.5 per 75Tb-QD	$A\alpha_{AD1}$	α_{AD1*}	k_{FRET1}	α_{AD1}	τ_{AD1} (ms)	$A\alpha_{AD2}$	α_{AD2*}	k_{FRET2}	α_{AD2}	τ_{AD2} (ms)	$A\alpha_{AD3}$	α_{AD3*}	τ_{AD3} (ms)	χ^2	τ_{AD} (ms)	QD τ_D(ms)	E_{FRET} $\tau_{AD1\&2}$
0	\	\	\	\	\	\	\	\	\	\	\	\	\	\	\	0.87	\
1	595	0.40	12.34	0.15	0.073	591	0.40	2.21	0.85	0.28	297	0.20	1.1	1.165	0.25	0.73	66%
2	799	0.42	10.95	0.17	0.081	728	0.39	2.05	0.83	0.29	361	0.19	1.1	1.166	0.25	0.72	65%
4	1243	0.41	11.73	0.18	0.077	1184	0.39	2.44	0.82	0.27	579	0.19	1.1	1.218	0.24	0.79	70%
8	879	0.45	12.08	0.17	0.074	747	0.39	2.13	0.83	0.28	309	0.16	0.99	1.300	0.24	0.70	65%
10	1077	0.42	12.46	0.16	0.072	1076	0.42	2.41	0.84	0.26	437	0.17	0.95	1.396	0.23	0.70	67%
15	1257	0.44	12.90	0.17	0.069	1173	0.41	2.41	0.83	0.25	450	0.16	0.89	1.248	0.22	0.63	65%
20	617	0.44	14.15	0.16	0.063	595	0.42	2.63	0.84	0.23	200	0.14	0.82	1.475	0.20	0.58	65%
30	534	0.45	13.76	0.18	0.064	488	0.41	2.68	0.82	0.22	160	0.14	0.75	1.376	0.19	0.54	64%
40	340	0.35	21.30	0.11	0.043	484	0.49	3.93	0.89	0.17	161	0.16	0.64	1.394	0.16	0.51	70%
50	127	0.33	20.98	0.11	0.043	198	0.52	3.98	0.89	0.16	56.6	0.15	0.59	1.176	0.15	0.44	67%
60	48.5	0.22	140.06	0.03	0.007	119	0.54	9.25	0.97	0.08	52.9	0.24	0.34	1.262	0.08	0.36	77%

Note: Average values (and the resulting errors) of both tables were used to calculate the FRET efficiencies presented in **Figure 4.18d** in the manuscript. Experiments shown in red font were not used for the calculations of the data in **Figure 4.18d** because the PL intensities were too low or the background of unquenched Tb PL was too high.

7.4 Energy transfer from Tb donors to AuNPs

7.4.1 Stability of the AuNPs in buffer

The stability of the biotinylated particles in different buffers was studied for 50 nm biot-AuNP and 80 nm biot-AuNP, by measuring extinction and resonant light scattering spectra. Two buffers were investigated: PBS (Phosphate-buffered saline, 10 mM phosphate, pH 7.2, 137 mM NaCl, 2.7 mM KCl) and Tris-HCl buffer (4 mM, pH 8.4). A suspension of the same particles diluted in purified deionized water was used in comparison.

The extinction spectra in water (**Figure 7.4**) remain stable, whereas in Tris-HCl and PBS some loss of nanoparticles occurred, in particular after 24 hours. Interestingly, the shapes of the spectra did not change, indicating that the disappearance is not due to nanoparticle aggregation but rather to nanoparticles sticking to the cuvette windows.

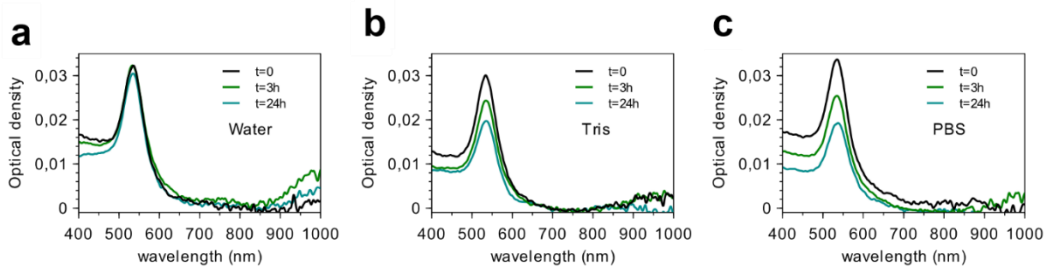

Figure 7.4. Extinction spectra of 50nm biot-AuNP at t=0 min, at t=3 hours and t=24 hours in the three different buffers: **(a)** water, **(b)** Tris-HCl, **(c)** PBS

In order to further ascertain the stability of biot-AuNPs we also investigated the normalized extinction and light scattering spectra (**Figure 7.5 and 7.6**).

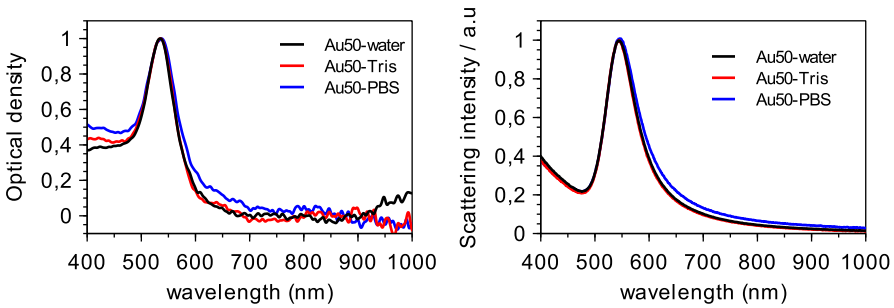

Figure 7.5. Normalized extinction **(left)** and light scattering **(right)** spectra of 50nm biot-AuNP after 24 hours in buffers.

The optical spectra of 50 nm biot-AuNPs (**Figure 7.5**) showed a good stability of the particles in both buffers. The shapes and position of the plasmon resonance bands did not change over time. Similar effects were observed for biot-Au80 (**Figure 7.6**). There was no wavelength shift of the maxima and the shapes of the resonance bands remained the same, indicating an absence of AuNP aggregates.

We found that some material was lost by adhesion to the walls of the cuvette upon prolonged standing (24h and longer). This effect was most pronounced when using PBS. Tris-HCl buffer then was selected as the best solvent to work with the particles on a time scale of several hours.

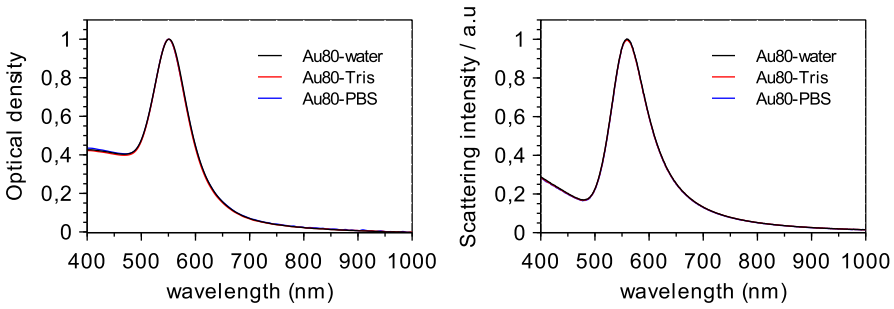

Figure 7.6. Extinction **(left)** and light scattering **(right)** spectra of 80 nm biot-AuNP after 24 hours in buffer.

7.4.2 Time-resolved PL decays of Tb-sAv-biot-AuNP assemblies

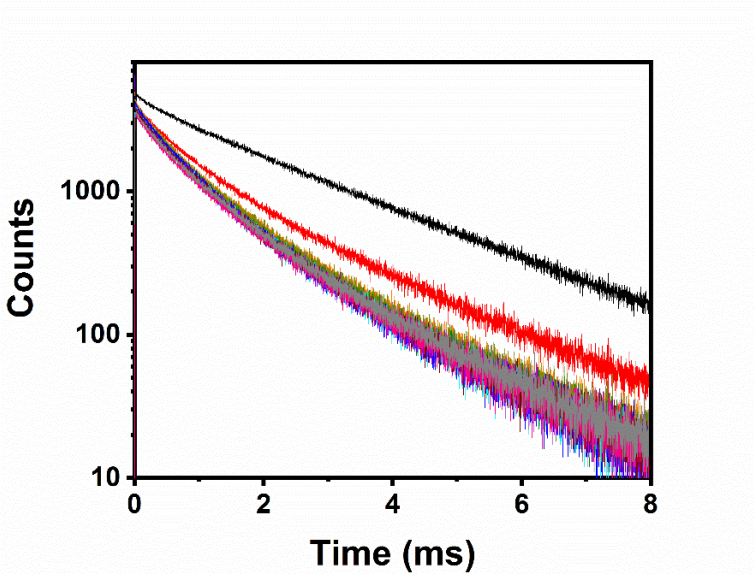

Figure 7.7. PL decay curves detected in the Tb donor channel for increasing ratios of (x biot-AuNPs) per (y Tb-sAv) for **5 nm biot-AuNPs** with y = 6 Tb-sAv. black: x = 0; red: x = 0.1; orange: x = 0.5; dark yellow: x = 1; green: x = 2; cyan: x = 3; blue: x = 4; violet: x = 5; pink: x = 6; wine: x = 7; gray: x = 8).

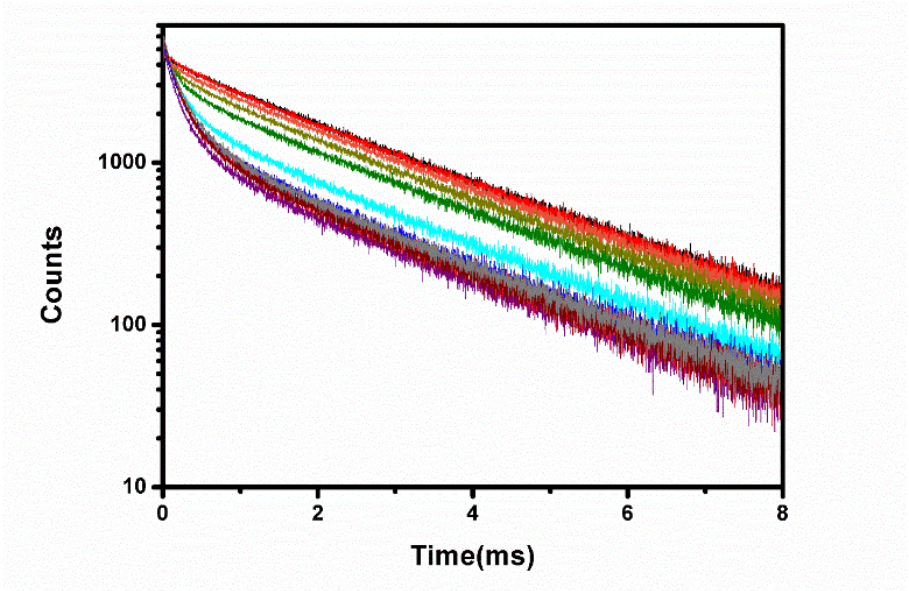

Figure 7.8. PL decay curves detected in the Tb donor channel for increasing ratios of (x biot-AuNPs) per (y Tb-sAv) for **30 nm biot-AuNPs** with y = 225 Tb-sAv. black: x = 0; red: x = 0.1; orange: x = 0.2; dark yellow: x = 0.5; green: x = 1; cyan: x = 2; blue: x = 3; violet: x = 4; pink: x = 5; wine: x = 6; gray: x = 8).

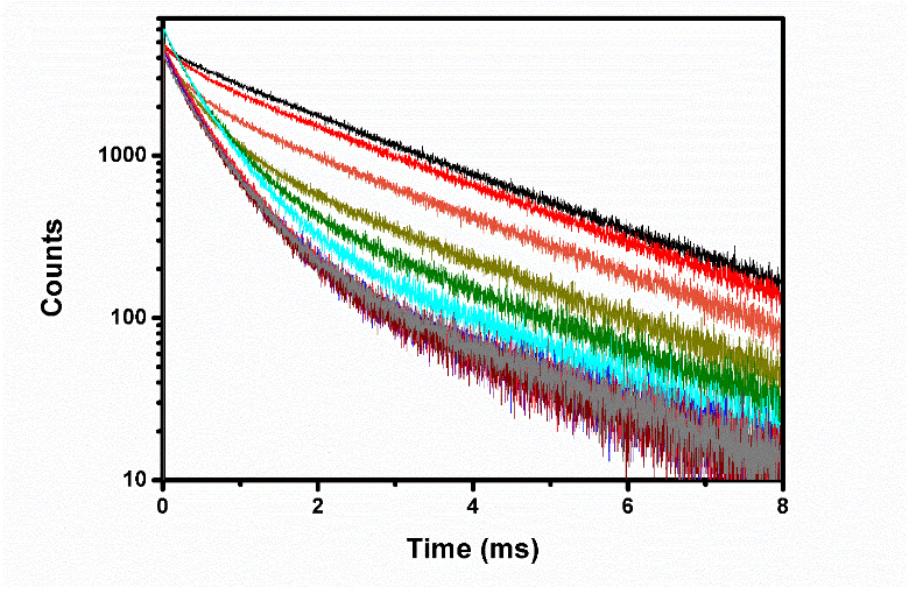

Figure 7.9. PL decay curves detected in the Tb donor channel for increasing ratios of (x biot-AuNPs) per (y Tb-sAv) for **50 nm biot-AuNPs** with y = 625 Tb-sAv. black: x = 0; red: x = 0.1; orange: x = 0.2; dark yellow: x = 0.5; green: x = 1; cyan: x = 2; blue: x = 3; violet: x = 4; pink: x = 5; wine: x = 6; gray: x = 8)

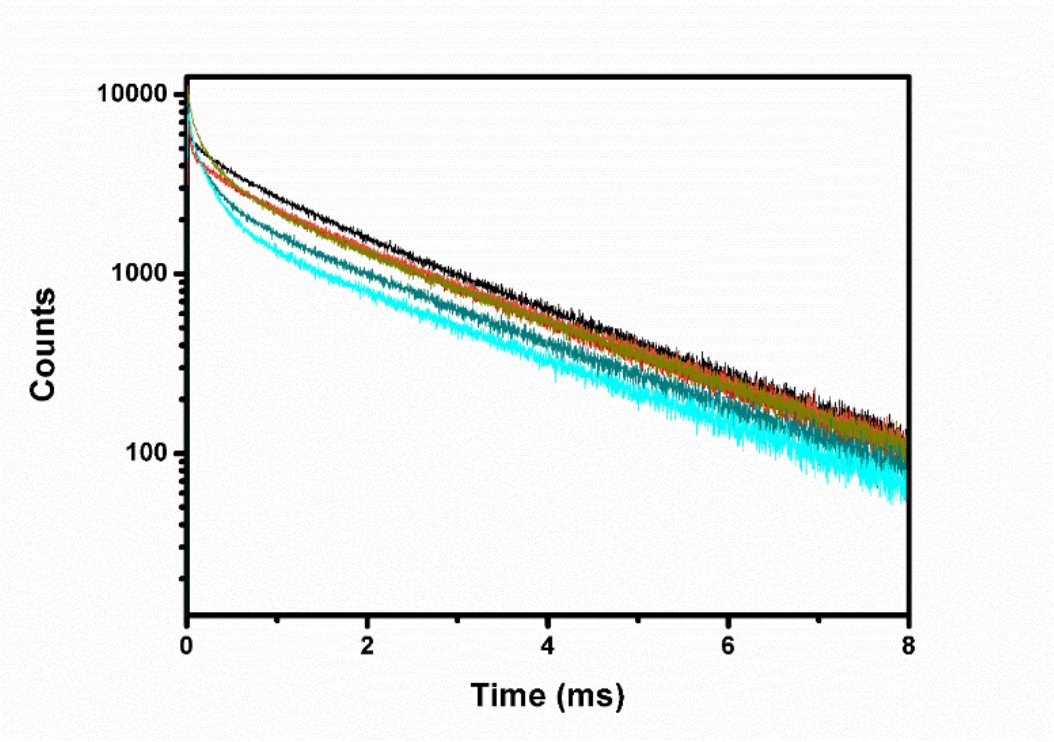

Figure 7.10. PL decay curves detected in the Tb donor channel for increasing ratios of (x biot-AuNPs) per (y Tb-sAv) for **80 nm biot-AuNPs** with y = 1600 Tb-sAv. black: x = 0; red: x = 0.1; orange: x = 0.2; dark yellow: x = 0.5; green: x = 1; cyan: x = 2).

Table 7.12. Multi-exponential fits of Lumi4-Tb-sAv-biot-5 nm Au NPs.

NO.	%	τ_1	E_1	A_1	α_{DA*1}	α_{DA1}	τ_2	E_2	A_2	α_{DA*2}	α_{DA2}
0	0						540	0.75	577	0.13	1.00
1	10	350	0.84	663	0.18	0.27	940	0.56	1802	0.50	0.73
2	50	370	0.83	926	0.26	0.30	990	0.54	2120	0.59	0.70
3	100	370	0.83	454	0.15	0.18	990	0.54	2080	0.67	0.82
4	200	390	0.82	884	0.26	0.30	970	0.55	2047	0.60	0.70
5	300	380	0.82	833	0.25	0.28	960	0.55	2124	0.63	0.72
6	400	310	0.86	722	0.20	0.23	920	0.57	2371	0.67	0.77
7	500	350	0.84	747	0.23	0.26	940	0.56	2112	0.64	0.74
8	600	410	0.81	885	0.27	0.32	990	0.54	1912	0.59	0.68
9	700	320	0.85	594	0.20	0.23	940	0.56	1956	0.64	0.77
10	800	350	0.84	643	0.20	0.24	950	0.56	1984	0.63	0.76
average 1-10		360	0.83			0.26	960	0.55			0.74
					fraction:	26%				fraction:	74%

NO.	%	τ_0 (fixed)	A_0	α_{DA*0}	$\langle\tau\rangle$	z(D)	$\langle\tau_{DA}\rangle$	$\langle E\rangle$
0	0	2400	3792	0.87	2150			
1	10	2400	1162	0.32	1300	0.05	790	0.63
2	50	2400	555	0.15	1050	0.02	810	0.62
3	100	2400	550	0.18	1150	0.03	890	0.59
4	200	2400	480	0.14	1020	0.02	800	0.63
5	300	2400	430	0.13	1000	0.02	800	0.63
6	400	2400	451	0.13	980	0.02	780	0.64
7	500	2400	455	0.14	1010	0.02	790	0.63
8	600	2400	452	0.14	1030	0.02	810	0.62
9	700	2400	486	0.16	1050	0.02	800	0.63
10	800	2400	512	0.16	1060	0.02	810	0.62
average 1-10		2400					810	0.62

Table 7.13. Multi-exponential fits of Lumi4-Tb-sAv-biot-30 nm Au NPs.

NO.	%	τ_1	E_1	A_1	α_{DA*1}	α_{DA1}	τ_2	E_2	A_2	α_{DA*2}	α_{DA2}
0	0						550	0.75	455	0.11	1.00
1	10	80	0.96	217	0.05	0.29	590	0.73	528	0.12	0.71
2	20	140	0.94	249	0.06	0.35	640	0.71	468	0.11	0.65
3	50	140	0.94	454	0.12	0.44	710	0.68	568	0.14	0.56
4	100	150	0.93	959	0.24	0.61	690	0.69	614	0.15	0.39
5	200	170	0.92	1726	0.28	0.72	720	0.67	659	0.11	0.28
6	300	180	0.92	1911	0.51	0.74	690	0.69	686	0.18	0.26
7	400	180	0.92	1870	0.54	0.74	640	0.71	648	0.19	0.26
8	500	180	0.92	2176	0.55	0.75	690	0.69	736	0.19	0.25
9	600	180	0.92	2239	0.56	0.75	680	0.69	735	0.18	0.25
10	800	190	0.91	2284	0.55	0.75	680	0.69	744	0.18	0.25
average 4-10		170	0.92			0.65	680	0.69			0.35
					fraction:	65%				fraction:	35%

NO.	%	τ_0(fixed)	A_0	α_{DA*0}	$\langle\tau\rangle$	z(D)	$\langle\tau_{DA}\rangle$	$\langle E\rangle$
0	0	2400	3754	0.89	2200			
1	10	2400	3696	0.83	2070	0.10	430	0.80
2	20	2400	3399	0.83	2060	0.10	460	0.79
3	50	2400	2922	0.74	1900	0.09	450	0.80
4	100	2400	2445	0.61	1600	0.07	350	0.84
5	200	2400	3823	0.62	1600	0.07	300	0.86
6	300	2400	1171	0.31	960	0.04	310	0.86
7	400	2400	927	0.27	860	0.03	290	0.87
8	500	2400	1026	0.26	850	0.03	300	0.86
9	600	2400	1026	0.26	840	0.03	300	0.86
10	800	2400	1144	0.27	880	0.03	300	0.86
average 4-10		2400					310	0.86

Table 7.14. Multi-exponential fits of Lumi4-Tb-sAv-biot-50 nm Au NPs.

NO.	%	τ_1	E_1	A_1	α_{DA*1}	α_{DA1}	τ_2	E_2	A_2	α_{DA*2}	α_{DA2}
0	0						470	0.79	471	0.11	1.00
1	10	170	0.92	351	0.08	0.32	580	0.74	737	0.17	0.68
2	20	200	0.91	575	0.16	0.38	590	0.73	929	0.26	0.62
3	50	290	0.87	1215	0.32	0.46	600	0.73	1453	0.38	0.54
4	100	240	0.89	1161	0.24	0.28	550	0.75	2984	0.61	0.72
5	200	240	0.89	1020	0.21	0.23	540	0.75	3432	0.70	0.77
6	300	240	0.89	761	0.21	0.23	540	0.75	2574	0.70	0.77
7	400	270	0.88	939	0.25	0.28	560	0.74	2471	0.67	0.72
8	500	240	0.89	798	0.21	0.22	550	0.75	2788	0.72	0.78
9	600	230	0.89	599	0.18	0.19	550	0.75	2520	0.74	0.81
10	800	250	0.89	544	0.16	0.18	550	0.75	2491	0.74	0.82
average 2-10		240	0.89			0.28	560	0.74			0.72
					fraction:	28%				fraction:	72%

NO.	%	τ_0 (fixed)	A_0	α_{DA*0}	$\langle\tau\rangle$	z(D)	$\langle\tau_{DA}\rangle$	$\langle E\rangle$
0	0	2400	3847	0.89	2190			
1	10	2400	3234	0.75	1910	0.09	450	0.79
2	20	2400	2053	0.58	1570	0.07	440	0.80
3	50	2400	1114	0.29	1030	0.04	460	0.79
4	100	2400	726	0.15	750	0.02	460	0.79
5	200	2400	484	0.10	660	0.01	470	0.79
6	300	2400	321	0.09	640	0.01	470	0.79
7	400	2400	283	0.08	630	0.01	480	0.78
8	500	2400	299	0.08	630	0.01	480	0.78
9	600	2400	283	0.08	650	0.01	490	0.78
10	800	2400	324	0.10	680	0.01	500	0.77
average 2-10		2400					470	0.79

Table 7.15. Multi-exponential fits of Lumi4-Tb-sAv-biot-80 nm Au NPs.

NO.	%	τ_1	E_1	A_1	α_{DA*1}	α_{DA1}	τ_2	E_2	A_2	α_{DA*2}	α_{DA2}
0	0						680	0.62	1818	0.36	1.00
1	10	190	0.89	473	0.11	0.27	830	0.53	1300	0.29	0.73
2	20	170	0.90	519	0.12	0.31	780	0.56	1164	0.26	0.69
3	50	160	0.91	2317	0.36	0.62	660	0.63	1403	0.22	0.38
4	100	170	0.90	1928	0.40	0.69	710	0.60	874	0.18	0.31
5	200	180	0.90	2501	0.50	0.75	590	0.67	831	0.17	0.25
average 3-5		170	0.90			0.69	650	0.63			0.31
					fraction :	69%				fraction :	31%

NO.	%	τ_0(fixed)	A_0	α_{DA*0}	$\langle\tau\rangle$	z(D)	$\langle\tau_{DA}\rangle$	$\langle E\rangle$
0	0	2400	3238	0.64	1780			
1	10	2400	2651	0.60	1700	0.34	650	0.63
2	20	2400	2790	0.62	1720	0.35	540	0.70
3	50	2400	2682	0.42	1210	0.24	250	0.86
4	100	2400	2054	0.42	1210	0.24	230	0.87
5	200	2400	1659	0.33	990	0.19	190	0.89
average 3-5		2400					220	0.87

7.4.3 Analysis of Tb PL decays for 5 nm, 30 nm, 50 nm and 80 nm AuNPs using Kohlrausch decay laws

We analyzed the data with Kohlrausch ('stretched exponential') decay laws for comparison with the analysis of the PL decay using multiexponential decays (**Chapter 5**), which describes the overall relaxation of systems with an underlying distribution of relaxation rates using a minimal number of adjustable parameters.[240]–[242] The Kohlrausch decay law is given by **Equation 7.1**:

$$I(t) = A \exp\left[-\left(t/\tilde{\tau}\right)^{\beta}\right] \tag{7.1}$$

For $\beta = 1$, a mono-exponential decay is obtained; the underlying distribution is then a Dirac function centered at the decay time constant. For β going from 1 toward 0, the underlying distribution becomes increasingly broad. The average decay time

constant for a Kohlrausch decay law is given by **Equation 7.2**, where Γ is the gamma function.[240]

$$\langle\tau\rangle = \tilde{\tau}\,\Gamma\left(1+\frac{1}{\beta}\right) \tag{7.2}$$

The experimental PL decay of Tb-sAv in buffer is well described by the Kohlrausch decay law **Equation 7.2**, with $\tilde{\tau}_{\mathrm{D}} = 2.07$ ms and $\beta_{\mathrm{D}} = 0.88$, which yields $\langle\tau\rangle_{\mathrm{D}} = 2.19$ ms. This average decay constant is very close to the average decay constant obtained from a biexponential fit ($\langle\tau\rangle_{\mathrm{D}} = 2.2$ ms, **Figure 5.4a**). The advantage of using the Kohlrausch decay law is that it requires one less parameter to be optimized compared to a biexponential decay law. The close fit of this decay law to the data demonstrates its relevance for the analysis of non-exponential PL decays of Tb complexes coupled to proteins, where a distribution of decay constants is expected and observed.

When bio-AuNPs are added to the solution, Tb-sAv/biot-AuNP donor-acceptor assemblies are formed leading to a mixture of free Tb-sAv donors and Tb-sAv/biot-AuNP assemblies. The overall PL decay can be considered to be the sum of the individual decays of these two species, each described by a Kohlrausch decay, with the subscripts D and DA referring to the free donor and the donor-acceptor assemblies, respectively (**Equation 7.3**).

$$I(t) = A_{\mathrm{D}}\exp\left[-\left({}^{t}/_{\tilde{\tau}_{\mathrm{D}}}\right)^{\beta_{\mathrm{D}}}\right] + A_{\mathrm{DA}}\exp\left[-\left({}^{t}/_{\tilde{\tau}_{\mathrm{DA}}}\right)^{\beta_{\mathrm{DA}}}\right] \tag{7.3}$$

For the values of $\tilde{\tau}_{\mathrm{D}}$ and β_{D} we used the values obtained from the measurement of the pure Tb-sAv donor, and we keep these fixed throughout our analysis, leaving only A_{D}, A_{DA}, $\tilde{\tau}_{\mathrm{DA}}$ and β_{DA} to be determined. This was achieved by fitting the model **Equation 7.3** to the data using the 'lmfit' package[243] in Python, by minimizing the residuals with the Levenberg-Marquardt algorithm. The residual for each time bin was weighted by $1/\sqrt{N_{\mathrm{counts}}}$, where N_{counts} is the number of photons counted in the time bin. Reduced χ^2 values for the fits thus obtained were in the range of 1.25 to 1.45.

The results of the PL decay titration of Tb-sAv with biot-Au50-NP are shown in **Figure 7.11**. In presence of increasing biot-AuNP concentrations, the PL decay of the Tb-sAv donor is gradually replaced with a shorter PL decay component. This

component is attributed to the PL of Tb-sAv attached to the biot-AuNPs.

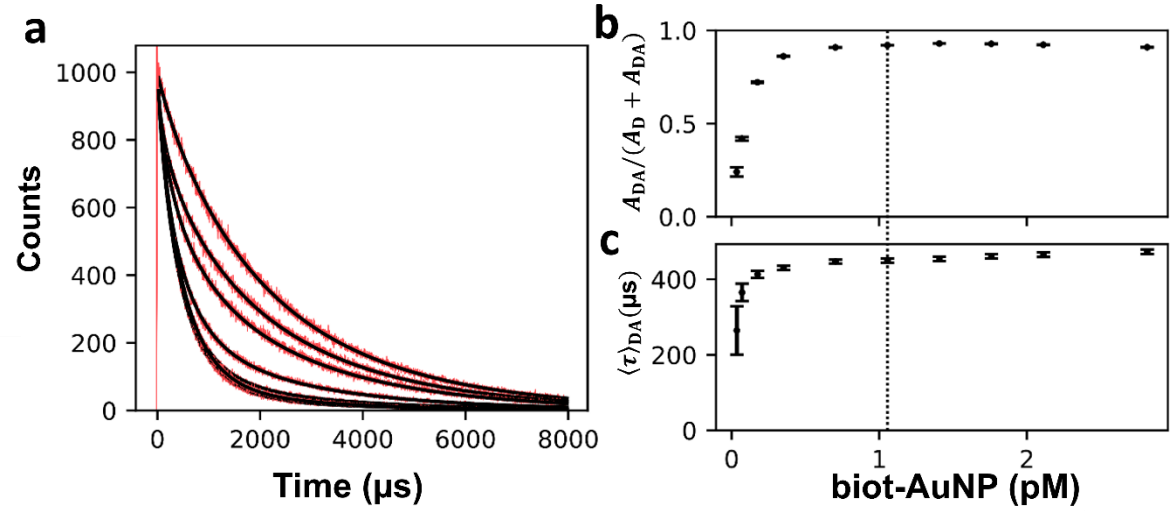

Figure 7.11. Analysis of PL decays of Tb-sAv (0.22 nM) in the presence of increasing amounts of 50 nm biot-AuNP in buffer. **(a)** Experimental decay traces (red), with fitted two-component Kohlrausch decay laws (black). The traces were scaled to equal initial amplitude for clarity. **(b)** Amplitude fraction of the Tb-sAv/biot-AuNP donor-acceptor assembly PL decay in the total PL decay as a function of biot-AuNP concentration, obtained from the curve fits. **(c)** Average PL decay times for the Tb-sAv/AuNP assemblies. The dotted line indicates the minimal biot-AuNP concentration to bind all available Tb-sAv (*i.e.* 208 Tb-sAv per biot-AuNP). The error bars indicate 95% confidence intervals.

From the fits of the model to the data, we obtained the amplitudes of the donor and the donor-acceptor assemblies (A_D resp. A_{DA}), as well as the kinetic parameters for the donor-acceptor assemblies, $\tilde{\tau}_{DA}$ and β_{DA}, as a function of 50nm biot-AuNPs concentration. From $\tilde{\tau}_{DA}$ and β_{DA}, we obtained the average decay time constant $\langle\tau\rangle_{DA}$ using **Equation 7.2**. The donor-acceptor amplitude A_{DA} and average decay time $\langle\tau\rangle_{DA}$ are plotted in **Figure 7.11b** and **7.11c**, as a function of biot-AuNPs concentration. The amplitude fraction of the signal of the Tb-AuNPs donor-acceptor assemblies gradually increased with increasing concentration of biot-AuNPs and reached a plateau near 0.9, indicating a small fraction of Tb-sAv that are inactive in terms of binding to biotin. The luminescence decay due to this non-binding fraction contributes to the signal of the donor-only decay (described by amplitude A_D and lifetime $\langle\tau\rangle_D$) but does not affect the determination of lifetime $\langle\tau\rangle_{DA}$ of the donor-acceptor assembly in the curve fits since the model used effectively separates donor and donor-acceptor contributions.

The average PL decay time of the donor-acceptor assemblies remains constant

when excess biot-AuNPs is present, *i.e.* in the cases where only few Tb-sAv are attached to each biot-AuNP. In contrast, the PL decay becomes shorter when the density of Tb-sAv per biot-AuNPs is higher (conditions of excess Tb-sAv). We tentatively ascribe this to energy transfer interactions between Tb-complexes at the surface of the nanoparticles at high Tb-sAv loading levels. Another, less likely, explanation may be that a dense packing of Tb-sAv at the biot-AuNP surface changes the structure of the PEG-biotin ligand shell in such a way as to reduce the average distance between Tb complexes and AuNP surface. In order to avoid such effects, only the measurements at low loading (higher biot-AuNPs concentrations – where $\langle\tau\rangle_{DA}$ remains constant) are included in energy transfer analysis. In these cases we are approaching the idealized situation where one Tb-complex interacts purely with one AuNP.

Similar behavior was observed with the 5 nm, 30 nm and 80 nm biot-AuNPs (**Figures 7.12, 7.13 and 7.14**). Using the same analysis procedure based on the Kohlrausch decay law, we are able to find the average decay times of Tb(III) luminescence in the donor-acceptor complex.

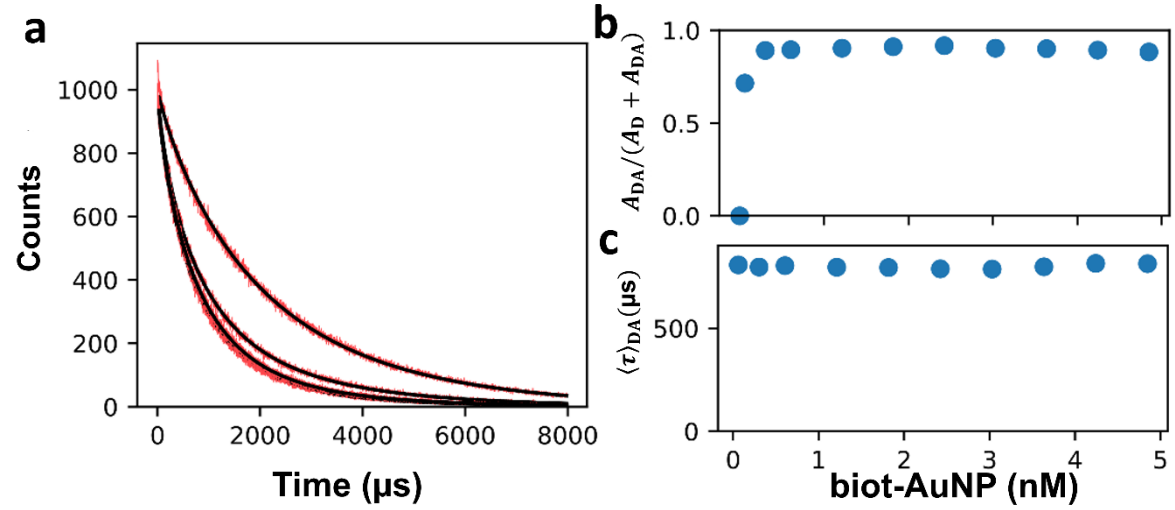

Figure 7.12. PL decays of Tb-sAv (0.91 nM) in the presence of increasing amounts of 5 nm biot-AuNPs in buffer. **(a)** Experimental decay traces (red), with fitted two-component Kohlrausch decay laws (black). The traces were scaled to equal initial amplitude for clarity. **(b)** Amplitude fraction of the Tb-sAv/biot-AuNP donor-acceptor assembly PL decay in the total PL decay as a function of biot-AuNP concentration, obtained from the curve fits. **(c)** Average PL decay times for the Tb-sAv/AuNP assemblies.

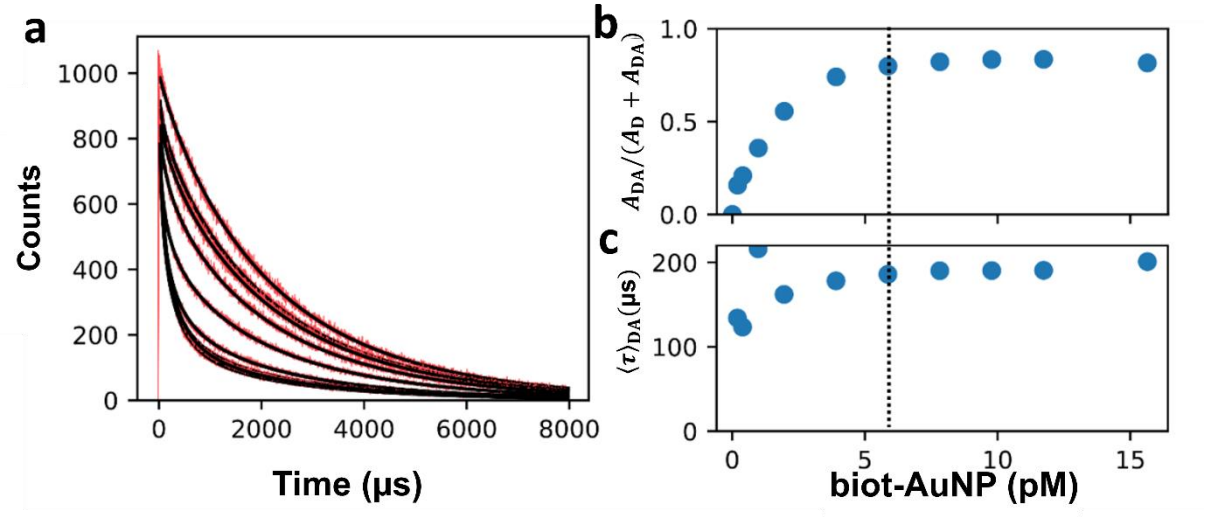

Figure 7.13. PL decays of Tb-sAv (0.44 nM) in the presence of increasing amounts of 30 nm biot-AuNPs in buffer. **(a)** Experimental decay traces (red), with fitted two-component Kohlrausch decay laws (black). The traces were scaled to equal initial amplitude for clarity. **(b)** Amplitude fraction of the Tb-sAv/biot-AuNP donor-acceptor assembly PL decay in the total PL decay as a function of biot-AuNP concentration, obtained from the curve fits. **(c)** Average PL decay times for the Tb-sAv/AuNP assemblies. The dotted line indicates the minimal biot-AuNP concentration to bind all available Tb-sAv (*i.e.* 75 Tb-sAv per biot-AuNP).

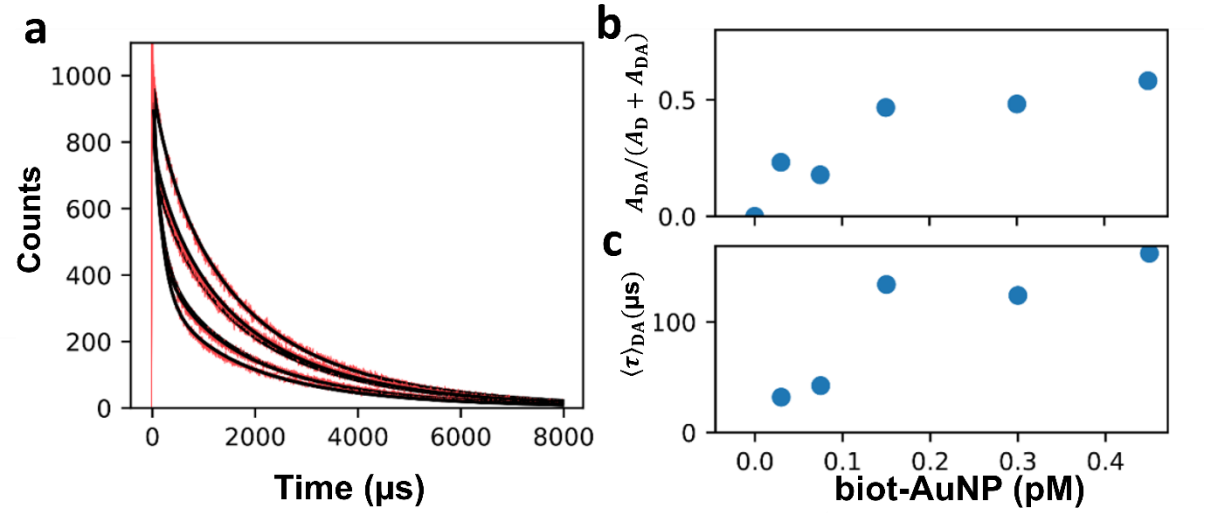

Figure 7.14. PL decays of Tb-sAv (0.24 nM) in the presence of increasing amounts of 80 nm biot-AuNPs in buffer. **(a)** Experimental decay traces (red), with fitted two-component Kohlrausch decay laws (black). The traces were scaled to equal initial amplitude for clarity. **(b)** Amplitude fraction of the Tb-sAv/biot-AuNP donor-acceptor assembly PL decay in the total PL decay as a function of biot-AuNP concentration, obtained from the curve fits. **(c)** Average PL decay times for the Tb-sAv/AuNP assemblies.

We consider the average decay time constants for the Tb-sAv/biot-AuNP at low Tb-sAv loading (*i.e.* high biot-AuNPs concentrations) in order to evaluate the energy transfer efficiency from the Tb complex to the gold nanoparticle, using **Equation**

7.4:

$$E = 1 - \frac{\langle\tau\rangle_{\mathrm{DA}}}{\langle\tau\rangle_{\mathrm{D}}} \tag{7.4}$$

In all cases, the energy transfer efficiency was larger than 50%, but less than 95%, leaving some Tb(III) luminescence available for detection. In spite of the giant oscillator strengths of the localized plasmon resonance, luminescence quenching is incomplete, and incorporation of photoluminescent entities into assemblies of plasmonic particles for fluorescence tracking and sensing purposes remains feasible.

8. Bibliography

[1] Lakowicz, J. R. *Principles of Fluorescence Spectroscopy*, 3rd ed.; Springer US: Boston, MA, 2006.

[2] Hildebrandt, N.; Medintz, I. *FRET – Förster Resonance Energy Transfer*; Wiley-VCH Verlag GmbH and Co. KGaA: Weinheim, Germany, 2013.

[3] Hildebrandt, N.; Spillmann, C. M.; Algar, W. R.; Pons, T.; Stewart, M. H.; Oh, E.; Susumu, K.; Díaz, S. A.; Delehanty, J. B.; Medintz, I. L. Energy Transfer with Semiconductor Quantum Dot Bioconjugates: A Versatile Platform for Biosensing, Energy Harvesting, and Other Developing Applications. *Chem. Rev.* **2017**, *117* (2), 537–711.

[4] Berney, C.; Danuser, G. FRET or No FRET: A Quantitative Comparison. *Biophys. J.* **2003**, *84* (6), 3992–4010.

[5] Corry, B.; Jayatilaka, D.; Rigby, P. A Flexible Approach to the Calculation of Resonance Energy Transfer Efficiency between Multiple Donors and Acceptors in Complex Geometries. *Biophys. J.* **2005**, *89* (6), 3822–3836.

[6] Deplazes, E.; Jayatilaka, D.; Corry, B. ExiFRET: Flexible Tool for Understanding FRET in Complex Geometries. *J. Biomed. Opt.* **2012**, *17* (1), 011005.

[7] Raicu, V. Efficiency of Resonance Energy Transfer in Homo-Oligomeric Complexes of Proteins. *J. Biol. Phys.* **2007**, *33* (2), 109–127.

[8] Clapp, A. R.; Medintz, I. L.; Mauro, J. M.; Fisher, B. R.; Bawendi, M. G.; Mattoussi, H. Fluorescence Resonance Energy Transfer Between Quantum Dot Donors and Dye-Labeled Protein Acceptors. *J. Am. Chem. Soc.* **2004**, *126* (1), 301–310.

[9] Efros, A. L.; Efros, A. L. Interband Light Absorption in Semiconductor Spheres. *Sov. Phys Semicond.* **1982**, *16* (7), 772–775.

[10] Ekimov, A.; Onushchenko, A. Quantum Size Effect in the Optical Spectra of Semiconductor Microcrystals. *Sov. Phys Semicond.* **1982**, *16* (7), 775–778.

[11] Rossetti, R.; Nakahara, S.; Brus, L. E. Quantum Size Effects in the Redox Potentials, Resonance Raman Spectra, and Electronic Spectra of CdS Crystallites in Aqueous Solution. *J. Chem. Phys.* **1983**, *79* (2), 1086–1088.

[12] Murray, C. B.; Norris, D. J.; Bawendi, M. G. Synthesis and Characterization of Nearly Monodisperse CdE (E = Sulfur, Selenium, Tellurium) Semiconductor Nanocrystallites. *J. Am. Chem. Soc.* **1993**, *115* (19), 8706–8715.

[13] Alivisatos, A. P. Perspectives on the Physical Chemistry of Semiconductor Nanocrystals. *J. Phys. Chem.* **1996**, *100* (31), 13226–13239.

[14] Yoffe, A. D. Semiconductor Quantum Dots and Related Systems: Electronic, Optical, Luminescence and Related Properties of Low Dimensional Systems. *Adv. Phys.* **2001**, *50* (1), 1–208.

[15] Chan, W. C.; Nie, S. Quantum Dot Bioconjugates for Ultrasensitive Nonisotopic Detection. *Science* **1998**, *281* (5385), 2016–2018.

[16] Bruchez Jr., M.; Moronne, M.; Gin, P.; Weiss, S.; Alivisatos, A. P. Semiconductor Nanocrystals as Fluorescent Biological Labels. *Science* **1998**, *281* (5385), 2013–2016.

[17] Reiss, P.; Carrière, M.; Lincheneau, C.; Vaure, L.; Tamang, S. Synthesis of Semiconductor Nanocrystals, Focusing on Nontoxic and Earth-Abundant Materials. *Chem. Rev.* **2016**, *116* (18), 10731–10819.

[18] Algar, W. R.; Susumu, K.; Delehanty, J. B.; Medintz, I. L. Semiconductor Quantum Dots in Bioanalysis: Crossing the Valley of Death. *Anal. Chem.* **2011**, *83* (23), 8826–8837.

[19] Resch-Genger, U.; Grabolle, M.; Cavaliere-Jaricot, S.; Nitschke, R.; Nann, T. Quantum Dots versus Organic Dyes as Fluorescent Labels. *Nat. Methods* **2008**, *5* (9), 763–775.

[20] Chen, O.; Zhao, J.; Chauhan, V. P.; Cui, J.; Wong, C.; Harris, D. K.; Wei, H.; Han, H.-S.; Fukumura, D.; Jain, R. K.; et al. Compact High-Quality CdSe–CdS Core–shell Nanocrystals with Narrow Emission Linewidths and Suppressed Blinking. *Nat. Mater.* **2013**, *12* (5), 445–451.

[21] Yu, J. H.; Kwon, S.-H.; Petrášek, Z.; Park, O. K.; Jun, S. W.; Shin, K.; Choi, M.; Park, Y. Il; Park, K.; Na, H. Bin; et al. High-Resolution Three-Photon Biomedical Imaging Using Doped ZnS Nanocrystals. *Nat. Mater.* **2013**, *12* (4), 359–366.

[22] Kim, Y.; Kim, W.; Yoon, H.-J.; Shin, S. K. Bioconjugation of Hydroxylated Semiconductor Nanocrystals and Background-Free Biomolecule Detection. *Bioconjug. Chem.* **2010**, *21* (7), 1305–1311.

[23] Algar, W. R.; Krull, U. J. Adsorption and Hybridization of Oligonucleotides on Mercaptoacetic Acid-Capped CdSe/ZnS Quantum Dots and Quantum Dot−Oligonucleotide Conjugates. *Langmuir* **2006**, *22* (26), 11346–11352.

[24] Wilson, R.; Spiller, D. G.; Beckett, A.; Prior, I. A.; Sée, V. Highly Stable Dextran-Coated Quantum Dots for Biomolecular Detection and Cellular Imaging. *Chem. Mater.* **2010**, *22* (23), 6361–6369.

[25] Kongkanand, A. Interfacial Water Transport Measurements in Nafion Thin Films Using a Quartz-Crystal Microbalance. *J. Phys. Chem. C* **2011**, *115* (22), 11318–11325.

[26] Freeman, R.; Gill, R.; Shweky, I.; Kotler, M.; Banin, U.; Willner, I. Biosensing and Probing of Intracellular Metabolic Pathways by NADH-Sensitive Quantum Dots. *Angew. Chem. Int. Ed.* **2009**, *48* (2), 309–313.

[27] Mitchell, G. P.; Mirkin, C. A.; Letsinger, R. L. Programmed Assembly of DNA Functionalized Quantum Dots. *J. Am. Chem. Soc.* **1999**, *121* (35), 8122–8123.

[28] Hoshino, A.; Fujioka, K.; Oku, T.; Suga, M.; Sasaki, Y. F.; Ohta, T.; Yasuhara, M.; Suzuki, K.; Yamamoto, K. Physicochemical Properties and Cellular Toxicity of Nanocrystal Quantum Dots Depend on Their Surface Modification. *Nano Lett.* **2004**, *4* (11), 2163–2169.

[29] Hering, V. R.; Gibson, G.; Schumacher, R. I.; Faljoni-Alario, A.; Politi, M. J. Energy Transfer between CdSe/ZnS Core/Shell Quantum Dots and Fluorescent Proteins. *Bioconjug. Chem.* **2007**, *18* (6), 1705–1708.

[30] Mattoussi, H.; Mauro, J. M.; Goldman, E. R.; Anderson, G. P.; Sundar, V. C.; Mikulec, F. V.; Bawendi, M. G. Self-Assembly of CdSe−ZnS Quantum Dot Bioconjugates Using an Engineered Recombinant Protein. *J. Am. Chem. Soc.* **2000**, *122* (49), 12142–12150.

[31] Kang, E.-C.; Ogura, A.; Kataoka, K.; Nagasaki, Y. Preparation of Water-Soluble PEGylated Semiconductor Nanocrystals. *Chem. Lett.* **2004**, *33* (7), 840–841.

[32] Akerman, M. E.; Chan, W. C. W.; Laakkonen, P.; Bhatia, S. N.; Ruoslahti, E. Nanocrystal Targeting in Vivo. *Proc. Natl. Acad. Sci.* **2002**, *99* (20), 12617–12621.

[33] Susumu, K.; Mei, B. C.; Mattoussi, H. Multifunctional Ligands Based on Dihydrolipoic Acid and Polyethylene Glycol to Promote Biocompatibility of Quantum Dots. *Nat. Protoc.* **2009**, *4* (3), 424–436.

[34] Mei, B. C.; Susumu, K.; Medintz, I. L.; Mattoussi, H. Polyethylene Glycol-Based Bidentate Ligands to Enhance Quantum Dot and Gold Nanoparticle Stability in Biological Media. *Nat. Protoc.* **2009**, *4* (3), 412–423.

[35] Uyeda, H. T.; Medintz, I. L.; Jaiswal, J. K.; Simon, S. M.; Mattoussi, H. Synthesis of Compact Multidentate Ligands to Prepare Stable Hydrophilic Quantum Dot Fluorophores. *J. Am. Chem. Soc.* **2005**, *127* (11), 3870–3878.

[36] Dubertret, B.; Skourides, P.; Norris, D. J.; Noireaux, V.; Brivanlou, A. H.; Libchaber, A. In Vivo Imaging of Quantum Dots Encapsulated in Phospholipid Micelles. *Science* **2002**, *298* (5599), 1759–1762.

[37] Nann, T.; Mulvaney, P. Single Quantum Dots in Spherical Silica Particles. *Angew. Chem. Int. Ed.* **2004**, *43* (40), 5393–5396.

[38] Gerion, D.; Pinaud, F.; Williams, S. C.; Parak, W. J.; Zanchet, D.; Weiss, S.; Alivisatos, A. P. Synthesis and Properties of Biocompatible Water-Soluble Silica-Coated CdSe/ZnS Semiconductor Quantum Dots †. *J. Phys. Chem. B* **2001**, *105* (37), 8861–8871.

[39] Darbandi, M.; Thomann, R.; Nann, T. Single Quantum Dots in Silica Spheres by Microemulsion Synthesis. *Chem. Mater.* **2005**, *17* (23), 5720–5725.

[40] Selvan, S. T.; Tan, T. T.; Ying, J. Y. Robust, Non-Cytotoxic, Silica-Coated CdSe Quantum Dots with Efficient Photoluminescence. *Adv. Mater.* **2005**, *17* (13), 1620–1625.

[41] Selvan, S. T.; Patra, P. K.; Ang, C. Y.; Ying, J. Y. Synthesis of Silica-Coated Semiconductor and Magnetic Quantum Dots and Their Use in the Imaging of Live Cells. *Angew. Chem. Int. Ed.* **2007**, *46* (14), 2448–2452.

[42] Gao, F.; Ye, Q.; Cui, P.; Zhang, L. Efficient Fluorescence Energy Transfer System between CdTe-Doped Silica Nanoparticles and Gold Nanoparticles for Turn-On Fluorescence Detection of Melamine. *J. Agric. Food Chem.* **2012**, *60* (18), 4550–4558.

[43] Wu, C.-S.; Khaing Oo, M. K.; Fan, X. Highly Sensitive Multiplexed Heavy Metal Detection Using Quantum-Dot-Labeled DNAzymes. *ACS Nano* **2010**, *4* (10), 5897–5904.

[44] Chen, C.; Ao, L.; Wu, Y.-T.; Cifliku, V.; Cardoso Dos Santos, M.; Bourrier, E.; Delbianco, M.; Parker, D.; Zwier, J. M.; Huang, L.; et al. Single-Nanoparticle Cell Barcoding by Tunable FRET from Lanthanides to Quantum Dots. *Angew. Chem. Int. Ed.* **2018**, *57* (41), 13686–13690.

[45] Patolsky, F.; Gill, R.; Weizmann, Y.; Mokari, T.; Banin, U.; Willner, I. Lighting-Up the Dynamics of Telomerization and DNA Replication by CdSe−ZnS Quantum Dots. *J. Am. Chem. Soc.* **2003**, *125* (46), 13918–13919.

[46] Medintz, I. L.; Clapp, A. R.; Mattoussi, H.; Goldman, E. R.; Fisher, B.; Mauro, J. M. Self-Assembled Nanoscale Biosensors Based on Quantum Dot FRET Donors. *Nat. Mater.* **2003**, *2* (9), 630–638.

[47] Oh, E.; Hong, M.-Y.; Lee, D.; Nam, S.-H.; Yoon, H. C.; Kim, H.-S. Inhibition Assay of Biomolecules Based on Fluorescence Resonance Energy Transfer (FRET) between Quantum Dots and Gold Nanoparticles. *J. Am. Chem. Soc.* **2005**, *127* (10), 3270–3271.

[48] Shi, L.; De Paoli, V.; Rosenzweig, N.; Rosenzweig, Z. Synthesis and Application of Quantum Dots FRET-Based Protease Sensors. *J. Am. Chem. Soc.* **2006**, *128* (32), 10378–10379.

[49] Dennis, A. M.; Rhee, W. J.; Sotto, D.; Dublin, S. N.; Bao, G. Quantum Dot-Fluorescent Protein Fret Probes for Sensing Intracellular PH. *ACS Nano* **2012**, *6* (4), 2917–2924.

[50] Lu, H.; Schöps, O.; Woggon, U.; Niemeyer, C. M. Self-Assembled Donor Comprising Quantum Dots and Fluorescent Proteins for Long-Range Fluorescence Resonance Energy Transfer. *J. Am. Chem. Soc.* **2008**, *130* (14), 4815–4827.

[51] Algar, W. R.; Ancona, M. G.; Malanoski, A. P.; Susumu, K.; Medintz, I. L. Assembly of a Concentric Förster Resonance Energy Transfer Relay on a Quantum Dot Scaffold: Characterization and Application to Multiplexed Protease Sensing. *ACS Nano* **2012**, *6* (12), 11044–11058.

[52] Spillmann, C. M.; Ancona, M. G.; Buckhout-White, S.; Algar, W. R.; Stewart, M. H.; Susumu, K.; Huston, A. L.; Goldman, E. R.; Medintz, I. L. Achieving Effective Terminal Exciton Delivery in Quantum Dot Antenna-Sensitized Multistep DNA Photonic Wires. *ACS Nano* **2013**, *7* (8), 7101–7118.

[53] Kim, H.; Ng, C. Y. W.; Algar, W. R. Quantum Dot-Based Multidonor Concentric FRET System and Its Application to Biosensing Using an Excitation Ratio. *Langmuir* **2014**, *30* (19), 5676–5685.

[54] Wu, M.; Algar, W. R. Concentric Förster Resonance Energy Transfer Imaging. *Anal. Chem.* **2015**, *87* (16), 8078–8083.

[55] Wu, M.; Massey, M.; Petryayeva, E.; Algar, W. R. Energy Transfer Pathways in a Quantum Dot-Based Concentric FRET Configuration. *J. Phys. Chem. C* **2015**, *119* (46), 26183–26195.

[56] Conroy, E. M.; Li, J. J.; Kim, H.; Algar, W. R. Self-Quenching, Dimerization, and Homo-FRET in Hetero-FRET Assemblies with Quantum Dot Donors and Multiple Dye Acceptors. *J. Phys. Chem. C* **2016**, *120* (31), 17817–17828.

[57] Massey, M.; Kim, H.; Conroy, E. M.; Algar, W. R. Expanded Quantum Dot-Based Concentric Förster Resonance Energy Transfer: Adding and Characterizing Energy-Transfer Pathways for Triply Multiplexed Biosensing. *J. Phys. Chem. C* **2017**, *121* (24), 13345–13356.

[58] Clapp, A. R.; Medintz, I. L.; Fisher, B. R.; Anderson, G. P.; Mattoussi, H. Can Luminescent Quantum Dots Be Efficient Energy Acceptors with Organic Dye Donors? *J. Am. Chem. Soc.* **2005**, *127* (4), 1242–1250.

[59] Algar, W. R.; Kim, H.; Medintz, I. L.; Hildebrandt, N. Emerging Non-Traditional Förster Resonance Energy Transfer Configurations with Semiconductor Quantum Dots: Investigations and Applications. *Coord. Chem. Rev.* **2014**, *263–264*, 65–85.

[60] Hildebrandt, N.; Charbonnière, L. J.; Beck, M.; Ziessel, R. F.; Löhmannsröben, H.-G. Quantum Dots as Efficient Energy Acceptors in a Time-Resolved Fluoroimmunoassay. *Angew. Chem. Int. Ed.* **2005**, *44* (46), 7612–7615.

[61] Charbonnière, L. J.; Hildebrandt, N.; Ziessel, R. F.; Löhmannsröben, H.-G. Lanthanides to Quantum Dots Resonance Energy Transfer in Time-Resolved Fluoro-Immunoassays and Luminescence Microscopy. *J. Am. Chem. Soc.* **2006**, *128* (39), 12800–12809.

[62] So, M.-K.; Xu, C.; Loening, A. M.; Gambhir, S. S.; Rao, J. Self-Illuminating Quantum Dot Conjugates for in Vivo Imaging. *Nat. Biotechnol.* **2006**, *24* (3), 339–343.

[63] Huang, X.; Li, L.; Qian, H.; Dong, C.; Ren, J. A Resonance Energy Transfer between Chemiluminescent Donors and Luminescent Quantum-Dots as Acceptors (CRET). *Angew. Chem. Int. Ed.* **2006**, *45* (31), 5140–5143.

[64] Mattsson, L.; Wegner, K. D.; Hildebrandt, N.; Soukka, T. Upconverting Nanoparticle to Quantum Dot FRET for Homogeneous Double-Nano Biosensors. *RSC Adv.* **2015**, *5* (18), 13270–13277.

[65] Algar, W. R.; Wegner, D.; Huston, A. L.; Blanco-Canosa, J. B.; Stewart, M. H.; Armstrong, A.; Dawson, P. E.; Hildebrandt, N.; Medintz, I. L. Quantum Dots as Simultaneous Acceptors and Donors in Time-Gated Förster Resonance Energy Transfer Relays: Characterization and Biosensing. *J. Am. Chem. Soc.* **2012**, *134* (3), 1876–1891.

[66] Algar, W. R.; Malanoski, A. P.; Susumu, K.; Stewart, M. H.; Hildebrandt, N.; Medintz, I. L. Multiplexed Tracking of Protease Activity Using a Single Color of Quantum Dot Vector and a Time-Gated Förster Resonance Energy Transfer Relay. *Anal. Chem.* **2012**, *84* (22), 10136–10146.

[67] Claussen, J. C.; Hildebrandt, N.; Susumu, K.; Ancona, M. G.; Medintz, I. L. Complex Logic Functions Implemented with Quantum Dot Bionanophotonic Circuits. *ACS Appl. Mater. Interfaces* **2014**, *6* (6), 3771–3778.

[68] Afsari, H. S.; Cardoso Dos Santos, M.; Lindén, S.; Chen, T.; Qiu, X.; van Bergen en Henegouwen, P. M. P.; Jennings, T. L.; Susumu, K.; Medintz, I. L.; Hildebrandt, N.; et al. Time-Gated FRET Nanoassemblies for Rapid and Sensitive Intra- and Extracellular Fluorescence Imaging. *Sci. Adv.* **2016**, *2* (6), e1600265.

[69] Jiang, G.; Susha, A. S.; Lutich, A. A.; Stefani, F. D.; Feldmann, J.; Rogach, A. L. Cascaded FRET in Conjugated Polymer/Quantum Dot/Dye-Labeled DNA Complexes for DNA Hybridization Detection. *ACS Nano* **2009**, *3* (12), 4127–4131.

[70] Algar, W. R.; Khachatrian, A.; Melinger, J. S.; Huston, A. L.; Stewart, M. H.; Susumu, K.; Blanco-Canosa, J. B.; Oh, E.; Dawson, P. E.; Medintz, I. L. Concurrent Modulation of Quantum Dot Photoluminescence Using a Combination of Charge Transfer and Förster Resonance Energy Transfer: Competitive Quenching and Multiplexed Biosensing Modality. *J. Am. Chem. Soc.* **2017**, *139* (1), 363–372.

[71] Schlücker, S. Surface-Enhanced Raman Spectroscopy: Concepts and Chemical Applications. *Angew. Chem. Int. Ed.* **2014**, *53* (19), 4756–4795.

[72] Moore, E. G.; Samuel, A. P. S.; Raymond, K. N. From Antenna to Assay: Lessons Learned in Lanthanide Luminescence. *Acc. Chem. Res.* **2009**, *42* (4), 542–552.

[73] Eliseeva, S. V.; Bünzli, J.-C. G. Lanthanide Luminescence for Functional Materials and Bio-Sciences. *Chem. Soc. Rev.* **2010**, *39* (1), 189–227.

[74] Sherry, A. D.; Green, K. N.; Ratnakar, S. J.; Kovacs, Z.; Viswanathan, S. Alternatives to Gadolinium-Based Metal Chelates for Magnetic Resonance Imaging † . *Chem. Rev.* **2010**, *110* (5), 2960–3018.

[75] Eliseeva, S. V.; Bünzli, J.-C. G. Rare Earths: Jewels for Functional Materials of the Future. *New J. Chem.* **2011**, *35* (6), 1165–1176.

[76] Bünzli, J.-C. G.; Piguet, C. Taking Advantage of Luminescent Lanthanide Ions. *Chem. Soc. Rev.* **2005**, *34* (12), 1048–1077.

[77] Debroye, E.; Parac-Vogt, T. N. Towards Polymetallic Lanthanide Complexes as Dual Contrast Agents for Magnetic Resonance and Optical Imaging. *Chem. Soc. Rev.* **2014**, *43* (23), 8178–8192.

[78] Pershagen, E.; Borbas, K. E. Designing Reactivity-Based Responsive Lanthanide Probes for Multicolor Detection in Biological Systems. *Coord. Chem. Rev.* **2014**, *273–274*, 30–46.

[79] Bünzli, J.-C. G. Lanthanide Luminescence for Biomedical Analyses and Imaging. *Chem. Rev.* **2010**, *110* (5), 2729–2755.

[80] Li, G.; Tian, Y.; Zhao, Y.; Lin, J. Recent Progress in Luminescence Tuning of Ce^{3+} and Eu^{2+}-Activated Phosphors for Pc-WLEDs. *Chem. Soc. Rev.* **2015**, *44* (23), 8688–8713.

[81] Zhou, B.; Shi, B.; Jin, D.; Liu, X. Controlling Upconversion Nanocrystals for Emerging Applications. *Nat. Nanotechnol.* **2015**, *10* (11), 924–936.

[82] Liu, Y.; Tu, D.; Zhu, H.; Chen, X. Lanthanide-Doped Luminescent Nanoprobes: Controlled Synthesis, Optical Spectroscopy, and Bioapplications. *Chem. Soc. Rev.* **2013**, *42* (16), 6924.

[83] Zhang, K. Y.; Yu, Q.; Wei, H.; Liu, S.; Zhao, Q.; Huang, W. Long-Lived Emissive Probes for Time-Resolved Photoluminescence Bioimaging and Biosensing. *Chem. Rev.* **2018**, *118* (4), 1770–1839.

[84] Heffern, M. C.; Matosziuk, L. M.; Meade, T. J. Lanthanide Probes for Bioresponsive Imaging. *Chem. Rev.* **2014**, *114* (8), 4496–4539.

[85] Xu, J.; Corneillie, T. M.; Moore, E. G.; Law, G. L.; Butlin, N. G.; Raymond, K. N. Octadentate Cages of Tb(III) 2-Hydroxyisophthalamides: A New Standard for Luminescent Lanthanide Labels. *J. Am. Chem. Soc.* **2011**, *133* (49), 19900–19910.

[86] Bünzli, J. C. G. On the Design of Highly Luminescent Lanthanide Complexes. *Coord. Chem. Rev.* **2015**, *293–294*, 19–47.

[87] Dong, H.; Du, S.-R.; Zheng, X.-Y.; Lyu, G.-M.; Sun, L.-D.; Li, L.-D.; Zhang, P.-Z.; Zhang, C.; Yan, C.-H. Lanthanide Nanoparticles: From Design toward Bioimaging and Therapy. *Chem. Rev.* **2015**, *115* (19), 10725–10815.

[88] Auzel, F. Upconversion and Anti-Stokes Processes with f and d Ions in Solids. *Chem. Rev.* **2004**, *104* (1), 139–174.

[89] Shen, J.; Chen, G.; Vu, A.-M.; Fan, W.; Bilsel, O. S.; Chang, C.-C.; Han, G. Engineering the Upconversion Nanoparticle Excitation Wavelength: Cascade Sensitization of Tri-Doped Upconversion Colloidal Nanoparticles at 800 Nm. *Adv. Opt. Mater.* **2013**, *1* (9), 644–650.

[90] Xie, X.; Gao, N.; Deng, R.; Sun, Q.; Xu, Q.-H.; Liu, X. Mechanistic Investigation of Photon Upconversion in Nd^{3+}-Sensitized Core–Shell Nanoparticles. *J. Am. Chem. Soc.* **2013**, *135* (34), 12608–12611.

[91] Wang, Y.-F.; Liu, G.-Y.; Sun, L.-D.; Xiao, J.-W.; Zhou, J.-C.; Yan, C.-H. Nd^{3+}-Sensitized Upconversion Nanophosphors: Efficient In Vivo Bioimaging Probes with Minimized Heating Effect. *ACS Nano* **2013**, *7* (8), 7200–7206.

[92] Wang, F.; Deng, R.; Wang, J.; Wang, Q.; Han, Y.; Zhu, H.; Chen, X.; Liu, X. Tuning Upconversion through Energy Migration in Core–shell Nanoparticles. *Nat. Mater.* **2011**, *10* (12), 968–973.

[93] Cardoso Dos Santos, M.; Hildebrandt, N. Recent Developments in Lanthanide-to-Quantum Dot FRET Using Time-Gated Fluorescence Detection and Photon Upconversion. *TrAC - Trends Anal. Chem.* **2016**, *84*, 60–71.

[94] Hildebrandt, N.; Wegner, K. D.; Algar, W. R. Luminescent Terbium Complexes: Superior Förster Resonance Energy Transfer Donors for Flexible and Sensitive Multiplexed Biosensing. *Coord. Chem. Rev.* **2014**, *273–274*, 125–138.

[95] Mathis, G. Rare Earth Cryptates and Homogeneous Fluoroimmunoassays with Human Sera. *Clin. Chem.* **1993**, *39* (9), 1953–1959.

[96] Geißler, D.; Linden, S.; Liermann, K.; Wegner, K. D.; Charbonnière, L. J.; Hildebrandt, N. Lanthanides and Quantum Dots as Förster Resonance Energy Transfer Agents for Diagnostics and Cellular Imaging. *Inorg. Chem.* **2014**, *53* (4), 1824–1838.

[97] Sapsford, K. E.; Berti, L.; Medintz, I. L. Materials for Fluorescence Resonance Energy Transfer Analysis: Beyond Traditional Donor–Acceptor Combinations. *Angew. Chem. Int. Ed.* **2006**, *45* (28), 4562–4589.

[98] Dsouza, R. N.; Pischel, U.; Nau, W. M. Fluorescent Dyes and Their Supramolecular Host/Guest Complexes with Macrocycles in Aqueous Solution. *Chem. Rev.* **2011**, *111* (12), 7941–7980.

[99] Sauer, M.; Hofkens, J.; Enderlein, J. *Handbook of Fluorescence Spectroscopy and Imaging*; Wiley-VCH Verlag GmbH & Co. KGaA: Weinheim, Germany, 2011.

[100] Eisfeld, A.; Briggs, J. S. The J- and H-Bands of Organic Dye Aggregates. *Chem. Phys.* **2006**, *324* (2–3), 376–384.

[101] Rösch, U.; Yao, S.; Wortmann, R.; Würthner, F. Fluorescent H-Aggregates of Merocyanine Dyes. *Angew. Chem. Int. Ed.* **2006**, *45* (42), 7026–7030.

[102] Hestand, N. J.; Spano, F. C. Molecular Aggregate Photophysics beyond the Kasha Model: Novel Design Principles for Organic Materials. *Acc. Chem. Res.* **2017**, *50* (2), 341–350.

[103] Halpert, J. E.; Tischler, J. R.; Nair, G.; Walker, B. J.; Liu, W.; Bulović, V.; Bawendi, M. G. Electrostatic Formation of Quantum Dot/J-Aggregate FRET Pairs in Solution. *J. Phys. Chem. C* **2009**, *113* (23), 9986–9992.

[104] Walker, B. J.; Bulović, V.; Bawendi, M. G. Quantum Dot/J-Aggregate Blended Films for Light Harvesting and Energy Transfer. *Nano Lett.* **2010**, *10* (10), 3995–3999.

[105] Walker, B. J.; Nair, G. P.; Marshall, L. F.; Bulović, V.; Bawendi, M. G. Narrow-Band Absorption-Enhanced Quantum Dot/J-Aggregate Conjugates. *J. Am. Chem. Soc.* **2009**, *131* (28), 9624–9625.

[106] Levitt, J. A.; Matthews, D. R.; Ameer-Beg, S. M.; Suhling, K. Fluorescence Lifetime and Polarization-Resolved Imaging in Cell Biology. *Curr. Opin. Biotechnol.* **2009**, *20* (1), 28–36.

[107] Sahoo, H. Förster Resonance Energy Transfer – A Spectroscopic Nanoruler: Principle and Applications. *J. Photochem. Photobiol. C Photochem. Rev.* **2011**, *12* (1), 20–30.

[108] Yan, Y. Analysis of Protein Interactions Using Fluorescence Technologies. *Curr. Opin. Chem. Biol.* **2003**, *7* (5), 635–640.

[109] Zhegalova, N. G.; He, S.; Zhou, H.; Kim, D. M.; Berezin, M. Y. Minimization of Self-Quenching Fluorescence on Dyes Conjugated to Biomolecules with Multiple Labeling Sites via Asymmetrically Charged NIR Fluorophores. *Contrast Media Mol. Imaging* **2014**, *9* (5), 355–362.

[110] Ghukasyan, V. Fluorescence Lifetime Dynamics of Enhanced Green Fluorescent Protein in Protein Aggregates with Expanded Polyglutamine. *J. Biomed. Opt.* **2010**, *15* (1), 016008.

[111] Koushik, S. V.; Vogel, S. S. Energy Migration Alters the Fluorescence Lifetime of Cerulean: Implications for Fluorescence Lifetime Imaging Forster Resonance Energy Transfer Measurements. *J. Biomed. Opt.* **2008**, *13* (3), 031204.

[112] Song, X.; Swanson, B. I. Rapid Assay for Avidin and Biotin Based on Fluorescence Quenching. *Anal. Chim. Acta* **2001**, *442* (1), 79–87.

[113] Saha, K.; Agasti, S. S.; Kim, C.; Li, X.; Rotello, V. M. Gold Nanoparticles in Chemical and Biological Sensing. *Chem. Rev.* **2012**, *112* (5), 2739–2779.

[114] Daniel, M.-C.; Astruc, D. Gold Nanoparticles: Assembly, Supramolecular Chemistry, Quantum-Size-Related Properties, and Applications toward Biology, Catalysis, and Nanotechnology. *Chem. Rev.* **2004**, *104* (1), 293–346.

[115] Subramaniam, C.; Pradeep, T.; Chakrabarti, J. Flow-Induced Transverse Electrical Potential across an Assembly of Gold Nanoparticles. *Phys. Rev. Lett.* **2005**, *95* (16), 164501.

[116] Schmid, G.; Simon, U. Gold Nanoparticles: Assembly and Electrical Properties in 1–3 Dimensions. *Chem. Commun.* **2005**, No. 6, 697–710.

[117] Halas, N. J.; Lal, S.; Chang, W.-S.; Link, S.; Nordlander, P. Plasmons in Strongly Coupled Metallic Nanostructures. *Chem. Rev.* **2011**, *111* (6), 3913–3961.

[118] Su, K.-H.; Wei, Q.-H.; Zhang, X.; Mock, J. J.; Smith, D. R.; Schultz, S. Interparticle Coupling Effects on Plasmon Resonances of Nanogold Particles. *Nano Lett.* **2003**, *3* (8), 1087–1090.

[119] Dyadyusha, L.; Yin, H.; Jaiswal, S.; Brown, T.; Baumberg, J. J.; Booy, F. P.; Melvin, T. Quenching of CdSe Quantum Dot Emission, a New Approach for Biosensing. *Chem. Commun.* **2005**, No. 25, 3201–3203.

[120] Chen, Y.; Donoghue, M. B. O.; Huang, Y.; Kang, H.; Phillips, J. A.; Chen, X.; Estevez, M.-C.; Yang, C. J.; Tan, W.; O'Donoghue, M. B.; et al. A Surface Energy Transfer

Nanoruler for Measuring Binding Site Distances on Live Cell Surfaces. *J. Am. Chem. Soc.* **2010**, *132* (11), 16559–16570.

[121] Singh, M. P.; Strouse, G. F. Involvement of the LSPR Spectral Overlap for Energy Transfer between a Dye and Au Nanoparticle. *J. Am. Chem. Soc.* **2010**, *132* (27), 9383–9391.

[122] Singh, M. P.; Jennings, T. L.; Strouse, G. F. Tracking Spatial Disorder in an Optical Ruler by Time-Resolved NSET. *J. Phys. Chem. B* **2009**, *113* (2), 552–558.

[123] Jennings, T. L.; Singh, M. P.; Strouse, G. F. Fluorescent Lifetime Quenching near d = 1.5 nm Gold Nanoparticles: Probing NSET Validity. *J. Am. Chem. Soc.* **2006**, *128* (16), 5462–5467.

[124] Seelig, J.; Leslie, K.; Renn, A.; Kühn, S.; Jacobsen, V.; van de Corput, M.; Wyman, C.; Sandoghdar, V. Nanoparticle-Induced Fluorescence Lifetime Modification as Nanoscopic Ruler: Demonstration at the Single Molecule Level. *Nano Lett.* **2007**, *7* (3), 685–689.

[125] Samanta, A.; Zhou, Y.; Zou, S.; Yan, H.; Liu, Y. Fluorescence Quenching of Quantum Dots by Gold Nanoparticles: A Potential Long Range Spectroscopic Ruler. *Nano Lett.* **2014**, *14* (9), 5052–5057.

[126] Pons, T.; Medintz, I. L.; Sapsford, K. E.; Higashiya, S.; Grimes, A. F.; English, D. S.; Mattoussi, H. On the Quenching of Semiconductor Quantum Dot Photoluminescence by Proximal Gold Nanoparticles. *Nano Lett.* **2007**, *7* (10), 3157–3164.

[127] Jin, S.; DeMarco, E.; Pellin, M. J.; Farha, O. K.; Wiederrecht, G. P.; Hupp, J. T. Distance-Engineered Plasmon-Enhanced Light Harvesting in CdSe Quantum Dots. *J. Phys. Chem. Lett.* **2013**, *4* (20), 3527–3533.

[128] Zhang, X.; Marocico, C. A.; Lunz, M.; Gerard, V. A.; Gun'ko, Y. K.; Lesnyak, V.; Gaponik, N.; Susha, A. S.; Rogach, A. L.; Bradley, A. L.; et al. Distance Dependence of Nonradiative Energy Transfer to a Plane of Gold Nanoparticles. *ACS Nano* **2012**, *6* (10), 9283–9290.

[129] Vaishnav, J. K.; Mukherjee, T. K. Long-Range Resonance Coupling-Induced Surface Energy Transfer from CdTe Quantum Dot to Plasmonic Nanoparticle. *J. Phys. Chem. C* **2018**, *122* (49), 28324–28336.

[130] Saraswat, S.; Desireddy, A.; Zheng, D.; Guo, L.; Lu, H. P. P.; Bigioni, T. P. T. P.; Isailovic, D. Energy Transfer from Fluorescent Proteins to Metal Nanoparticles. *J. Phys. Chem. C* **2011**, *115* (35), 17587–17593.

[131] Chen, C.; Midelet, C.; Bhuckory, S.; Hildebrandt, N.; Werts, M. H. V. Nanosurface Energy Transfer from Long-Lifetime Terbium Donors to Gold Nanoparticles. *J. Phys. Chem. C* **2018**, *122* (30), 17566–17574.

[132] Kapur, A.; Aldeek, F.; Ji, X.; Safi, M.; Wang, W.; Del Cid, A.; Steinbock, O.; Mattoussi, H.; Sa, M.; Wang, W.; et al. Self-Assembled Gold Nanoparticle − Fluorescent Protein Conjugates as Platforms for Sensing Thiolate Compounds via Modulation of Energy Transfer Quenching. *Bioconjug. Chem.* **2017**, *28* (2), 678–687.

[133] Persson, B. N. J.; Lang, N. D. Electron-Hole-Pair Quenching of Excited States near a Metal. *Phys. Rev. B* **1982**, *26* (10), 5409–5415.

[134] Jennings, T. L.; Schlatterer, J. C.; Singh, M. P.; Greenbaum, N. L.; Strouse, G. F. LETTERS NSET Molecular Beacon Analysis of Hammerhead RNA Substrate Binding and Catalysis. *Nano Lett.* **2006**, *6* (7), 1318–1324.

[135] Yun, C. S.; Javier, A.; Jennings, T.; Fisher, M.; Hira, S.; Peterson, S.; Hopkins, B.; Reich, N. O.; Strouse, G. F. Nanometal Surface Energy Transfer in Optical Rulers, Breaking the FRET Barrier. *J. Am. Chem. Soc.* **2005**, *127* (9), 3115–3119.

[136] Becker, W. Fluorescence Lifetime Imaging--Techniques and Applications. *J. Microsc.* **2012**, *247* (2), 119–136.

[137] Lu, Y.; Zhao, J.; Zhang, R.; Liu, Y.; Liu, D.; Goldys, E. M.; Yang, X.; Xi, P.; Sunna, A.; Lu, J.; et al. Tunable Lifetime Multiplexing Using Luminescent Nanocrystals. *Nat. Photonics* **2014**, *8* (1), 32–36.

[138] Baggaley, E.; Botchway, S. W.; Haycock, J. W.; Morris, H.; Sazanovich, I. V.; Williams, J. A. G.; Weinstein, J. A. Long-Lived Metal Complexes Open up Microsecond Lifetime Imaging Microscopy under Multiphoton Excitation: From FLIM to PLIM and Beyond. *Chem. Sci.* **2014**, *5* (3), 879–886.

[139] Gan, C.; Zhang, Y.; Battaglia, D.; Peng, X.; Xiao, M. Fluorescence Lifetime of Mn-Doped ZnSe Quantum Dots with Size Dependence. *Appl. Phys. Lett.* **2008**, *92* (24), 241111.

[140] Chen, C.; Zhang, P.; Gao, G.; Gao, D.; Yang, Y.; Liu, H.; Wang, Y.; Gong, P.; Cai, L. Near-Infrared-Emitting Two-Dimensional Codes Based on Lattice-Strained Core/(Doped) Shell Quantum Dots with Long Fluorescence Lifetime. *Adv. Mater.* **2014**, *26* (36), 6313–6317.

[141] Jana, S.; Srivastava, B. B.; Jana, S.; Bose, R.; Pradhan, N. Multifunctional Doped Semiconductor Nanocrystals. *J. Phys. Chem. Lett.* **2012**, *3* (18), 2535–2540.

[142] Martín-Rodríguez, R.; Geitenbeek, R.; Meijerink, A. Incorporation and Luminescence of Yb^{3+} in CdSe Nanocrystals. *J. Am. Chem. Soc.* **2013**, *135* (37), 13668–13671.

[143] Smith, A. M.; Mohs, A. M.; Nie, S. Tuning the Optical and Electronic Properties of Colloidal Nanocrystals by Lattice Strain. *Nat. Nanotechnol.* **2009**, *4* (1), 56–63.

[144] Zhang, L.; Chen, C.; Li, W.; Gao, G.; Gong, P.; Cai, L. Living Cell Multilifetime Encoding Based on Lifetime-Tunable Lattice-Strained Quantum Dots. *ACS Appl. Mater. Interfaces* **2016**, *8* (21), 13187–13191.

[145] Jiang, K.; Wang, Y.; Cai, C.; Lin, H. Activating Room Temperature Long Afterglow of Carbon Dots via Covalent Fixation. *Chem. Mater.* **2017**, *29* (11), 4866–4873.

[146] Stamplecoskie, K. G.; Kamat, P. V. Size-Dependent Excited State Behavior of Glutathione-Capped Gold Clusters and Their Light-Harvesting Capacity. *J. Am. Chem. Soc.* **2014**, *136* (31), 11093–11099.

[147] Chen, L.-Y.; Wang, C.-W.; Yuan, Z.; Chang, H.-T. Fluorescent Gold Nanoclusters: Recent Advances in Sensing and Imaging. *Anal. Chem.* **2015**, *87* (1), 216–229.

[148] Abdukayum, A.; Chen, J. T.; Zhao, Q.; Yan, X. P. Functional near Infrared-Emitting Cr^{3+}/Pr^{3+} Co-Doped Zinc Gallogermanate Persistent Luminescent Nanoparticles with Superlong Afterglow for in Vivo Targeted Bioimaging. *J. Am. Chem. Soc.* **2013**, *135* (38), 14125–14133.

[149] Jin, D.; Piper, J. A. Time-Gated Luminescence Microscopy Allowing Direct Visual Inspection of Lanthanide-Stained Microorganisms in Background-Free Condition. *Anal. Chem.* **2011**, *83* (6), 2294–2300.

[150] Chen, C.; Corry, B.; Huang, L.; Hildebrandt, N. FRET-Modulated Multihybrid Nanoparticles for Brightness-Equalized Single-Wavelength Barcoding. *J. Am. Chem. Soc.* **2019**, *141* (28), 11123–11141.

[151] Byrne, A.; Burke, C. S.; Keyes, T. E. Precision Targeted Ruthenium(II) Luminophores; Highly Effective Probes for Cell Imaging by Stimulated Emission Depletion (STED) Microscopy. *Chem. Sci.* **2016**, *7* (10), 6551–6562.

[152] del Rosal, B.; Ortgies, D. H.; Fernández, N.; Sanz-Rodríguez, F.; Jaque, D.; Rodríguez, E. M. Overcoming Autofluorescence: Long-Lifetime Infrared Nanoparticles for Time-Gated In Vivo Imaging. *Adv. Mater.* **2016**, *28* (46), 10188–10193.

[153] Ortgies, D. H.; Tan, M.; Ximendes, E. C.; del Rosal, B.; Hu, J.; Xu, L.; Wang, X.; Martín Rodríguez, E.; Jacinto, C.; Fernandez, N.; et al. Lifetime-Encoded Infrared-

Emitting Nanoparticles for in Vivo Multiplexed Imaging. *ACS Nano* **2018**, *12* (5), 4362–4368.

[154] Fan, Y.; Wang, P.; Lu, Y.; Wang, R.; Zhou, L.; Zheng, X.; Li, X.; Piper, J. A.; Zhang, F. Lifetime-Engineered NIR-II Nanoparticles Unlock Multiplexed in Vivo Imaging. *Nat. Nanotechnol.* **2018**, *13* (10), 941–946.

[155] Smith, A. M.; Mancini, M. C.; Nie, S. Second Window for in Vivo Imaging. *Nat. Nanotechnol.* **2009**, *4* (11), 710–711.

[156] Welsher, K.; Liu, Z.; Sherlock, S. P.; Robinson, J. T.; Chen, Z.; Daranciang, D.; Dai, H. A Route to Brightly Fluorescent Carbon Nanotubes for Near-Infrared Imaging in Mice. *Nat. Nanotechnol.* **2009**, *4* (11), 773–780.

[157] Wang, Y.; Shyy, J. Y.-J.; Chien, S. Fluorescence Proteins, Live-Cell Imaging, and Mechanobiology: Seeing Is Believing. *Annu. Rev. Biomed. Eng.* **2008**, *10* (1), 1–38.

[158] Becker, W. *Advanced Time-Correlated Single Photon Counting Techniques*; Castleman, A. W., Toennies, J. P., Zinth, W., Eds.; Springer Series in Chemical Physics; Springer Berlin Heidelberg: Berlin, Heidelberg, 2005; Vol. 81.

[159] Suhling, K.; Hirvonen, L. M.; Levitt, J. a.; Chung, P.-H.; Tregidgo, C.; Le Marois, A.; Rusakov, D. a.; Zheng, K.; Ameer-Beg, S.; Poland, S.; et al. Fluorescence Lifetime Imaging (FLIM): Basic Concepts and Some Recent Developments. *Med. Photonics* **2015**, *44*, 3–40.

[160] Wu, T.-J.; Tzeng, Y.-K.; Chang, W.-W.; Cheng, C.-A.; Kuo, Y.; Chien, C.-H.; Chang, H.-C.; Yu, J. Tracking the Engraftment and Regenerative Capabilities of Transplanted Lung Stem Cells Using Fluorescent Nanodiamonds. *Nat. Nanotechnol.* **2013**, *8* (9), 682–689.

[161] Chen, C.; Zhang, P.; Zhang, L.; Gao, D.; Gao, G.; Yang, Y.; Li, W.; Gong, P.; Cai, L. Long-Decay near-Infrared-Emitting Doped Quantum Dots for Lifetime-Based in Vivo PH Imaging. *Chem. Commun.* **2015**, *51* (56), 11162–11165.

[162] Yaghini, E.; Turner, H. D.; Le Marois, A. M.; Suhling, K.; Naasani, I.; MacRobert, A. J. In Vivo Biodistribution Studies and Ex Vivo Lymph Node Imaging Using Heavy Metal-Free Quantum Dots. *Biomaterials* **2016**, *104*, 182–191.

[163] Zijlstra, P.; Chon, J. W. M.; Gu, M. Five-Dimensional Optical Recording Mediated by Surface Plasmons in Gold Nanorods. *Nature* **2009**, *459* (7245), 410–413.

[164] Han, M.; Gao, X.; Su, J. Z.; Nie, S. Quantum-Dot-Tagged Microbeads for Multiplexed Optical Coding of Biomolecules. *Nat. Biotechnol.* **2001**, *19* (7), 631–635.

[165] Pregibon, D. C.; Toner, M.; Doyle, P. S. Multifunctional Encoded Particles for High-Throughput Biomolecule Analysis. *Science* **2007**, *315* (5817), 1393–1396.

[166] Cao, Y. C.; Jin, R.; Mirkin, C. A. Nanoparticles with Raman Spectroscopic Fingerprints for DNA and RNA Detection. *Science* **2002**, *297* (5586), 1536–1540.

[167] Li, X.; Lan, T.-H.; Tien, C.-H.; Gu, M. Three-Dimensional Orientation-Unlimited Polarization Encryption by a Single Optically Configured Vectorial Beam. *Nat. Commun.* **2012**, *3* (1), 998.

[168] Leng, Y.; Sun, K.; Chen, X.; Li, W. Suspension Arrays Based on Nanoparticle-Encoded Microspheres for High-Throughput Multiplexed Detection. *Chem. Soc. Rev.* **2015**, *44* (1), 5552–5595.

[169] Andreiuk, B.; Reisch, A.; Lindecker, M.; Follain, G.; Peyriéras, N.; Goetz, J. G.; Klymchenko, A. S. Fluorescent Polymer Nanoparticles for Cell Barcoding In Vitro and In Vivo. *Small* **2017**, *13* (38), 1701582.

[170] Lu, Y.; Lu, J.; Zhao, J.; Cusido, J.; Raymo, F. M.; Yuan, J.; Yang, S.; Leif, R. C.; Huo, Y.; Piper, J. A.; et al. On-the-Fly Decoding Luminescence Lifetimes in the Microsecond Region for Lanthanide-Encoded Suspension Arrays. *Nat. Commun.* **2014**, *5* (1), 3741.

[171] Rees, P.; Wills, J. W.; Brown, M. R.; Tonkin, J.; Holton, M. D.; Hondow, N.; Brown, A. P.; Brydson, R.; Millar, V.; Carpenter, A. E.; et al. Nanoparticle Vesicle Encoding for Imaging and Tracking Cell Populations. *Nat. Methods* **2014**, *11* (11), 1177–1181.

[172] Jennings, T. L.; Becker-Catania, S. G.; Triulzi, R. C.; Tao, G.; Scott, B.; Sapsford, K. E.; Spindel, S.; Oh, E.; Jain, V.; Delehanty, J. B.; et al. Reactive Semiconductor Nanocrystals for Chemoselective Biolabeling and Multiplexed Analysis. *ACS Nano* **2011**, *5* (7), 5579–5593.

[173] Wegner, K. D.; Hildebrandt, N. Quantum Dots: Bright and Versatile in Vitro and in Vivo Fluorescence Imaging Biosensors. *Chem. Soc. Rev.* **2015**, *44* (14), 4792–4834.

[174] Gorris, H. H.; Wolfbeis, O. S. Photon-Upconverting Nanoparticles for Optical Encoding and Multiplexing of Cells, Biomolecules, and Microspheres. *Angew. Chem. Int. Ed.* **2013**, *52* (13), 3584–3600.

[175] Rogach, A. L.; Franzl, T.; Klar, T. A.; Feldmann, J.; Gaponik, N.; Lesnyak, V.; Shavel, A.; Eychmuller, A.; Rakovich, Y. P.; Donegan, J. F. Aqueous Synthesis of Thiol-Capped CdTe Nanocrystals: State-of-the-Art. *J. Phys. Chem. C* **2007**, *111* (40), 14628–14637.

[176] Faklaris, O.; Cottet, M.; Falco, A.; Villier, B.; Laget, M.; Zwier, J. M.; Trinquet, E.; Mouillac, B.; Pin, J. P.; Durroux, T. Multicolor Time-Resolved Förster Resonance Energy Transfer Microscopy Reveals the Impact of GPCR Oligomerization on Internalization Processes. *FASEB J.* **2015**, *29* (6), 2235–2246.

[177] Delbianco, M.; Sadovnikova, V.; Bourrier, E.; Mathis, G.; Lamarque, L.; Zwier, J. M.; Parker, D. Bright, Highly Water-Soluble Triazacyclononane Europium Complexes to Detect Ligand Binding with Time-Resolved FRET Microscopy. *Angew. Chem. Int. Ed.* **2014**, *53* (40), 10718–10722.

[178] Butler, S. J.; Delbianco, M.; Lamarque, L.; McMahon, B. K.; Neil, E. R.; Pal, R.; Parker, D.; Walton, J. W.; Zwier, J. M. EuroTracker® Dyes: Design, Synthesis, Structure and Photophysical Properties of Very Bright Europium Complexes and Their Use in Bioassays and Cellular Optical Imaging. *Dalt. Trans.* **2015**, *44* (11), 4791–4803.

[179] Cardoso Dos Santos, M.; Goetz, J.; Bartenlian, H.; Wong, K.-L.; Charbonnière, L. J.; Hildebrandt, N. Autofluorescence-Free Live-Cell Imaging Using Terbium Nanoparticles. *Bioconjug. Chem.* **2018**, *29* (4), 1327–1334.

[180] Gahlaut, N.; Miller, L. W. Time-Resolved Microscopy for Imaging Lanthanide Luminescence in Living Cells. In *Cytometry Part A*; 2010; Vol. 77 A, pp 1113–1125.

[181] Zwier, J. M.; Hildebrandt, N. Time-Gated FRET Detection for Multiplexed Biosensing. In *Reviews in Fluorescence 2016*; Geddes, C. D., Ed.; Springer, 2017; pp 17–43.

[182] Qiu, X.; Guo, J.; Xu, J.; Hildebrandt, N. Three-Dimensional FRET Multiplexing for DNA Quantification with Attomolar Detection Limits. *J. Phys. Chem. Lett.* **2018**, *9* (15), 4379–4384.

[183] Claussen, J. C.; Algar, W. R.; Hildebrandt, N.; Susumu, K.; Ancona, M. G.; Medintz, I. L. Biophotonic Logic Devices Based on Quantum Dots and Temporally-Staggered Förster Energy Transfer Relays. *Nanoscale* **2013**, *5* (24), 12156–12170.

[184] Qiu, X.; Hildebrandt, N. Rapid and Multiplexed MicroRNA Diagnostic Assay Using Quantum Dot-Based Förster Resonance Energy Transfer. *ACS Nano* **2015**, *9* (8), 8449–8457.

[185] Geißler, D.; Charbonnière, L. J.; Ziessel, R. F.; Butlin, N. G.; Löhmannsröben, H. G.; Hildebrandt, N. Quantum Dot Biosensors for Ultrasensitive Multiplexed Diagnostic. *Angew. Chem. Int. Ed.* **2010**, *49* (8), 1396–1401.

[186] Morgner, F.; Geißler, D.; Stufler, S.; Butlin, N. G.; Löhmannsröben, H. G.; Hildebrandt, N. A Quantum-Dot-Based Molecular Ruler for Multiplexed Optical Analysis. *Angew. Chem. Int. Ed.* **2010**, *49* (41), 7570–7574.

[187] Díaz, S. A.; Lasarte-Aragones, G.; Lowery, R. G.; Aniket; Vranish, J. N.; Klein, W. P.; Susumu, K.; Medintz, I. L. Quantum Dots as Förster Resonance Energy Transfer

Acceptors of Lanthanides in Time-Resolved Bioassays. *ACS Appl. Nano Mater.* **2018**, *1* (6), 3006–3014.

[188] Wegner, K. D.; Jin, Z.; Linden, S.; Jennings, T. L.; Hildebrandt, N. Quantum-Dot-Based Forster Resonance Energy Transfer Immunoassay for Sensitive Clinical Diagnostics of Low-Volume Serum Samples. *ACS Nano* **2013**, *7* (8), 7411–7419.

[189] Wegner, K. D.; Lindén, S.; Jin, Z.; Jennings, T. L.; Khoulati, R. el; van Bergen en Henegouwen, P. M. P.; Hildebrandt, N. Nanobodies and Nanocrystals: Highly Sensitive Quantum Dot-Based Homogeneous FRET Immunoassay for Serum-Based EGFR Detection. *Small* **2014**, *10* (4), 734–740.

[190] Wegner, K. D.; Lanh, P. T.; Jennings, T.; Oh, E.; Jain, V.; Fairclough, S. M.; Smith, J. M.; Giovanelli, E.; Lequeux, N.; Pons, T.; et al. Influence of Luminescence Quantum Yield, Surface Coating, and Functionalization of Quantum Dots on the Sensitivity of Time-Resolved FRET Bioassays. *ACS Appl. Mater. Interfaces* **2013**, *5* (8), 2881–2892.

[191] Wegner, K. D.; Morgner, F.; Oh, E.; Goswami, R.; Susumu, K.; Stewart, M. H.; Medintz, I. L.; Hildebrandt, N. Three-Dimensional Solution-Phase Förster Resonance Energy Transfer Analysis of Nanomolar Quantum Dot Bioconjugates with Subnanometer Resolution. *Chem. Mater.* **2014**, *26* (14), 4299–4312.

[192] Qiu, X.; Wegner, K. D.; Wu, Y.; van Bergen en Henegouwen, P. M. P.; Jennings, T. L.; Hildebrandt, N. Nanobodies and Antibodies for Duplexed EGFR/HER2 Immunoassays Using Terbium-to-Quantum Dot FRET. *Chem. Mater.* **2016**, *28* (22), 8256–8267.

[193] Annio, G.; Jennings, T. L.; Tagit, O.; Hildebrandt, N. Sensitivity Enhancement of Förster Resonance Energy Transfer Immunoassays by Multiple Antibody Conjugation on Quantum Dots. *Bioconjug. Chem.* **2018**, *29* (6), 2082–2089.

[194] Dagher, M.; Kleinman, M.; Ng, A.; Juncker, D. Ensemble Multicolour FRET Model Enables Barcoding at Extreme FRET Levels. *Nat. Nanotechnol.* **2018**, *13* (10), 925–932.

[195] Xing, Y.; Chaudry, Q.; Shen, C.; Kong, K. Y.; Zhau, H. E.; Chung, L. W.; Petros, J. A.; O'Regan, R. M.; Yezhelyev, M. V; Simons, J. W.; et al. Bioconjugated Quantum Dots for Multiplexed and Quantitative Immunohistochemistry. *Nat. Protoc.* **2007**, *2* (5), 1152–1165.

[196] Reiss, P.; Protière, M.; Li, L. Core/Shell Semiconductor Nanocrystals. *Small* **2009**, *5* (2), 154–168.

[197] Wu, P.; Yan, X.-P. Doped Quantum Dots for Chemo/Biosensing and Bioimaging. *Chem. Soc. Rev.* **2013**, *42* (12), 5489–5521.

[198] Smith, A. M.; Nie, S. Semiconductor Nanocrystals: Structure, Properties, and Band Gap Engineering. *Acc. Chem. Res.* **2010**, *43* (2), 190–200.

[199] Lim, S. J.; Zahid, M. U.; Le, P.; Ma, L.; Entenberg, D.; Harney, A. S.; Condeelis, J.; Smith, A. M. Brightness-Equalized Quantum Dots. *Nat. Commun.* **2015**, *6* (1), 8210.

[200] Arppe-Tabbara, R.; Carro-Temboury, M. R.; Hempel, C.; Vosch, T.; Sørensen, T. J. Luminescence from Lanthanide(III) Ions Bound to the Glycocalyx of Chinese Hamster Ovary Cells. *Chem. - A Eur. J.* **2018**, *24* (46), 11885–11889.

[201] Grabolle, M.; Kapusta, P.; Nann, T.; Shu, X.; Ziegler, J.; Resch-Genger, U. Fluorescence Lifetime Multiplexing with Nanocrystals and Organic Labels. *Anal. Chem.* **2009**, *81* (18), 7807–7813.

[202] Hoffmann, K.; Behnke, T.; Drescher, D.; Kneipp, J.; Resch-Genger, U. Near-Infrared-Emitting Nanoparticles for Lifetime-Based Multiplexed Analysis and Imaging of Living Cells. *ACS Nano* **2013**, *7* (8), 6674–6684.

[203] Hoffmann, K.; Behnke, T.; Grabolle, M.; Resch-Genger, U. Nanoparticle-Encapsulated Vis- and NIR-Emissive Fluorophores with Different Fluorescence Decay Kinetics for Lifetime Multiplexing. *Anal. Bioanal. Chem.* **2014**, *406* (14), 3315–3322.

[204] Qiu, X.; Guo, J.; Jin, Z.; Petreto, A.; Medintz, I. L.; Hildebrandt, N. Multiplexed Nucleic Acid Hybridization Assays Using Single-FRET-Pair Distance-Tuning. *Small* **2017**, *13* (25), 1700332.

[205] Liao, Z.; Tropiano, M.; Faulkner, S.; Vosch, T.; Sørensen, T. J. Time-Resolved Confocal Microscopy Using Lanthanide Centred near-IR Emission. *RSC Adv.* **2015**, *5* (86), 70282–70286.

[206] Carro-Temboury, M. R.; Arppe, R.; Vosch, T.; Sørensen, T. J. An Optical Authentication System Based on Imaging of Excitation-Selected Lanthanide Luminescence. *Sci. Adv.* **2018**, *4* (1), e1701384.

[207] Xiong, R.; Mara, D.; Liu, J.; Van Deun, R.; Borbas, K. E. Excitation- and Emission-Wavelength-Based Multiplex Spectroscopy Using Red-Absorbing Near-Infrared-Emitting Lanthanide Complexes. *J. Am. Chem. Soc.* **2018**, *140* (35), 10975–10979.

[208] Kovacs, D.; Lu, X.; Mészáros, L. S.; Ott, M.; Andres, J.; Borbas, K. E. Photophysics of Coumarin and Carbostyril-Sensitized Luminescent Lanthanide Complexes: Implications for Complex Design in Multiplex Detection. *J. Am. Chem. Soc.* **2017**, *139* (16), 5756–5767.

[209] Guo, J.; Mingoes, C.; Qiu, X.; Hildebrandt, N. Simple, Amplified, and Multiplexed Detection of MicroRNAs Using Time-Gated FRET and Hybridization Chain Reaction. *Anal. Chem.* **2019**, *91* (4), 3101–3109.

[210] Guo, J.; Qiu, X.; Mingoes, C.; Deschamps, J. R.; Susumu, K.; Medintz, I. L.; Hildebrandt, N. Conformational Details of Quantum Dot-DNA Resolved by Förster Resonance Energy Transfer Lifetime Nanoruler. *ACS Nano* **2019**, *13* (1), 505–514.

[211] Kang, J.; Kaczmarek, O.; Liebscher, J.; Dähne, L. Prevention of H-Aggregates Formation in Cy5 Labeled Macromolecules. *Int. J. Polym. Sci.* **2010**, *2010*, 1–7.

[212] Selvin, P. R. The Renaissance of Fluorescence Resonance Energy Transfer. *Nat. Struct. Biol.* **2000**, *7* (9), 730–734.

[213] Ha, T. Single-Molecule Fluorescence Resonance Energy Transfer. *Methods* **2001**, *86* (1), 78–86.

[214] Weiss, S. Measuring Conformational Dynamics of Biomolecules by Single Molecule Fluorescence Spectroscopy. *Nat. Struct. Biol.* **2000**, *7* (9), 724–729.

[215] Sekar, R. B.; Periasamy, A. Fluorescence Resonance Energy Transfer (FRET) Microscopy Imaging of Live Cell Protein Localizations. *J. Cell Biol.* **2003**, *160* (5), 629–633.

[216] Li, M.; Cushing, S. K.; Wang, Q.; Shi, X.; Hornak, L. A.; Hong, Z.; Wu, N. Size-Dependent Energy Transfer between CdSe/ZnS Quantum Dots and Gold Nanoparticles. *J. Phys. Chem. Lett.* **2011**, *2* (17), 2125–2129.

[217] Guo, W.; Wei, Y.; Dai, Z.; Chen, G.; Chu, Y.; Zhao, Y. Nanostructure and Corresponding Quenching Efficiency of Fluorescent DNA Probes. *Materials (Basel).* **2018**, *11* (2), 272.

[218] Li, N.; Chang, C.; Pan, W.; Tang, B. A Multicolor Nanoprobe for Detection and Imaging of Tumor-Related MRNAs in Living Cells. *Angew. Chem. Int. Ed.* **2012**, *51* (30), 7426–7430.

[219] Vilela, P.; Heuer-Jungemann, A.; El-Sagheer, A.; Brown, T.; Muskens, O. L.; Smyth, N. R.; Kanaras, A. G. Sensing of Vimentin MRNA in 2D and 3D Models of Wounded Skin Using DNA-Coated Gold Nanoparticles. *Small* **2018**, *14* (12), 1703489.

[220] Zhong, Y.; Zeng, F.; Chen, J.; Wu, S.; Hou, C.; Tong, Z. Modulation of Fluorescence of a Terbium-Complex-Containing Polymer by Gold Nanoparticles through Energy Transfer. *J. Inorg. Organomet. Polym. Mater.* **2007**, *17* (4), 679–685.

[221] Comby, S.; Gunnlaugsson, T. Luminescent Lanthanide-Functionalized Gold Nanoparticles: Exploiting the Interaction with Bovine Serum Albumin for Potential Sensing Applications. *ACS Nano* **2011**, *5* (9), 7184–7197.

[222] Ipe, B. I.; Yoosaf, K.; Thomas, K. G. Functionalized Gold Nanoparticles as Phosphorescent Nanomaterials and Sensors. *J. Am. Chem. Soc.* **2006**, *128* (6), 1907–1913.

[223] Hendrickson, W. A.; Pahler, A.; Smith, J. L.; Satow, Y.; Merritt, E. A.; Phizackerley, R. P. Crystal Structure of Core Streptavidin Determined from Multiwavelength Anomalous Diffraction of Synchrotron Radiation. *Proc. Natl. Acad. Sci.* **1989**, *86* (7), 2190–2194.

[224] Navarro, J. R. G.; Werts, M. H. V. Resonant Light Scattering Spectroscopy of Gold, Silver and Gold–silver Alloy Nanoparticles and Optical Detection in Microfluidic Channels. *Analyst* **2013**, *138* (2), 583–592.

[225] Loumaigne, M.; Midelet, C.; Doussineau, T.; Dugourd, P.; Antoine, R.; Stamboul, M.; Débarre, A.; Werts, M. H. V. Optical Extinction and Scattering Cross Sections of Plasmonic Nanoparticle Dimers in Aqueous Suspension. *Nanoscale* **2016**, *8* (12), 6555–6570.

[226] Midelet, J.; El-Sagheer, A. H.; Brown, T.; Kanaras, A. G.; Débarre, A.; Werts, M. H. V. Spectroscopic and Hydrodynamic Characterisation of DNA-Linked Gold Nanoparticle Dimers in Solution Using Two-Photon Photoluminescence. *ChemPhysChem* **2018**, *19* (7), 827–836.

[227] Deželić, G.; Kratohvil, J. P. Determination of Size of Small Particles by Light Scattering. Experiments on Ludox Colloidal Silica. *Kolloid-Zeitschrift* **1960**, *173* (1), 38–48.

[228] Englebienne, P. Use of Colloidal Gold Surface Plasmon Resonance Peak Shift to Infer Affinity Constants from the Interactions between Protein Antigens and Antibodies Specific for Single or Multiple Epitopes. *Analyst* **1998**, *123* (7), 1599–1603.

[229] Ghosh, S. K.; Pal, T. Interparticle Coupling Effect on the Surface Plasmon Resonance of Gold Nanoparticles: From Theory to Applications. *Chem. Rev.* **2007**, *107* (11), 4797–4862.

[230] Hildebrandt, N. How to Apply FRET: From Experimental Design to Data Analysis. In *FRET – Förster Resonance Energy Transfer*; Medintz, I., Hildebrandt, N., Eds.; Wiley-VCH Verlag GmbH and Co. KGaA: Weinheim, Germany, 2013; pp 105–163.

[231] Wu, P.; Brand, L. Resonance Energy Transfer: Methods and Applications. *Anal. Biochem.* **1994**, *218* (1), 1–13.

[232] Sillen, A.; Engelborghs, Y. The Correct Use of "Average" Fluorescence Parameters. *Photochem. Photobiol.* **1998**, *67* (5), 475–486.

[233] Loumaigne, M.; Praho, R.; Nutarelli, D.; Werts, M. H. V; Débarre, A. Fluorescence Correlation Spectroscopy Reveals Strong Fluorescence Quenching of FITC Adducts on PEGylated Gold Nanoparticles in Water and the Presence of Fluorescent Aggregates of Desorbed Thiolate Ligands. *Phys. Chem. Chem. Phys.* **2010**, *12* (36), 11004.

[234] Navarro, J. R. G.; Plugge, M.; Loumaigne, M.; Sanchez-Gonzalez, A.; Mennucci, B.; Débarre, A.; Brouwer, A. M.; Werts, M. H. V. Probing the Interactions between Disulfide-Based Ligands and Gold Nanoparticles Using a Functionalised Fluorescent Perylene-Monoimide Dye. *Photochem. Photobiol. Sci.* **2010**, *9* (7), 1042–1054.

[235] Nerambourg, N.; Praho, R.; Werts, M. H. V.; Thomas, D.; Desce, M. B. Hydrophilic Monolayer-Protected Gold Nanoparticles and Their Functionalisation with Fluorescent Chromophores. *Int. J. Nanotechnol.* **2008**, *5* (6/7/8), 722.

[236] Huang, T.; Murray, R. W. Quenching of $[Ru(Bpy)_3]^{2+}$ Fluorescence by Binding to Au Nanoparticles. *Langmuir* **2002**, *18* (18), 7077–7081.

[237] Ji, X.; Wang, W.; Mattoussi, H. Controlling the Spectroscopic Properties of Quantum Dots via Energy Transfer and Charge Transfer Interactions: Concepts and Applications. *Nano Today* **2016**, *11* (1), 98–121.

[238] Selvin, P. R.; Hearst, J. E. Luminescence Energy Transfer Using a Terbium Chelate: Improvements on Fluorescence Energy Transfer. *Proc. Natl. Acad. Sci.* **1994**, *91* (21), 10024–10028.

[239] Bohren, C. F.; Huffman, D. R. *Absorption and Scattering of Light by Small Particles*; Bohren, C. F., Huffman, D. R., Eds.; Wiley-VCH Verlag GmbH: Weinheim, Germany, 1998.

[240] Berberan-Santos, M. N.; Bodunov, E. N.; Valeur, B. Mathematical Functions for the Analysis of Luminescence Decays with Underlying Distributions 1. Kohlrausch Decay Function (Stretched Exponential). *Chem. Phys.* **2005**, *315* (1–2), 171–182.

[241] Johnston, D. C. Stretched Exponential Relaxation Arising from a Continuous Sum of Exponential Decays. *Phys. Rev. B* **2006**, *74* (18), 184430.

[242] Zwier, J. M.; Van Rooij, G. J.; Hofstraat, J. W.; Brakenhoff, G. J. Image Calibration in Fluorescence Microscopy. *J. Microsc.* **2004**, *216* (1), 15–24.

[243] Newville, M.; Stensitzki, T.; Allen, D. B.; Ingargiola, A. LMFIT: Non-Linear Least-Square Minimization and Curve-Fitting for Python; Zenodo. 10.5281/Zenodo.11813. *Zenodo* **2014**.

9. Synthèse en français

« Toute science commence comme philosophie et se termine en art ; elle surgit dans l'hypothèse et coule dans l'accomplissement ».

— Will Durant

Cette citation est extraite du livre intitulé « Histoire de la philosophie ». Nous pouvons également l'appeler « La beauté de la philosophie ». Nous savons que la philosophie naturelle est considérée comme le précurseur des sciences naturelles. Mais pourquoi chaque science se termine en art ? Qu'est-ce que l'art? À mon avis, l'art est l'expression d'idées originales, conceptuelles et imaginatives, avec une habileté technique et un pouvoir émotionnel, ou on peut aussi dire que la beauté est un art. L'identité d'Euler montre un lien profond entre les nombres les plus fondamentaux en mathématiques et en montre la beauté mathématique. Les équations de Maxwell établissent une théorie électromagnétique unifiée. Ils associent électricité, magnétisme et lumière en tant que différentes manifestations du même phénomène et témoignent de la beauté physique. Je veux aussi découvrir la beauté dans mon domaine de recherche, et je pense que cela existe déjà.

Figure 1.1. Le travail imitatif de « La persistance de la mémoire » (à gauche) et le tableau original de Salvador Dali (à droite)

Le but de cette thèse est d'étudier le mécanisme de transfert d'énergie par

résonance de type Förster (FRET) dans des systèmes basés sur les lanthanides-points quantiques (QD)-colorants fluorescents et d'utiliser la nanoparticule multi-hybride modulée par FRET pour le multiplexage résolu en temps et l'étude du mécanisme de transfert d'énergie des terbium (Tb) à longue durée de vie de photoluminescence aux nanoparticules d'or (AuNPs). Le multiplexage résolu en temps présente de nombreux avantages et nous trouvons également la beauté du multiplexage temporel. Les trois fenêtres de détection optique temporelles peuvent être considérées comme une métaphore des trois horloges de « La persistance de la mémoire» de Dali (**Figure 1.1**, à droite). Inspiré par ce tableau, nous avons conçu une image (**Figure 1.1**, à gauche), dans laquelle les trois horloges de couleur rouge, verte et bleue représentent parfaitement l'idée de celle utilisée pour le codage à barres RVB (rouge, vert, bleu). D'autres objets de cette peinture ont également été remplacés par des éléments utilisés dans notre étude, notamment une nanoparticule (l'horloge orange recouverte de fourmis dans l'original) en bas à gauche, un objectif de microscope (le « monstre » dans l'original) au centre (en dessous de l'horloge bleue) et une lame de microscope avec des cellules de codage (la plate-forme ou le bassin dans l'original) en haut à gauche.

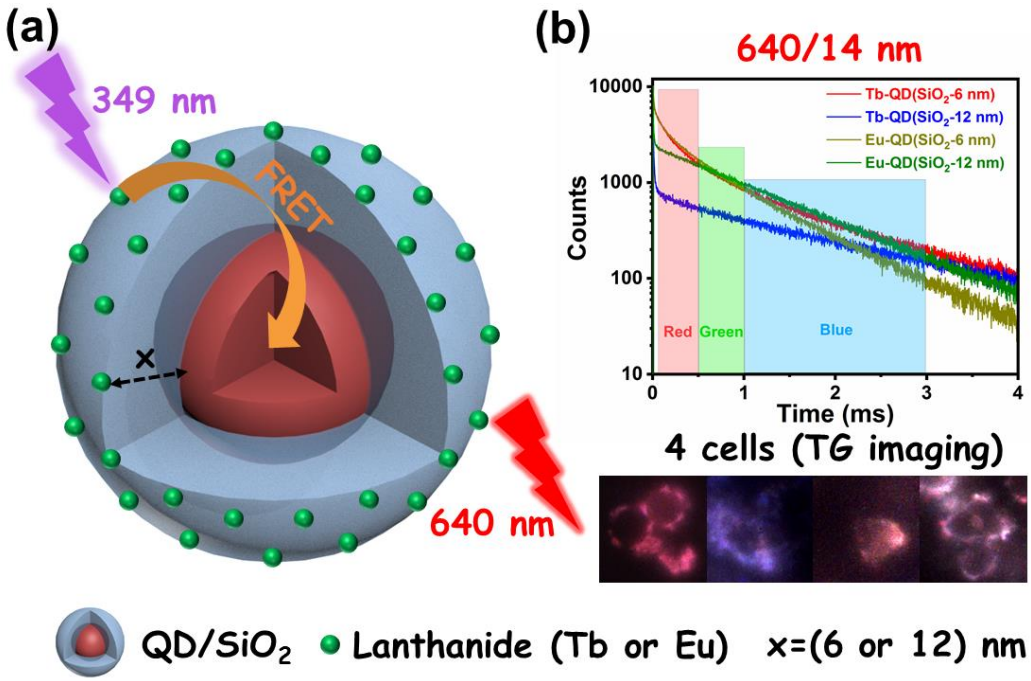

Figure 1.2. (a) QDs avec des couches SiO_2 d'épaisseurs différentes (x = 6 ou 12 nm) fonctionnalisés avec Eu-1 ou Lumi4-Tb pour le codage à barres temporel PL à longueur d'onde unique. (b) Le principe de codage RGB basé sur trois fractions d'intensité TG distinctes pour chacune des quatre durées de vies PL spécifiques au FRET et quatre cellules codées.

Après cette introduction, une présentation théorique du transfert d'énergie par résonance, des QDs, des lanthanides luminescents, des colorants fluorescents, des AuNPs et des mesures résolues en temps sera présentée (**chapitre 2**). Trois études expérimentales suivront sous forme de papier avec une introduction, du matériel et une méthode, des résultats et une discussion, ainsi qu'une conclusion. Un résumé des résultats des études expérimentales sera présenté et un aperçu des recherches futures. Annexe et bibliographie suivent à la fin de la thèse.

La première étude (**chapitre 3**) illustre la possibilité du codage à barres des cellules à une nanoparticule unique basée sur le FRET de complexe de lanthanides à QD. Afin d'obtenir le codage optique avec une capacité supérieure, la majorité du principe consistait à mélanger différentes molécules luminescentes ou nanoparticules dans des microbilles ou des cellules. Concevoir différents codes indépendants de la concentration sans mélanger diverses nanoparticules et utiliser une seule source d'excitation et une émission pour une imagerie multiplexée est extrêmement difficile. Comme illustré dans la **Figure 1.2**, nous rapportons la synthèse des QDs revêtus de SiO_2 avec des coquilles d'épaisseurs différentes (6 et 12 nm). La fixation de complexes de lanthanide (Ln) (Tb ou Eu) avec de longues durées de vies de photoluminescence (PL) sur les coquilles de SiO_2 ont entraînés des distances différentes de Ln à QD, ce qui a conduit à des durées de vies PL différentes en raison de la dépendance en distance du FRET. Ainsi, quatre durées de vies PL QD spécifiques (toutes à 640 nm lors suivant excitation des complexes Ln à 349 nm) ont été conçues avec Tb-QD (SiO_2-6nm), Tb-QD (SiO_2-12nm), Eu-QD (SiO_2-6nm) et Eu-QD (SiO_2-12nm) et utilisés comme codes bien définis à une particule unique pour marquer des cellules vivantes. Pour reconnaître les codes de cellules vivantes, la microscopie à fluorescence résolue en temps a été utilisée et quatre types de cellules différentes ont pu être distingués par une seule mesure. La densité d'informations du codage d'une seule particule peut être encore augmentée en utilisant des donneurs avec divers complexes de Ln et des accepteurs de QDs avec différentes couleurs. Ainsi, notre concept de FRET Ln-à-QD résolu en temps a le potentiel de faire progresser considérablement le codage des cellules de fluorescence. Cependant, un inconvénient important de cette stratégie est la variation significative de la luminosité des différents codes. Nous

aborderons ce problème dans la deuxième étude.

La seconde étude (**chapitre 4**) porte sur plusieurs systèmes de FRET donneurs-accepteurs avec des QDs. Les QDs sont les fluorophores les plus polyvalents pour le FRET car ils peuvent fonctionner à la fois comme donneur et accepteur pour une multitude de fluorophores fixés à leur surface. Cependant, une compréhension complète des réseaux de FRET multi-donneurs-accepteurs sur les QD et leur utilisation avancée dans la détection et l'imagerie de fluorescence n'ont pas été accomplies. Dans ce chapitre, nous proposons une analyse photophysique globale de tels systèmes de FRET multi-donneurs-QD-multi-accepteurs, à l'aide de la spectroscopie résolue en temps et à l'état stationnaire, ainsi que de simulations de Monte Carlo. Plusieurs donneurs du complexe terbium (Tb) (1 à 191 unités) et des accepteurs du colorant Cy5.5 (1 à 60 unités) ont été attachés à un QD central et la gamme complète de combinaisons de voies simples et multiples de FRET a été étudiée par la PL du Tb, QD et Cy5.5. Les résultats expérimentaux et de simulation étaient en excellent accord et pouvaient démêler les contributions distinctes de l'hétéro-FRET, de l'homo-FRET et de la dimérisation par le colorant. L'efficacité du FRET était indépendante du nombre de donneurs de Tb et dépendante du nombre d'accepteurs de Cy5.5, ce qui pourrait être utilisé pour adapter indépendamment l'intensité de la PL en fonction du nombre de donneurs de Tb et de sa durée de vie en fonction du nombre d'accepteurs de Cy5.5. Comme le montre la **Figure 1.3**, nous avons utilisé cette capacité de réglage unique pour préparer des conjugués Tb-QD-Cy5.5 avec des durées de vie PL de QDs différentes, mais des intensités PL des QDs similaires. Ces nanoparticules de FRET multi-hybrides à égalisation de luminosité ont été appliquées au codage à barres optique via trois fenêtres de détection d'intensité de PL résolue en temps, ce qui a abouti à un codage des courbes de durées de vie de PL distinctes en simples rapports RVB. L'applicabilité directe a été démontrée par une distinction RVB efficace de différentes microbilles codées par des nanoparticules dans le même champ de vision, avec excitation à une seule longueur d'onde et détection sur un microscope à fluorescence standard. En plus de l'imagerie et de la biodétection, le réglage photophysique contrôlé de QD multi-hybrides modulés par FRET pour le codage PL à longueur d'onde unique peut faire progresser d'autres applications

photoniques, telles que le stockage de données, l'étiquetage de sécurité, l'optogénétique ou l'informatique moléculaire.

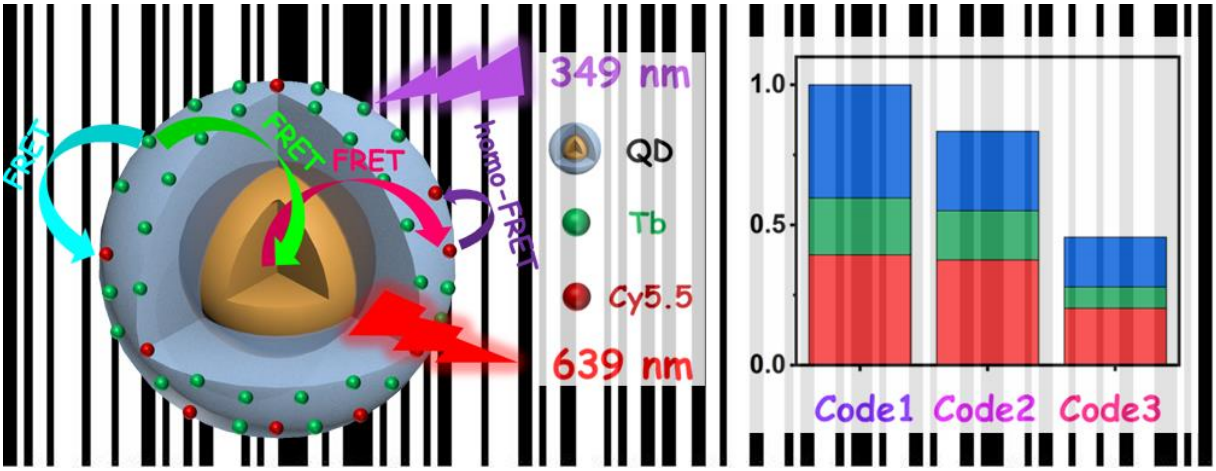

Figure 1.3. Nanoparticules multi-hybrides modulées par FRET pour le codage à barres à longueur d'onde unique et égalisation de la luminosité.

La troisième étude (**chapitre 5**) tente de comprendre le mécanisme de transfert d'énergie des donneurs de Tb à longue durée de vie aux AuNPs. L'application de l'extinction des PL par les AuNPs a élargi les possibilités d'application des méthodologies de sondes optiques en biochimie, biodiagnostic et imagerie biomoléculaire. Comprendre le mécanisme de transfert d'énergie joue un rôle fondamental dans le développement de méthodologies de règles optiques. Le transfert d'énergie par résonance de type Förster (FRET, dépendance en distance ~ R^{-6}) et le transfert d'énergie à la nanosurface (NSET, dépendance à la distance ~ R^{-4}) ont été considérés comme la théorie correcte pour le mécanisme d'extinction de la PL. Cependant, des différences significatives entre la dépendance à la distance de ces deux mécanismes de transfert d'énergie par résonance peuvent entraîner de fortes variations dans le processus de transfert d'énergie. Dans ce chapitre, nous étudions la diminution de la durée de vie des complexes de terbium (Tb) conjugués à la streptavidine lorsqu'ils sont liés à des NP Au-biotinylés de différents diamètres (5, 30, 50 et 80 nm) (**Figure 1.4**). La liaison de la streptavidine marquée au Tb (Tb-sAv) à des AuNPs biotinylés (biot-AuNPs) a été étudiée par spectroscopie de diffusion de la lumière. La diminution de la PL de Tb-sAv lors de sa liaison à des biot-AuNP de différents diamètres (5, 30, 50, 80 nm) a été étudiée par spectroscopie de PL résolue en temps. Les efficacités de transfert d'énergie se

sont avérées pratiquement indépendantes de la taille de l'AuNP. L'analyse selon la théorie FRET a donné des distances donneur-accepteur incohérentes et bien au-delà de la distance attendue Tb-AuNP. En revanche, le modèle NSET a donné un bon accord entre la distance de surface de Tb à AuNP estimée à partir de la géométrie de l'ensemble Tb-sAv / biotine-AuNP (4,5 nm) et celles calculées à partir de l'analyse de la durée de vie PL, allant de 4,0 à 6,3 nm. Nos résultats suggèrent fortement que NSET (et non FRET) est le mécanisme opérationnel dans l'extinction de la PL par les AuNPs, une information importante pour le développement, la caractérisation et l'application de nanobiocapteurs basés sur l'extinction de PL par les AuNP.

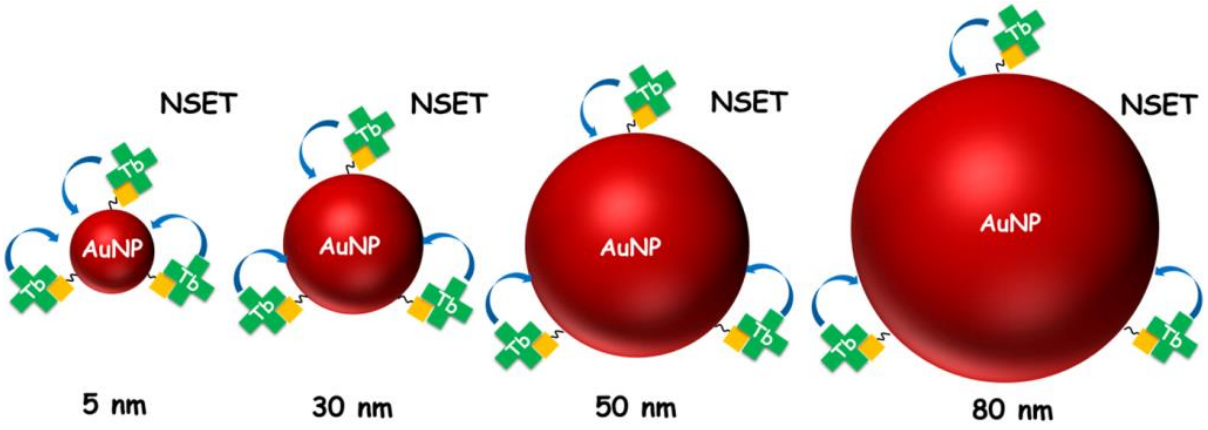

Figure 1.4. Modèle NSET utilisant de la streptavidine (sAv) marqués au Tb et des NP-Au biotinylés.

Dans l'ensemble, cette thèse permet de mieux comprendre le transfert d'énergie aux AuNP et au multi donneur / acceptor par FRET avec des semi-conducteurs QD et présente de nouveaux concepts de multiplexage d'ordre supérieur pour la biodétection et l'imagerie avancées.

université PARIS-SACLAY

ÉCOLE DOCTORALE
Physique et ingénierie : électrons, photons, sciences du vivant (EOBE)

Titre : Transfert d'énergie entre lanthanides et nanoparticules: des mécanismes fondamentaux aux biosenseurs multiplexés

Mots clés : points quantiques, terbium, multiplexage, fluorescence, code à barres, FRET

Résumé : Le multiplexage optique basé sur des nanoparticules offre de nombreux avantages pour la biodétection et l'imagerie à multiparamètres. Toutefois, les modifications apportées à un paramètre entraînent également la modification d'autres paramètres. Par conséquent, la couleur, la durée de vie ou l'intensité ne peuvent pas être utilisées, respectivement, comme paramètre indépendant. Cette thèse peut être divisée en deux aspects. Le premier concerne le développement d'un multiplexage à une seule nanoparticule avec un temps résolu, basé sur le transfert d'énergie par résonance de type Förster (FRET) des complexes de lanthanides aux points quantiques (QD) et ensuite aux colorants fluorescents. Une investigation systématique de toutes les différentes combinaisons avec une large gamme de donneurs et d'accepteurs sur le QD est présentée, et les résultats expérimentaux sont comparés à la modélisation théorique. Le résultat ne contribue pas seulement à une compréhension complète de ces voies de transfert d'énergie compliquée entre multi donneurs / accepteurs sur des nanoparticules, mais offre également la possibilité d'utiliser les modèles pour développer de nouvelles stratégies permettant de preparer le QD avec une couleur, une durée de vie et une intensité réglables de manière indépendante. Le deuxième aspect porte sur le mécanisme de transfert d'énergie du Tb à la nanoparticule d'or (AuNP). Le transfert d'énergie par nanosurface (NSET) s'est révélé être un mécanisme opérationnel pour l'extinction des PL par les AuNP, une information importante pour le développement, la caractérisation et l'application de nanobiocapteurs basés sur l'extinction des PL par les AuNP.

Title : Lanthanide energy transfer donors on nanoparticles surfaces: from fundamental mechanisms to multiplexed biosensing

Keywords : quantum dots, terbium, multiplexing, fluorescence, barcoding, FRET

Abstract : Optical multiplexing based on nanoparticles provides many advantages for multiparameter biosensing and imaging. However, the changes in one parameter also lead to changing of other parameters, and thus, color, lifetime, or intensity could not be used as an independent parameter, respectively. This thesis can be divided into two aspects. The first one focuses on developing time-resolved single-nanoparticle multiplexing based on Förster resonance energy transfer (FRET) from lanthanide complexes to quantum dot (QD) to fluorescent dyes. Systematical investigation of all different combinations with a broad range of numbers of donors and acceptors on QD are presented, and the experimental results are compared with theoretical modelling. The result do not only contribute to a full understanding of such complicated multi donor-acceptor energy transfer pathways on nanoparticles but also open the opportunity to use the models for developing new strategies to achieve the QD with independent tunable color, lifetime and intensity. The second aspect focuses on the energy transfer mechanism from Tb to gold nanoparticle (AuNP). Nanosurface energy transfer (NSET) proved to be an operational mechanism in PL quenching by AuNPs, which is important information for the development, characterization, and application of nanobiosensors based on PL quenching by AuNPs.

Université Paris-Saclay
Espace Technologique / Immeuble Discovery
Route de l'Orme aux Merisiers RD 128 / 91190 Saint-Aubin, France